Development of a Free-Running Readout ASIC for the $\overline{\text{P}}$ANDA Micro Vertex Detector and Investigation of the Performance to Reconstruct $\overline{\text{p}}\text{p} \rightarrow \overline{\Xi}^{+}\Xi^{-}(1690)$

Dissertation

zur Erlangung des Grades eines
Doktors der Naturwissenschaften

in der Fakultät für Physik und Astronomie
der Ruhr-Universität Bochum

von
André Zambanini
geb. Goerres

aus
Aachen

Bochum (2015)

Versicherung gemäß §7 Abs. 2 Nr. 6 PromO 2011
Hiermit versichere ich, dass ich meine Dissertation selbstständig und ohne unerlaubte fremde Hilfen angefertigt und verfasst habe und keine anderen als die angegebenen Hilfsmittel und Hilfen benutzt habe. Meine Dissertation habe ich in dieser oder ähnlicher Form noch bei keiner anderen Fakultät der Ruhr-Universität Bochum oder bei einer anderen Hochschule eingereicht.

Erster Gutachter:	Prof. James Ritman, Ph.D.
Zweiter Gutachter:	Prof. Dr. Ulrich Wiedner
Datum der Abgabe:	21.07.2015
Datum der Disputation:	08.12.2015

Contents

Abstract

The $\bar{\text{P}}$ANDA experiment is a multi-purpose particle detector, investigating hadron physics topics in the strange and charm quark mass regime. $\bar{\text{P}}$ANDA will measure antiproton-proton annihilation reactions at the Facility for Antiproton and Ion Research, which is currently under construction. The $\bar{\text{p}}$p annihiliations give rise to a broad physics program, including hyperon studies on ground and excited cascade states. Here, experimental input is required to verify the production models. However, the signal event signatures from $\bar{\text{p}}$p annihiliations are similar to background processes making it impossible to preselect interesting events based on a few, fast sub-detectors that start the readout of the complete detector. Hence, self-triggering readout electronics is required throughout all sub-detectors. The innermost sub-detector, the Micro Vertex Detector, is based on silicon sensors with pixel and microstrip segmentation. This thesis describes the development of a readout solution (PASTA) for the microstrip sensors and the preparations for a characterization setup to perform laboratory measurements with this readout prototype. Furthermore, an exploratory study on the reconstructability of the reaction $\bar{\text{p}}\text{p} \to \bar{\Xi}^{+}\Xi^{-}(1690)$ with $\bar{\text{P}}$ANDA's software framework is presented.

Das $\bar{\text{P}}$ANDA-Experiment ist ein Vielzweck-Teilchendetektor, der hadronenphysikalische Themen im Bereich der Strange- und Charm-Quark-Massen untersuchen wird. Dazu wird $\bar{\text{P}}$ANDA am im Bau befindlichen FAIR-Komplex Vernichtungsreaktionen von Antiprotonen und Protonen messen. Diese Reaktionen ermöglichen ein vielfältiges Physikprogramm, einschließlich der Messung von Hyperonen im Grund- und angeregten Zuständen. Um die Produktionsmodelle zu verifizieren sind experimentelle Daten nötig. Allerdings weisen die Signal-Signaturen der Vernichtungsreaktion Ähnlichkeiten zu den Signaturen von Hintergrundereignissen auf, weshalb es nicht möglich ist aufgrund von wenigen, schnellen Teildetektoren eine Selektion vorzunehmen. Daher muss die Ausleseelektronik des gesamten Detektors autonom über die Datennahme entscheiden. Der innerste Teildetektor, der Mikro-Vertex-Detektor, basiert auf Silizium-Sensoren, die in Pixel- und Mikrostreifen segmentiert sind. Diese Arbeit beschreibt die Entwicklung einer integrierten Schaltung (PASTA) zur Auslese der Mikrostreifen sowie der Vorbereitung eines Auslesesystems für Charakterisierungsmessungen im Labor. Außerdem wird die Untersuchung der Rekonstruierbarkeit der Reaktion $\bar{\text{p}}\text{p} \to \bar{\Xi}^{+}\Xi^{-}(1690)$ mit $\bar{\text{P}}$ANDAs Software-Framework präsentiert.

1 Preface

Formulating models that describe nature is an important step towards the understanding of the underlying processes. Being able to explain the inner structure of an object can corroborate a describing model for it. Over time, smaller and smaller structures have been found. The atom, previously thought to be the elementary component of matter, showed an internal structure in the α particle scattering experiments performed by Rutherford at the beginning of the 20th century.

Since then, the smallest detectable structures shrunk to the elementary particles known today: quarks and leptons. They are described by the Standard Model of Physics (SM) along with their fundamental interactions. The SM was developed throughout the latter half of the 20th century, driven by theoretical and experimental physicists' efforts alike. Even though the Standard Model demonstrates great success in predicting the experimental results, it is not able to describe all observed phenomena. An example is the mass of hadrons, which cannot be solely explained by the mass of their valence quarks. Comprehensive measurements of the particles' properties are required to formulate and validate new models and achieve a deeper understanding of the strong interaction itself.

The increasingly demanding experimental requirements lead to large-scale experiments that are pushing the boundaries of technical feasibility. One of these experiments is the future multi-purpose detector Antiproton Annihilation at Darmstadt ($\bar{\text{P}}$ANDA) at the FAIR facility, which is currently under construction. $\bar{\text{P}}$ANDA is operated with an antiproton beam with center-of-mass energies of up to $\sqrt{s} = 5.5\,\text{GeV}$, enabling investigations of hadrons with strange and charm quarks up to excited charmonium states. One particular aspect is hyperon studies with strange quark content. Experimental data on the production of ground and excited cascade-anticascade states with $\bar{\text{p}}\text{p}$ annihilation is sparse, but required to verify production models.

Antiproton-proton annihilations not only give rise to a broad physics program, but also create interesting physics events with similar topologies as background-like events. Thus, a novel data acquisition scheme based on online event reconstruction is employed. For that, the complete detector data has to be readout by self-triggering readout electronics, whose data is sent to off-detector computing farms and then selected online by sophisticated algorithms for permanent storage.

$\bar{\text{P}}$ANDA is divided into sub-detectors optimized for individual tasks. The innermost one, the Micro Vertex Detector (MVD), is designed for precise particle vertex reconstruction. It is segmented into silicon pixel and microstrips. Positioned close to the interaction point, the MVD's electronics need to be compact, withstand high radiation doses, and cope with high hit rates. Above all, the readout has to have a low power consumption and be able to process data autonomously. Since no readout solution is available to fulfill these requirements, the development of a custom solution was initiated leading to the $\bar{\text{P}}$ANDA Strip ASIC (PASTA).

This thesis describes the development of the PASTA readout front-end, the preparations for a laboratory readout system for front-end prototypes, and an exploratory study on the reconstruction of excited cascade hyperons with $\bar{\text{P}}$ANDA. It is structured as follows:

Chapter 2 gives a concise introduction into the Standard Model with a focus on the strong interaction.

After that, the FAIR facility is outlined in Chapter 3, describing the accelerator complex and the experiments.

Chapter 4 focuses on the introduction of the $\bar{\text{P}}$ANDA experiment itself. First, $\bar{\text{P}}$ANDA's physics program and detector concept are introduced. Then, the MVD and the readout chain are presented. The chapter concludes with the software environment used for simulations with $\bar{\text{P}}$ANDA.

In Chapter 5, the developments conducted towards the readout solution for the MVD's microstrip sensors – PASTA – are presented. The focus is laid on the digital part.

The enhancements of a readout system for front-end prototypes are described in Chapter 6. The major contribution here is the implementation of an Ethernet connection.

Chapter 7 investigates the reconstructability of an excited hyperon in the process $\bar{\text{p}}\text{p} \rightarrow \overline{\Xi}^{+}\Xi^{-}(1690)$ with $\bar{\text{P}}$ANDA's readout framework. The event topology is investigated and the reconstruction resolution and efficiency is determined.

Finally, Chapter 8 summarizes the results obtained in this thesis.

Physics Background 2

2.1 The Standard Model of Particle Physics

The favored model specifying the composition and behavior of the elementary particles in the universe is the *Standard Model of particle physics* (SM). It combines the three fundamental forces of electromagnetism, weak and strong interactions with their exchange particles as well as the elementary particles. The latter can be grouped in three generations of quarks and leptons and their corresponding antiparticles. Since the 1960s and '70s when it was mainly developed, it has been tested extensively with experiments. A *theory of everything*, including also the fourth force of gravitation, is yet to be found.

The elementary particles combined in the SM can be sorted into two groups depending on their spin: *fermions* with half-integer spin (e.g. $^1/_2$, $^3/_2$, ...) and *bosons* with integer spin (e.g. 0, 1, 2, ...). The former group is typically associated to build compound states with the support of the latter which mediates the interaction[1]. The known fermions and bosons are summarized in Table 2.1 and Table 2.2, respectively.

In a mathematical description the SM is classified as a renormalizable[2] quantum field theory (QFT). It follows the successful description of the electromagnetic interactions with quantum electrodynamics (QED) [3] and expands it for the other interactions. A basic requirement of these field theories is that their underlying Lagrangian[3] is invariant under local transformations. In other words, the result of a measurement is independent of alterations to the chosen coordinate system, like a rotation. Such a theory is called *gauge theory* and their invariance of a transformation a *symmetry*. The symmetry for the SM is based on the $\mathrm{SU}(3) \times \mathrm{SU}(2) \times \mathrm{U}(1)$[4] gauge group.

[1] This distinction is not absolute, as compound states might be built from bosons entirely (glueballs for instance, introduced in Section 4.1.2.2).

[2] Renormalization describes the specification of an energy scale for the parameter entering a field theory to avoid divergent expressions.

[3] The Lagrangian $\mathcal{L}$, or more precisely the Lagrangian density, is a mathematical description of the dynamics of a system. Its big advantage is its independence of the chosen coordinate system. The Lagrangian L is the spacial integral of $\mathcal{L}$, leaving only the time-like coordinate. The additional integrating over time leads to the action S from which equations of motion can be derived.

[4] The *unitary group* of degree n, $\mathrm{U}(n)$, and the *special unitary group* of degree n, $\mathrm{SU}(n)$, both denote a set of unitary matrices with dimension $n \times n$. A matrix U is unitary if it results in the identity matrix I when multiplied with its conjugate transpose $U^\dagger U = I$. The special unitary group additionally requires the matrices to have a determinant of 1.

Table 2.1: Overview of the fermions in the Standard Model with their masses and electrical charges, sorted into quarks (top half) and leptons (bottom half) and in groups of three generation. Each particle has a spin of $^1/_2$ and an associated antiparticle with opposite charge. In sum, 24 fermions are listed in the SM. Data from [1].

	1. Generation	2. Generation	3. Generation
	Up-type Quarks		
Symbol	**u**	**c**	**t**
Charge / e	$^2/_3$	$^2/_3$	$^2/_3$
Mass / (GeV/c^2)	2.3×10^{-3}	1.28	173.2
	Down-type Quarks		
Symbol	**d**	**s**	**b**
Charge / e	$-^1/_3$	$-^1/_3$	$-^1/_3$
Mass / (GeV/c^2)	4.8×10^{-3}	0.095	4.18
	Charged Leptons		
Symbol	**e**	$\boldsymbol{\mu}$	$\boldsymbol{\tau}$
Charge / e	-1	-1	-1
Mass / (MeV/c^2)	0.511	105.7	1.78×10^3
	Neutrinos		
Symbol	$\boldsymbol{\nu_e}$	$\boldsymbol{\nu_\mu}$	$\boldsymbol{\nu_\tau}$
Charge / e	0	0	0
Mass / (MeV/c^2)	$<2 \times 10^{-6}$	<0.19	<18.2

The electroweak component of the symmetry group, the group SU(2) × U(1), combines the description of electromagnetic and weak interactions [4]. The theory involves one massless mediator particle (the photon) and three bosons with mass (W^+, W^-, and Z) [4]. The latter remove the renormalizability from the theory because of their masses. Renormalizability is again restored by the concept of *spontaneous symmetry breaking* which is included with the Higgs mechanism[5] to the SM that introduces a potential with an unstable initial vacuum state. The stable ground state is different from the vacuum one and moreover non-symmetric, giving rise to the particle masses. By combining the aforementioned symmetry group with the Higgs mechanism, one achieves a consistent renormalizable quantum field theory for electroweak interactions.

The SU(3) part of the SM originates from the strong interaction mediators. The physics simulation presented in this thesis considers strongly interacting particles, thus a focus is laid on this in the next sections.

[5]The Higgs mechanism, actually called *Englert-Brout-Higgs-Guralnik-Hagen-Kibble mechanism*, is named after the first publication to the subject by HIGGS [5]. Other scientists published their work on the same subject shortly thereafter and the first three were awarded the Nobel Prize in 2013 [6]. An overview is available at [7].

Table 2.2: Overview of the bosons in the Standard Model with their masses, electrical charges, and integer spins. The first four bosons represent the gauge bosons for the interactions included in the SM, while the last line lists the Higgs boson, giving particles their masses. Adapted from [2], data from [1].

Associated Field	Boson	Spin / $\hbar$	Charge / e	Mass / (GeV/c^2)
Electromagnetic	$\boldsymbol{\gamma}$	1	0	0
Weak	$\mathbf{W}^{\pm}$	1	± 1	80.4
	$\mathbf{Z}$	1	0	91.2
Strong	$\mathbf{g}$ (8)	1	0	0
Higgs	$\mathbf{H}$	0	0	125.7

Having all parts of the symmetry group SU(3) × SU(2) × U(1) expressed as renormalizable QFTs makes the theory of the SM a coherent formulation. The predicted constituents of the SM have been measured extensively by several experiments since the 1970s with the final experimental proof achieved just recently by Large Hadron Collider (LHC) experiments with the discovery of the Standard Model Higgs boson at a mass of 125 GeV/c^2 [8, 9].

2.2 Interactions with the Strong Force

Quarks are fundamental constituents of hadrons with protons and neutrons as the most prominent ones. They are bound by the *strong* force, outweighing the electromagnetic repulsion. A residual strong force, or *nuclear* force, causes protons and neutrons to form nuclei and thus the most massive building blocks of visible matter (atoms, plasma) around us. The underlying theory is part of the SM and called the theory of quantum chromodynamics (QCD), using similar principles as the interactions described in QED. QCD is a development with many contributing researchers and two Nobel Prizes awarded directly to this field. The first was granted to Murray Gell-Mann in 1969 [10] for his work on classifying particles and their interactions. More recently, a second one was given to Gross, Politzer, and Wilczek in 2004 [3] for the discovery of asymptotic freedom in strong interaction.

2.2.1 Quarks, Gluons, and Color Charge

Looking at the building blocks of a nucleus mentioned above, protons (uud) and neutrons (udd) are both bound states of three quarks each. While these hadrons make up the common matter visible to us, more states composed of three quarks have been seen. The delta particle Δ^{++} with (uuu) quark content is one example.

All constituents of the Δ^{++} are u quarks so their electrical charge is identical. The particle's net spin angular momentum is $J = {}^3/_2$ [1], therefore all spins need to be aligned and all three fermions have all the same configuration of charge and spin quantum numbers. However, the Pauli exclusion principle forbids two identical fermions, i.e. fermions with the same quantum numbers, to be in the same bound system.

To solve this problem, a new quantum number is introduced for quarks, which is hidden for the measurable bound states[6]. Based on an analogy to color theory where the three primary colors (red, green, and blue) add to create a neutral one (white), the quantum numbers are called *color charges*. Following this, a (anti-)quark can carry either a (anti-)red, (anti-)green, or (anti-)blue charge.

Gluons as the quantization of the associated field couple to these charges. In contrast to photons, the mediators of the electric field, gluons themselves carry a charge and anticharge each. As a consequence, the strong field interacts with itself and gluons are attracted towards each other. Separating two color charges not only requires overcoming the particle's attraction but also the stretching of the field itself. The result is a linearly increasing potential between two static quarks. At some point, it becomse energetically more favorable to create a new quark-antiquark pair than to increase the potential even further. This explains why detectable systems are all confined to be color neutral. To put it the other way around, the closer two particles get, the more they can be considered as free in terms of the strong interaction, hence the descriptive name *asymptotic freedom*.

In a more formal representation, the strength of the strong interaction is given by the interaction's coupling constant α_s. As described in [11], perturbation theory yields the expression of the coupling constant dependent on the 4-momentum transfer Q^2:

$$\alpha_s(Q^2) = \frac{\alpha_s(\mu^2)}{1 + \frac{\alpha_s(\mu^2)}{12\pi}(33 - 2n_f)\log(Q^2/\mu^2)} \,. \tag{2.1}$$

It includes the number of flavors n_f accessible for a given energy scale μ, i.e. the corresponding quark masses are below μ. For high Q^2 the value of α_s decreases and the particles asymptotically approach freedom.

The current status of measurements performed for different energy scales are depicted in Figure 2.1. A common scale to evaluate and compare values of α_s is at the Z boson's mass, $m_Z = 91.2\,\mathrm{GeV}/c^2$:

$$\alpha_s(m_Z) \;=\; 0.1185 \pm 0.0006 \quad [1].$$

For sufficiently low Q^2 though, α_s increases and eventually surpasses the range where it is describable with perturbation theory. The energy scale at which this happens is customarily labeled with Λ (or Λ_{QCD} to not confuse it with the Λ hyperon). With

$$\Lambda^2_{QCD} = \mu^2 \exp\left(\frac{-12\pi}{(33 - 2n_f)\,\alpha_s(\mu^2)}\right),$$

Equation 2.1 can be rewritten as

$$\alpha_s(Q^2) = \frac{12\pi}{(33 - 2n_f)\log(Q^2/\Lambda^2_{QCD})} \,. \tag{2.2}$$

[6] A proton, for instance, is seen as one particle, independent of the newly assigned quantum number. So a $(u_r u_g d_b)$ state is indistinguishable from a $(u_b u_r d_g)$ state, when r, g, and b denote these quantum numbers.

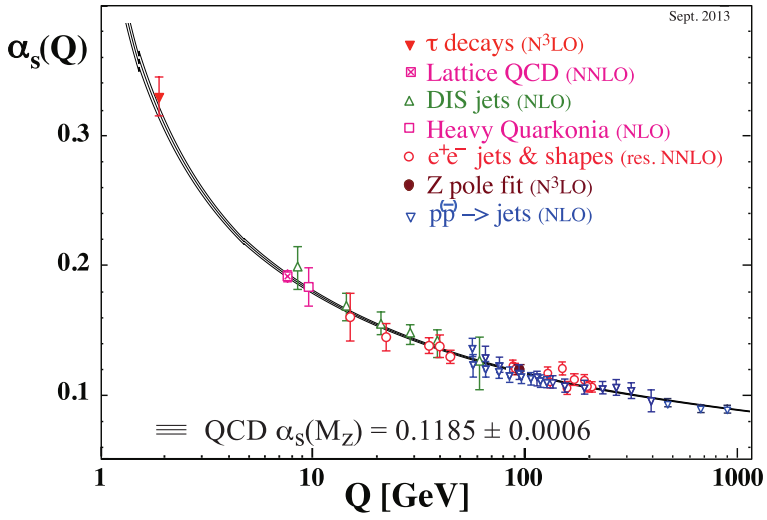

Figure 2.1: Shown are combined measurements for the strong coupling constant α_s as a function of the energy scale Q. The data points use different levels of perturbation to extract the value of α_s, from NLO (next-to-leading order) to N^{3}LO corrections (next-to-next-to-next-to-leading order) as stated in brackets. Image from [1].

The energy scale Λ_{QCD} below which perturbation theory cannot be applied is on the order of a few 100 MeV [12]. Other approaches need to be considered, a prominent one is using a discretization of spacetime to calculate the behavior of the system. This approach is called *lattice QCD* and is computational very intensive, thus requiring large supercomputers to solve [1]. An alternative exploits the confinement for low energies and simplifies the system so that the exchange is described by hadrons instead of gluons. This so called *chiral perturbation theory* is an effective field theory proposed by WEINBERG [13] and uses power counting to include higher orders of a perturbative expansion. However, low-energy constants need to be extracted from experimental data.

2.2.2 Bound States of Quarks

Generally, bound states based on the strong interaction are called *hadrons*. Their properties are based on the constituent quarks. A basic classification into two types of bound states often is made: *baryons* (antibaryons) with three quarks (antiquarks) and *mesons* with a quark-antiquark pair. Both classifications can fulfill the requirement of a color neutrality. Other, more complex combinations are subject to experimental and theoretical research (see also Section 4.1.2).

The relevant quantum numbers for particles are the electromagnetic charge Q, the total angular momentum J as the sum of spin (S) and orbital angular momentum (L), and the parity P. The number of strange quarks and antiquarks is denoted in this thesis with S_q to differentiate from the spin S. All mentioned quantum numbers are also collected in Table 2.3 and can be used to naturally classify the states.

For hadrons in the ground state without angular momentum excitation, i.e. $L = 0$, a classification can be done based on their quark flavor content. Two groups emerge for hadrons

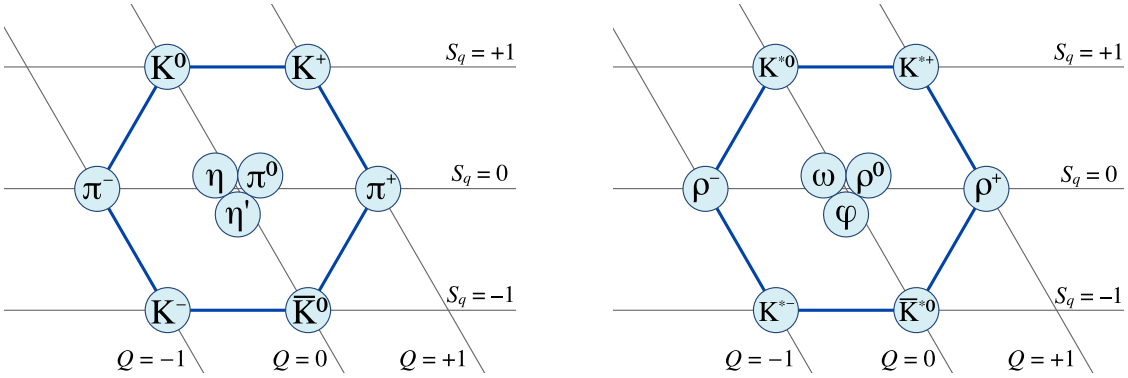

(a) Meson nonet for $J^P = 0^-$.

(b) Meson nonet for $J^P = 1^-$.

Figure 2.2: The ground state mesons without orbital angular momentum ($L = 0$) consisting of the three lightest quarks (u, d, and s), ordered by electromagnetic charge Q and strangeness S_q. Adapted from [2, 14, 15].

of u, d, and s (anti-)quarks, split by the total angular momentum J. Mesons are arranged into nine states (a nonet) with $J^P = 0^-$ and another nonet of $J^P = 1^-$, called pseudoscalar and vector mesons, respectively. They are shown in Figure 2.2, ordered by their strangeness and electromagnetic charge. A similar scheme can be found for the lightest ground state baryons, shown in Figure 2.3, where all have positive parity ($P = +1$). Baryons with total angular momentum $J = {}^1/_2$ form an octet while those with $J = {}^3/_2$ are grouped togther in a decuplet.

Table 2.3: Relevant quantum numbers to classify hadrons comprised of u, d, and s quarks.

Quantum Number	Symbol	Comment
Electromagnetic Charge	Q	All integer values of the elementary charge e.
Spin Angular Momentum	S	In hadrons, the spin is based on the alignment of the quarks' spins (each ${}^1/_2\hbar$) to one another.
Orbital Angular Momentum	L	The quarks' rotation around each other, given in integer increments of $\hbar$.
Total Angular Momentum	J	The sum of the spin and orbital angular momentum vectors, hence it ranges in half-integer increments of $\hbar$ from $\lvert L-S\rvert \leq J \leq \lvert L+S\rvert$.
Parity	P	Negative and positive parity denote the particle's behavior under parity (mirroring) operation.
Isospin	I, I_3	The isospin is $I = {}^1/_2$ for the light (anti-)quarks and $I = 0$ for others. The component I_3 is different for u ($+{}^1/_2$) and d ($-{}^1/_2$) quarks, antiquarks have opposite sign.
Strangeness	S_q	The number of strange (anti-)quarks.

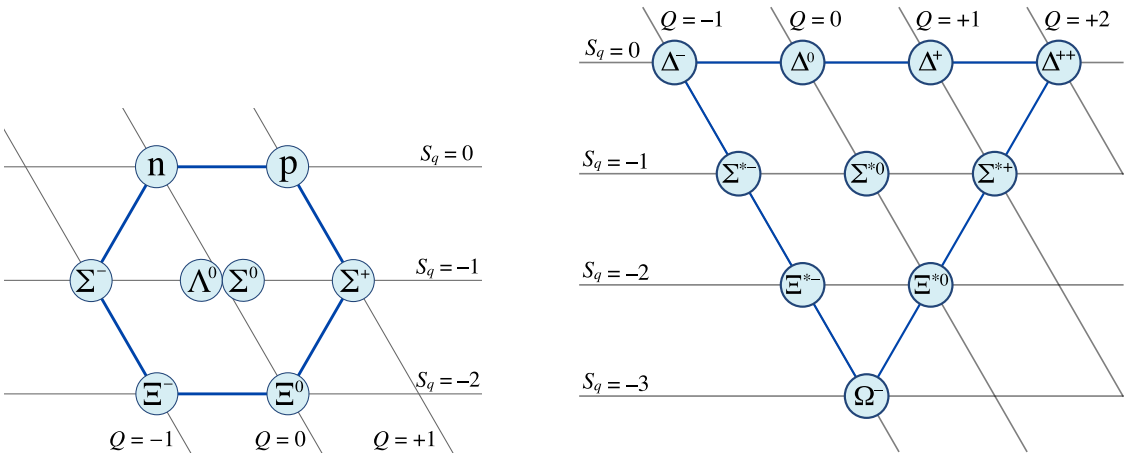

(a) Baryon octet for $J^P = {}^1/_2{}^+$.

(b) Baryon decuplet for $J^P = {}^3/_2{}^+$.

Figure 2.3: The ground state baryons without orbital angular momentum ($L = 0$) consisting of the three lightest quarks (u, d, and s), ordered by electromagnetic charge Q and strangeness S_q. Adapted from [2, 16, 17].

2.2.3 Hyperons

Out of the possible baryon states, hyperons are those with at least one strange or heavier quark content. Hyperons are shown in Figure 2.3 in the rows with strangeness $S_q \neq 0$. Ground state hyperons may only decay weakly to a lighter baryon, since strangeness is conserved by strong and electromagnetic interactions. This gives hyperons a significant decay time in the order of $\tau = \mathcal{O}\left(10^{-10}\,\mathrm{s}\right)$, corresponding to typical distances of $\mathcal{O}(\mathrm{cm})$ in the laboratory reference frame. This results in a distinct signature when measured in a particle detector.

The production of hyperon-antihyperon pairs from an annihilation reaction is determined by the strong interaction and its corresponding coupling constant α_s. Since strange-antistrange quarks are produced by converting light quark-antiquark pairs, the energy scale is governed by the strange quark's mass of $m_s \approx 100\,\mathrm{MeV}/c^2$. By measuring hyperon-antihyperon pairs, the strong interaction can be probed in a regime close to the cut-off parameter Λ_{QCD}. This is described in Section 2.2.1 and can be seen in Figure 2.1.

An overview of the current spectrum of the lowest Λ, Σ, Ξ, and Ω hyperon states is shown in Figure 2.4 in comparison to predictions from two theoretical models. It is evident that experimental and theoretical results are not always in agreement. While these lower states have at least some experimental data, the amount gets very sparse and is nonexistent for higher excited states and often data on the particles' quantum numbers is missing (refer to baryon data in [1]).

2.2.4 Ξ Cascade Baryon States

The lightest double-strange hyperons are the Ξ states with a quark content of (uss) for Ξ^0 and (dss) for Ξ^-. Both hyperons decay weakly by changing the strange flavor into the light u and d quarks twice. This sequence causes the Ξ to have a cascade of two significantly long decay

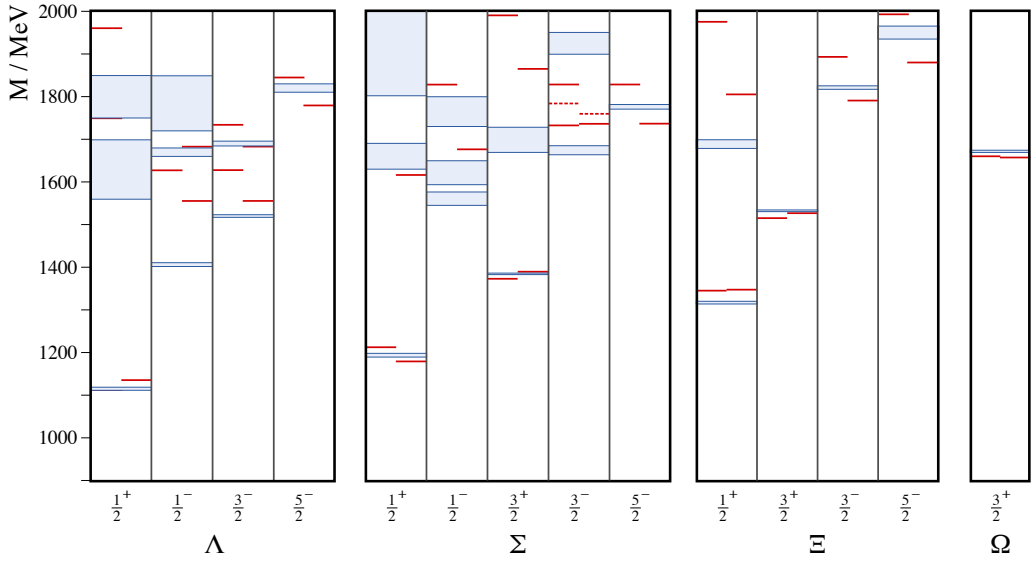

Figure 2.4: The hyperon spectrum for the lowest Λ, Σ, Ξ, and Ω states with measurement results including uncertainty (blue areas) and theoretical predictions (red lines) from two different models (left: one gluon exchange; right: Goldstone boson exchange). The dashed lines in the $J^P = {}^3/_2{}^-$ Σ spectrum are eigenstates without an experimental counterpart yet. Adapted from [18].

vertices, hence their name *cascade particle*. A typical process of $\bar{p}p \to \bar{\Xi}^+\Xi^-$ is sketched in Figure 2.5. The Ξ^- almost exclusively decays to $\Lambda\pi^-$ with a branching fraction of $(99.887 \pm 0.035)\,\%$ [1].

Cascade states in general are not well investigated experimentally. So far, only one bubble chamber experiment in the 1960s at the European Organization for Nuclear Research (CERN) saw three $\bar{\Xi}^+\Xi^-$ pairs from $\bar{p}p$ production, corresponding to a cross section of $(2 \pm 1)\,\mu b$ [20]. From a theoretical point, different approaches are used to describe the Ξ production and estimate the production cross section, as summarized in Table 2.4.

One key difference in these approaches is the model used for the transition from protons to cascades. A naive approach is to assume simultaneous annihilations of two $u\bar{u}$-pairs, emitting a gluon each which then produce an $s\bar{s}$-pair. This double-gluon process is shown in Figure 2.6(a) and used by [21]. A similar exchange, but annihilating a quasi-bound state of two quarks (*diquark*) inside the hadron is used by [22], shown in Figure 2.6(b). Finally, one can also look at a simplified picture of exchanging mesons, which is justified by the low energy regime in which the reaction occurs. There, the strong force is strong enough for hadronisation. The works in [19, 21] calculate with a pseudomeson exchange (a K for instance) while [21, 23] use vector mesons (e.g. K^*) to transform a proton into an intermediate baryon with one s quark (Λ or Σ) and then further into the double-strange cascades. This process is shown in Figure 2.6(c).

The different theoretical approaches lead to significant variations in the cross section spreading over two orders of magnitude: from $\sim 0.01\,\mu b$ up to a few μb. They are obtained for a beam momentum of $3\,\text{GeV}/c$. This is about 100 MeV in the center-of-mass (CM) frame above the production threshold for a $\bar{\Xi}^+\Xi^-$ pair in ground state. A good observable to probe different

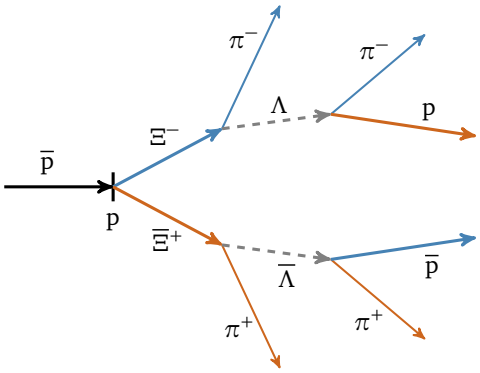

Figure 2.5: A typical cascade reaction from $\bar{p}p \to \bar{\Xi}^+\Xi^-$ with the most probable decays according to [1]. The color code is orange (→) for electrically positive, blue (→) for negative and gray (→) for neutral particles. Adapted from [12].

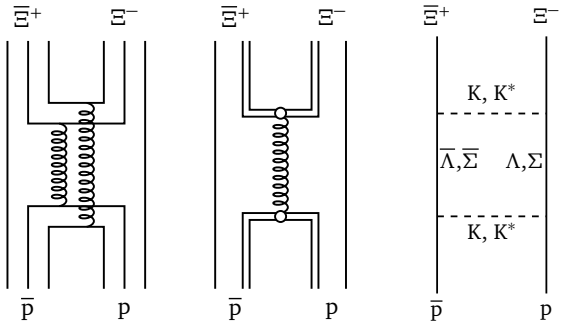

(a) Double gluon exchange. **(b)** Diquark annihilation. **(c)** Meson exchange picture.

Figure 2.6: Different exchange models used to calculate the hyperon production in $\bar{p}p$ processes. On the left, a gluonic exchange converts two light quarks into strange quarks, the center shows a diquark annihilation, and on the right the exchange is done by mesons, mainly kaons. Adapted from [19].

production models is the angular distribution in the overall CM frame. Depending on the model, the momentum transfer and thus the angular distribution varies. Therefore, a precise measurement of the angular distribution is desirable and helps to select a describing model.

No concrete predictions exist for the production of excited cascade states in antiproton-proton collisions. Judging from measurements [24] and predictions [21] of other excited baryons

Table 2.4: Total cross section σ_{tot} predictions for $\bar{p}p \to \bar{\Xi}^+\Xi^-$ reactions with different models at 3 GeV/c antiproton beam momentum. This momentum is ∼ 100 MeV in the center-of-mass frame above the production threshold. References to the cross section distributions in the appendix are given. Finally, one estimation for σ_{tot} from a bubble chamber experiment at CERN is given.

Reference	σ_{tot} / μb	Model
Genz, Nowakowski, and Woitschitzky [21]	0.01	Pseudoscalar meson exchange.
	1.9	Vector meson exchange.
	7.4	Quark annihilation, gluon exchange.
Kroll, Quadder, and Schweiger [22]	4.95	Diquark annihilation (Figure A.2).
Haidenbauer, Holinde, and Speth [19]	0.34	Pseudoscalar meson (K) exchange (Figure A.1(a)).
Kaidalov and Volkovitsky [23]	0.45	Vector meson (K*, K**) exchange (Figure A.3).
Musgrave, Petmezas, Riddiford, *et al.* [20]	2 ± 1	Experimental result (3 $\bar{\Xi}^+\Xi^-$ events).

like $\bar{p}p \to \overline{\Lambda}\Lambda^*$ or $\bar{p}p \to \overline{\Sigma}\Sigma^*$, the cross section is in the same order of magnitude as their corresponding ground states. Since predictions for cascade production varies significantly already depending on the model, the range of values presented in Table 2.4 are also used for the cross section of the reaction $\bar{p}p \to \overline{\Xi}^+\Xi^-(1690)$ with one excited Ξ.

Overview of FAIR 3

The Facility for Antiproton and Ion Research (FAIR) is the laboratory complex hosting several experiments, including $\bar{\text{P}}$ANDA, which will conduct research in various fields investigating fundamental structures of matter. With the support of an international collaboration, the facility is currently under construction in Darmstadt, Germany, next to the already existing GSI. The research activities are centered around a sophisticated accelerator complex providing high-precision and -intension antiproton and heavy ion beams to the experimental stations. A brief overview of those is given in the next section, followed by the accelerator structures (Section 3.2).

3.1 Research Pillars

Four different pillars of research will be carried out at FAIR, two employing a main detector (CBM and $\bar{\text{P}}$ANDA) and two comprising of a set of smaller experiments (APPA and NuSTAR).

3.1.1 APPA

The Atomic, Plasma Physics and Applications (APPA) program is combining experiments located in plasma physics, radiation effects on material and influence studies of ultra-strong electromagnetic fields. Together, five experiments are embedded in APPA:

3.1.1.1 BIOMAT

The collaboration for Biology and Material Research (BIOMAT) targets the influence of heavy ion beams with energies up to 10 A GeV on a variety of biological and solid targets. The biological program focuses on radiation effects on organisms like humans which is inevitably present on long-term space programs. With a better understanding of the minimal requirements for protection, the expensive shielding of space vessels can be optimized. Concerning the material science, the program is set up to investigate heavy ion radiation effects on material under extremely high pressure, provided by a $\sim$ 30 t multi-anvil apparatus [25].

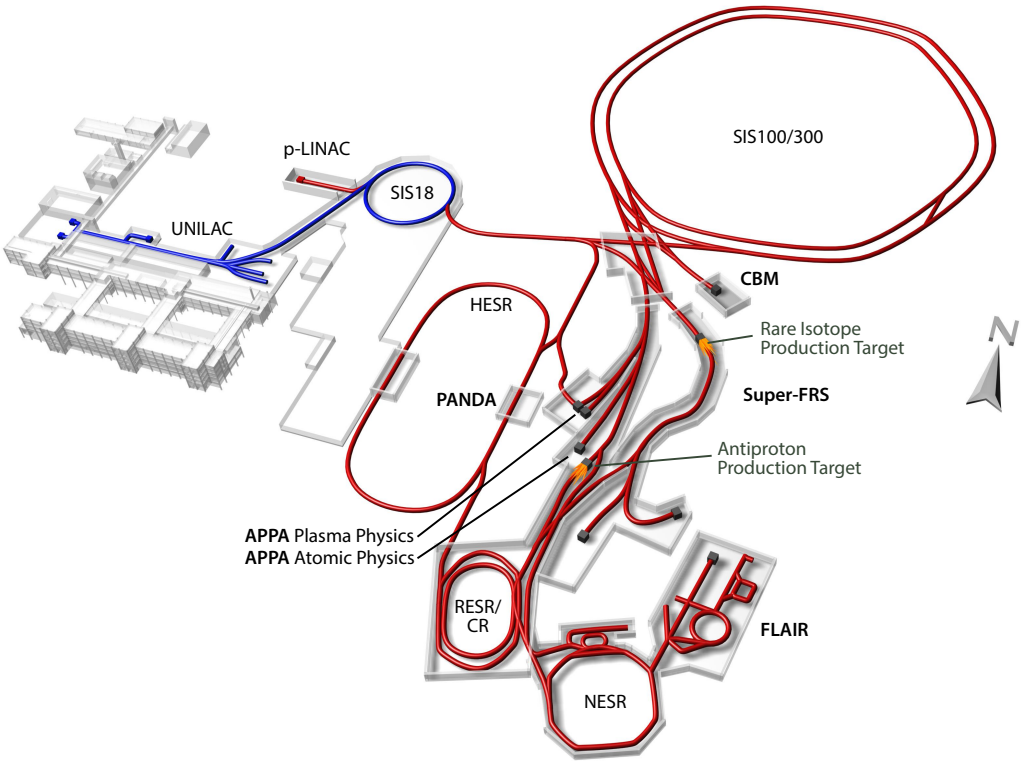

Figure 3.1: Overview of the future FAIR facility with annotations for accelerator structures and planned experiments (bold characters). The current GSI complex is shown on the left, along with the already existing accelerator lines (blue). Planned beam lines are shown in red. Image from [2].

3.1.1.2 FLAIR

Low-energetic antiprotons and highly-charged ions are the focus of the Facility for Low-Energy Antiprotons and Heavy Ion Research (FLAIR) program. With the former, FLAIR continues the antimatter research performed at the Antiproton Decelerator (AD) at CERN. This involves precision spectroscopy of anti-protonic atoms like $\overline{\text{p}}$-He and anti-hydrogen as well as trapping anti-hydrogen to investigate the gravitational influence on antimatter [26].

3.1.1.3 HEDgeHOB

The High Energy Density Matter generated by Heavy Ion Beams (HEDgeHOB) experiments are designed to research matter in high-energy-density conditions. By heating the material with FAIR's heavy ion beam, a more homogeneous heat transfer can be achieved for the produced plasma than it can be with traditional approaches of dynamic shock compression. Both dynamical and stationary properties of such heated system are then accessible [27].

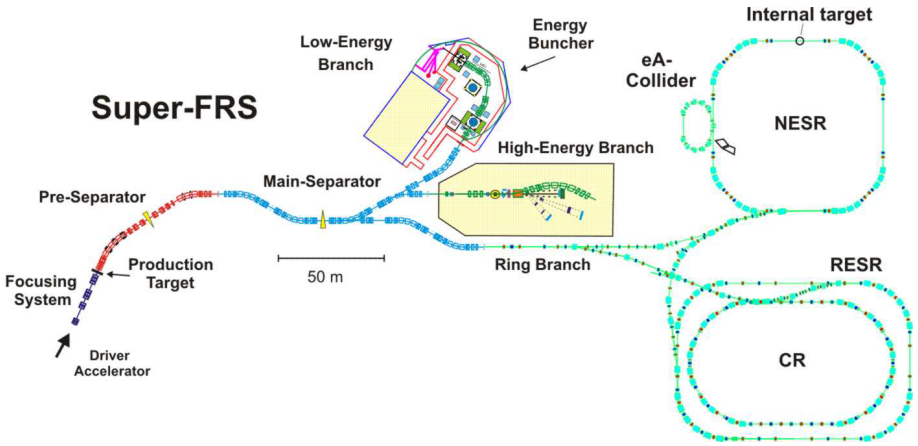

Figure 3.2: The structures involved in NuSTAR, aligned around the Super-FRS. Image from [29].

3.1.1.4 SPARC

The physics program of Stored Particle Atomic Physics Collaboration (SPARC) is split into two categories. The first involves collision dynamics in strong electromagnetic fields from relativistic heavy ion beams. In the produced ultra-short pulses of high-intensive fields the limits of the perturbative predictions for lepton pair production can be probed. Secondly, fundamental interactions between electrons and heavy nucleic will be investigated. By using highly-charged ions, properties of stable and unstable nuclei can be measured and QED in strong electromagnetic fields can be tested [28].

3.1.1.5 WDM

A set of experiments for Warm Dense Matter (WDM) research is planned to investigate the energy regime where free and bound electrons become strongly correlated. This transition region of condensed matter to ionized plasma lacks proper descriptions, partially because the required conditions are experimental challenging. The planned setup will combining FAIR's heavy ion beam with a petawatt PHELIX laser beam [29].

3.1.2 NuSTAR

Nuclear Structure, Astrophysics and Reactions (NuSTAR) is an umbrella collaboration joining together seven experiments that are focused on nuclear structures and properties of heavy, radioactive elements. These elements are naturally formed in star collapses, thus the research has strong interconnections to the astrophysical field. The experiments are aligned around the central fragment separator Super-FRS, providing radioactive ions to them. An overview sketch is shown in Figure 3.2.

3.1.2.1 Super-FRS

The Super Fragment Separator (Super-FRS) is the central component that produces a secondary beam with rare isotopes and separates it to the individual experimental halls. The separation is done in-flight for beam energies up to 1.5 A GeV on short timescales with $\mathcal{O}(100\,\text{ns})$, allowing

research with extremely short-living elements. Three different branches are provided with the beam: a low and a high energy branch as well as a ring branch (see Figure 3.2) [30].

3.1.2.2 DESPEC/HISPEC

The two experiments Decay Spectroscopy (DESPEC) and High-resolution In-flight Spectroscopy (HISPEC) are closely intertwined. With low-energy, radioactive beams of energies from 3 A MeV to 150 A MeV, both will study elements with exotic proton-to-neutron ratios. HISPEC covers measuring the beam while DESPEC measures stopped and implanted elements [31].

3.1.2.3 ELISe

With the Electron-Ion Scattering in a Storage Ring (ELISe) experiment, (in-)elastic and quasi-free electron scattering is examined at the intersection of ion and electron storage rings. The experiment plans to measure nuclei far off the valley of stability to determine their charge density distributions and investigate electro fission [32].

3.1.2.4 EXL

The Exotic nuclei in light-ion induced reactions at the NESR storage ring (EXL) program will utilize light-ion scattering with inverse kinematics to achieve very low kinematic energies (less than 1 A MeV). With that, exotic, neutron-rich nuclei from a secondary beam can be investigated towards their matter distribution [33].

3.1.2.5 ILIMA

Precision measurements of nuclear masses and lifetimes of exotic nuclei are the agenda of Isometric Beams, Lifetimes and Masses (ILIMA), as the name suggests. The possibility to investigate bare to few-electron ions enables the simulation of conditions similar to hot stellar environments. Both, cooled beams with long-living isotopes and hot beams with short-living isotopes can be measured [34].

3.1.2.6 LaSpec

With the multi-purpose Laser Spectroscopy (LaSpec) stopped, cooled, and bunched radioactive elements can be surveyed. Hyperfine structure effects become visible through the laser, enabling nuclear spin, magnetic dipole and electric quadrupole moment measurements [35].

3.1.2.7 MATS

The Precision Measurement of very short-lived nuclei with Advanced Trapping System (MATS) experiment shares an experimental hall with the LaSpec experiment because the targeted elements are similar. The method, though, is different as MATS employs a high-precision ion trap for mass measurements [36].

3.1.2.8 R3B

Finally, the Reactions with Relativistic Radioactive Beams (R3B) program joins a variety of scattering experiments, for instance for heavy-ion induced electromagnetic excitations, knockout

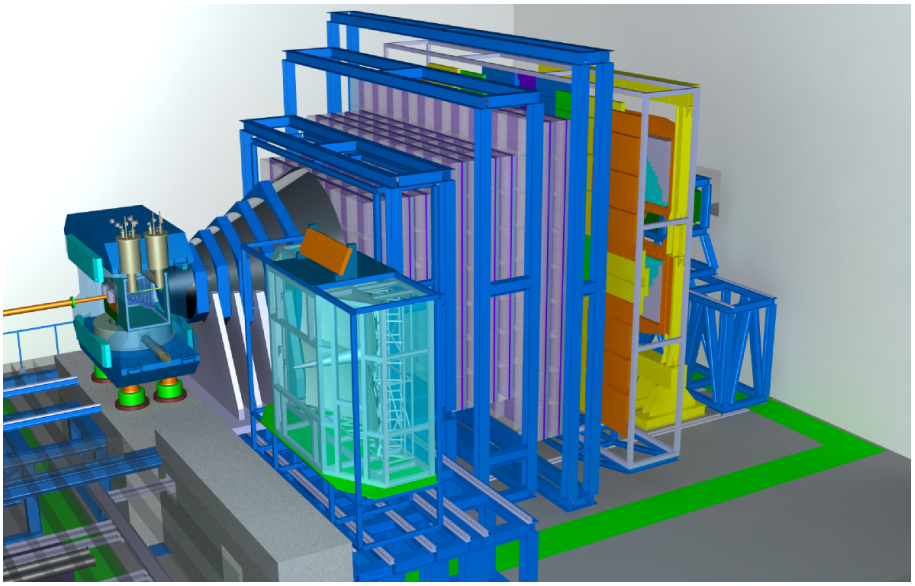

Figure 3.3: A rendering of the CBM detector that is planned as a forward spectrometer with the beam entering from the left. From the two operation modes available to CBM, the RICH detector is here shown in stand-by and the muon chamber system in measurement position. Image from [37].

and breakup reactions, or for inverse kinematical light-ion scattering. It is installed in the high-energy branch and measures γ and target recoil particles in different detectors.

3.1.3 CBM

The main goal of the Compressed Baryonic Matter (CBM) experiment is conducting measurements of the QCD phase diagram in regions of high net-baryon densities and moderate temperatures. Increasing the density and thus the baryon-chemical potential is expected to eventually transition from the hadronic phase into quarkyonic matter. Other topics on the agenda are the search for chiral phase transistions, deconfinement towards quark-gluon plasma, and matter in neutron star-like densities [37].

To facilitate this rich physics program, the CBM detector is planned to measure high-energy nucleus-nucleus collisions with ion projectile energies of 10 A GeV to 45 A GeV, provided from the SIS100/SIS300 synchrontrons. For an early start, the program may already start with only the SIS100, delivering energies of 2 A GeV to 11 A GeV [38].

Much like $\bar{\text{P}}$ANDA, a variety of particles are of interest (multi-strange hyperons, charmed particles, and vector mesons decaying into leptopn paris), thus self-triggering front-end electronics are used exclusively. Disentangling the high interaction rate of 0.1 to 10 million collisions per second requires a fast detector readout. A rendering of the spectrometer is shown in Figure 3.3.

3.1.4 $\bar{\text{P}}$ANDA

The last experimental pillar of the scientific FAIR program is the Antiproton Annihilation at Darmstadt ($\bar{\text{P}}$ANDA) experiment. The multi-purpose detector aims at measuring the outcome of

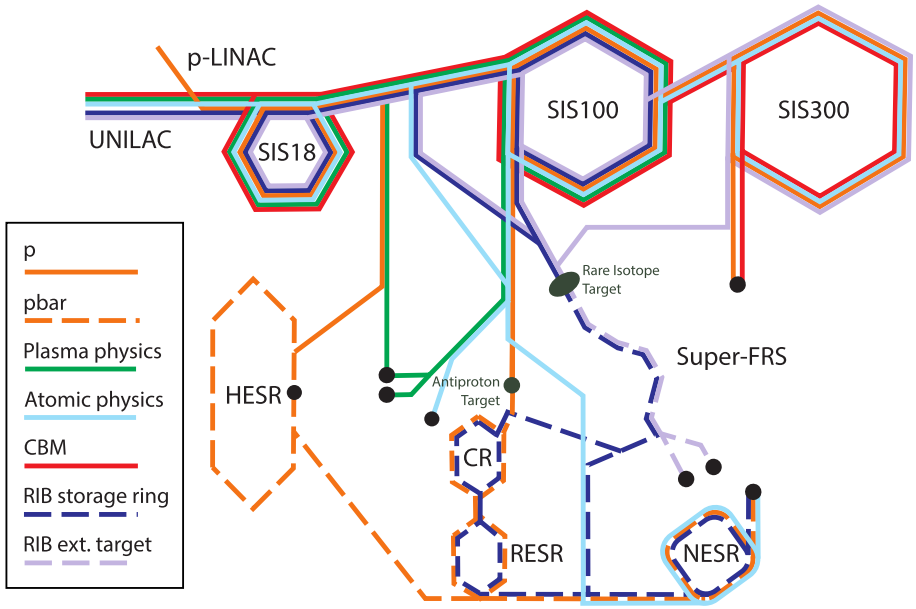

Figure 3.4: The different beam lines of FAIR's accelerator and storage ring complex. Up to four beam lines can be operated in parallel with the orange being the most relevant for $\bar{\text{P}}$ANDA. Image from [2, 29].

proton-antiproton annihilations in the charm mass regime. The $\bar{\text{P}}$ANDA detector and its physics program is presented in detail in Section 4.2.

3.2 Accelerators and Storage Rings

The experimental project planned within the FAIR facility have different requirements for heavy ion and antiproton beams. In order for them to measure efficiently, a complex of accelerators and collection and storage-cooler rings is foreseen to supply up to four research programs with truly parallel beams. Different beam line paths are visualized in Figure 3.4. The most relevant for the $\bar{\text{P}}$ANDA experiment are the proton and antiproton beam lines, shown in orange, whose parts are described in the following. If not stated otherwise, the information presented in this section is taken from [29, 39].

3.2.1 Linear Accelerators

The first step of the accelerator complex are two linear accelerators. The already existing UNILAC will be used for ion acceleration. For protons however, an optimized injection stage will be included, the Proton Linear Accelerator (p-LINAC). It will produce 100 ns pulses of 50 mA protons with a rate of 5 Hz to synchronize with the following synchrotron ring.

3.2.2 Synchrotrons

After the linear accelerators, the particles are injected into SIS18 which boosts the particles and prepares them for further acceleration. In one cycle, SIS18 collects and accelerates protons

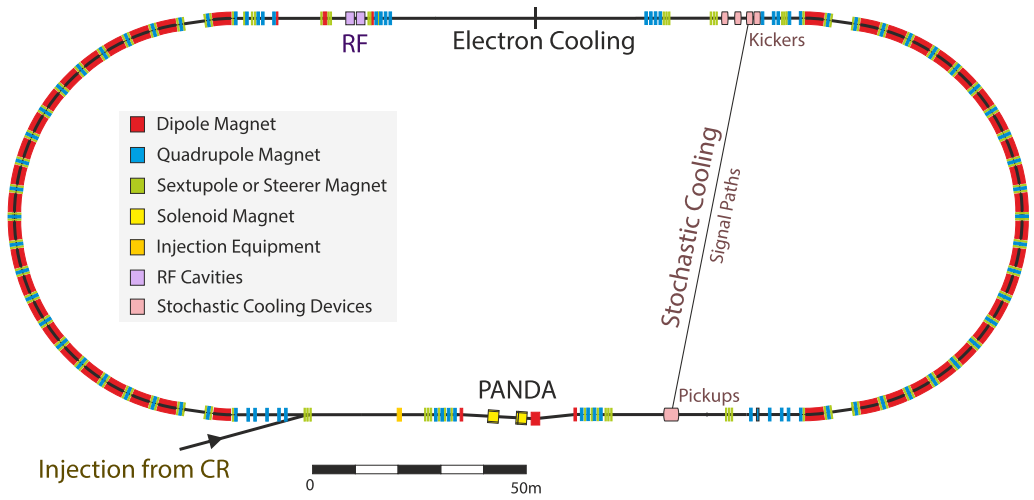

Figure 3.5: Schematic view of the HESR storage ring for antiproton beams with different magnets, acceleration, and cooling components color coded. Image from [2].

to a kinetic energy of 2 GeV. The ring measures 216 m in circumference and has a rigidity of 18 T · m.

The protons then get injected into the next synchrotron stage, the SIS100 with a rigidity of 100 T · m. Here, they get accelerated up to 29 GeV which is the final energy for antiproton production. In a later stage of FAIR it is foreseen to build a further synchrotron ring SIS300 for proton and heavy ion research. Both rings are planned on top of each other with a circumference of 1084 m.

With a repetition rate of 1 Hz, 4×10^{13} protons are extracted from SIS100 in compressed pulses of 25 ns and sent to the antiproton production target.

3.2.3 Antiproton Production and Collection

Here, the proton beam interacts with a light metal target to produce antiprotons amongst other particles. Only the antiprotons are used consequently and are filtered by a magnetic horn. The target's concept follows the AD's target design used at CERN.

Per cycle, $\sim 10^8$ antiprotons with an energy of 3 GeV and a momentum spread of ±3 % are collected into the Collector Ring (CR) which also pre-cools the beam with stochastic cooling. After 10 s, the beam is sent to the following storage ring, the Recuperated Experimental Storage Ring (RESR). It accumulates the antiprotons from CR before sending it further. In case of low-energetic antiproton measurements, the beam is transferred to the New Experimental Storage Ring (NESR), otherwise to the High Energy Storage Ring (HESR).

3.2.4 High Energy Storage Ring

The final structure for the antiproton beam is the High Energy Storage Ring (HESR). Antiprotons are injected with an energy of 3 GeV and get accelerated/decelerated to the desired energy.

Table 3.1: The modules defined for FAIR, including the Modularized Start Version (modules 0-3).

Module	Content
0	SIS100, required for all science programs
1	Experimental halls for CBM, HADES, and APPA
2	Super-FRS
3	Antiproton facility: p-LINAC, $\overline{\text{p}}$ target, CR, HESR, hall for $\bar{\text{P}}$ANDA
4	NESR, halls for NuSTAR and FLAIR
5	RESR

A range of 0.83 GeV to 14.1 GeV is accessible, equivalent to a beam momentum range of 1.5 GeV/c to 15 GeV/c [40].

The ring has a circumference of 574 m and is comprised of 44 dipole magnets with a combined bending power of 50 T · m. The $\bar{\text{P}}$ANDA experiment, acceleration cavities, and cooling equipment are located on the two straight sections of 132 m each. Cooling the antiprotons is done with two approaches. The first, stochastic cooling, is used with the signal pickup downstream of $\bar{\text{P}}$ANDA and the application of the correction with kicker magnets on the opposite site. For antiproton energies of up to 8 GeV, an 4.5 MeV electron cooler is applicable as well, preceded at the beginning by a smaller version with 2 MeV electrons [41].

Through the extensive cooling efforts, a minimal momentum spread of $\Delta p/p = 4 \times 10^{-5}$ is achievable in a so-called *high-precision mode*. Both beam luminosity and momentum are limited though, caused by the electron cooler's range. Thus, a second mode is foreseen with 10-fold higher luminosity $\mathcal{L} = 2 \times 10^{32}/(\text{cm}^2\,\text{s})$ and the full momentum range of 1.5 GeV/c to 15 GeV/c at the cost of a larger momentum spread ($\Delta p/p = 10^{-4}$). This mode is called the *high-luminosity mode*.

3.2.5 Modularized Start Version

The components of the FAIR complex are grouped into six modules to enable an expeditious start of FAIR [42]. The first four modules (0-3) compose FAIR's initial version, the so called Modularized Start Version (MSV). They include the mandatory accelerator components of SIS100 and the connection to the existing GSI structures (both module 0) as well as the experimental halls for CBM, High-Acceptance Dielectron Spectrometer (HADES), and APPA (module 1). The antiproton infrastructure is included in module 3, comprising the storage rings CR and HESR as well as the hall for $\bar{\text{P}}$ANDA. All modules are collected in Figure 3.6. A graphical overview is given in Figure 3.6.

The four modules of the MSV provide most experiments the possibility to swiftly start their measurements. When the funding for the remaining modules becomes available, they will be build subsequently. This includes the rings NESR and RESR as well as NuSTAR and FLAIR.

Since the RESR is intended for antiproton collection but missing in the MSV, the task is taken over by the HESR. Every 10 s it gets 10^8 antiprotons transferred from the CR where they have been collected. Over 1000 s, HESR accumulates antiprotons until accumulation is halted and

Figure 3.6: Overview of the modules in FAIR's Modularized Start Version. Image from [2, 42].

further acceleration and cooling is applied. Therefore, the maximum number of antiprotons in the MSV is 10^{10} instead of 10^{11} required for the high-luminosity mode. Since it requires time to accumulate the antiprotons, the duty cycle of HESR is also reduced. As a consequence, $\bar{\text{P}}$ANDA will not be able to measure with the high-luminosity mode from the start.

The $\bar{\text{P}}$ANDA Experiment 4

This chapter focuses on the introduction of the $\bar{\text{P}}$ANDA experiment. First, the physics program of $\bar{\text{P}}$ANDA is presented in Section 4.1. Then, the main detector with its several sub-components are introduced in Section 4.2. A special focus is laid on the MVD in Section 4.3 because part of the development done in this thesis concerned this sub-detector. After that, the data acquisition of $\bar{\text{P}}$ANDA is briefly described in Section 4.4. Finally, an introduction into the software framework simulating the detector is given in Section 4.5, which has been used for the simulation in Chapter 7.

4.1 Physics of $\bar{\text{P}}$ANDA

The Antiproton Annihilation at Darmstadt ($\bar{\text{P}}$ANDA) experiment will explore collisions from an antiproton beam with a fixed proton target. Such an annihilation reaction enables a wide range of produceable particles that can not be directly created in e^+e^- colliders. The allowed initial states in leptonic colliders are given by the quantum numbers of the intermediate photon. Other states are only accessible via production reactions of particle decays which limit the statistics.

With a high-intensive, phase-space cooled beam delivered by the HESR, an unprecedented physics program can be carried out to further extend the knowledge of the strong interaction and the hadron structure. The momentum range between 1.5 GeV/c and 15 GeV/c is chosen to produce states in the overlap of perturbative and non-perturbative QCD regimes with center of mass energies from $\sqrt{s} = 2.26\,\text{GeV}$ to $\sqrt{s} = 5.48\,\text{GeV}$. A sketch of the potential physics program to be investigated with $\bar{\text{P}}$ANDA is given in Figure 4.1.

4.1.1 Hadron Spectroscopy

One of the key physics programs is the investigation and classification of the hadronic bound state spectrum. A special interest is given to mesons with charm content as well as to baryons with strange and charm content.

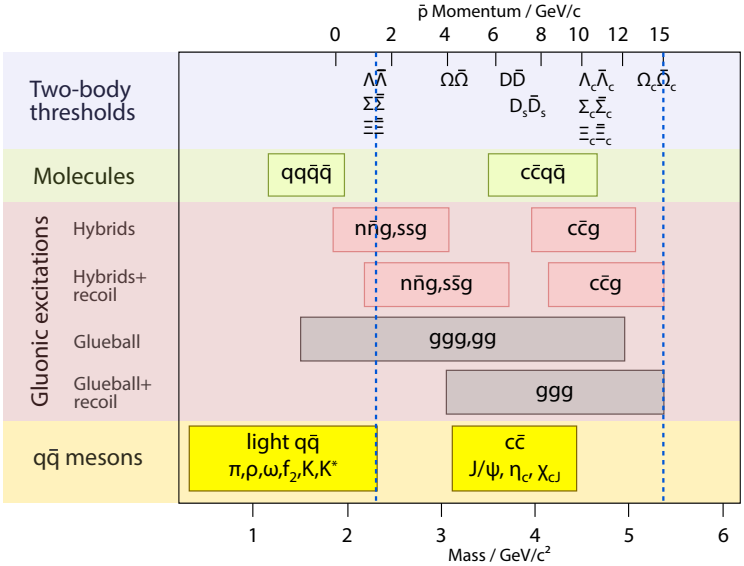

Figure 4.1: The physics spectrum available to HESR and within the blue dashed lines to PANDA. The antiproton beam momentum is given on the top axis, the according center of mass energies on the bottom axis. Image from [2, 43].

4.1.1.1 Open Charm Spectroscopy

A meson with *open charm* is understood to be comprised of one charm and one light quark – its charm quantum number is not zero. *Hidden charm* on the other hand is present when both a charm antiquark and a charm quark are present, leaving no net-charm for the combined charmonium state. The investigation of hidden charm is the topic of Section 4.1.1.2.

The first discoveries of a heavy-light[1] mesons in the charm sector – or D mesons according to the nomenclature[2] – were both published in 1976, the neutral D^0 found by the group of GOLDHABER, PIERRE, ABRAMS, *et al.* [47] and the charged $D^{\pm}$ by PERUZZI, PICCOLO, FELDMAN, *et al.* [48]. After this discovery at the Stanford Linear Accelerator Center (SLAC), many more states have been found. Together with some predictions from a relativistic quark model, as done by [44, 45], the current spectrum of open charm mesons with strange content is shown in Figure 4.2.

It is obvious that observation and prediction do not fit well together, especially for the recently found excited D_s states close to and above the DK decay threshold. The open-charm meson spectrum provides a good possibility to investigate the dynamics of a strongly bound system. The configuration of a heavy-light system is comparable to the hydrogen atom, with a significant heavier constituent almost resting in the center, surrounded by a lighter partner. Much like the electromagnetic theory was verified and refined by measuring the hydrogen atom extensively, open-charm spectroscopy provides good access to probe the dynamics of a strongly bound system.

[1] The name originates from the combination of a light and a heavy (anti-)quark.
[2] In case a strange quark is involved, an index is added: D_s.

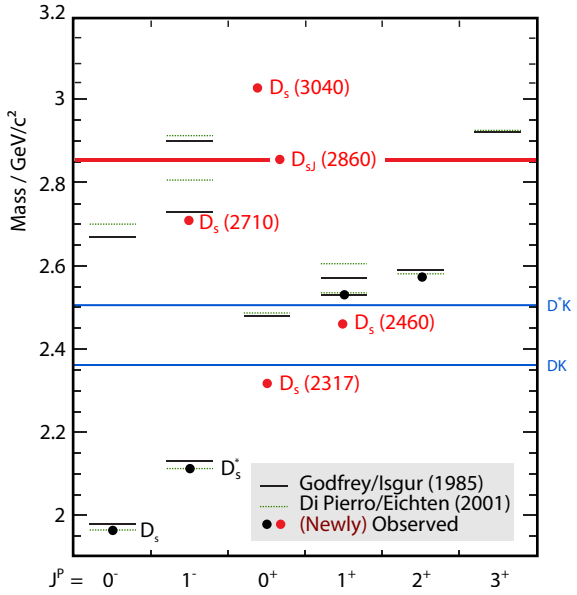

Figure 4.2: The D_s meson spectrum with measured results (black and red dots, the latter recently discovered ones) and two different predictions (black solid line from [44]; green dotted line from [45]). The states are sorted in columns by J^P quantum numbers and with increasing mass. The thresholds for decays into DK and D*K are shown as blue lines. Image from [2, 46].

Therefore, this field is an active research topic which P̄ANDA will contribute to with high resolution measurements. To pick one example, the $D_s(2317)$ has been first seen by BaBar [49] and has a small decay width due to its mass being below the DK decay threshold. Therefore, the strange content cannot be transferred to the kaon and has to decay weakly. The current upper limit of $\Gamma < 3.8\,\mathrm{MeV}/c^2$ at 95 % CL [1, 50] can be measured significantly more precisely with P̄ANDA to $\mathcal{O}\left(100\,\mathrm{keV}/c^2\right)$ [51] because of the HESR's cooled antiproton beam. Depending on the result, this will help to rule out some theoretical models predicting different widths of the $D_s(2317)$.

4.1.1.2 Charmonium Spectroscopy

In contrast to open charm mesons, which can only be produced in pairs from an annihilation reactions, hidden charm mesons can be produced without a partner due to their charm quark-antiquark pair. Such a bound system is called *charmonium* or generally for any heavier flavor *quarkonium*. The first excited charmonium was detected in 1974 with the J/ψ ($J^P = 1^-$), found simultaneously by the groups of RICHTER, AUGUSTIN, BOYARSKI, *et al.* [52] at SLAC and TING, AUBERT, BECKER, *et al.* [53] at the Brookhaven National Laboratory. Both group leaders got awarded with a Nobel Prize in 1976 [54], just two years later and a series of discoveries in particle physics[3] from many groups followed.

Similar to the open charm spectrum, the charmonium spectrum has grown over the years with many recent discoveries by high-energy physics experiments. In Figure 4.3, the current spectrum is shown, which also presents many states in disagreement with theoretical predictions.

[3] This period is called *November Revolution* because the J/ψ discovery was published in November.

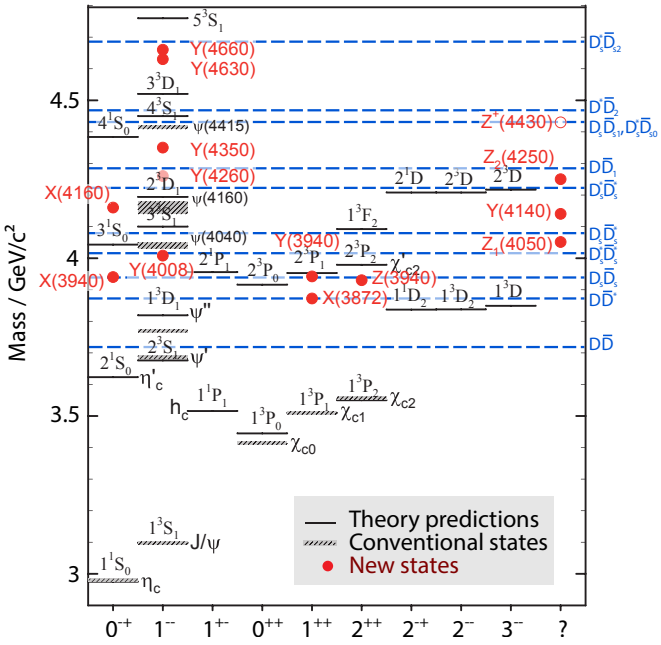

Figure 4.3: The charmonium spectrum with predicted (black solid lines) and measured states. The latter are given either as shaded black lines or red dots for conventional states and recently found XYZ states, respectively. The decay thresholds for D meson pairs are shown as blue dashed lines. Image from [2, 46].

This is especially true for resonances above the $D\overline{D}$ threshold for which the X(3872) is a good example. It lies in a region where radial excited charmonia are expected generally. Even though it has been measured first by Belle [55] and subsequently confirmed by other experiments [56–58], no theoretical model predicts such a state at this mass. Even more intriguing is its decay, which dominantly produces a J/ψ and a $\pi^{\pm}$ pair but is too narrow to be explainable via strong interaction which would be expected. To label this particle and others with similar exotic behavior accordingly, they are called X, Y, or Z indicating that the describing model is still to be determined. Especially the charged Z states like the $Z_c(3900)$ are clear indications for a four quark state. Section 4.1.2 concentrates on the exotic nature of these states.

PANDA will not only be able to measure these newly discovered excitations more precisely, the initial $\overline{p}p$ reaction makes the right part of the spectrum in Figure 4.3 with higher radial excitations accessible. Moreover, the resolution of mass and width measurements will be enhanced for established states like the η_c and η_c'[4]. Compared to the older, charmonium-oriented experiments at Fermilab, E760 and E835, PANDA will have a 10-fold higher momentum resolution and luminosity[5] as well as better angular coverage and detection efficiency. As a result, several thousand charmonium states will be producable per day, narrowing mass and width measurements down to resolutions of $\mathcal{O}(100\,\text{keV})$ and $\mathcal{O}(10\,\%)$, respectively [59].

[4]The measurements of Belle, BaBar, and CLEO show discrepancies while having some properties with large relative uncertainties like for the width $\Gamma(\eta_c') = (19 \pm 10)\,\text{MeV}/c^2$ [43].

[5]Resolution and luminosity improvements are referring to different operational modes of HESR: high resolution and high luminosity. The modes are exclusively and only one can be used at a time, see Section 3.2.4.

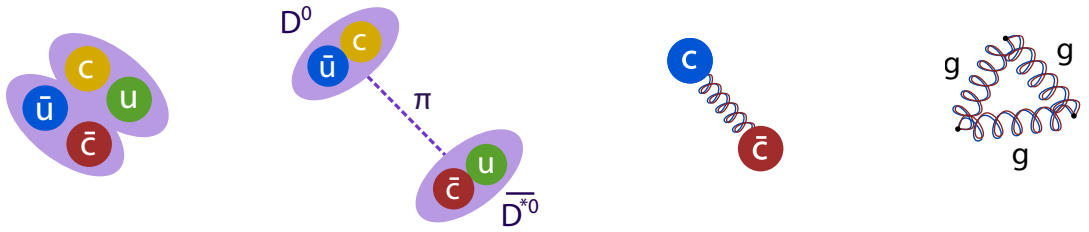

(a) Tetraquark. **(b)** Quark molecule. **(c)** Hybrid meson. **(d)** Glueball.

Figure 4.4: Possible explanations of hadronic states not predicted by the common quark models of mesons and baryons. The first two use more than three quarks while the last two include gluonic excitations. Images (a)–(c) from [2].

4.1.1.3 Baryon Spectroscopy

Besides meson spectroscopy, also baryons will be investigated with P̄ANDA. The background on baryons with strangeness has already been introduced in Section 2.2.3 and more specifically on double strange hyperons in Section 2.2.4. From the baryon lists in the »Review of Particle Physics« [1] it is obvious that for many states the properties like mass and width as well as the different decay channels are roughly measured, at best. Often, they are missing concrete data and have been seen only qualitatively. Moreover, Figure 2.4 gives a good impression, that theoretical models are lacking a proper description.

P̄ANDA will facilitate a comprehensive spectroscopy program for strange and charmed baryons with a baryon to meson production rate of around 1:1 for $p_{\text{beam}} = 3\,\text{GeV}/c$ up to around 2:1 for $p_{\text{beam}} = 12\,\text{GeV}/c$ [59]. This high rate of final state baryons is supported by the $\bar{\text{p}}\text{p}$ annihilation, which allow a direct production of hyperon pairs, reducing the threshold by not having to create additional D or K mesons. In HESR's high luminosity mode, the production rate of baryons with threefold strangeness (Ω) is expected to be around 700 Ωs per hour [59]. The comparably long lifetimes of hyperons cause displayed vertices of daughter particles requiring good tracking capabilities for the P̄ANDA detector.

4.1.2 Exotic Bound States

The previous sections show that many discovered states are not explainable as mesons or baryons based on valence quark constituents. This leads to building models involving different bound states allowed by QCD, the so called *exotic states*.

4.1.2.1 Multiquark States

Similar to atoms forming molecules, multiquark systems with a combination of hadrons are not forbidden by QCD. They introduce another degree of freedom for excitations, possibly explaining some unmatched states. The idea of a bound system of two mesons was first suggested for the light scalar mesons a(980) and f(980) [60] and has been picked up [61] for the already mentioned X(3872) particle, seen by Belle [55]. Another, more recent discovery is the $\text{Z}_\text{c}(3900)$, which has been seen simultaneously by Belle [62] and BESIII [63]. Through the

Table 4.1: Possible J^{PC} combinations for charmonium hybrid states ($c\bar{c}g$) in S wave. The quantum number configurations marked in red are impossible to reach just with quarks as constituents.

	Gluons	$^1S_0$ States	$^3S_0$ States		
Positive Parity	1^{+-}	1^{++}	$\mathbf{0^{+-}}$	1^{+-}	$\mathbf{2^{+-}}$
Negative Parity	1^{-+}	1^{--}	0^{-+}	$\mathbf{1^{-+}}$	2^{-+}

rapid decay into $J/\psi\,\pi^{\pm}$, charm-anticharm constituents in the $Z_c(3900)$ are likely, but with a net charge unequal to zero other quarks are required than just a $c\bar{c}$ pair. A tetraquark combination of a diquark-antidiquark system as shown in Figure 4.4(a) could explain the observed state.

With a similar concept but looser connection, molecular states are also conceivable as shown in Figure 4.4(b). Here, binding can be maintained by a light π meson. Such states could couple two mesons together, or a meson and a baryon, as proposed for the $\Lambda(1405)$. Lattice QCD calculations show for this state that an antikaon-nucleon ($\bar{\text{K}}$N) molecule is a sensible prediction [64]. Measurements try to account for this theory but lack of statistics for a definite answer [65]. $\bar{\text{P}}$ANDA could significantly improve the situation with more precise data.

4.1.2.2 Gluonic Excitations

The gluons, mediators of the strong interaction, carry color charge as the quarks do. Hence, a bound state involving gluons as principal constituents is not prohibited by QCD. However, such a state has not been confirmed with measurements yet. Conceivable are systems in which a valence gluon is part of a $q\bar{q}$ pair (*hybrids*) or even systems solely comprised of gluons (*glueballs*).

Hybrids A hybrid system is a meson which has a gluonic excitation, i.e. an additional valence gluon as shown in Figure 4.4(c). In such a system, the quantum numbers from the gluon ($J^P = 1^{\pm}$) would add up to the quark-antiquark pair, enabling settings otherwise forbidden to reach only with quarks. A charmonium hybrid ($c\bar{c}g$) without orbital angular excitations (S wave) for instance has eight possible J^{PC} combinations, three of which are only possible with an additional gluon (see Table 4.1).

Two particle candidates for hybrids with a distinct signature formed in $\bar{\text{p}}$p annihilation are the $\pi_1(1400)$ [66] and $\pi_1(1600)$ [67]. Both were measured at the Crystal-Barrel experiment at CERN and Lattice QCD calculations predict an agreement of J^{PC} quantum numbers and masses [68]. An identification in $\bar{\text{P}}$ANDA is possible by comparing the formation[6] with the production[7] spectra and look for missing excitations in the formation's spectrum.

Glueballs Another version of a gluonic excitations are glueballs, a bound system of gluons. Lattice QCD calculations predict 15 glueball states accessible with the momentum range of HESR

[6] Formation processes create particles directly from the annihilation reaction with a single-particle intermediate state.

[7] In production reactions, the particle of interest is created along with other particles through multi-particle intermediate states.

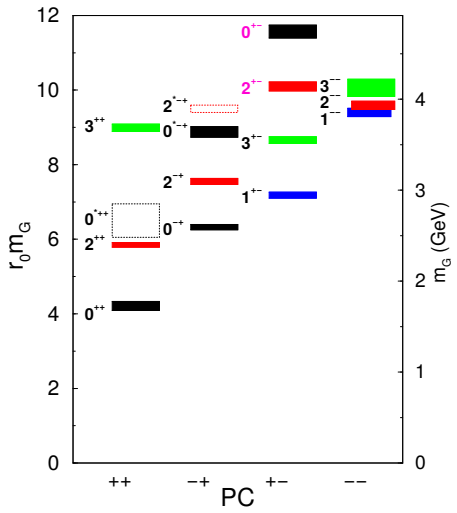

Figure 4.5: The predicted glueball spectrum from lattice QCD calculations accessible by PANDA. The numbers next to the states represent their quantum number configuration J^{PC} (pink numbers are oddball states) and the color sorts the states based on their total angular momentum J. On the left axis the mass is given in units of the hadronic scale parameter r_0 as multiples of $r_0^{-1} = 410\,\text{MeV}$ [69] and on the right axis directly in GeV/c^2. Image from [2, 68].

[69]. They are depicted in Figure 4.5. Glueballs with an exotic quantum number configuration that are not feasible just with quarks are called *oddballs*. Since they cannot mix with regular mesons, their identification is expected to be rather easy [43].

Out of the 15 mentioned states, two are such oddballs: $J^{PC} = 2^{+-}$ and $J^{PC} = 0^{+-}$ with the former predicted to be the lighter of the two at a mass of 4.3 GeV/c^2. Since glueballs can be formed directly in $\bar{\text{p}}$p annihilations, their investigation is a particular interesting subject of the PANDA experiment. PANDA will also be able to identify the lighter, regular glueballs more easily and thus collect more statistics compared to existing measurements [43].

4.1.3 Nucleon Structure

Besides the measurement of new and already discovered states, the nucleons as the everyday constituents of matter are also subject of investigation in PANDA. The theoretical framework describing their internal structure in non-perturbative regimes has just recently been developed [43]. These generalized parton distributions (GPDs) are accessible via $\bar{\text{p}}$p annihilations using a *handbag* approach: the reaction in the Wide Angle Compton Scattering ($\bar{\text{p}}\text{p} \to \gamma\gamma$ with a large polar angle between the two photons in their CMS) is split into hard[8] and soft parts which are described by conventional QCD and non-perturbative GPD methods respectively. Measuring the amplitudes in this process gives rise to parameters of the GPD.

The double photon production has a small cross-section so that only a few thousand events are expected per month [70], assuming high luminosity of HESR and $\sqrt{s} = 3.2\,\text{GeV}$. The statistics may be increased by also investigating a similar reaction with one photon replaced by

[8] The hard part refers to the quark-antiquark annihilation into a photon pair.

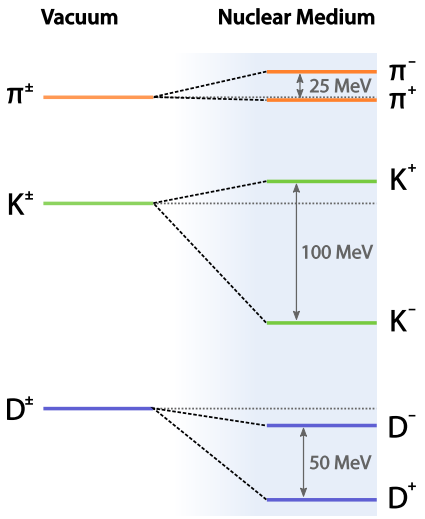

Figure 4.6: Visualization of mass splittings for charge-conjunctive mesons in a nuclear environment compared to their vacuum masses. The splitting of D mesons is not yet measured and based on predictions. Adapted from [43].

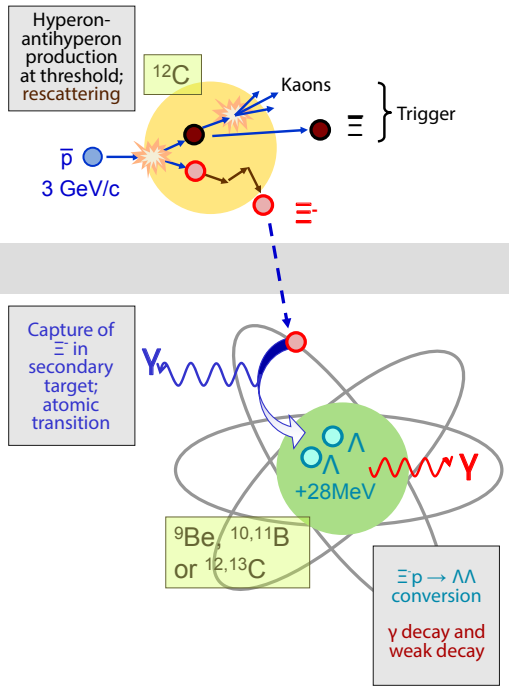

Figure 4.7: The production process of double-Λ hypernuclei with an antiproton beam in PANDA: Slow Ξ from the initial reaction will be stopped in a secondary target (^{12}C) and captured in a nucleus where they will decay into two Λs. Image from [2, 59].

a pseudoscalar meson like a π^0 [59]. Measuring the π^0 reveals its origin (proton or antiproton) and thus enables a study on a possible proton-antiproton asymmetry.

The momentum distribution of quarks within a nucleon can also be investigated with Drell-Yan processes. There, the annihilation of a quark pair forms a virtual photon with two leptons in the final state (e.g. $\bar{p}p \rightarrow \mu^-\mu^+X$). The angular distributions of the final leptons then provide access to the initial quark momentum states.

Finally, electric G_E and magnetic G_M form factors are accessible by electron positron formation ($\bar{p}p \rightarrow e^-e^+$) and provide insight into non-perturbative and regular QCD regimes likewise. Measurements often assume equality of the two factors ($|G_E| = |G_M|$), especially for high energy transfers Q^2. At $Q^2 \approx 15\,\text{GeV}^2$, only the Fermilab experiments E760 and E835 could provide a few data points [71, 72]. PANDA will not only be able to get more statistics up to and above $20\,\text{GeV}^2$, but also be able to distinguish between the two form factors up to around 9 GeV.

4.1.4 Hadrons in Nuclei

Placing mesons or other hadrons in nuclear matter affects their properties due to the surrounding interactions. A fundamental aspect is a modification of the spectral processes of mesons compared to their in-vacuum mass and an additional splitting of meson-antimeson masses (see

also Figure 4.6). Theoretical explanations of this involve a chiral symmetry breaking pattern of QCD and a partial restoration of this symmetry in the hadronic environment [59]. Other experiments have investigated this in-medium mass shift and splitting but none have exploited $\bar{p}p$ annihilations which enable implanting hadrons in a nuclear environment with low momenta, where the effects are most pronounced.

From the beam momentum range provided, charmed mesons in nuclear matter become accessible with high statistics. While for some states like the J/ψ a mass shift of only 5 MeV/c^2 to 10 MeV/c^2 is expected, others like D mesons are predicted to have a shift of 50 MeV/c^2 [73] up to 100 MeV/c^2 [74], depending on the used model. Investigating D mesons in matter is additionally interesting due to their large constituent mass difference, giving insights into the dynamics of the system.

4.1.5 Hypernuclei

Another topic involving nuclear matter is the implantation of strange quarks into nuclei. Following the naming of hyperons, these systems are called *hypernuclei*. The additional quantum number in such a system increases its degrees of freedom, allowing the hyperons to occupy low level energy states which would have otherwise been prohibited by Pauli's principle. After doing so, the hypernuclei become quasi-stable as a decay would form a nucleon with already occupied quantum configurations. The changes in the resulting system's dynamics give insight into the nucleus' structure and, vice versa, also on the effects of hyperons embedded into nuclei.

The existence of hypernulcei is known since the 1950s [75, 76] and so far only six double-Λ hypernuclei have been detected [43]. The production is done by effectively replacing one nucleon in the nucleus with a hyperon (Λ, Σ, Ξ, or Ω). In $\bar{\text{P}}$ANDA, single- and double-Λ hypernuclei can be investigated. The latter would be produced via intermediate Ξ production which get decelerated in a secondary target (see also Figure 4.7). Therefore, the innermost detector would need to be moved out due to limited space and increased radiation. Finally, the slow Ξ can be captured in nuclei where they decay into two Λs. Assuming a production cross section of 2 μb, an hourly rate of $\mathcal{O}(5000)$ Ξ^- with low enough momenta[9] for capture could be produced, leading to $\approx$ 80 observed γ-spectroscopic measurements of double-Λ hypernuclei per month [59].

4.2 Detector Systems

$\bar{\text{P}}$ANDA's measurement system is designed to reconstruct particle trajectories and energies with a nearly full 4π angular coverage. The spatial resolution in the $r-\phi$ plane is designed to be suited for track reconstruction in a momentum range from 100 MeV/c up to 8 GeV/c. In the high-luminosity mode of HESR 2×10^7/s interactions happen on average with an exponential distribution of time between two events. The broad physics program does not provide simple event topologies that can be used to trigger the readout with dedicated components but rather require a continuous analysis of the data stream and thus a triggerless readout.

The sub-detector systems of $\bar{\text{P}}$ANDA are divided into a central part, the *Target Spectrometer* depicted in Figure 4.8, and a forward oriented part, the *Forward Spectrometer* shown in Figure

[9] Less than 500 MeV/c.

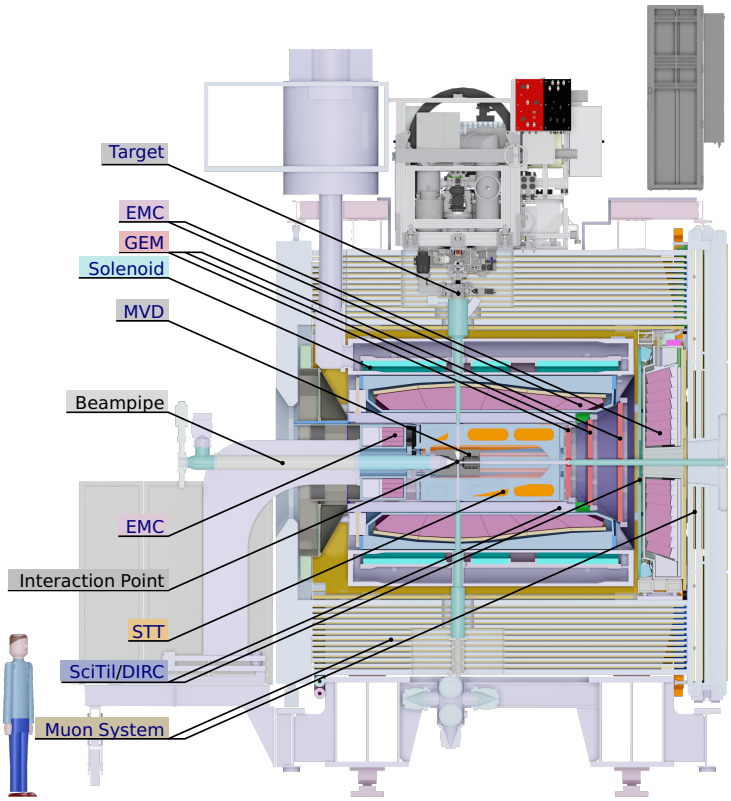

Figure 4.8: The Target Spectrometer of PANDA with labels for sub-systems. Image from [2, 77].

4.9. The former is oriented around the interaction region in a cylindric shape. In there, the barrel-like components cover polar angles >22°. Smaller angles are handled by detectors in endcaps. Reducing the polar angle even further below 10° will involve the Forward Spectrometer. Its purpose is the reconstruction of high-energy, forward-boosted particles resulting from the fixed-target kinematics of the experiment. In total, the layout has a length of around 13 m.

In the following an overview of the most important detector sub-systems is given, starting with the targets (Section 4.2.1) and magnets (Section 4.2.2). After that, the tracking detectors (Section 4.2.3), systems for particle identification (Section 4.2.4), and the calorimetric detectors (Section 4.2.5) are introduced.

4.2.1 Target Systems

Two different target systems are evaluated to provide collision partners for the antiproton beam: the *cluster-jet target* and the *pellet target* [78]. Their requirements are manifold, especially concerning a high target area density to enable high luminosity while introducing only a low contamination of the beam pipe's vacuum. Both systems aim at target areal densities larger than 10^{15} atoms/cm^2. An overview of their parameters is given in Table 4.2.

Cluster-Jet Target The working principle of cluster-jet targets is to send pre-cooled gas through a laval-type nozzle (see Figure 4.10). By expanding the gas in this nozzle, adiabatic

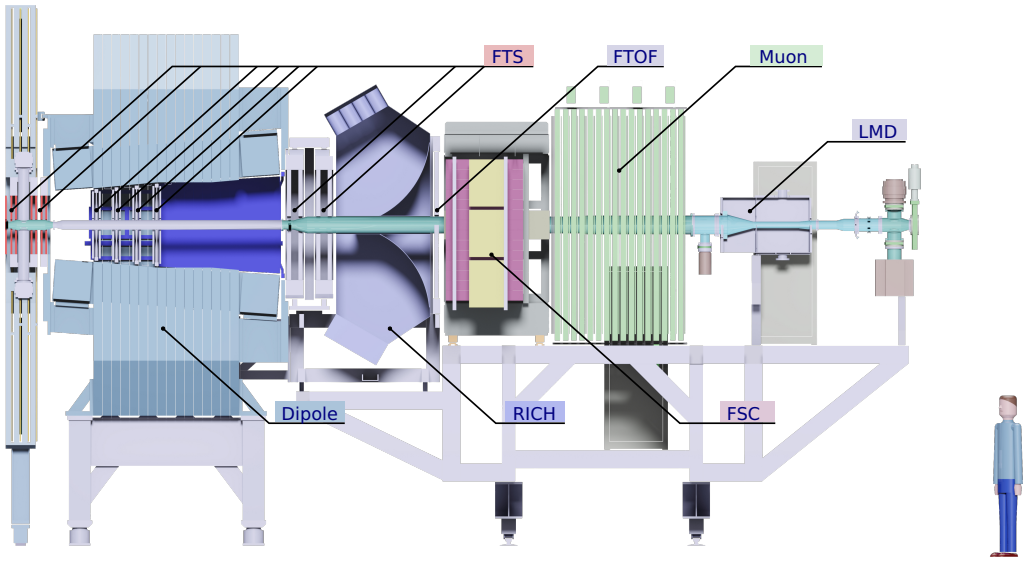

Figure 4.9: The Forward Spectrometer of PANDA with labels for sub-systems. Image from [2, 77].

Table 4.2: Key parameters of the two target systems for PANDA [78].

	Cluster-Jet Target	Pellet Target
Effective Target Thickness	1×10^{15} atoms/cm^2	5×10^{15} atoms/cm^2
Volume Density Distribution	homogeneous	granular
Size Transversal to $\overline{\text{p}}$ Beam	2 mm to 3 mm	<3 mm
Size Longitudinal to $\overline{\text{p}}$ Beam	15 mm	<3 mm
Target Particle Size	$\mathcal{O}$(nm)	20 µm
Mean Vertical Particle Distance	<10 µm	2 µm to 20 µm
Target Material	H_2, D_2 (heavier gases optional)	H_2, D_2, N_2, Ar (heavier gases optional)

cooling can be achieved and a supersonic stream is produced. The gas then clusters together to typically 10^3 to 10^5 atoms per cluster with sizes of $\mathcal{O}$(nm). This cluster beam then passes skimmer and collimator stages to narrow it down. The excess gas is extracted by turbomolecular vacuum pumps to minimize contamination in the antiproton beam pipe. In contrast to other cluster-jet targets, PANDA's target will operate with incoming material at temperatures of 25 K to 35 K and pressures up to 25 bar, resulting in hydrogen fluid. PANDA's initial version will be equipped with the cluster-jet target system.

Pellet Target A second development is done for the pellet target which will be inserted at a later stage. The target features frozen pellets for high effective target areal densities to achieve the high luminosity as planned. The pellets are produced by injecting the desired material as a cryogenic jet into a triple-point chamber containing the same material or helium close to

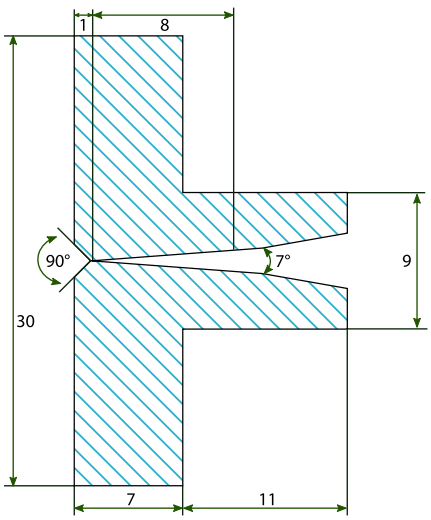

Figure 4.10: An illustration of the cluster-jet target's nozzle. The gas enters from the left through a narrow gap ($\mathcal{O}(10\,\mu m)$) and gets expanded subsequently. Numbers are in mm. Image from [78].

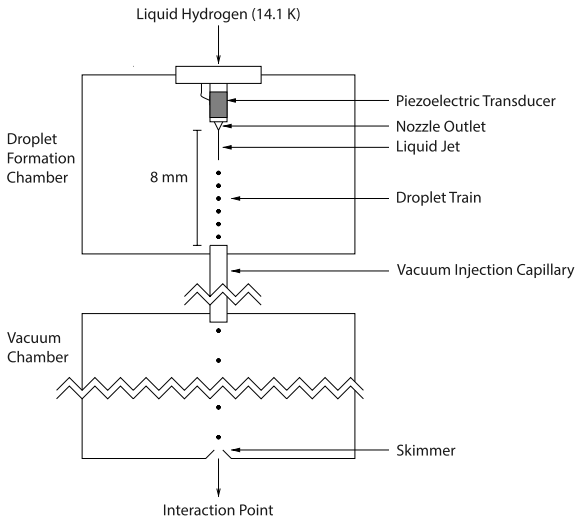

Figure 4.11: A schematic description of the pellet target's working principle. Image from [79].

triple-point[10] conditions. The chamber ensures a stable and precise drop flow rate without disturbances from evaporation. At the outlet, the jet passes injection capillaries into the vacuum system. The passage cools the jet until it freezes into pellets of ∼20 µm diameter, which also get accelerated in the vacuum chamber due to the gas flow. This leads to an effective target areal density up to five times above the cluster-jet target's density. An additional advantage besides the high density is the possibility for pellet tracking via optical systems. Placed 2 m to 2.5 m above and below the antiproton beam line, they aim for a resolution of <0.2 mm at the interaction point.

4.2.2 Magnets

The reconstruction of charged particles in PANDA is based on the curvature of their trajectories in a magnetic field. This bending is achieved by two magnet systems: a superconductive solenoid in the Target Spectrometer and a resistive dipole magnet in the Forward Spectrometer [80].

Solenoid Magnet Surrounding the interaction region, a superconductive magnet creates a solenoid field with a strength of 2 T along the beam axis. The field has a homogeneity of ±2 % in the tracker regions and only small radial field components. All the sub-detectors of the Target Spectrometer except the muon chambers are embedded into the magnet's volume of 4 m in length and 1.9 m in diameter.

[10] The triple-point of a substance denotes the temperature and pressure conditions where gas, liquid, and solid phases coexist.

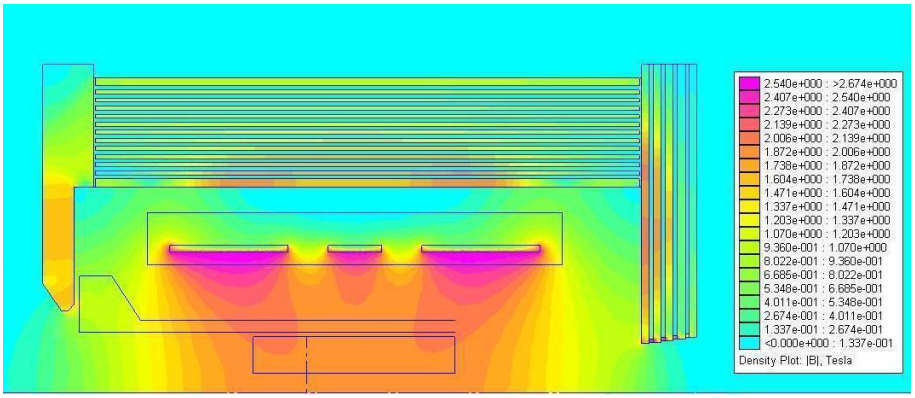

Figure 4.12: A simulation of the magnetic flux density of the solenoid magnet. The rectangular shape in the orange field is the outline of the tracker, the antiproton beam enters from the bottom left corner of the image. Image from [80].

The NbTi coils are split into three sub-coils to accommodate the target pipe. The coils are shown in Figure 4.12 as outlines and located just above the highest field densities displayed in pink. The operating current is at 5 kA and liquid helium is used to maintain superconductivity.

Dipole Magnet A resistive dipole magnet is placed at 3.5 m downstream from the interaction point (IP) in the Forward Spectrometer. It provides a big aperture of 1 m × 3 m and a bending power of 2 T · m, achieved by copper coils with an operating current of 2.16 kA. The resistive design is chosen because of its simpler design, especially without the need of liquid helium coolant, and the well-known behavior of resistive magnets.

With the field aligned perpendicular to the beam direction, it deflects the antiprotons by 2.2° at full momentum (15 GeV/c). Thus, additional dipole magnets are placed before and after $\bar{\text{P}}$ANDA (see the beam line's kink in Figure 3.5) to correct for this diversion. Antiprotons are not immediately at the desired momentum and have to be accelerated. To go along with this acceleration process, $\bar{\text{P}}$ANDA's dipole magnet has to ramp up from 25 % to 100 % of its maximum field within 60 s.

4.2.3 Tracking Detectors

The task of the tracking detectors is to measure the trajectories of charged particles through the magnetic fields, leading to measurements of the particles' momenta. In the following, $\bar{\text{P}}$ANDA's tracking detectors are introduced.

4.2.3.1 Micro Vertex Detector

The innermost detector is the Micro Vertex Detector (MVD) with the closest sensors just 2.5 cm away from the IP. As the name already indicates, the MVD is optimized to measure primary and secondary vertices of charged particles. Moreover, it contributes to the momentum reconstruction by providing additional spatial information from the particle's trajectory. Also energy-loss measurements are done in the MVD to assist in particle identification. The development work

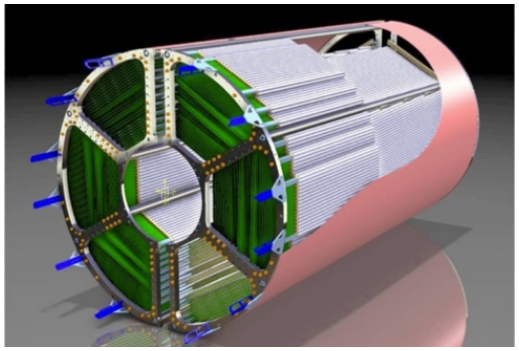

Figure 4.13: A CAD drawing of the STT showing the structure. The MVD is located within the hole in the center. Image from [81].

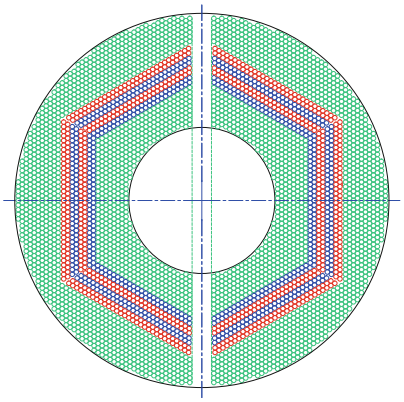

Figure 4.14: A cross section of the straw layers in the x-y projection. Green are parallel to the beam axis, red and blue are skewed by ±2.9°. Image from [81].

done in the course of this thesis is related to this detector, thus Section 4.3 introduces the MVD in more detail.

4.2.3.2 Straw Tube Tracker

Outside of the MVD follows $\bar{\text{P}}$ANDA's main tracking detector for charged particles in the Target Spectrometer: the Straw Tube Tracker (STT) [81]. It has a cylindrical arrangement of 4636 gas-filled straws in up to 27 layers (see Figure 4.13. The light construction yields in a low material budget of only $X/X_0 = 1.23\,\%$ radiation length in radial direction. Still, a good spatial resolution enables tracking of particles in a broad momentum range from a few 100 MeV/c up to around 8 GeV/c. The STT also provides valuable information for particle identification by means of energy-loss measurements especially for protons, kaons, and pions below 1 GeV/c.

The straws are filled with an Ar/CO_2 (90:10 mixture) gas and contained within thin walls of 27 µm thick Mylar foil. The conductive inner side of the wall functions as a cathode and an anode wire is stretched along the cylinder axis with a tension of 50 g. This holds the wire at a central position but also adds up to a total tension equivalent of 232 kg for the complete STT. To compensate this, the gas inside the wire is held at an overpressure of 1 bar, making the STT self-sustaining. Between the anode and cathode, an electric field of a few kV ensures a drift of the produced charges with a maximum drift time of 200 ns. A single tube provides a detection efficiency of 99.5 %.

The straws are arranged together in layers, up to 19 of those have a parallel orientation to the z axis. These straws yield a spacial resolution in x-y direction of 150 µm. The remaining 8 layers are skewed by an angle of ±2.9° to also get a position information along z with a resolution of 3 mm (see straw alignment in Figure 4.14). In total, the STT is 2.5 m long and covers polar angles from 10° to 140°.

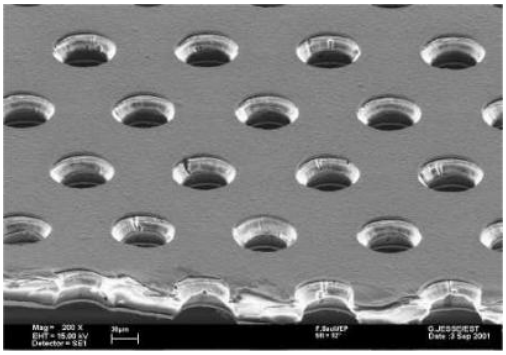

Figure 4.15: A electron microscope picture of a typical GEM electrode with etched holes of 70 µm diameter. Image from [82].

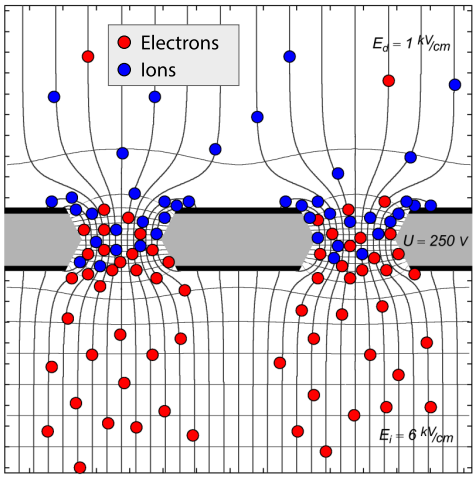

Figure 4.16: A sketch of the GEM's working principle. Strong electric fields lead to gas amplification in the holes. Most ions (blue) are then collected on the back side while electrons (red) continue drifting towards measuring anodes. Image from [83].

4.2.3.3 Gas Electron Multiplier

Towards shallow angles, the STT's coverage decreases, providing fewer hit points for particle trajectories. Thus, a Gas Electron Multiplier (GEM) detector will be installed in the upstream part of the Target Spectrometer [43]. Comprising of three disc stations that will be placed at distances of 1.1 m, 1.4 m, and 1.9 m, the GEM detector will measure forward directed particles in an angular range of 3° to 22°. Per station, two hit points are produced.

The GEM disc stations are drift volumes that contain thin Kapton foils (around 50 µm) with copper coated sides. Holes are etched into the foils, creating a regular pattern. See Figure 4.15 for an electron microscope image of a typical GEM foil. By applying a high voltage between the two sides, strong electric fields of $\mathcal{O}(50\,\mathrm{kV/cm})$ form a dense package of field lines in the holes which causing avalanche multiplication of the drifting electrons. The sketch in Figure 4.16 graphically explains this. The generated electron cloud is then collected by readout anodes behind the GEM foil.

4.2.3.4 Forward Tracking System

$\bar{\mathrm{P}}$ANDA's character as a fixed target experiment favors particles to fly in forward direction. The Forward Tracking System (FTS) is designed to measure those particles with shallow angles of less than 5° in vertical and 10° in horizontal direction [84]. Six tracking stations are planned, two in front of, two inside, and two after the dipole magnet (see Figure 4.17).

Each station consists of four sets of double layers of straw tubes, with two layers in a set aligned vertically to the beam axis and two skewed by ±5°. The number of straws per stations increases in downstream direction from 1024 for the first station up to 4736 in the last station, in total over 13,000 straws. Apart from their lengths, the straws are identical to the STT's

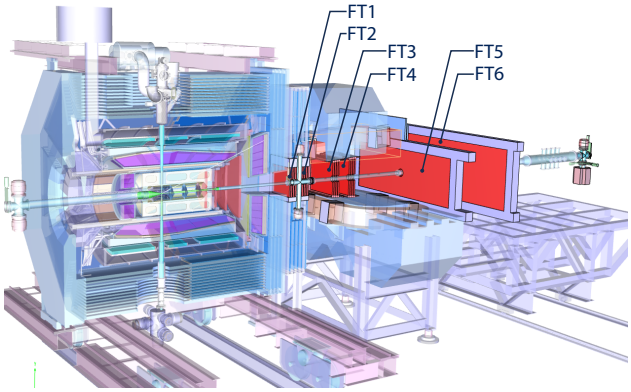

Figure 4.17: The positions of the six FTS stations highlighted in the in the Forward Spectrometer of PANDA's setup. Image from [2].

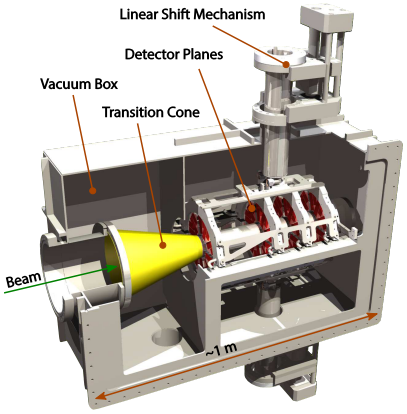

Figure 4.18: A CAD drawing of the LMD system. Image from [2, 85].

straws and will also be filled with Ar/CO_2 (90:10 mixture). Due to the different magnetic field configuration, the maximum drift times are a bit lower than in the STT with values from 130 ns to 150 ns, depending on the dipole's field strength.

4.2.3.5 Luminosity Detector

The most downstream detector system of PANDA is the Luminosity Detector (LMD) (depicted in Figure 4.18) [85]. Its intention is an accurate determination of the absolute and relative integrated luminosity with precisions of 5 % and 1 %, respectively. Elastic scattered antiprotons from the IP are measured in very shallow polar angles of 3 mrad to 8 mrad. Starting at 10.5 m downstream, the LMD needs to track the antiprotons to enable a back-propagation towards the IP. For that purpose, four discs with partially overlapping high-voltage monolithic active-pixel sensors (HV-MAPSs) are employed. They provide a channel pitch of 80 µm in both directions, totaling to around 60,000 pixels for one HV-MAPS sensor.

To minimize the influence of the beam pipe, the scattered antiprotons enter the detector volume through a transition cone (see yellow cone in Figure 4.18). The cone's walls are $\sim 10\,\mu m$ thin and keep the LMD's volume in vacuum. This is pumped synchronously with the vacuum of the HESR beam pipe.

4.2.4 Particle Identification

Besides the contribution of energy-loss measurement from the tracking detectors, dedicated detectors are planned for measuring particle velocities. Together, this enables reliable particle identification.

4.2.4.1 Cherenkov Detectors

A powerful method to extract particle identification information is to measure the light emitted from particles traversing a material faster than the speed of light in that material. The light

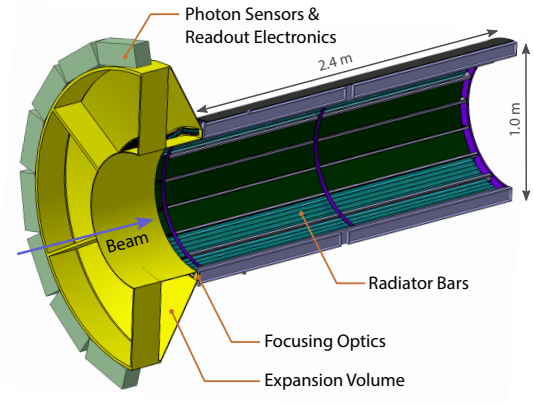

Figure 4.19: The barrel DIRC of the Target Spectrometer with the radiator bars in dark colors and the focusing optics and expansion volume in yellow on the left. Adapted from [86].

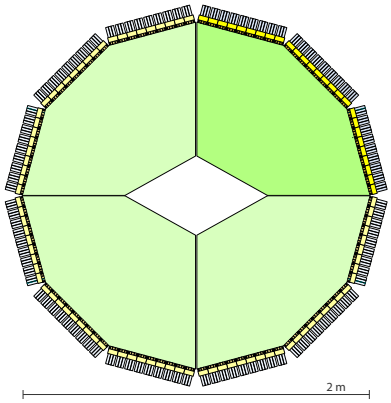

Figure 4.20: The four sectors of the disc DIRC with a hole in the middle for the beam. The focusing optics and readout electronics are placed on the edges. Image from [87].

is emitted at a characteristic angle θ_C creating a *Cherenkov cone*. The cone's angle depends on the particles velocity $\beta = \frac{v}{c}$. Combining this with the momentum from the tracking yields the particle's mass. The measurement is commonly done outside of the central detector where space is limited and the material budget should be kept to a minimum. The light cone is guided towards the readout, where focusing optics and expansion volumes ensure a clean, detectable signal. In $\bar{\text{P}}$ANDA, the particle identification system's goal is a separation power of 3σ for π/K up to 4 GeV/c. This is achieved with three different detectors based on the Cherenkov effect.

Barrel DIRC The first detection of internally reflected Cherenkov light (DIRC) detector in the Target Spectrometer is the barrel DIRC [88, 89]. Its cylindrical shape fits around the STT tracking detector and comprises rectangular radiator bars. The bars have a length of 2.4 m and are 17 mm thick. The resulting cylinder covers polar angles from 140° down to 22°.

The scintillators are connected to filter optics and expansion volumes, guiding the light to the photon sensors (Figure 4.19). Micro-channel plate photomultiplier tubes (MCP-PMTs) are used to convert the light into an electrical signal with a sum of around 15,000 channels. The arrival time is measured with a precision of ∼100 ps and the angular resolution is 8 mrad to 10 mrad.

Disc DIRC The same measurement principle but with a disc-shaped configuration is used by the disc DIRC. It covers polar angles of 22° down to 10° and 5° for horizontal and vertical direction respectively. Shaped like a regular dodecagon, the disc DIRC has four identical but optically separated sub-detectors. Their focusing optics and light readout is placed on the outside (see Figure 4.20).

The proposed readout solution is based on the TOFPET ASIC [87]. It has a digital resolution of 50 ps and is thus a valid candidate for a high precision timing of 100 ps that is required for the disc DIRC. The ASIC is the predecessor to the PASTA and is introduced in Section 5.1.3.

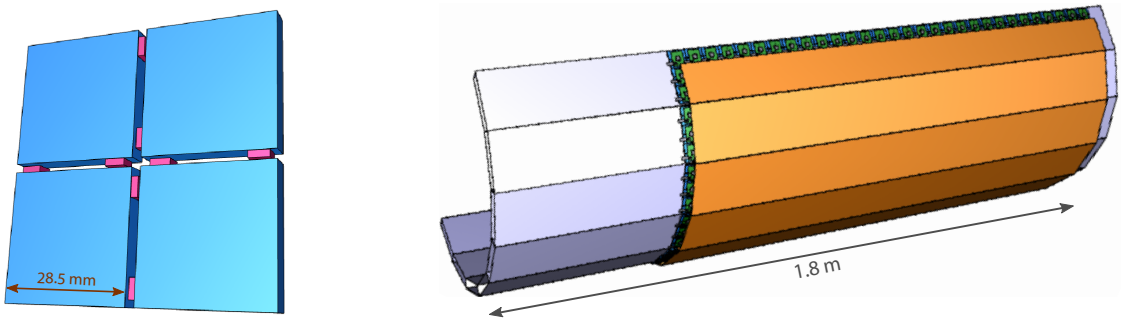

(a) Four scintillator tiles (blue) and read out (pink) combined to a module.

(b) A half-barrel of the SciTil as it will be inserted in the Target Spectrometer around the barrel DIRC.

Figure 4.21: Renderings of the SciTil detector. Images from [91].

Forward RICH The last Cherenkov detector is the forward Ring-imaging Cherenkov (RICH) in the Forward Spectrometer [90]. It is located at approximately 6.5 m downstream of the IP and covers an area of 3 m × 1.02 m, equivalent to polar angles <10° and <5° for horizontal and vertical directions respectively. The Cherenkov cones are produced from a 2-layer aerogel with refractive indices of $n_1 = 1.050$ and $n_2 = 1.047$.

4.2.4.2 Scintillator Tile Hodoscope

Two time of flight (TOF) detectors are planned within PANDA, one in the Target Spectrometer and another one in the Forward Spectrometer. With their fast response time, they provide an accurate timing information for the particles.

PANDA does not include a start TOF layer, thus the event start time t_0 has to be reconstructed otherwise. By combining different detector information like the target and forward TOFs, a relative measurement can be done. When a value for t_0 is available, the velocity of slow particles can be determined.

Additionally, the TOF detectors help disentangling PANDA's continuous data stream into single events. The stream has an average time between two events of 50 ns at its highest luminosity. Since the interval follows an exponential distribution, 63 % have Δt values less than the average. Thus, a precise timing information is required.

The TOF for the Target Spectrometer is the Scintillator Tile Hodoscope (SciTil), a barrel-shaped scintillator with <2 cm radial thickness equivalent to 2 % radiation length X/X_0 [91]. The SciTil will be inserted into the small gap between the DIRC and the EMC. In total, 1440 modules will make up the SciTil barrel, each comprising of four tiles (28.5 mm × 28.5 mm) with the silicon photomultiplier (SiPM) and readout electronics facing inside (Figure 4.21(a)).

The SciTil's timing resolution has a projected performance of 100 ps for the full system of scintillator and readout. Similar to the disc DIRC, the TOFPET application-specific integrated circuit (ASIC) is under investigation as a readout solution [92].

4.2.4.3 Forward TOF

Another TOF detector is foreseen in the Forward Spectrometer, the Forward time of flight (FTOF) [93]. Like the SciTil, it detects particles by fast-responding scintillators but is arranged as a wall of 140 cm height and 2.5 cm thickness. The width for the scintillators depends on their proximity to the beam axis, with 10 cm for the far and 5 cm for the near modules. Part of the wall is planned to be placed in the dipole magnet, thus the readout photomultipliers need to be insusceptible to its magnetic field. Therefore, SiPMs are a favorable option. The system's timing is targeted to be between 50 ps and 100 ps.

4.2.4.4 Muon System

A proper detection of muons in $\bar{\text{P}}$ANDA is crucial for a series of measurements like the identification of J/ψ or investigation of Drell-Yan processes. Especially the latter has a large momentum spread from sub-GeV/c up to 10 GeV/c. Thus, a dedicated muon system is planned as a final detector layer [94]. It uses iron absorbers to filter out hadronic particles and get clean muon samples.

In the Target Spectrometer, the system is split into two parts, a barrel and an endcap. They are integrated into the yoke of the solenoid target magnet to simultaneously use the iron as an absorber and as guide for the outlying magnetic field. For the barrel, 13 layers of 3 cm iron alternate with 3 cm detector. To adjust to the higher momentum of forward boosted particles, the iron layers of the endcap are 6 cm thick. Downstream of the endcap, additional 4 alternating layers follow in the so called muon filter. Besides extending the endcap's muon detection it also enhances the magnetic shielding between the two magnetic fields. Finally, the forward muon system consists of 16 iron layers of 6 cm thickness alternating with detection layers. The forward system will be located behind the forward calorimeter in the Forward Spectrometer. All involved muon components are shown in Figure 4.22.

The detectors producing the detection signals are mini-drift tube (MDT). They are a robust and proven detection system based on gas amplification. $\bar{\text{P}}$ANDA's MDTs will be operated in proportional mode, providing a position signal along the internal wire. The second coordinate is delivered by external strip electrodes. Both have a pitch of 1 cm.

4.2.5 Calorimetry

As one of the last steps of the particle's path, its energy is determined in a calorimeter[11]. The entering particle creates an electromagnetic shower whose energy is measured. For $\bar{\text{P}}$ANDA, two calorimeters are planned with one for Target and Forward Spectrometer each.

4.2.5.1 Target Electromagnetic Calorimeter

The target's Electromagnetic Calorimeter (EMC) is placed inside the solenoid magnet of the Target Spectrometer [95]. It covers 99 % of the full 4π solid angle and is designed to have an energy resolution of $\frac{\sigma_E}{E} = 1\,\% \oplus \frac{<2\,\%}{\sqrt{E/\text{GeV}}}$. The full calorimeter is divided into three sections: the

[11] Muons are an exception since they pass the calorimeter and are measured in the muon system with a higher stopping power.

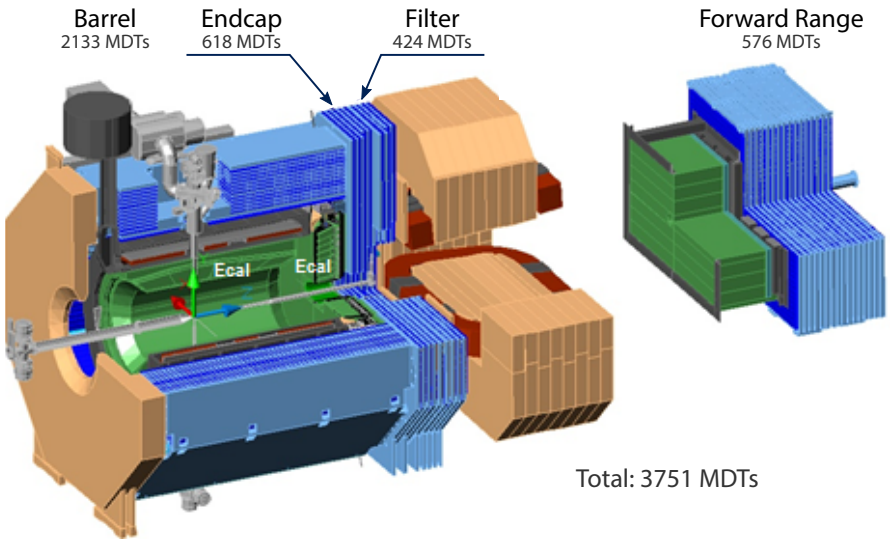

Figure 4.22: The four parts of the muon system of PANDA together with their number of MDTs for the readout. Image from [2, 94].

forward endcap EMC for tracks above 5°, the barrel EMC for >22°, and the backward endcap for >140° (see Figure 4.23). The barrel calorimeter has an inner radius of 0.57 m from the IP, the forward and backward endcaps are positioned at 2.1 m downstream and −1 m upstream, respectively.

To combine tracks from the tracking detectors with the energy measurement and provide a position information for photons[12], the calorimeter has to provide a high granularity. Additionally, the space is limited from the surrounding superconductive coils and a high radiation dose of up to 125 Gy annually is expected. Lead-tungstate ($PbWO_4$) crystals fulfill these requirements as scintillating material. They are designed for $20\,X_0$ radiation lengths, resulting in ~ 20 cm long crystals. In total, 11,360 crystals are employed in the barrel part, 3600 in the forward and 592 in the backward endcap. The target of the low-energy threshold is 10 MeV to 20 MeV for photons for all calorimeter sections.

4.2.5.2 Forward Spectrometer Calorimeter

For the forward boosted particles, the Forward Spectrometer Calorimeter (FSC) provides a $4\,m^2$ area at around 7 m downstream to measure their energies [96]. Even though the FSC only covers 0.74 % of the full solid angle, it has an acceptance of 8 % for inclusive produced photons. Similar to the EMC, it has a low-energy threshold for photons of 10 MeV to 20 MeV and an energy resolution of $\frac{\sigma_E}{E} = 1\,\% \oplus \frac{<3\,\%}{\sqrt{E/\mathrm{GeV}}}$.

The used principle for the calorimeter is called *shashlik calorimeter* and introduces wavelength shifting fibers into the scintillators to extract the produced light. This is a cost-efficient and high-performance solution for calorimetry. The downside is an inhomogeneous light output

[12] Photons are invisible for the tracking detectors, so the calorimeter is the only detector recognizing those.

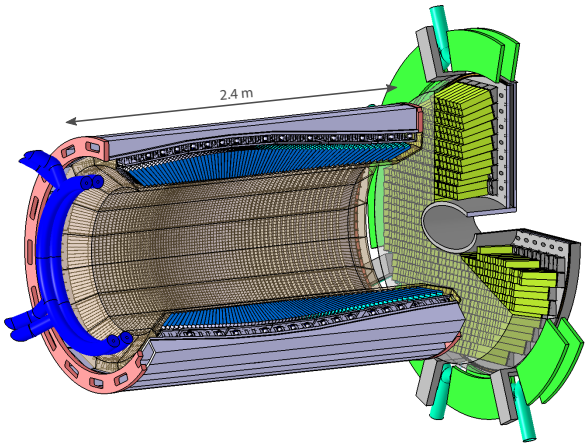

Figure 4.23: The design of the EMC in the Target Spectrometer with cyrstals of the barrel part (blue) and forward endcap (green). Image from [95].

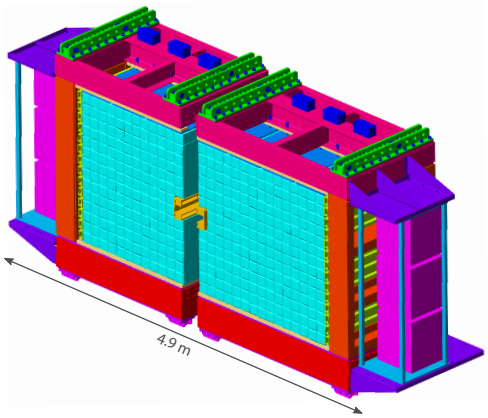

Figure 4.24: A rendering of the FSC detector with scintillator cells in turquoise. Image from [96].

depending on the angle of entrance but this is negligible in the Forward Spectrometer because of the large distance to the IP. In total, 1512 cells make up the full detector (depicted in Figure 4.24), each providing a radiation length of $20\,X_0$.

4.3 The Micro Vertex Detector

4.3.1 Detector Purpose and Requirements

4.3.1.1 Motivation for the MVD

In $\bar{\text{P}}$ANDA's physics program, the measurement of charm and strange hadrons plays a key role. Thus, identifying those particles is a major task of the detector. The states often have significant decay lengths in the range of $\mathcal{O}\left(100\,\mu\text{m}\right)$ (e.g. $c\tau(\text{D}^0) = 123\,\mu\text{m}$, $c\tau(\text{D}^\pm) = 312\,\mu\text{m}$) up to a few cm (e.g. $c\tau(\Lambda) = 7.9\,\text{cm}$, $c\tau(\Xi^-) = 4.9\,\text{cm}$) [1]. A good vertex reconstruction can identify those displaced vertices. This is achieved by the Micro Vertex Detector (MVD) which provides 3D hit information very close to the IP.

Moreover, the relatively fast responding detectors help in disentangling the event stream and the energy loss in the sensor layers contributes to the particle identification. The latter is especially true for slower protons, kaons, and pions. The presented information in this section is taken from the »Technical Design Report for the: $\bar{\text{P}}$ANDA Micro Vertex Detector« [98] if not otherwise mentioned.

4.3.1.2 Detector Requirements

Above all, the position information of charged particles should be obtained as close to the IP as possible. Based on this basic design goal, a set of requirements emerges.

- The spatial resolution needs to be around $100\,\mu\text{m}$ in z and a few tens of μm in $x - y$ direction to achieve the required vertex resolution.

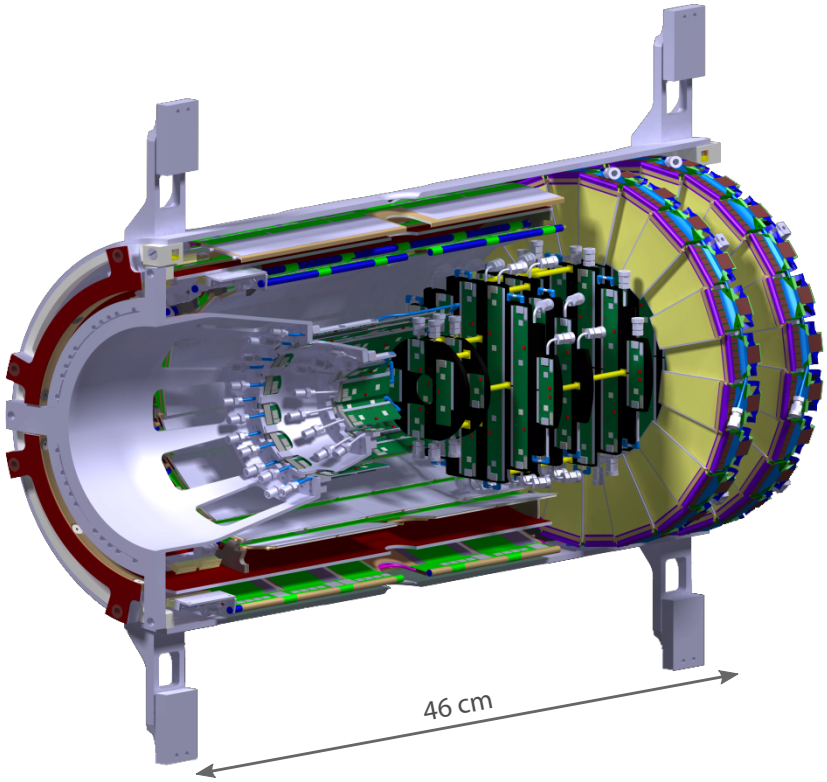

Figure 4.25: A CAD rendering of the MVD with one half of the barrel removed for visibility reasons. The antiproton beam enters from the left. In green on black surfaces are the pixel disk sensor modules, the yellow areas are the trapezoidal strip sensors. Image from [97].

- Almost the full solid angle should be covered to maximize the MVD's acceptance. From surrounding detectors and structures the polar angle range is limited to 3° to 150°.

- To reduce the impact on the outer detectors and the worsening of momentum resolution due to multiple scattering, the material budget of the MVD should be kept to a minimum. A limit of $X/X_0 = 10\,\%$ relative radiation length is set.

- The closeness to the IP simultaneously increases the radiation density. During the expected $\bar{\text{P}}$ANDA operation time[13], accumulated radiation doses of $\mathcal{O}\left(10^{14}\,\text{n/cm}^2\right)$ for 1 MeV neutron equivalents and $\mathcal{O}\left(100\,\text{kGy}\right)$ of ionization dose is predicted. Adequate measures have to be taken to protect electronics and sensor material.

- Finally, a good time resolution of $\mathcal{O}(10\,\text{ns})$ is required to disentangle the incoming event stream. Together with the spatial hit information, this contributes to the task of sorting particles to individual events.

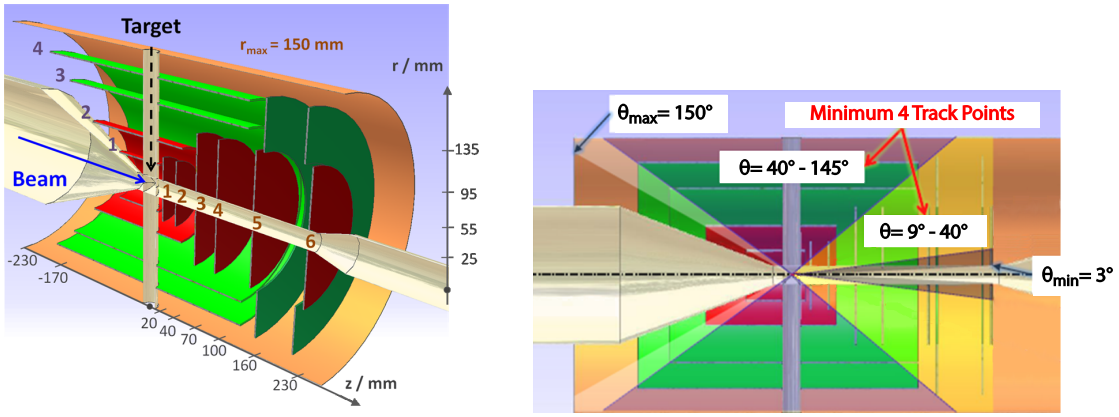

(a) The layer orientation and positions, units are in mm.

(b) Side view to visualize the polar angle coverage.

Figure 4.26: The basic layout of the MVD tracking detector. Shown in red are the silicon pixel sensors and in green the silicon strip sensors. Images from [98].

4.3.1.3 Overview of the Detector Layout

The general layout of the MVD is divided two-fold. A geometrical separation is done in a cylindrical barrel part and a disc part in forward direction. They cover angles from 9° to 145° and meet at 40°, as shown in Figure 4.26(b). The second separation is done based on the sensor segmentation, pixel-like sensors for the inner layers and strip-like sensors further outside. Two of the barrel and all six disc layers contain pixel sensors while the two outer barrel layers and the two furthest disc layers are equipped with strip sensors. This can be seen in Figure 4.26(a).

The MVD's outer radius is limited to 15 cm by the STT, hence the outermost barrel layer is located at 13.5 cm. In z direction, the MVD spreads roughly ±23 cm around the IP. This results in at least 4 hit points in a polar angle range from 9° to 145°, see Figure 4.27(a). Towards the IP, the closest distance is 2.5 cm for the innermost barrel layer and 2 cm for the innermost disc layer. The operation temperature of the MVD is at around 30 °C, kept stable by a cooling system. Low-pressurized water is used as a coolant with an inlet temperature of 16 °C. The room-temperature-like condition avoids condensation of water vapor from the air in the experimental hall. Otherwise, the MVD would have to be kept in a closed case with vacuum or nitrogen filling, introducing additional material.

Concerning the material budget, the primary contributions come from support structures (28.5 %) and routing of cooling pipes (13.6 %) and cables for data and supply voltage (37.7 %). Only a fraction is introduced by the active material itself (15.2 % plus 5 % for electronics). A simulation of the angular distribution of introduced material budget from the MVD is depicted in Figure 4.27(b). These results show that light-weight support structures and efficient cooling concepts are required. Optimizing the electronics immediately helps reducing the supply effort, which was a major objective for the developments described in Chapter 5.

[13] 10 years and a duty cycle of 50 % are assumed.

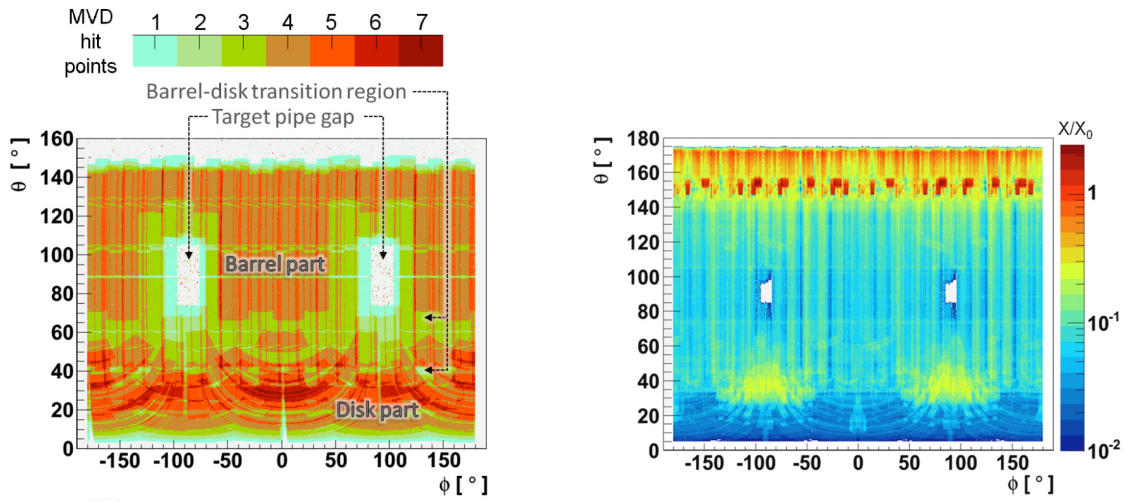

(a) Hit multiplicity in the MVD for pions with a momentum of 1 GeV/c from the IP.

(b) The introduced material budget from the MVD in relative radiation lengths.

Figure 4.27: Simulations performed on the layout of the MVD. Images from [98].

4.3.1.4 Signal Generation in Silicon Detectors

The sensors producing the signal in the MVD are silicon-based, both for pixel and strip sensors. An ionizing particle passing the material will deposit some of its energy there, mostly by means of inelastic scattering on shell electrons generating negatively and positively charged carriers. The mean energy loss per passed distance ($\frac{dE}{dx}$) is described by the Bethe equation [1] and shown in Figure 4.28. Creating an electron-hole pair requires an average energy of 3.6 eV, much less than in gaseous detectors (20 eV to 30 eV per pair). Therefore, silicon sensors can be produced thinner while still extracting a good signal.

Since the charge carrier production is a statistical process, the amount of energy deposited is not constant but rather follows a distribution with large fluctuations. This is especially true for thin materials. The probability for the energy deposit in such a thin layer can be described by a Landau distribution as shown in Figure 4.29.

The charge carriers produced by the just described ionization process need to be detected. To suppress the number of intrinsic charges, a depletion zone is created in the p-n junction of two differently doped[14] areas of a semiconductor. The n-doped area has an excess of electrons which will drift into the p-doped area to fill holes there if no external field is applied. This leaves the n-doped area positively charged and the p-doped area negatively charged, creating an electric field and hindering additionally generated charge carriers to travel freely. Applying an external electric field counteracting this drift enlarges the electrically neutral volume (*depletion zone*). This process is called *reverse biasing*. Now, the additionally charge carriers can move relatively freely and will follow the applied electric field.

[14] Doping is a process in which a few atoms different from the semiconductor's element are inserted, creating impurities in the base material. The electric potential of the surrounding area causes an electron to be loosely bound (n-doped) or a hole to be created (p-doped), both able to travel freely through the semiconductor.

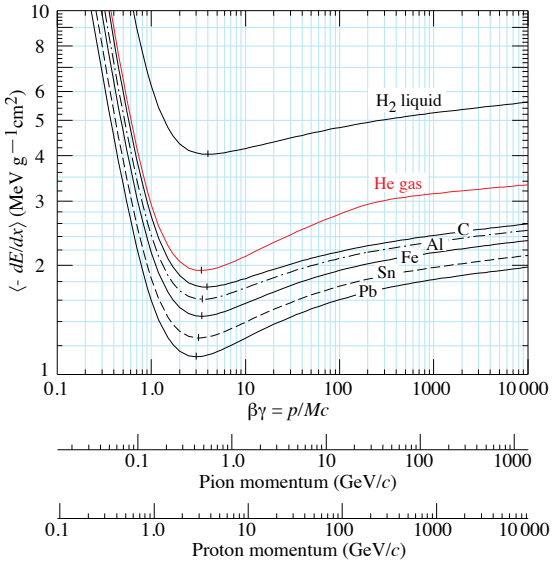

Figure 4.28: The mean specific energy loss in different materials as a function of the particle momentum. Image from [1].

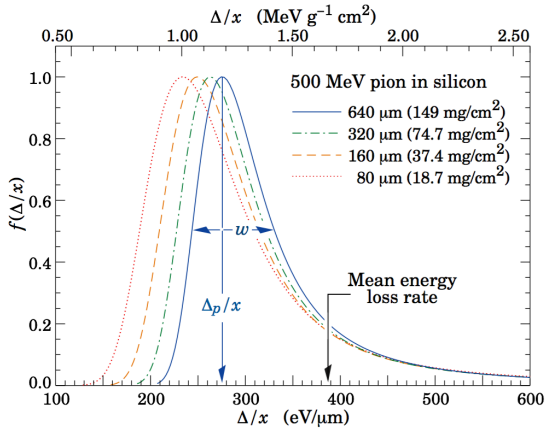

Figure 4.29: The energy loss distribution for 500 MeV/c pions for different silicon thicknesses. Image from [1].

Without any segmentation, only the amount of generated charge carriers, i.e. the deposited energy, can be measured. Segmenting the silicon into one-dimensional strips or two-dimensional pixels provides spatial information as well.

4.3.2 Pixel Detectors

4.3.2.1 Sensor

The pixel sensors used in the MVD are built as hybrid sensors that are flip-chip bonded to their readout. This is a proven technology for vertex trackers in particle physics experiments at the LHC. The sensors are produced by growing an epitaxial layer of thicknesses up to 150 μm on a substrate with the Czochralski (Cz) process. On top of the epitaxial layer is the segmentation into pixels which are soldered head-to-head to the readout ASIC. The Cz substrate is almost completely removed to minimize the material budget. Figure 4.30 shows a cross-section of the hybrid pixel sensor.

The pixel cells have a rectangular shape with 100 μm × 100 μm outer dimensions. A full readout matrix contains 116 × 110 pixel cells and has, thus, an active area of 1.3 cm^2. Different module sizes of 2, 4, 5, and 6 sensor chips are foreseen. Out of these modules, the barrel and disc layers are build together (see Figure 4.31). All pixel sensors taken together make up a total active silicon area of 0.106 m^2.

4.3.2.2 Readout

The Torino Pixel ASIC (ToPix) is the readout front-end of the hybrid pixel sensors. It is currently at its fourth prototype iteration, which is built in a reduced size to limit prototyping costs. The ASIC is produced in0.13 μm CMOS technology and uses the time over threshold (TOT) readout

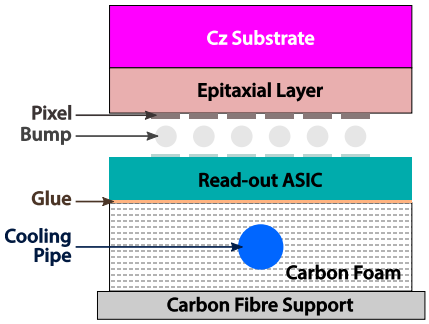

Figure 4.30: A cross-section of the bonding scheme for hybrid-pixel sensors. The Cz substrate layer is almost completely removed after bonding. Image from [98].

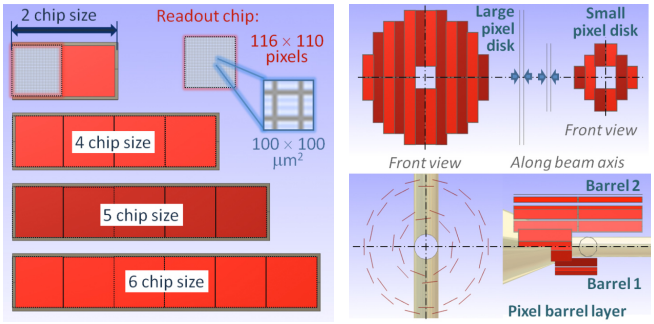

Figure 4.31: Sketches of the pixel sensor's geometrical structure. One readout chip comprises of 116×110 pixels which are bundled together to modules (left). These modules then form the disc (top-right) and barrel (bottom-right) layers. Image from [98].

concept, as PASTA does as well. In this concept, a channel produces a timestamp for the pulse's start and a length, the latter allowing to reconstruct the deposited energy.

The ToPix chip has a dynamic range for the input charges of up to 50 fC and a preamplifier noise level of $<200\,e^-$ equivalent noise charge (ENC). The power consumption of the ToPix 4 for a clock rate of 160 MHz is around 120 mW per chip, resulting in $<800\,mW/cm^2$ [97]. Its time resolution is based on the clock frequency, so 6.8 ns in case of 160 MHz. A total of 338 readout chips is foreseen for the barrel, 472 for the disc areas. This sums up to 10.3×10^6 readout channels in the pixel part. The connection to the off-detector components is done via optical fibers. Hence, ToPix is directly connected to the CERN developed, radiation hard Gigabit Transceiver ASIC (GBTX) chip [99]. It serializes the data stream onto an optical fiber with a bi-directional transmission speed of up to 4.8 Gbit/s.

4.3.3 Strip Detectors

A strip segmentation provides a precise measurement in one coordinate, the second coordinate is accessible through a second, tilted array of strips. The benefit is the vastly reduced amount of readout channels. However, too high track rates and densities lead to ambiguities when two particles leave signals in the measurement window. Therefore, strip sensors are employed in the MVD further outside from the IP.

4.3.3.1 Sensors

The sensors are double-sided silicon strip sensors that place the tilted strip array on the backside of one sensor. This optimizes the material budget because only one bulk is required but simultaneously increases the technical difficulty. Both sides need to be connected to the bias ring to develop the diffusion zone. If this would be done directly, a signal on one side would spread to all channels on the other side. The insulation is either done by a poly-silicon resistor or by punch-through biasing. In case of the latter, the strips are only indirectly connected by the developing depletion zone, otherwise they don't have a direct connection to the bias ring.

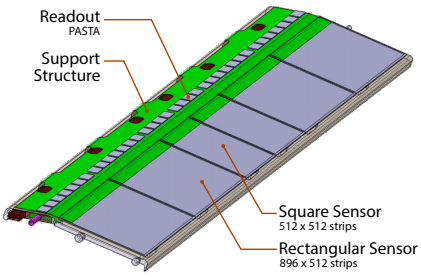

Figure 4.32: Rendering of a stave for the strip barrel part (distorted due to viewing angle). Image from [100].

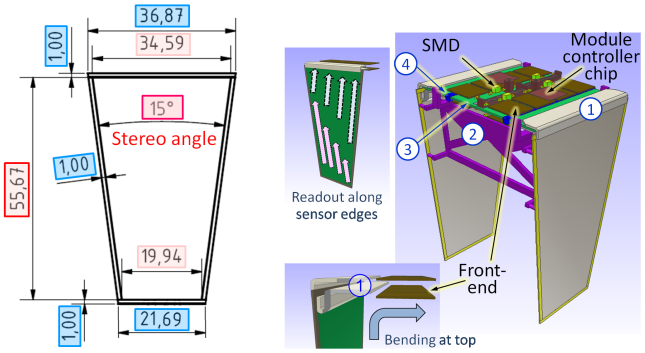

(a) The design parameters of the wedge sensor. **(b)** The assembly of wedge sensors into a module.

Figure 4.33: The wedge-shaped sensors for the strip disc part. Instead of 4 readout front-ends, as shown here, 6 will be used. Images from [98].

Depending on the location in the MVD, two different types of sensors are used. The barrel employs rectangular-shaped sensors aligned on a stave (see Figure 4.32). On there, two sizes are used with a combination of 512×896 and 512×512 strips on back and front side and with a pitch of 65 µm. Their bias connection is done with resistive biasing and they operate at up to 200 V reverse-bias voltage. For the disc modules, trapezoidal sensors in a wedge shape are designed (see Figure 4.33(a)). They have 768 strips on both sides and a stereo angle of 15° between them [101]. The first prototypes use punch-through biasing but it is planned to switch to a resistive connection for future versions [102]. Common for both sensor shapes is that the readout is done only every second strip to save readout channels. Simulations show only a slight impact on the position resolution if the signal to noise ratio (SNR) is $\mathcal{O}(20)$ [103]. In total, the strip sensors cover an active silicon area of 0.47 m^2.

4.3.3.2 Readout with PASTA

The chosen readout solution is a highly-integrated front-end, custom-made for the MVD. It is based on the TOFPET ASIC and is extensively described in Chapter 5. The ASIC is called P̄ANDA Strip ASIC (PASTA) and is produced in 0.11 µm CMOS technology. With 64 readout channels for one ASIC, the strip part sums up to 3112 PASTA chips and around 200,000 readout channels. This is ∼50 times less than for the pixel part while covering more than four times the area.

4.3.3.3 Module Concentrator

The next step from the strip readout front-ends is the Module Data Concentrator (MDC) [101]. It combines the information from a group of PASTA chips and will be installed on the same printed circuit boards (PCBs) as the front-ends, ensuring short electrical data paths. One MDC will multiplex the data stream from one sensor, thus combing 11 or 8 front-ends for the barrel part, respectively, and 12 for the trapezoidal sensors. The PASTA ASICs sort hits based on the

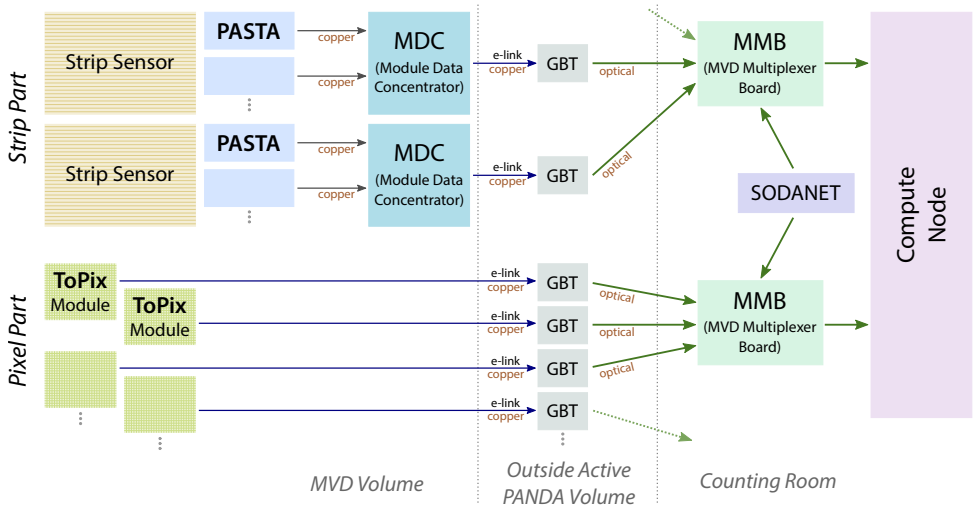

Figure 4.34: The schematic data path from the MVD sensors to the compute node. For the strip part, multiple PASTA ASICs send the data to an MDC which is connected to to a GBTX transceiver. The MDC is missing for the pixel part. In the GBTX, the signals are converted for optical transmission and are sent outside of the detector to the counting room. The MMB combines optical lines before sending the data further to the compute node.

finish of processing and then groups the hits into frames. While this is practical and efficient for the readout itself, it hinders a more sophisticated event building.

For that purpose the MDC buffers the data and orders the hits time-wise across the connected front-ends. Additionally, the MDC will provide simple feature extraction methods for 2D hit building and cluster finding by comparing deposited charges. This can already be used to reduce unnecessary data. Like the ToPix itself, the MDCs are connected to the radiation hard GBTX transceiver chip. This then sends the data to an external counting room where additional readout hardware is located, away from the harmful radiation.

4.4 Off-Detector Data Acquisition

4.4.1 MVD Data Multiplexing

The first off-detector component for the MVD is the MVD Multiplexer Board (MMB). Its task is to receive event data from and send configuration data to the front-ends. With the used Gigabit Transceiver (GBT) protocol, a bi-directional net throughput of up to 3.2 Gbit/s is achievable [99]. The MMB combines the inputs of four MVD front-ends. Data that is received will be processed with feature extraction and simple track finding algorithms. The available processing power is provided by a Xilinx Kintex-7 field programmable gate array (FPGA) and is flexible for algorithm updates and generally more performant than the MDCs close to the front-ends. The MMB is based on a Micro Telecommunications Computing Architecture (µTCA) board that has an uplink of 10 Gbit/s to the compute node [104].

Additionally, the MMB also extracts slow control data from the Synchronization of Data Acquisition (SODA) system and provides it to the front-ends via the optical line. Besides the

distribution of configuration, the SODA system is mainly intended for clock synchronization. This is required because all sub-detector systems run and take data independent of each other thus their timing is a priori not aligned. For a successful event reconstruction matching time stamps are indeed mandatory. Prototype measurements of the clock jitter have <20 ps root mean square (RMS) [105].

4.4.2 Online Event Reconstruction and Filtering

Data from the MMB and all other sub-detector systems are transferred to $\bar{\text{P}}$ANDA's compute nodes. These are fast event building and filtering clusters, combining detector information and sorting them into time slices. Algorithms are performed for hit clustering and track finding, matching of different sub-systems[15], and particle identification. Less complex algorithms filter the data so that more complex algorithms only have to process a subset of the data. In total, the compute nodes are supposed to reduce the data stream by $\mathcal{O}(10)$. The compute note's cores are FPGAs, in the current prototype Xilinx Virtex-5, with a large memory of 4 GB random-access memory (RAM). The FPGAs are mounted on µTCA boards and connected to a motherboard.

From the compute node, the data is sent to the final step of the online data acquisition, the computing farm. Here, the most sophisticated algorithms extract features like momentum, vertices, and invariant masses to reconstruct the complete event topology. Based on this, a final decision is made to store the event on long-term storage or not. More information on $\bar{\text{P}}$ANDA's data acquisition scheme is available in [43].

4.5 Software Framework

A powerful software toolkit is available to simulate the behavior and response of $\bar{\text{P}}$ANDA's sub-detectors to physics reactions. Its central component is the deeply-integrated framework PandaRoot which is explained in this section along with other relevant software tools.

4.5.1 Basic Frameworks

PandaRoot is an extension of the software frameworks FairRoot and ROOT, all based on the C++ programming language. ROOT, as the highest level of these framework layers, is a versatile, objective oriented data analysis package developed at CERN from the late 90s until now [106]. Included are several classes and methods for common analysis tasks like visualizing data in histograms or storing them efficiently in data objects[16]. Along with ROOT comes an interpreter to process scripts and make interactive analyses. This allows for swift development cycles of the analysis.

Relevant for simulation tasks is the inclusion of the Virtual Monte Carlo (VMC) functionality. It acts as a wrapper to simulation tools for particle transport (GEANT-3 for instance, explained in Section 4.5.2.2). Thus, the user code stays the same while the internal simulation may be easily exchanged.

[15] Matching means for instance finding clusters in the EMC that match tracks from the tracking detectors.

[16] ROOT's favorite object for storage are `TTrees`, a fast table-like structure that may contain any structured object.

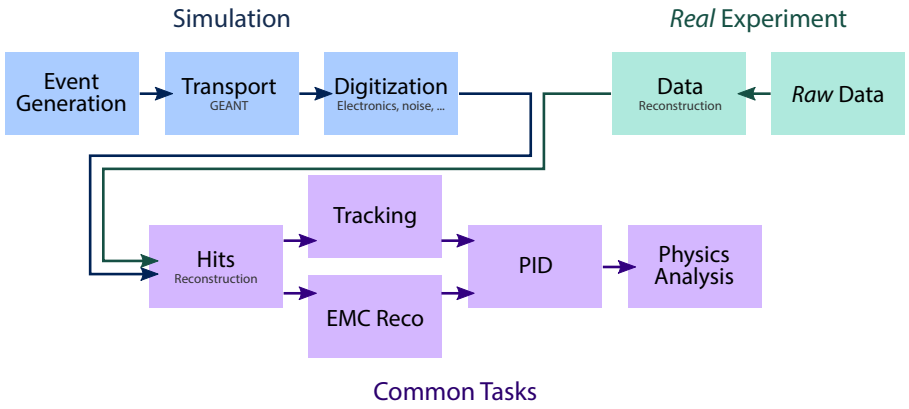

Figure 4.35: The conceptual data flow in the PandaRoot framework. The raw data generation differs from simulation (blue) to the real experiment (green). After this, their paths merge and follow the same subsequent steps of reconstruction and analysis (violet). Image from [2].

The next framework layer is **FairRoot** [107]. It extends ROOT by computing tasks common for particle physics experiments and was originally developed for FAIR experiments CBM, $\bar{\text{P}}$ANDA and R3B. Among others, FairRoot involves classes to describe detector geometries and include magnetic field maps. It also introduces a task-based structure: Computational extensive operations are outsourced into compiled classes which are called and set up within a macro executed by ROOT's interpreter.

Finally, PandaRoot introduces the individual detector descriptions and algorithms specifically optimized for the properties of $\bar{\text{P}}$ANDA's data output [108]. To analyze the detector's response to physics events, either in simulation or later with the real experiment, data processing follows the logical flow as shown in Figure 4.35. For simulation, events are first generated and the passage of the produced particles through the detector and the resulting sensor information are evaluated. Simulation and real experiment will then undergo the steps of reconstruction and analysis. The relevant steps for this thesis and involved tools are explained in the following sections.

4.5.2 Particle Simulation

4.5.2.1 Generators

The first step of the simulation is the event generation. A set of generators are available within PandaRoot, the two relevant for the analysis in Chapter 7 are introduced here[17].

EvtGen The particle decay simulation package EvtGen originates from the electron-positron collider experiments BaBar and CLEO. Due to the package's modularity, the original focus on B-meson decays is vastly extended by now and includes many meson and baryon decays. Instead of using probabilities, EvtGen uses the decay amplitudes to calculate each node of the

[17] Other generators are the `BoxGenerator` that simulates single particles with a specific momentum and angle configuration, *UrQMD* to simulate heavy ion collisions, or *Pythia*, a versatile event generator used, for instance, at the LHC experiments.

entire decay chain, including all angular and time-dependent correlations [109]. Internally, the decay amplitudes and particle parameters are stored in text-based databases, which can be extended easily. A common usage for EvtGen is the simulation of a dedicated physics reaction, specified by a decay file.

DPM Another event generator available in PandaRoot is based on the Dual Parton Model (DPM). In this model, the interactions of two hadrons, two nuclei, or a combination of both are described. The model is phenomenologically motivated because no available theoretical tools can describe the processes occuring in hadronic colliders with low traverse momenta properly [110, 111]. This generator is commonly used for background studies without the input of a specific production channel.

4.5.2.2 Propagators

After the initial reaction has been generated, the particles need to be propagated through the detector and its magnetic field. The two propagators GEANT-3 and Geant4 are available for this purpose. Both are developed by groups involved in CERN experiments but use different programming language bases: GEANT-3 works with a Fortran base while the more recent version Geant4 is based on C++ [112].

The propagators use an abundant set of physics models to simulate the particle's passage through and interaction with materials. This is done in a step-wise approach, each time evaluating the probabilities for bremsstrahlung, multiple scattering, particle decay, and so on. While the Geant packages propagate the particle itself, a different toolkit, *GEANE*, handles the error propagation [113]. GEANE internally calls Geant as well and is used in PandaRoot for the track reconstruction phase.

4.5.2.3 Digitization

The last step in simulating the detector's behavior is the digitization. Here, the sensor signals are modified according to the expected readout characteristics. This is specific for each sub-detector technology with the goal to be as close to realistic hit information as possible.

4.5.3 Reconstruction

The reconstruction operations are the same for simulated and real events. Neutral candidates, which are invisible for the tracking detectors, are reconstructed by analyzing the EMC hit clusters. Charged particles, however, do leave hits in tracking detectors, thus a trajectory can be extrapolated.

4.5.3.1 Pattern Recognition

In a first step, pattern recognition[18] is performed to sort hits together which belong to one particle. This is done by applying a track hypothesis. For the Target Spectrometer the magnetic field is assumed to be homogeneous in z direction, leading to helix trajectories. The algorithms performing this task already work well for particles originating from the IP [114] but are

[18] Alternatively called *track finding*.

still under development for displayed vertices. Those introduce another degree of freedom and thus are more challenging to find[19]. When simulation input data is available, ideal pattern recognition provides an alternative for the track finding. Here, the hit's origin from the propagator is extracted and the hits are grouped based on this information. This has an efficiency of 100 %, thus giving an upper limit for the reconstructability.

4.5.3.2 Track Filtering

When a track candidate is found, a track filter is applied to increase the track's accuracy. A Kalman filter realistically propagates the particle along the track candidate and includes the hit position and uncertainties to calculate the most probable track. For PandaRoot, the *GENFIT* package acts as a wrapper for such a Kalman filter, providing a track-fitting toolkit [115].

4.5.3.3 Particle Identification

Finally, the particle's type is determined. In this particle identification step, different sub-detector information are combined, like $\frac{dE}{dx}$ values from the MVD and STT, the Cherenkov angle from the DIRCs, or the energy deposit in the EMC. This input is then compared with the expected values generated from γ, e, μ, π, K, p, and their corresponding antiparticles and a probability is given to match one of these hypotheses.

The particles are sorted into lists, which serve as an input to the following analysis, where specialized algorithms are performed and conditions are applied for the investigated channel. The procedure described in Chapter 7 fits into this category.

[19] Assuming the track started from the IP fixes already one parameter of the helix.

The P̄ANDA Strip ASIC (PASTA)

5

This chapter is dedicated to the work done for the PASTA readout front-end. First, an introduction is given into ASIC design in general, effects of radiation to ASICs, and the predecessor chip (Section 5.1). Then, PASTA's motivation and working principle are outlined (Section 5.2), proceeded by the ASIC-wide developments that have been done (Section 5.3). Going into more detail of the operation of PASTA, the descriptions of the analog (Section 5.4) and digital parts (Section 5.5 and Section 5.6) follow. The chapter is concluded with the final design of PASTA (Section 5.7).

5.1 Introduction

5.1.1 ASIC Production

5.1.1.1 Device Technologies and Fabrication

The first decision one has to take towards a readout solution is selecting the general device technology. Different needs in the application are approached by different strategies. One approach for an integrated circuit (IC) design is using FPGAs as flexible devices with fast development cycles. With the flexibility comes a larger footprint, higher power consumption, and less radiation hardness, everything too severe for the readout front-end of the MVD strip sensors.

Alternatively, one has the option for a *full-custom* ASIC where all aspects of the project are tailored for the particular application. This includes dimensioning and placing of all transistors, capacitors, and wires of the analog design manually. The overhead of drafting, simulating, and verifying the arrangement is quite significant, thus a typical design cycle is in the order of one year. For digital parts, which can get quite complicated rather soon, a different approach is usually chosen: a *standard-cell* ASIC. A library of predefined standard cells is provided from a foundry to enable automatic placement of basic logic components based on a hardware description code. For PASTA, a combination of full-custom design for the analog part and standard-cell modules in the digital part is chosen.

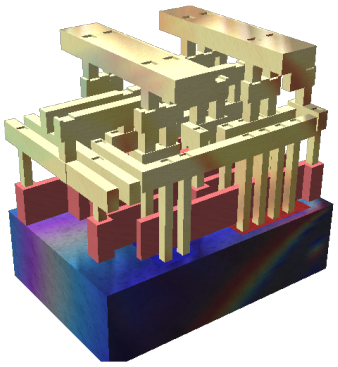

Figure 5.1: Rendering of a small standard cell with three metal layers (■) on the crystalline silicon bulk (■). Vertical metal structures are called *vias*, horizontal *wires*. Polysilicon gates are between the metal and bulk layers (■). Image from [116].

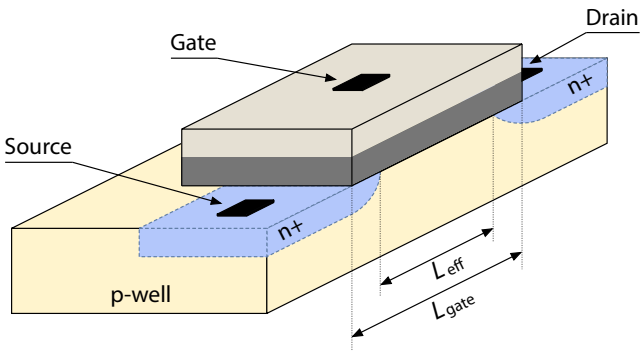

Figure 5.2: A schematic view of an nMOS transistor with source, drain, and gate connections. The length of the gate, L_{gate}, is also associated with the *length of the transistor*. The smallest available length in a manufacturing process determines the minimum structure size, e.g. 130 nm.

After developing and testing the design, the ASIC's plan is handed to the foundry, a company providing fabrication of ICs. The design is composed of many overlapping layers with structures of different conductivity attributes. In Figure 5.1 an example of a simple standard cell visualizes this concept. The desired pattern within the layers is defined on a *mask* for each layer individually and then transferred by light onto a silicon substrate, the so called *wafer*. This process, the *photolithography*, has to be repeated for all layers, typically around 10 to 15 times. More details on the general production procedure of ASICs are available in [117].

An important classification of a provided technology is the used circuit area. It is expressed as the *structure size* which refers to the smallest achievable length of transistors. See Figure 5.2 for a graphical explaination of the length. The structure size of manufacturing processes continues to shrink, currently reaching 14 nm for computer processors [118].

5.1.1.2 CMOS Technology

Complementary metal-oxide-semiconductor (CMOS) is a technology to construct integrated circuits by using both p-channel transistors (pMOS) and n-channel transistors (nMOS) simultaneously in the design [119]. A typical digital design will connect the source or drain of a complementary pair of transistors together to achieve a logical representation. Figure 5.3 shows an example of an inverter using both a p- and n-type transistor. The concept of the complementary metal-oxide-semiconductor (CMOS) was introduced in 1967 by WANLASS [120].

Currently, more than 95 % of ICs are produced using the CMOS technology. It offers the great advantage of a small layout area with a low power consumption while being relatively noise resistant.

5.1.1.3 Standard Cell Design Workflow

This work done for this thesis focuses on the digital components of PASTA, therefore only the main aspects of the digital development process will be described here. The goal is to reach a valid design that matches the logical input on the one hand, i.e. what the ASIC is supposed to do for a certain combination of inputs, and a layout of polysilicon and metal layer occupation for fabrication on the other hand.

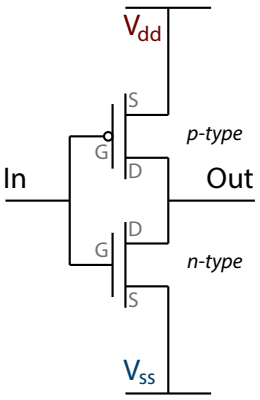

Figure 5.3: A logical inverter in CMOS technology. If the input is low, the p-type transistor will develop an electrical field from gate to drain (high voltage level) and thus will get conductive, while the n-type will become insulating. The output is then connected to the high level of the drain, the inverse level of the input.

This process might end up to several thousand logical instances, also known as *gates*[1]. Therefore, an automatable routine is required. The most relevant steps are:

Functional Description In this first step, the functional description is developed on a register-transfer level (RTL). This abstraction layer is close to structures existing in hardware circuits but is more readable than a series of connection assignments. It is usually written in a hardware description language (HDL), in case of PASTA VHSIC Hardware Description Language (VHDL) is used for the overall concept and Verilog for the library definitions of standard cells. Part of the functional description is a constraints file handling timing and driving load information on input and output (I/O) signals of the top level cell.

Simulation Together with the functional description, a *test bench* is being developed to enable simulation of selected cells. The test bench defines how input signals to the selected cell change over time and monitors the output signals. The investigated cell might be a submodule of the whole project for quick tests or the top level cell for a full digital simulation. Especially for ASIC development, thorough simulations are an essential part of the process since iteration cycles for prototypes are expensive and take a significant time.

Synthesize After the design is formulated with a HDL, a compiler translates the project's logic description into available standard cells. In Listing 5.1 and Figure 5.4 an example for the synthesis of a simple circuit is shown. The compiler also incorporates the design constraints and applies simplification where possible. For instance, it will remove redundant signals if not told otherwise[2]. At the end of this step, a netlist file contains the used cells and defines their interconnections.

Place and Route The netlist file from the previous step is taken as an input to the last step towards a layout. Together with layout instructions such as I/O placement, floor plan dimensions,

[1] In PASTA, the global controller and each of the 64 TDC controller use 138,897 and 707 gates respectively. In total, 184,145 gates are used in the digital part of PASTA.

[2] This will become especially relevant for the introduced redundancy as a radiation effect countermeasure (Section 5.3.3).

```
D <= not Q;

process(clk)
begin
  if rising_edge(clk) then
    Q <= D;
  end if;
end process;
```

Listing 5.1: VHDL code of a simple FF switching its value on every clock cycle.

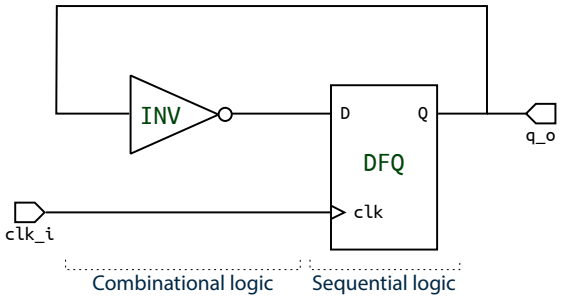

Figure 5.4: A possible translation of the RTL description seen in the listing in the left to standard cells.

power grid definition, and available metal layers for routing, the cells are first placed and then their interconnections are routed. The routing is particularly computing intensive because only horizontal or vertical wires are allowed. To avoid short circuits of crossing lines, the routing algorithm has to change up or down to another metal layer. It takes several iterations until all constraints for a valid fabrication can be matched and a coherent timing achieved.

For PASTA, an analog-on-top approach is chosen, meaning that the final routing and placement of design components will be done with analog tools. Therefore, the final digital layout is saved in a Graphic Database System II (GDSII) stream file, the most commonly used format for design transfer to lithographic processes [121, 122]. After importing this into the complete design, further tests are applied to verify the interaction of digital and analog parts. Finally, a GDSII stream is generated to be sent to the foundry.

5.1.2 Effects of Radiation

A very important aspect in designing an ASIC for a high energy physics experiment is the consideration of radiation effects during operation. A particle detector generally uses the ionizing character of high energetic particles to detect them. This affects not only the sensor generating a detectable signal but also the front-end electronics converting this signal. The consequence might be sudden or long-term changes in the desired operation.

Failures in electronics in connection with radiation have been first reported in the period of 1954 till 1957 during nuclear bomb tests [123]. It was believed these were random electronic anomalies and the cause was not investigated further. Only starting in the late 1970s, first investigations on the effects of α particles [124] or cosmic ray radiation [125] on computer memories have been performed.

If a single high energetic particle interacts with the electronic's material and leads to an alteration in the IC's behavior, it is called a single event effect (SEE). Irreversible changes of the material structure are classified as *hard errors* while *soft errors* just cause temporary effects on the expected operation.

5.1.2.1 Hard Errors

Semiconductors rely on a certain level of doping in well defined areas. Heavy particles like neutrons, protons, or other baryons can change the arrangement of the lattice which worsens the analog properties of the structure (*lattice displacement*). Over time, semiconductor junctions, as used in transistors, change their depletion extension. This can be compensated to a certain extent by adjusting the supply voltage but with continuous radiation affecting the device, transistors and other elements will fail ultimately.

Moreover, some of the generated holes from ionization can accumulate in the oxide layer of CMOS transistors [126]. This is an effect of the total ionizing dose exposed to the circuit and makes n-type transistors easier and p-type transistors more difficult to switch on over time.

5.1.2.2 Soft Errors

Due to downscaling and more optimized ICs, operation voltage levels drop and the induced charge from a single ionizing particle can be enough to misinterpret a signal or to discharge a buffering cell like a flip-flop. The latter might happen to a single bit or to multiple bits at the same time. Both are grouped together as single event upsets (SEUs), a term introduced by GUENZER, WOLICKI, and ALLAS's article »Single Event Upset of Dynamic Rams by Neutrons and Protons« from 1979 [127].

The impact of SEUs depends on their location. Short-term effects just cause a temporary change of value that gets updated regularly, for instance a state machine with an update cycle based on the clock. In case of an upset in a long-term stored value as it is used for configuration, only a complete reset of the ASIC would resolve this upset. Section 5.3.3 focuses on the measures taken to prevent SEUs in the digital domain of PASTA and ensure a stable operation.

5.1.3 The TOFPET ASIC as PASTA's Predecessor

Before coming to the parts focused on PASTA, this section introduces the predecessor ASIC of PASTA, sharing a common measurement concept (see Section 5.2.2) and some elements of the ASIC design. This predecessor chip, the Time of Flight for Positron Electron Tomography (TOFPET) ASIC, was developed for the EndoTOFPET-US project as a readout solution for scintillating crystals. The project jointly exploits the technologies of TOF in a positron emission tomography (PET) experiment with ultrasound (US) endoscopy to increase detection efficiency in medical examinations of cancerous patients [128].

5.1.3.1 The EndoTOFPET-US Experiment

A PET scanner is based on a radioactive β^+ biomarker induced into a patient. The biomarker is designed to reach an area of interest, for instance prostate or pancreas tumors, and emits positrons from there. They will annihilate shortly, producing two annihilation photons each which can be detected in photosensitive detectors. The common approach for such a system lies in a ring of detector elements surrounding the patient, where a coincident response in opposing elements creates a line of response (LOR) with a constant probability for the origin to be somewhere along this LOR (see Figure 5.5) [129]. Overlaying a number of these lines slowly exposes the origin of the radiation.

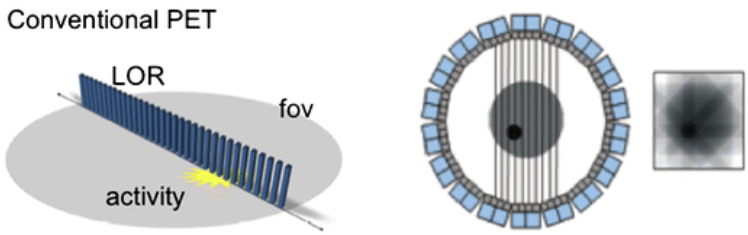

Figure 5.5: The measurement principle with a conventional PET scanner: the annihilation photons create coincident signals in a ring of detectors (middle), leading to a line of response (left). Overlaying multiple lines of response slowly exposes the activities origin. Image from [129].

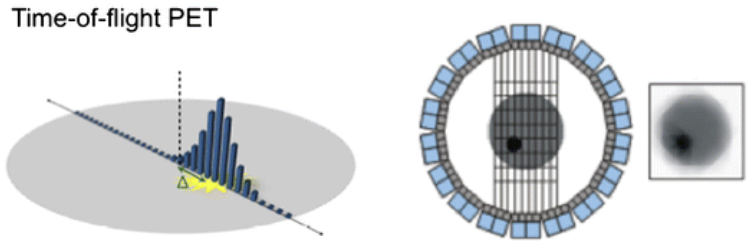

Figure 5.6: Introducing a TOF information to a PET scanner gives a probability for the location of the radiation's origin along the line of response (left). The additional information increases the SNR which leads to a clearer image (right). Image from [129].

Introducing a time measurement to this concept reveals a region of interest along the LOR (see Figure 5.6). Exploiting this additional information helps to reduce the noise influence from surrounding organs and thus increases the SNR, ultimately leading to a shortened exposure of the patient to the radioactive material [130].

The resolution along the LOR is aimed to be $\Delta x = 3\,\text{cm}$, leading to a time resolution of the detection system of around 200 ps [131]. The detection system consists of two parts, an endoscopic PET head combined with an ultrasound sensor and an external PET plate. The latter consists mainly of LYSO crystals coupled to monolithic multi-pixel photon counters (MPPCs) which serves as a fast photon detection system. The MPPC's output is forwarded to a front-end board with the TOFPET ASIC mounted on it, digitizing the signals [128].

5.1.3.2 Description of the TOFPET ASIC

The digitization of signals is done in a 64-channel front-end. It is designed to get a precise timing information on the MPPC's signal for a accurate position along the LOR. To counteract time walks effects, the threshold is set as low as possible, even below the signal of one photo electron. As a consequence, electronic noise from the sensor would also trigger the readout. A secondary higher threshold enables a distinction between spurious and valid signals.

This measurement principle is realized in a 64-channel ASIC as depicted in Figure 5.7. It consumes a footprint of $25\,\text{mm}^2$ with a channel input pitch of $102\,\mu\text{m}$. Several techniques like regional substrates, deep moats, and segmented I/O rings and power domains are used to

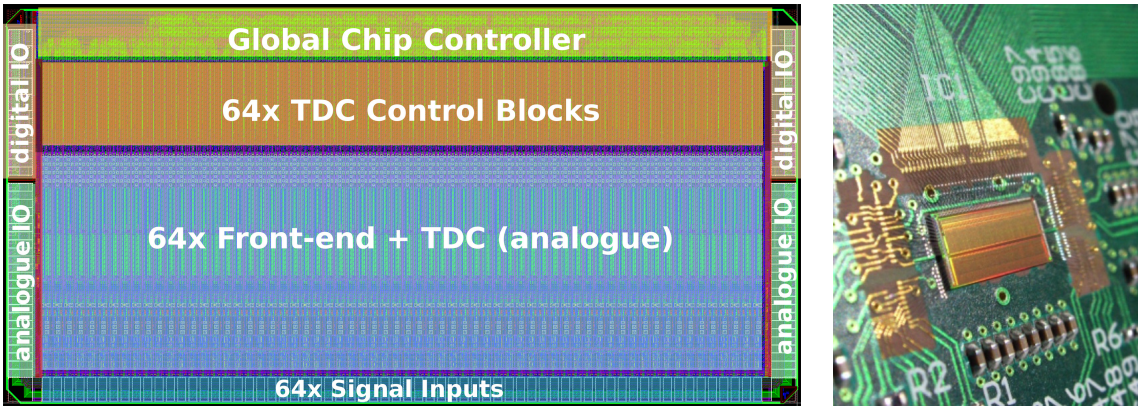

Figure 5.7: The floor plan of the TOFPET ASIC (left) and integrated into the prototype readout system (right). It contains 64 channels in a 25 mm^2 area (7.15 mm × 3.55 mm outer dimensions). The top side is pad-free to allow a 128-channel twin chip configuration with two chips placed back to back. Images from [131] (left) and [132] (right).

minimize the noise effects [131]. Its pads are on three edges, leaving the option to place two chips back-to-back to create a configuration with 128 channels.

The ASIC has been designed in 130 nm CMOS technology. Measurements show a power consumption of <10 mW/ch and an input rate capability of 160,000 ev/(ch s) [132]. The timing resolution for a single photon was measured to be at 200 ps full width at half maximum (FWHM) for the full system including crystals and MPPCs. With two channels reading out the same crystal, a coincident time resolution of 100 ps FWHM could be obtained (both results from [133]). An extensive description of the TOFPET ASIC is given in »Integrated Circuit Design for Time-of-Flight PET« (ROLO, [132]).

5.2 PASTA's Working Principle

5.2.1 Motivation

The decision to develop a specific front-end for the MVD's strip sensors is mainly driven by $\bar{\text{P}}$ANDA's approach to a continuous data acquisition. This sets particular demands to readout electronics. Above all else, the distinction between event signals and detector noise has to be done inside the electronics without a dedicated trigger provided externally. The produced data on the front-end should be transmitted digitally to simplify further event building means. If not mentioned otherwise, the design parameters mentioned in this section rely on [98].

In the digital data stream, hits to a channel in the strip sensors of the MVD need to encode, in addition to the channel number, a precise timing along with a measurement of the deposited charge. The timescale follows from $\bar{\text{P}}$ANDA's reaction rate of up to 20 million collisions per second [59], leading to an event every 50 ns on average. To ensure a distinction between the Poissonian distributed collisions, a resolution of 10 ns to 20 ns needs to be achieved by the digitization. Additionally, a charge measurement is to be performed with the resolution in an order of 8 bit or higher. This enables a contribution to the particle identification (PID) process

Table 5.1: Key data for the PASTA chip. Parameters marked with a † are design parameters because they either have to be tested with the first prototype or have not been addressed, yet (charge resolution).

Parameter	Value	Comment
Process technology	110 nm CMOS	(half-node)
Input clock frequency	160 MHz	
Power consumption†	4 mW/ch	(total: 256 mW per chip)
Input charge	10 fC to 35 fC	
Input capacitance	<38 pF	
Max. input rate	≈100,000 $\frac{\text{ev}}{\text{ch s}}$	(predicted, see Section 5.6.4.5)
Time binning	50 ps to 400 ps	(for 160 MHz to 20 MHz internal clock freq.)
Charge resolution†	8 bit	(over dynamic range)
Number of channels	64	
Outer dimensions	$(3.4 \times 4.5)\,\text{mm}^2$	
Radiation dose†	up to 100 kGy	(total ionization dose)

and, moreover, to a better spacial resolution from cluster building by exploiting information on the shared charge between neighboring strips.

Being the innermost detector that is supposed to resolve vertices precisely, the MVD is designed rather compact. This inherently leads to limited possibilities for cable routing and cooling as well as placement of the front-end itself. Thus, the front-end must be compact in size[3] and not use more than 4 mW/ch according to simulations[4]. Another conclusion from being located close to the interaction point is a high rate of particles passing the sensors. This leads to high event rates of up to 40,000 ev/(ch s) and high accumulated radiation doses. Simulations expect values of up to 100 kGy ionization dose and $10^{13}\,\text{n}_{\text{eq}}/\text{cm}^2$ neutron equivalent dose throughout the planned runtime of ten years [51, 98].

All of these requirements are very demanding for readout electronics and an ASIC fulfilling all could not be found. Thus, a custom development exploiting the in-house experience with the TOFPET development has started, leading to the PANDA Strip ASIC (PASTA). In the course of this thesis, the predecessor's code base has been modified to match PANDA's requirements, for instance by including SEU protection[5], and generally improve the design, especially for the TDC controller. After introducing the measurement principle in the next section, the developments particularly done for the PASTA chip will be explained. It focuses on the digital components as this was the work done for this thesis.

[3] There is no exact upper limit to the outer dimensions of the front-end because different approaches for the placement and routing are possible. As long as the ASIC does not exceed an area of roughly 5 mm × 5 mm, a solution can be found.

[4] The original simulations done for the technical design report (TDR) [98] estimated a power consumption of 8 mW to be acceptable but this turned out to be too high.

[5] Other important overall changes were shrinking the occupied area and reducing the consumed power.

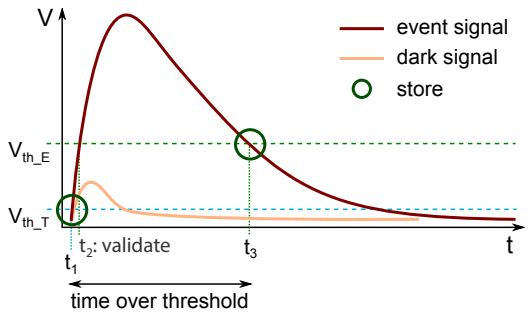

Figure 5.8: Concept of the PASTA chip: A low threshold gives a good time resolution on the rising edge of the signal pulse while a second, higher threshold delivers time over threshold information.

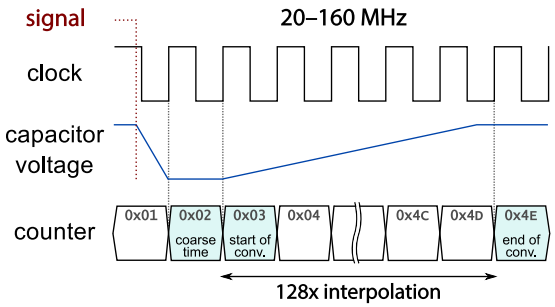

Figure 5.9: To get a higher temporal precision for the offset of the signal to the clock, the time difference is transferred into a proportional voltage difference in a capacitor. It is then recharged to the reference voltage with a lower current and by that stretching the time.

5.2.2 Measurement Concept

PASTA's measurement concept of a free-running readout is based on the TOFPET ASIC which has already been introduced in Section 5.1.3. Generally, points in time are measured based on two leading-edge discriminator outputs. The first one is aimed to resolve the beginning of the signal pulse precisely and its branch is consequently associated with the name *time*. A second discriminator measures a second point on the falling edge to get a pulse length information which corresponds to the deposited charge. This method, called TOT, contributes to the energy-loss measurement used for particle identification and is thus named *energy* branch. Because the falling edge of the pulse is much slower than the rising edge, it is more susceptible to noise influences, increasing the jitter[6] on the timestamp. Therefore another discriminator with a higher threshold is used for the second timestamp. The sketch in Figure 5.8 visualizes this method.

The chip runs with an external clock of up to 160 MHz which leads to an intrinsic time resolution of 6.25 ns. The coarse timestamp is taken with this precision. To achieve a higher resolution of up to 50 ps, a charge transfer is applied. Between the asynchronous transition of the threshold and a synchronous transition of the clock, a storage capacitor is discharged with a constant current (see also Figure 5.9 and Figure 5.10). The resulting voltage difference to a reference voltage is proportional to the offset of the signal to the clock and thus called time to analog converter (TAC).

Before it is converted to a digital value with a time to digital converter (TDC), the charge inside the capacitor is then transferred to another, four times larger capacitor (TDC capacitor)[7]. In there, the voltage is increased by a constant current 32 times lower than the discharging current in the first step. Both factors lead to a stretching factor of 128 of the time difference and therefore increasing the time resolution by a factor 128 to ≈50 ps for the fine time. For

[6] Jitter describes the time-wise fluctuations on a signal transition. These transitions are used in this case to store timestamps which might lead to inaccurate time information.

[7] This step is skipped in Figure 5.9 to simplify the sketch.

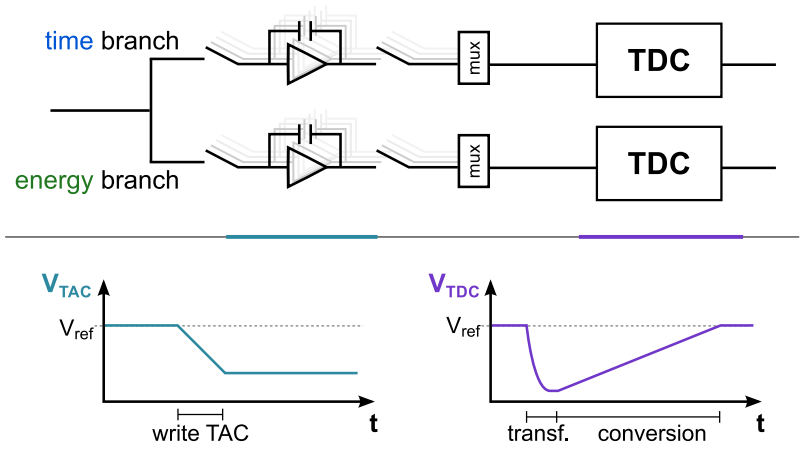

Figure 5.10: Detailed concept for time interpolation. First, the selected TAC capacitor (out of four) is discharged with a constant current for the time until a clock edge arrives (*write TAC*). This charge is transferred in a second step to the TDC capacitor (*transf.*) and recharged with a lower current (*conversion*), achieving a proportional amplification.

more information on this process see [134]. Since this method is at the cost of a higher dead time in the order of a few microseconds, each channel has an extra redundancy by four TAC units to minimize the risk of a missed event. If one TAC is still busy, a following event will be stored in the next TAC chosen by a round-robin scheme. This multi-buffer approach has been described in [134].

In the predecessor front-end – the TOFPET ASIC – the difference between noise hits and real signals is smaller than for the application of reading out microstrip sensors which have a higher capacitance. For the first prototype of PASTA, alternative ways to identify valid signals have been implemented along with configuration parameters allowing to test their effect on the performance.

5.2.3 The ASIC's Internal Structure

PASTA is divided into four major parts, which are also shown in Figure 5.11. The following list gives a short summary of their functions:

1. **Analog front-end**, amplifying the signal and applying thresholds. (→ Section 5.4.1)
2. **Analog TDC**, attaining finetime information by charging and discharging capacitors. (→ Section 5.4.2)
3. **Digital TDC controller**, selecting TAC branches, controlling the charge conversion, and initiate time stamp saving. (→ Section 5.5)
4. **Digital global chip controller**, collecting data from TDC controllers, transmitting data outwards, and distributing configuration. (→ Section 5.6)

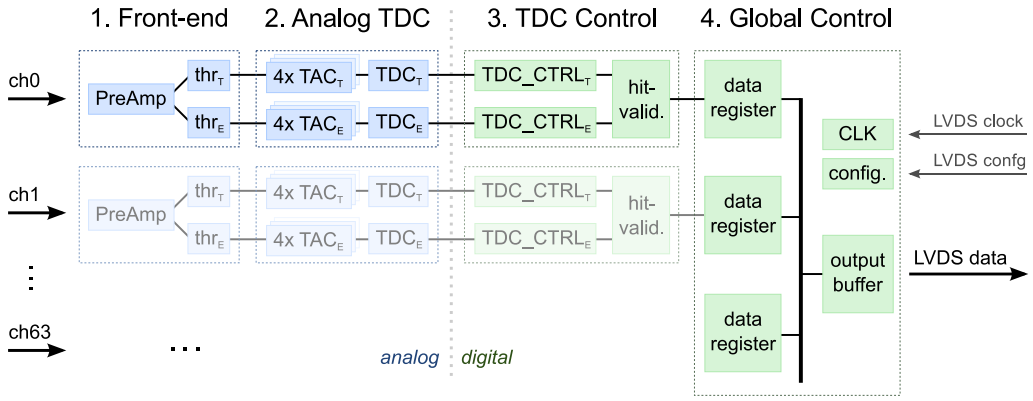

Figure 5.11: The PASTA chip has four main components, two for analog (blue) and digital (green) circuits each. In a very simplified picture, the signal arrives first at the analog front-end and is stored in the analog TDC, which is controlled by the digital TDC controller. Finally, data is collected and transmitted in the digital global controller, spanning over all channels.

Beside these central blocks, further auxiliary circuits exist:

- **Calibration circuit**, generating test pulses with a configurable amplitude. Another configuration setting selects the channel for which the pulse will be used.
- **Output driver**, transforming outgoing signals to LVDS standard.
- **Bias cells**, providing the necessary voltage levels for the analog components.

These blocks are not essential for the understanding of signal processing and have not been part of the development for this thesis. Thus, they are not described further.

5.3 ASIC-wide Developments

5.3.1 Switch of Technology

One of the major adaptations from the TOFPET ASIC towards PASTA and part work of this thesis is the change of technology and manufacturer for production. Custom designs of ASICs are developed with a set of standard cells and constraints for their composition in the metal layers. Both are given by the foundry producing the chip later on. While the TOFPET ASIC was designed in a 130 nm CMOS process, PASTA uses a 110 nm *half node* process, i.e. an intermediate step between two major process sizes which is achieved by shrinking the next larger one. In this case this means that the ASIC is designed in 130 nm and a scaling factor of 0.9 is applied at the end.

One of the biggest advantages of using the different technology is an economic one. Half-nodes typically have reduced costs since the research and development costs are rather low compared to the development of a new fabrication node with different structures. Moreover,

choosing a pure-play manufacturer that is focused on production for other companies and projects helps reducing costs even further.

The different technology comes with different standard cells which is of particular interest for the digital part. Compared to the process the TOFPET ASIC uses, the cells are more optimized for smaller footprints by offering more versions of the same cell matching different load conditions or by combining commonly used gates together in one cell. For instance, combining four signals with a logical `AND` would require three regular `AND` gates with two in- and one output. The used technology, on the other hand, provides cells with four inputs which are internally combined. The reduced footprint is additionally enforced by the smaller structure size hence slightly smaller gates.

Area-wise, one gains only 19 % by this a reduction in the footprint without any modification to the design. In prospect of making a radiation hard design, the smaller structure sizes also leads to smaller oxide layers which immediately reduces the probability of collecting electron-hole pairs. Therefore, the resistance towards the total ionizing dose effects rises [126] (see also Section 5.1.2). At the same time the total ionizing dose effects get reduced, temporary upsets in operation become more probable because the operation voltage gets lower with smaller structure sizes. Hence, the same amount of generated charge might lead to a pulse height high enough to have an effect on the digital circuits which interpret voltage levels as `0` or `1`. The countermeasures to this are described in Section 5.3.3.

The major disadvantage, however, from changing the technology emerges in an almost complete redesign of the analog part because carefully adjusted parameters change and result in a sequence of adaptations. Partially, this was necessary nonetheless because the front-end with its preamplifier will be connected to a sensor with completely different parameters[8]. The changes for the digital part from the technology change affect mainly the automatic procedures in *synthesis* and *place and route*. Different control parameter and constraints had to be chosen with several iterations in order to reach a successful digital design.

A very specific change that had to be done for the global back-end was modifying a set of provided cells. The next section describes that alteration.

5.3.2 Modified Well Tap Cells

Transistors use differently doped areas with depletion zones at their junction to achieve the transistor's switching functionality. For transistors produced with the CMOS process, four different voltages are required for biasing the depletion zones: source and drain supply (V_{ss} and V_{dd}) for the transistor itself and p-well and n-well for the bulk material (see Figure 5.12). All of these need to have a voltage supply which is provided by *well tap cells*. The well connections are often short-circuited to the source and drain supplies to simplify the routing and decrease the failure rate of the automatic routing. Short-circuiting the well connection makes the n-well especially susceptible to noise from digital switching, which is not a problem for the digital part itself[9].

[8] Mainly, the sensors of PASTA have a higher capacitance than TOFPET and therefore produce a much lower signal.

[9] The noise level is much less than the defined logic levels, therefore no misinterpretation of voltage levels happens.

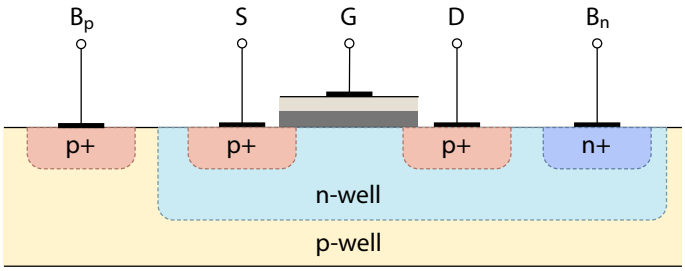

Figure 5.12: Cross section of differently doped areas of a pMOS transistor in silicon. Image from [135].

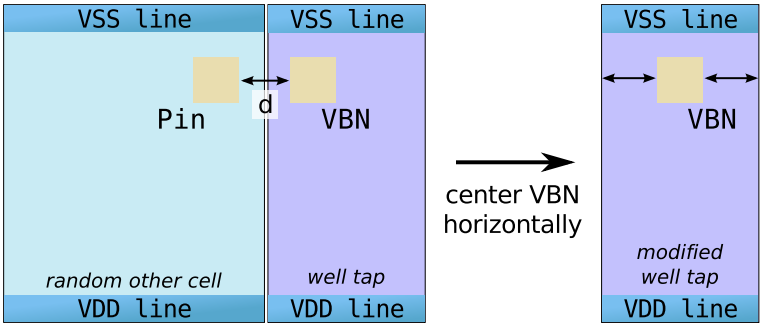

Figure 5.13: Well tap cells from the standard library have their bulk connection pin (VBN) left-oriented with the minimal distance (d) to a potential adjacent cell with a right-aligned pin. In the modified cell the bulk connection is horizontally centered, increasing the space to adjacent cells.

The production of an ASIC results in a continuous substrate throughout the chip. Consequently, this also connects the bulk of the analog part with the digital part. Since the analog part with its very sensitive amplifiers needs a stable supply, any noise should be avoided. To counteract this effect, the producer offers well tap cells with a direct contact to the substrate [136].

In PASTA, well tap cells with individual connections for the n-well (VBN) are used. To ensure a supply with a stable level in the entire digital part, these cells are placed regularly in a chessboard pattern[10]. This automatic placement works well with smaller designs as for the TDC controller. When it comes to the large design of the global controller, this procedure fails and creates design rule violations for spacing. It is explainable by the sequence of steps in the automatic layout generation. First, all cells are placed on the floor plan, after that the routing is done. In the step of placement, no violations occur because the minimal allowed distances are always contained.

This can be seen in Figure 5.13 where on the left side a regular cell placement is shown with a well tap cell and a random adjacent logic cell. Pins to connect cells to other instances or supply lines have to be placed somewhere between the source and drain supply lines (VSS and VDD) on top and bottom. The design rules from the manufacturer set a constraint on the minimal distance of metal fillings (d in Figure 5.13). The VBN pin of the well tap cell is left-aligned with

[10]The cells repeat every 50 µm in one line while the next line's cells are shifted by 25 µm. This creates the mentioned chessboard pattern.

$^{d}/_{2}$ to the left edge. This makes sure that the allowed distance is not undercut by a possible placement of an adjacent cell with a right-aligned pin and a minimal distance to the cell edge.

For routing it is often necessary to jump to other metal layers to enable routing without shorts. These jumps are done with vias that also come with design rule constraints. They require a bigger area than the pins of the cell. If then one of the neighboring pin connections needs to jump to a higher layer because of the surrounding routing, the spacing decreases below the allowed limit. Since the placement has been done before, the routing is not always able to solve this which eventually leads to unclean designs, i.e. some routes violate the design rules.

To remove this possibility from the routing process, an additional cell library was created, containing only well tap cells. These cells had an alteration in the pin positions, shifting the pin horizontally to the center of the cell. The increased spacing to neighboring cell pins helped to successfully create a valid global controller design.

5.3.3 Measures to Enhance Radiation Tolerance

In prospect of using PASTA in a radiation intense environment, appropriate measures for protection are another important general modification to the TOFPET's original design. Radiation effects itself have already been introduced in Section 5.1.2, this section focuses on SEUs which affect the digital part in particular.

A proper operation in the digital domain requires stable signal values for `0` and `1` for the whole runtime. Three groups of severity exists: *undetected glitches*, *compromised data*, and *operation critical*. While undetected glitches are naturally of no concern, compromised data should be kept to a minimum. Desirably, the amount should be as close to zero as possible, but the protection has to be weighted with the introduced downsides such as increased area and power consumptions and decreased data throughput. A compromise could be that affected data is flagged and thus just reduces the efficiency of data taking. This will be taken into account for the nevertheless necessary redesign of the data format for a second prototype. Finally, operation critical signals have to be protected against unexpected changes. Otherwise, the logic might enter undefined states and freezes until a reset of the whole front-end carried out. A few examples are given below where a SEU affects the operation.

Signal Glitch An induced charge in a combinational cell might connect the output briefly to one of the two voltage levels, causing the output to change. Depending on the timing of such a glitch, further processing can be affected and start a process unexpectedly. In PASTA, most digital circuits are sequential which are subject to timing constraints, i.e. they need a stable signal for a certain period. Therefore, no significant effect from glitches is expected, at least not for a stable operation.

Status Signals Instead of signals from combinational cells, sequential outputs might be modified as well. This can happen when a flip-flop, also known as a register, changes its internally buffered state from a SEU. It depends on the circuit, how long the modified state is kept before updating and which impact it has. Sometimes recorded data is altered, sometimes such a signal controls the next state of a finite-state machine (FSM). The latter can lead to uncontrolled behavior of the ASIC's logic and has to be dealt with.

State Machine Some parts of PASTA's logic use FSMs, especially in the global controller. Each state is encoded in a sequence of bits. A change in one of them sets the state machine either into a state out of sequence or, even worse, an undefined state. To prevent this, all state machines will fall back to their initial state if such an undefined state is reached. Moreover, states themselves are protected with redundancy to minimize the likelihood of operational disturbances.

Clock Corruption Similarly to the state machines, the central clock counter is a critical component. A SEU in this register will lead to corrupted counter values from this moment onwards. The result are wrong timestamps of following hits, making it impossible to assign them to the correct events. This is hard to detect and correct because the data, which is based on the counter, is still valid. Thus, the clock counter is also protected with additional redundancy.

Configuration Finally, the configuration buffers should be stable during operation. Otherwise, data can be produced in a different manner than expected from the user, for instance by randomly changing the threshold setting. The result is corrupted data from the moment of the SEU. Similar to the state machine's states, all configuration registers possess redundancy.

The following three section address methods which have been used in PASTA to introduce redundancy for protecting critical signals. For transmitted data, cyclic redundancy checks (CRCs) are used to register corrupted data, which has already been introduced with the TOFPET ASIC.

5.3.3.1 Triple-Mode Redundancy

One of the simplest approaches is to multiply the buffer cells storing a signal. Instead of having just one location where the information is stored, three identical cells hold the same information. In case one of those gets altered by a SEU, two others still hold the original value. Before using the stored information, a majority voter takes the most probable value. The concept has been introduced by NEUMANN [137] and has later been investigated to use in computer electronics [138].

While being a simple concept, it is not very efficient in performance and space, especially when some of the design goals are compact form factor and low power consumption (refer to Section 5.2.1). Therefore, only operational single bit signals have been protected with triple-mode redundancy (TMR), such as inputs to state machines.

To include TMR, an important pitfall has to be considered. The algorithms converting the register-transfer level description into available standard cells try to optimize as much as possible. This also includes the removal of unnecessary redundancies, which in most cases is desirable but explicitly intended for TMR. To prevent the algorithms of merging these redundant cells, one can either deactivate merging completely or specify, which cells should be kept untouched.

5.3.3.2 Parity Check

Another very simple approach to detect upsets is the *parity check*. Here, one bit is added to a block of bits representing the number of set bits in the message. Converted to a one bit

representation, an even number of 1s in the message results in a parity bit of `0` while an odd number in a 1. The effect of this is that the amount of set bits is always even[11] [139].

Occurring upsets of one bit, or any number of odd upsets, in such a stored block or transmitted message will lead to an odd number of 1s. This can be detected and appropriate measures (repeat transmission, discard data) can be taken. As soon as two upsets, or any even number, occur, the code seems valid and the error will not be detected. Nonetheless, the implementation of a parity check is very easy[12] and adds only a little overhead in data. It is thus a candidate for timestamp protection in the next prototype.

5.3.3.3 Hamming Encoding

Nomenclature, Ratio, and Distance A more efficient approach to protect multiple bit blocks is Hamming encoding, a type of block encoding introduced by HAMMING [139]. A nomenclature to determine the amount of message bits (m) and total bits (n) in a block is given by (n, m). From that one immediately gets the amount of parity bits $p = n - m$ and the code's rate

$$R = \frac{m}{n} \tag{5.1}$$

of useful information over total generated data. The aforementioned parity check on a 7 bit pattern would be called a $(8, 7)$ code or Hamming$(8, 7)$ with a rate of $R = 7/8 = 0.875$ while the TMR would be a $(3, 1)$ code with a ratio of $R = 1/3$. This rate alone would classify the parity check as more efficient than the TMR, but it neglects the susceptibility to upsets in the message. Therefore, Hamming introduced a *distance* of upsets until the information seems valid again. The parity check would have a distance of $d = 2$, because after two bit changes the check affirms the data again. For the TMR, this distance is $d = 3$, so it needs three upsets to not recognize any effect anymore. Hamming's interest was to increase the distance as much as possible while keeping the code rate high, leading to the Hamming encoding.

Hamming Code Scheme The scheme, as Hamming describes it in [139], follows simple rules. The basic idea is to use multiple parity bits, which point to the position of the upset in the data word. The amount of parity bit is determined by how many bits are needed to represent positions in the generated data block, i.e. the data after encoding. So given a word with a total length of 7 bit, one needs 3 bits for encoding all positions:

`0 : 000`, `1 : 001`, `2 : 010`, `3 : 011`, `4 : 100`, `5 : 101`, `6 : 110`, and `7 : 111`,

leading to a $(7, 4)$ code.

A few examples of valid combinations of data and parity bits are given in Table 5.2. Independent of the length, each parity bit covers an individual set of bits in the encoded data block. The first one covers all bits which have the first bit from the right set, so bits on position 1, 3, 5, 7, and so on. This can be seen more easily in the binary representation in Table 5.3(a). All positions which have the second bit set in binary representation are relevant for the second parity bit (see Table 5.3(b)). This continues for all parity bits (Table 5.3(c) and Table 5.3(d)).

[11] Alternatively, also *odd parity bits* exist, resulting in an odd number of 1s in every message.
[12] Even parity is achieved by simply combining all bits with an exclusive or (`XOR`).

Table 5.2: An overview of the first possible Hamming codes, all with a Hamming distance of $d = 3$.

Parity bits	Total bits	Message bits	Name	Ratio
2	3	1	Hamming(3, 1) or TMR	≈ 0.333
3	7	4	Hamming(7, 4)	≈ 0.571
4	15	11	Hamming(15, 11)	≈ 0.733
5	31	26	Hamming(31, 26)	≈ 0.839
⋮				
p	$n = 2^p - 1$	$m = n - p$	Hamming(n, m)	$R = {}^{n}/_{m}$

Table 5.3: The first bit positions in the encoded data word covered by the parity bits.

(a) First parity bit.

Decimal	Binary
1	**1**
3	1**1**
5	10**1**
7	11**1**
9	100**1**
11	101**1**
⋮	

(b) Second parity bit.

Decimal	Binary
2	**1**0
3	**1**1
6	1**1**0
7	1**1**1
10	10**1**0
11	10**1**1
⋮	

(c) Third parity bit.

Decimal	Binary
4	**1**00
5	**1**01
6	**1**10
7	**1**11
12	11**0**0
13	11**0**1
⋮	

(d) Fourth parity bit.

Decimal	Binary
8	**1**000
9	**1**001
10	**1**010
⋮	
24	11**0**00
25	11**0**01
⋮	

The positions of the parity bits in the encoded data word arise from the first position involved into the check. That means, the first parity bit is on position 1, the second on 2, third on 4, fourth on 8, and so on (confer Table 5.3). In between, data bits are placed in the same sequence, as it is shown in Table 5.4.

Table 5.4: The encoded data word with parity bits $p_\#$ and data bits $d_\#$ for a Hamming(7, 4) code.

Position	1	2	3	4	5	6	7
Content	p_1	p_2	d_1	p_3	d_2	d_3	d_4

Key to the detection of an upset in the encoded word are the parity bits. Together, they point to the position, where an upset occurred. If all are `0`, no error is detected[13]. Otherwise, their value converted to decimal determines the position of the upset which then can be corrected by the circuit.

An implementation of this general Hamming code for an arbitrary length in VHDL has been developed for this thesis and is available in [140].

Application in PASTA Hamming encoded registers are widely used in PASTA when it comes to operation critical buffers. This involves registers storing the current states of finite-state machines, multi-bit registers holding status information (like the status vector for the TACs, see Section 5.5.2.4), or the configuration registers for global and local configuration.

[13] While this usually means no upset happened, it might be that three upsets together formed a valid word.

Protecting the signal data itself is not done in the first prototype, mainly because it is already foreseen to change the data format in the future. This will lead to a partial redesign of the internal data handling, at which point data protection can be included. If this will be done with Hamming codes or a simple parity check, is not decided, yet.

5.3.3.4 Prevention Measures in the Analog Part

Permanent degradation of the analog circuitry is strongly dependent on the fabrication process and the materials used within. No comprehensive measurements have been conducted for the chosen technology, therefore the first prototype of PASTA will give a first insight of the severity of permanent radiation effects. One critical parameter is the gain of the pre-amplifier. A severe change there decreases the signal to noise ratio and ultimately leads to a signal which is too low for the discriminators to detect.

Even though no concrete data for radiation hardness is available, simulations were performed with changing parameters of crucial components in the range expected as fabrication variations. These turned out to have no significant impact on the performance. How much this applies for degradation from radiation one has to see with the final prototype.

In case radiation effects are more severe than expected and the predicted total ionizing dose will lead to an unfunctional design, further measures can be taken. One possibility will be to use enclosed layout transistors which use guard rings to prevent leakage to neighboring transistors [141, 142]. This would require a manual and time-consuming redesign of the relevant transistors, therefore this option was postponed until it becomes necessary.

5.4 Analog Components

The analog components use full customized circuits to adapt for given input specifications. By choosing every component's parameter, like the capacitance of a capacitor or the length and type of a transistor, one is very flexible in adjusting the circuits behavior and can optimize it with regards of high performance, low noise, and efficient power consumption. Especially when dealing with a continuous range of input signal parameters, custom analog designs offer a better adjustability to the dynamic range than standardized digital circuits.

To read out silicon microstrip sensors, the signal produced by the sensor has to be amplified and discretized, i.e. determining whether the signal is above or below a threshold. This task is done by the analog *front-end*. The specific concept of PASTA also requires additional circuits for the time interpolation, handled by the analog *time to digital converter*. They have not been part of this thesis but they play an essential role in the ASIC's functionality. Moreover, it is crucial for the development to understand the working principles of the connected parts in order to adjust the logic accordingly. Therefore, the two main analog components[14] are described in more detail in the following sections.

[14]There are further analog blocks that are important for the chip's operation but function more on an auxiliary level like the bias cells providing a stable voltage level.

5.4.1 Analog Front-end

The front-end of the ASIC is the very first part processing the input signal generated by the sensor. For PASTA's front-end, the start of the pulse as well as the pulse's charge are of interest, the latter acquired with the TOT method. The front-end is divided into five stages, explained subsequently.

Charge-Sensitive Preamplifier At first, the small current signal from the sensor is pre-amplified based on the signal's charge and outputs a voltage pulse. This charge-to-voltage conversion decouples the sensor from the further readout electronics. Additionally, the charge-sensitive preamplifier's gain is only dependent on the used feedback capacitor and not from the input capacitance, making it a suitable option for strips with different lengths.

Peaking Time Adjuster To control the time it takes for the preamplifier's output to reach the pulse's peak ($\mathcal{O}(10\,\text{ns})$ without modification), a dedicated stage has been introduced. This peaking time adjuster is fixed to a value of 30 ns right now. It might be changed to a configurable adjuster for a second version, when the tests of the first prototype with irradiated sensors show the need[15].

Current Buffer The main task of the current buffer is to provide the pulse from the preamplifier with a proper output impedance. Thus, the signal is able to drive the next stage. Additionally, the current buffer reduces the time constant of the preamplifier and the impedance for following stages, resulting in a more rapidly adapting pulse.

TOT Stage In the TOT stage the signal is amplified a second time. This time, the amplifier will saturate the signal at the maximum level allowed by the voltage supply. Only the rising and falling edges of the pulse and the time in between are of interest in the TOT method, thus the saturation is unproblematic.

Hysteresis Comparator The output of the last amplification is then fed into a comparator. Here, the signal is compared to a threshold voltage and an output line is set to a logical high ('1') if the signal is above this threshold. The special feature of a hysteresis comparator is its ability to apply a different, higher threshold for the rising transition than for the falling transition. With this, a higher resistance to noise fluctuations of the preceding electronics can be achieved while prolonging the TOT measurement and reducing the relative uncertainty.

Many simulations have been done to verify that the front-end's behavior is as expected. Two examples are shown in Figure 5.14(a) and Figure 5.14(b), showing simulations of the TOT linearity for increasing input charges and the noise introduced by the electronics for varying sensor capacitances, respectively. They predict a good linearity in the region of MIPs and only show a smooth deviation for higher charges which can be easily corrected with a calibration. The noise level is expected to stay well below the required maximum ENC of $1000\,\text{e}^-$ for $C_{\text{sensor}} = 25\,\text{pF}$ [98].

[15] Irradiated sensors produce different signals, depending on their polarization. Irradiation tests with the full system of sensor and readout have to show if an adjustment during runtime is required.

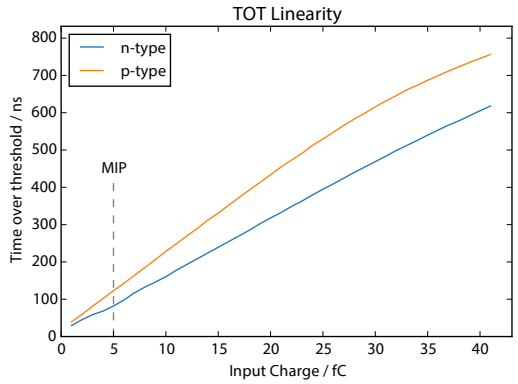

(a) Simulation of the TOT linearity for different input charges. They are mostly linear, especially in the regime of MIPs.

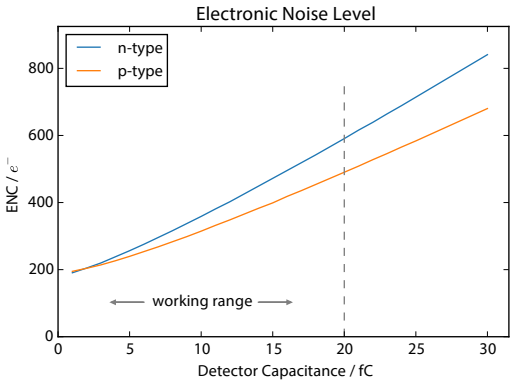

(b) Simulation of the introduced electronic noise level for different input capacitances. The ENC should stay below 1000 e^- for an input capacitance of 25 fC [98].

Figure 5.14: Examples of performed post-layout simulations with the analog front-end circuit with promising results towards a first PASTA prototype. Depending on the sensor configuration, partially different circuits are used, hence the curves vary for p- and n-type configuration. Adapted from [143].

5.4.2 Analog Time to Digital Converter

To determine a high resolution time information exceeding the intrinsic resolution of the clock, a time-interpolating time to digital converter (TDC) is employed as described in [144]. Its architecture is shown in Figure 5.15 along with the three phases of operation which are described in the following. All mentioned switches are controlled by the TDC controller, which is described in Section 5.5.

1. Discharge The switch at position 1 is closed (and $\overline{1}$ opened) when a trigger to measure a time mark is present. This will connect the capacitor C_{TAC} to the current source I_{TAC}, ensuring a constant current. Due to the inverting amplifier used in parallel to C_{TAC}, the voltage level in the capacitor then decreases from the reference voltage V_{ref}. When the switch is opened again synchronously with the clock, the time difference between trigger and clock edge is converted into a proportional voltage drop in the capacitor C_{TAC}.

2. Transfer In the second phase, the two capacitors C_{TAC} and C_{TDC} are connected by switch 2, balancing the voltage levels in both capacitors. The time period is chosen by the TDC controller design and needs to be sufficient to reach an equilibrium. After this step, the switch is opened again.

3. Conversion Finally, the conversion of the analog voltage drop to a time information is done. For that, switch 3 is closed, connecting the capacitor C_{TDC} with another current source I_{TDC}. Again, the current is kept constant while recharging. In parallel, a latched comparator constantly compares the voltage level in the capacitor to V_{ref} and signals the TDC controller about equality. This Wilkinson-type analog-to-digital converter (ADC) is a common approach for linear conversion of voltage to time conversion, see for instance [147].

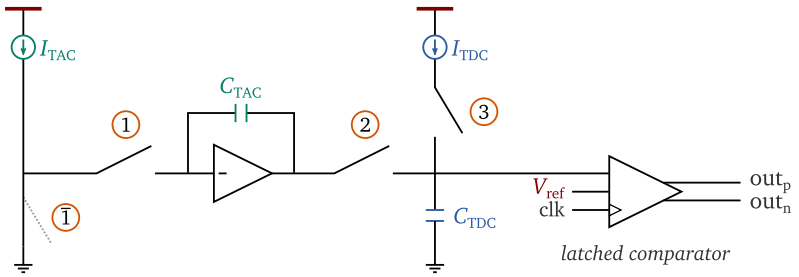

(a) The architecture of the analog TDC. The circled numbers label switches which are referenced in part (b) of this figure with the switches 1 and $\bar{1}$ always in opposite states. The latched comparator's outputs on the right are connect with the digital part.

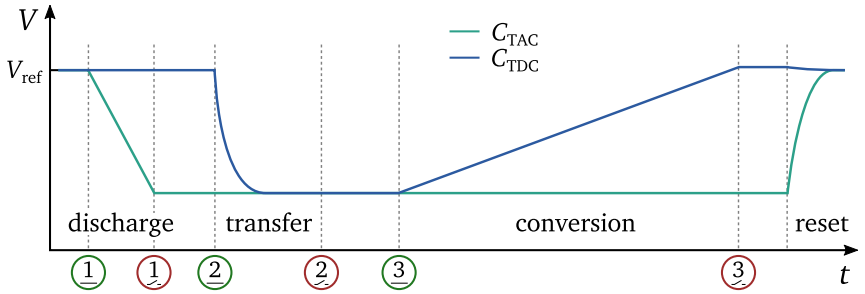

(b) The progress of the voltages in the two capacitors during event processing. The circled numbers indicate the closing (green circle, continuous line) and opening (red circle, disconnected line) of the switches labeled in part (a).

Figure 5.15: Schematic description of the analog TDC. Adapted from [145, 146].

To return back to the initial state, a reset is done for all involved capacitors, connecting them to the reference voltage. This is done simultaneously in PASTA, even though it is not required to be because the C_{TAC} capacitor may be reset after the transfer step.

5.5 Digital TDC Controller

5.5.1 Concept of Operation

The digital TDC controller is the bridge between the analog circuitry and the digital storing and transmission of data. During operation, the TDC controller constantly analyzes the inputs and decides based on the configuration whether the input shows a valid event or not. Depending on this decision and the applied settings, time stamps are taken and transferred to further readout components outside of the ASIC.

The logical idea itself is inherited from the TOFPET ASIC but the implementation has been vastly improved in the course of this thesis. The main part was a complete redesign of the VHDL basis, based on experiences with the TOFPET and with the goal of clearly separated tasks in the VHDL modules to prevent interferences. In the next sections, the most important parts of these implementations are explained.

5.5.1.1 Phases of Input Processing

The processing of an event can be split into two independently running phases with individual starting conditions, the *writing* and the *reading* phase.

Write TAC The first phase of digitizing the time information is transforming it into an analog representation, hence the component responsible for that is called a time to analog converter (TAC). This is equivalent to the first phase (discharge) of the analog TDC. The decision to start this process is handled by the trigger mechanism, described in Section 5.5.2.1, while stop is controlled by the synchronization chain length, explained in Section 5.5.2.3. Until the following readout logic is ready to process this particular event[16], the time information remains stored in the according TAC.

There are four TACs the write logic can choose from. The logic selects the next one to use in a round-robin scheme. More details on the TAC selection logic are described in Section 5.5.2.4. If all TAC capacitors are full, i.e. a time information is stored within, an incoming signal cannot be stored and consequently is ignored.

Read TAC The second phase involves the processing of the voltage level in the used TAC capacitor towards a digital representation. It follows three consecutive steps in a state machine with transition intervals dominated by a read clock enable signal provided from the global controller (Section 5.6.3 explains the clocking in PASTA in more detail).

Charge Transfer First, the charge from the TAC capacitor is transferred to a bigger capacitor in the TDC ($C_{\mathrm{TDC}} = 4 \cdot C_{\mathrm{TAC}}$). This is done until the next read clock enable signal arrives, by default after 16 clock cycles, giving the capacitors enough time to level the voltage.

Recharging Now, the TDC capacitor gets recharged with a constant current until the reference voltage V_{ref} is reached, checked by a latched comparator. This step corresponds to the conversion phase of the analog TDC. Together with the start of the ramping, a time stamp for the start of conversion (`SOC`) is stored. As soon as the comparator detects an equal or higher V_{TDC} than the reference, the ramping is stopped and the time value for the end of conversion (`EOC`) is stored.

Reset Finally, the involved capacitors are reset. This means they will be connected to the reference voltage until the next state machines transition, giving them enough time to adjust their voltage level and be ready to process the next event.

The described processes are applied for both branches individually, resulting in two measures of time, each with three time stamps: coarse time, start of conversion, end of conversion. Since the start of conversion is synchronized between the two branches, five time stamps have to be stored in total.

[16] An event stored in another TAC branch might occupy the read logic.

5.5.1.2 Time Amplification

The ASIC has an internal counter incremented by the clock to generate time stamps. Just using this counter to time events would lead to a precision based on the clock's period, or 6.25 ns for an input clock of 160 MHz. With the chosen scheme of converting the phase between a trigger and the clock into a proportional voltage drop and then recharge this, a time amplification is gained.

Two factors influence this amplification: a larger capacitance for the second capacitor

$$C_{\mathrm{TDC}} = 4 \cdot C_{\mathrm{TAC}} \tag{5.2}$$

and a lower recharging current

$$I_{\mathrm{TDC}} = {}^{1}/_{32} \cdot I_{\mathrm{TAC}} \; . \tag{5.3}$$

Using the relation for charge in a capacitor and constant currents

$$C \cdot U = Q = I \cdot t$$

one gets the gain of this method for the time after the process (t_{TDC}) versus the time before (t_{TAC}) by assuming the voltage level is equal after connecting both capacitors:

$$\begin{aligned} \frac{I_{\mathrm{TAC}} \cdot t_{\mathrm{TAC}}}{C_{\mathrm{TAC}}} \; = \; U_{\mathrm{TAC}} \quad &= \quad U_{\mathrm{TDC}} \; = \; \frac{I_{\mathrm{TDC}} \cdot t_{\mathrm{TDC}}}{C_{\mathrm{TDC}}} \\ \Rightarrow \quad t_{\mathrm{TDC}} \quad &= \quad t_{\mathrm{TAC}} \cdot \frac{I_{\mathrm{TAC}}}{I_{\mathrm{TDC}}} \cdot \frac{C_{\mathrm{TDC}}}{C_{\mathrm{TAC}}} \\ \overset{(5.2)\,\&\,(5.3)}{\Rightarrow} \quad &= \quad t_{\mathrm{TAC}} \cdot 32 \cdot 4 \; = \; t_{\mathrm{TAC}} \cdot 128 \; . \end{aligned} \tag{5.4}$$

That means that for a clock of 160 MHz one is able to theoretically measure the incoming trigger with a precision of ${}^{1}/_{128} \cdot 6.25\,\mathrm{ns} \approx 48.8\,\mathrm{ps}$ in the digital part. This value will not be achieved by the full system where PASTA will be integrated, mainly because of the slower charge collection in the sensor. However, the concept has been proven to work, as shown in [133][17], and is thus also applied for PASTA.

5.5.2 Details in Operation

5.5.2.1 Event Detection

Each channel measures timestamps independently from an external trigger source. Two basic conditions have to match to store event data: the presence of a *valid hit* (described in the next section) and the moment of interest which is stored as a timestamp (*trigger*). The two

[17] For the TOFPET system a time resolution of 200 ps FWHM for a single photon and the full detection system could be achieved.

Table 5.5: The different trigger modes are listed in two groups using discriminator inputs or the TEST_PULSE input.

Mode	Setting		Time Trigger	Energy Trigger
	test	trigger		
normal	0	00	rising edge of DOT	falling edge of DOE
slew rate	0	01	rising edge of DOT	rising edge of DOE
DOT only	0	10	rising edge of DOT	falling edge of DOT
DOE only	0	11	rising edge of DOE	falling edge of DOE
calibration	1	00	TACs are written for the duration of the test pulse.	
test 1	1	10	rising edge of TEST_PULSE	falling edge of TEST_PULSE
test 2	1	11	rising edge of TEST_PULSE	rising edge of TEST_PULSE

checks are done independent of each other and only a coincident existence of both will lead to a processed event.

In the default operation the discriminator outputs from time and energy branch are used to determine the moment of interest, hence the names *time trigger* for the first timestamp measurement and *energy trigger* for the second. This can be changed with three bits in the configuration, leading to other moments stored in the timestamps. An overview of all possible trigger modes is given in Table 5.5. Common for all is that two values are stored to keep the output data format consistent.

The trigger modes can be associated to two groups. The first one takes the discriminator output of time and energy branch (DOT and DOE) as an input[18]. Depending on the mode, it can trigger on the rising or falling edge of each signal. Similarly, the second group uses the external TEST_PULSE input[19]. The test mode bit of the channel configuration switches between the two groups.

Most trigger modes use the asynchronous rising or falling edge of an input signal as a start and a synchronous signal to stop charging the initial TAC capacitor (refer to Section 5.2.2 and Figure 5.9). As an exception, the calibration trigger mode also uses an asynchronous input signal (the falling edge of TEST_PULSE) to stop the charging process, enabling a more precise control on the charging time.

5.5.2.2 Event Validation

In parallel, the validation check is performed on the incoming data and the corresponding internal flag HIT_VALID is set. A noise hit might trigger the low threshold but not the higher one, leading to an invalid event. The following processing circuits are then mostly disabled if this flag is not set. The different modes of operation for this validation procedure are now explained in more detail.

[18] In other words, they use the analog front-end circuitry.

[19] The externally driven TEST_PULSE input line simulates an artificial signal and initiates data processing which is useful for characterization.

Synchronous Mode The synchronous mode for event validation is quite intuitive. Crossing the time threshold leads to an activation of the validation logic. If the higher energy threshold is exceeded as well within two clock cycles, the hit is considered valid and further processing is initialized. If the DOE signals stays low, the event is discarded as a noise event.

This mode mixes *combinational* and *sequential* circuits for the initial measurements. Combinational refers to a circuit that is solely comprised of logic gates like AND or OR, providing an immediate output. Sequential circuits on the other hand involve also buffering cells like flip-flops leading to a sequential update with the rate determined by the clock. In the synchronous mode, the validation comes from a sequential circuit while the time measurement is started by combinational paths. This introduces unnecessary switching and makes it more complicated to ensure a stable operation[20].

Prediction Mode Another approach is chosen for the prediction[21] mode. In case a valid event arrives, by definition it will cross both thresholds. So just observing the output of the higher one (DOE) is sufficient to determine the validity with the trade-off of loosing the high precision time due to the time-walk effect.

To counteract this, the lower threshold's output is delayed by a fixed amount of around 15 ns in the analog part[22]. When the DOT signal arrives, the event has already been validated and it can be measured. The following off-chip data analysis has to handle the correction of this introduced shift of the time trigger.

In contrast to the synchronous mode, this mode separates the combinational and sequential paths better. The start of the time measurement is purely combinational. That means timing violations for sequential components like flip-flops are not an issue. It also reduces switching activities for invalid events, but this is more relevant for PASTA's predecessor which read out silicon photomultipliers that have a high dark count rate.

Deactivated Validation PASTA also has the possibility to switch off the validation completely. This means that either the DOT or DOE signals can activate the readout chain. In most cases, this should be relatively similar to the prediction mode, with the exception that also events without an energy trigger are taken. To recognize these events, the fine time value of the energy branch is set to zero[23]. This is an unreasonable value because the end of conversion has to come after the start of conversion by design.

Together with a deactivatable delay line, this option enables measurements to conclude which validation method – if any – is best for PASTA's application.

[20] Every time a path crosses from a pure combinational to a sequential circuit, timing constraints have to be matched. This becomes complicated when using asynchronous inputs which might violate these constraints with respect to the clock (see also Section 5.5.2.3).

[21] The name »prediction mode« is explainable like this: When one starts the validation with the rise of DOT, which is deferred, the state of DOE is predicted.

[22] The exact time has to be determined by calibration measurements with the final prototype.

[23] Or, to be more precise, the end of conversion is set to be the same as start of conversion.

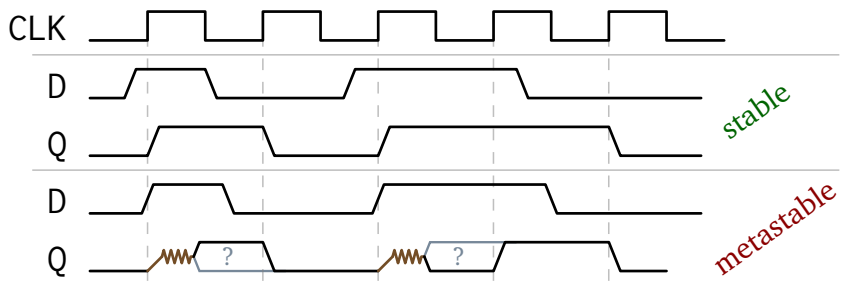

Figure 5.16: Metastability visualized for two different cases in a flip-flop: The **stable** one on top where the flip-flop's input (D) is well outside the rising clock region and thus produces a stable output at Q. Below is the **metastable** case, where the input is close to the clock and the output becomes undefined until it finally converges to a random value.

Test Mode Finally, a test mode can be activated. This will use the digital test pulse input TEST_PULSE to validate events and take timestamps according to this pulse. Details on which timestamp will be stored are shown in Table 5.5. While the test mode is active, the inputs from DOT and DOE are ignored.

5.5.2.3 Input Synchronization

When combining asynchronous signals, such as the discriminator outputs, with those of a synchronous circuit, one has to take care of clocked flip-flop characteristics. They scan the input on clock edges, leading to some timing constraints on their input signals. In case the input changes in a window around the clock edge, the output signal is not well defined anymore. It might take a longer time than normal to settle down to one state or the other. This phenomenon is called *metastability* and is visualized in Figure 5.16.

Metastable signals influence the following logical path which might interpret the signal wrongly (i.e. missing an event), or worse, inconsistently if one branch reads a 0 and another one reads a 1 (i.e. resulting in an unpredictable operation). To prevent that, two measures are taken.

The first one, a *synchronization chain* containing cascaded flip-flops, is a common approach to reduce the probability of having a metastable state as an input to further logic gates [117]. Each flip-flop reduces the probability, leading to an exponential reduction depending on the chain's length. A configurable multiplexer selects, which stage of the chain is used for further processing (see right part of Figure 5.17).

The side effect of this is an increased charging time of the TAC capacitor which will be transferred into an increased fine time value. This does not cause an issue for a proper time reconstruction because the stop signal for discharging is the same as for storing the coarse time. Therefore, the reference time from which the fine time has to be subtracted moves to a later point in time, but proportionally the fine time also increases.

A second measure makes sure not to lose events by using two *out of phase* scanning flip-flops in the first stage (see left part of Figure 5.17). An event is identified by having the input signal

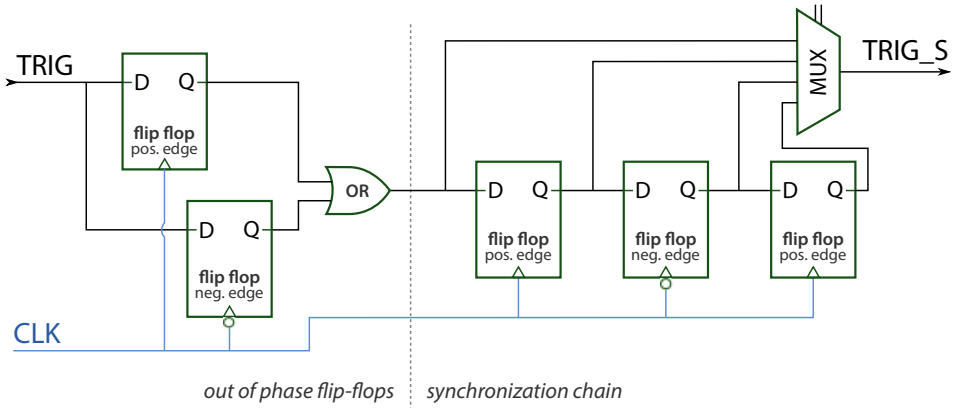

Figure 5.17: The synchronization circuit used to prevent metastable signals and missed events. Two flip-flops scanning on different clock edges are combined with an OR gate in the first stage. After that, a chain of three cascaded flip-flop follow, scanning on rising, falling, and rising edge, respectively. Which stage will be used for the following logic path is selected by the multiplexer (MUX), configurable by configuration bits 7 to 8.

above a certain threshold. Hence, the discriminator output and input to the chain is expected to rise to 1 at some point. By using two flip-flops scanning the input on different phases of the clock, i.e. one on the rising and one on the falling edge, it is ensured to have at least one flip-flop with a valid high state on the output. Since both outputs are combined with a logical OR, 1 will be propagated to the following gates and the event is not missed. To verify this behavior, the second flip-flop can be deactivated with a configuration setting.

5.5.2.4 TAC Selection Routine

When an event is marked as valid, the time measurement starts. Besides taking the coarse time information, the time interpolation as described in Section 5.5.1.2 has to be initiated. The first step for that is to discharge the TAC capacitor for the time from the trigger until a clock edge which is set by the length of the synchronization chain.

Four TACs are included in each branch to increase the burst rate capability and their addressing is handled by a module called TAC_SELECTOR. Its core is the status vector TAC_status[3:0], which stores with one bit the information of each TAC capacitor if it is »clean«, i.e. it was recharged to the reference voltage and awaits an event, or if it is »dirty«. The latter can mean that an event has caused a discharge or that it is scheduled for a refresh. A second status vector, TAC_valid[3:0], holds one bit for each TAC describing its validity. Only valid TACs will be fully processed and their data queued for transmission, the others will be reset.

The TAC_SELECTOR selects the TAC IDs that are next in line for writing or reading and distributes this information to other parts of the TDC controller. That way, the appropriate signals can be set to enable switches in the analog part and thus activate (dis)charging processes for the correct TAC capacitors.

The next TAC ID for writing (TAC_NEXT_WR[1:0]) is obtained by increasing the ID[24] from

[24] After reaching the end of range, the ID starts again at 0.

the current one selected and testing the TAC_status vector until a clean position is found. When the writing process is finished, the WRITE_TAC module distributes a strobe to notify the other parts. This TAC_WR_FINISH signal causes the register, which holds the next TAC ID for writing, to update its value. If no clean TAC can be found, the write enable flag is removed (TAC_WR_RDY) and the current ID for reading is taken, because it will be the first to get ready again. Analogous, the next ID for reading (TAC_NEXT_RD[1:0]) is the next dirty TAC with increasing ID or, if all are clean, it gets assigned to the current one selected for writing as it will be the next to see an event. The ID is updated as soon as the reading process is indicated as finished (TAC_RD_FINISH).

5.5.2.5 TAC Refresh

The TAC capacitors, as any real capacitors, encounter leakage currents that discharge them slowly as long as they are not connected to a supply. Keeping them connected after the reset would distort the time measurement, because the switch for disconnecting has to be activated before being able to discharge. This may be a short time, but long enough to be significant for an accurate time measurement.

Without correction, the slow discharging itself leads to a distortion in the measurement. An event produces a voltage difference proportional to the clock's phase, independent of the starting voltage. Therefore, the recharging operation will take longer because of the lower initial value and the data will indicate a larger phase.

To circumvent this, a refresh strobe for the capacitor is commenced after a configurable time. This is handled by counters, taking the time since the last activity for each TAC. Such a refresh strobe causes the currently selected TAC for writing to be labeled dirty, i.e. setting the corresponding TAC_status bit, and switching the IDs for next writing and reading to the next in line. This way, the TAC to be refreshed will be reset as soon as the read logic is ready. The configuration ranges from refresh strobes after 25.6 µs at 160 MHz (bit setting 0001) up to 419 ms at 160 MHz (bit setting 1111). It may also be deactivated by setting all bits to 0. The method how to achieve the time is described in Section B.2.2.3 in the appendix.

5.5.3 Probe Outputs

In order to have a possibility to measure intermediate internal signals, some probe output pads are available. There are 13 signals from the TDC controller connected to a bus spreading over all channels. By configuring the global test configuration, the user can activate this bus and select the channel, which should be enabled on the bus.

The signals from the TDC controller involve information from the following groups:

Discriminator Outputs The signals DOT and DOE are the outputs of the discriminator after the preamplifier stage for both branches. They are the basis for event detection and indicate if the analog front-end works.

Digital Event Processing During operation, five strobes initiate the storing of timestamps. All those strobes are copied onto the probe bus as well as the event valid flag. If all six signals are present for a given event, the channel is most probably operational.

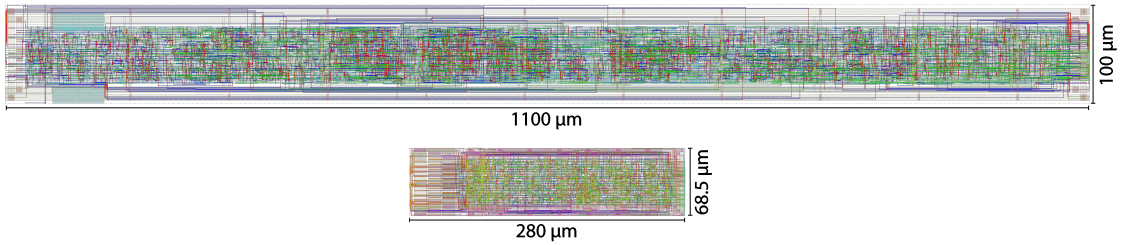

Figure 5.18: Two screenshots of the TDC controller design. The upper design is an extended TOFPET version with included SEU protection (ca. 80 % density, i.e. the ratio of available space filled with gates). After the redesign and with the new technology, the footprint shrunk significantly as the lower screenshot shows (ca. 89 % density). Both are drawn to relative scale.

TAC Status A central element in the TAC selection (see Section 5.5.2.4) is the four bit array `TAC_status[3:0]`, which is also part of the probe bus.

Comparator Outputs The comparator output for the recharging stage of the TDC operation is also available on the probe output. Their presence indicates a properly working analog TDC.

Additionally, one signal exists in the global controller. It is directly connected to the last bit of the shift register for incoming configuration data. This way, one is able to crosscheck if data arrived in the chip. More details on all probe signals are given in Section B.1.4 in the appendix.

5.5.4 Final TDC Controller Design

With the experience from the predecessor chip, the TDC controller could be vastly optimized. This involved a completely new implementation of the concept and removing unnecessary redundancy in the VHDL description. The important parts of this redesign have been described in previous sections.

Another, not yet mentioned step is the shift of the time buffers to the global controller. The goal has been to reduce the extent of the TDC controller for analog simulations to a pure controlling interface. Analog simulations of digital components require an immense processing time. Therefore, it is desirable to keep the digital involvement to a minimum and still enable a realistic operation. The digital behavior itself can be tested with digital simulation tools much faster because they just simulate three states (`0`, `1`, and undefined) instead of continuous voltage levels.

The result of the redesign and shift of buffers can be seen in Figure 5.18, showing a significant decrease in area usage and thus in used gates. The corresponding numbers are given in Table 5.6. To get an impression of the net gain, one has to subtract the buffers from the first design which have been just moved to another section. They make up approximately 13 % so that the new design's footprint lies at around 20 % of that of the old one.

Besides the area reduction, which helps to reduce the input pitch, a significant reduction of power consumption could be achieved. With more than a factor 6 less power consumed per

Table 5.6: Comparison between the two versions of the TDC controller. The first one, »v1«, is from the TOFPET ASIC with additional SEU protection and uses 130 nm CMOS technology. The second one, »v2«, is after the redesign and in 110 nm technology for PASTA. The last column gives an estimate on the power consumption achieved by applying the typical switching activity for these circuits.

Version	Dimensions	Area	Gates	Power
v1	1100 µm × 100 µm	110 mm^2	6524	1.57 mW
v2	280 µm × 68.5 µm	19.18 mm^2	846	0.25 mW

channel from the TDC controller, this part contributes considerably to a power efficient PASTA design.

5.6 Digital Global Controller

5.6.1 Overview of Operation

The global controller is the common back-end for the channels of PASTA and enables the connection to external components. It's structure has been mainly inherited from the TOFPET ASIC with minor modifications to the parts mentioned in the following sections[25]. More notable implementations are those of the clock divider (Section 5.6.3.2) and the already mentioned SEU protection (Section 5.3.3) and the switch of technology (Section 5.3.1). Especially the last two points were significant parts of the work done related to the global controller for this thesis.

The main tasks the global controller handles are the following:

Configuration Interface An important part for the operation of ASICs is to provide an interface for configuration. Insight into the processing of configuration is presented in Section 5.6.2.2 while the listing and effects of individual settings is described in the appendix in Section B.2.

Clock Distribution The external clock fed to the ASIC can be slowed internally to reduce digital activity. The resulting network is described in Section 5.6.3.

Global Time Counter The main data PASTA produces is based on timestamps. The global controller generates the input with a 42-bit-wide global time counter. It is then split into a 32 bit frame ID and a 10 bit timestamp for event data.

Test Pulse Generation The ASIC is able to internally generate a series of test pulses for calibration and testing purposes. The number of pulses, the time between them and their length are adjustable. The generator itself is described in more detail in Section B.3.3 in the appendix.

[25] As an example, a counter has been introduced for occurred SEUs and the possibility to read it out with a new command word. See also Section B.2.3.4 in the appendix for more details.

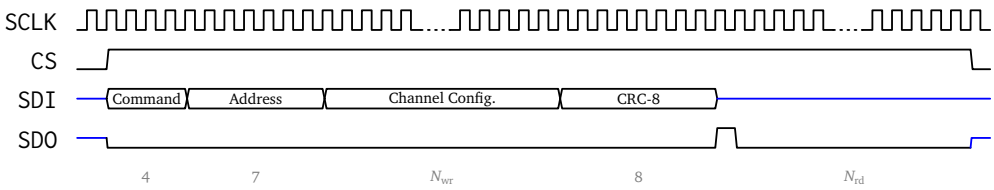

Figure 5.19: ASIC control interface with the timing information to write the channel configuration.

Channel Multiplexing All 64 channels are connected to the same configuration and data buffers. The configuration is divided into a global and local part. The global part is stored in the configuration interface and access lines copy it to all channels, whereas the local configuration needs to be stored in channel-specific buffers. For the data path, the event data is stored in local buffers before being transferred to the global buffers. The scheme of this process is described in Section 5.6.4.3.

Data Collection and Transfer The involved modules in the event data handling accumulate to the biggest item in the global controller. They collect data from the channels and encode it in the selected format. The detailed description is presented in Section 5.6.4.3.

5.6.2 ASIC Control Interface

5.6.2.1 Overview

The P̄ANDA Strip ASIC uses a fully digital configuration for the whole chip. The settings are split into global and local parts, the latter are individually adjustable for every channel. Each of the configurations, global and local, consist of digital, analog, and test circuit sections. While the digital sections (de-)activate certain functions or set time intervals, the analog ones mostly control digital to analog converter (DAC) values. Finally, the test circuit settings are used for calibration purposes and do not affect the ASIC during normal operation. All configuration settings are described in detail in Section B.2.

The module responsible for configuration is connected to a dedicated control interface. It comprises four lines: the slow clock `SCLK`, a chip select `CS`[26], slow data in `SDI`, and slow data out `SDO`. The configuration lines are independent of the data output and thus of the regular operation. Commands sent to the ASIC's control interface on `SDI` follow a general structure: 4 bit command, 7 bit channel address (if applicable), N bit command data (if applicable), and finally an 8 bit CRC. Depending on the command, the command data and sometimes even the channel address is not required and hence omitted (e.g. requesting the global counter value). The write commands require an idle period after that in which the configuration is pushed through a shift register. An exemplary timing diagram showing the use of the involved lines for writing global configuration is depicted in Figure 5.19.

5.6.2.2 Configuration Processing

The configuration is handled by a dedicated module, build around a FSM. This state machine controls the incoming data stream, stores it accordingly and handles appropriate responses. A visual representation of the state machine's sequence is shown in Figure 5.20.

[26] With the `CS` line it is possible to use common lines for all other configuration lines and just select the current receiver chip by enabling `CS`.

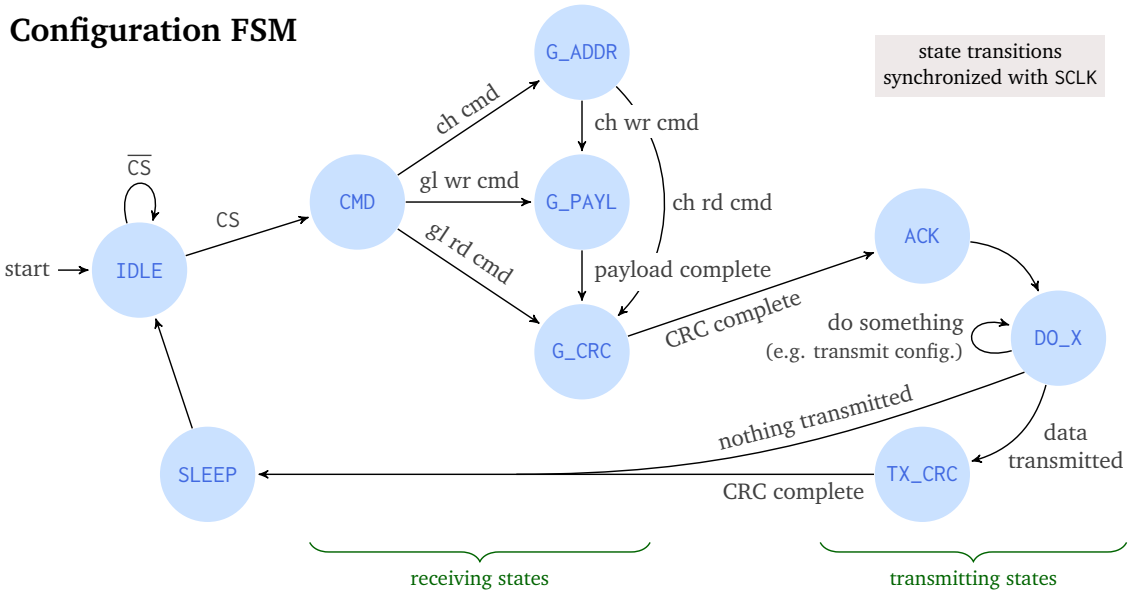

Figure 5.20: The symbolized FSM of the configuration module. The state machine starts with the IDLE state, each transition is checked with the SCLK. Some state names are shortened for a better display.

The initial state is IDLE where the FSM waits for a high channel select signal (CS). As soon as this signal arrives, the input (SDI) is scanned for command words (state CMD). Consequently, the channel select has to arrive coincidentally with the first data bits on the control link's input.

Depending on the 4-bit-long command word, some of the receiving states might be skipped. A channel command requires always an address of the channel in question, thus the next state in this case is GET_ADDRESS (G_ADDR in the sketch). The reception of payload data (state GET_PAYLOAD or short G_PAYL) may also be skipped, if only reading of information is requested. Otherwise, the data transmitted is received and stored into an internal shift register. The first bit of this shift register is accessible via the probe pin 14 (see also Section 5.5.3). Eventually, the last of the receiving states, GET_CRC or shortened G_CRC, is reached to obtain the CRC of received data.

While control data is received, a CRC-8 is calculated repeatedly and cross-checked with the transmitted CRC. The next state (ACK) transmits the result on the control link's output line (SDO): a 1 for a match and a 0 for a failed CRC check.

One of many states follows, executing something (state DO_X with the X as a placeholder). In case of one of the read commands, the state machine enters a transmission state (DO_RDCHCFG, DO_RDCHTEST, DO_RDCOUNT, DO_RDGCFG, DO_RDGTEST, or DO_RDGCOUNT) and transmits the requested data. To enable the detection of transmission errors, a CRC-8 code is sent afterwards in the state TX_CRC.
Another branch of commands is related to writing of configuration data (DO_WRCHCFG, DO_WRCHTEST, DO_WRGCFG, or DO_WRGTEST). While the global configuration is written in one clock cycle, the channel configuration is written through another shift register and thus needs

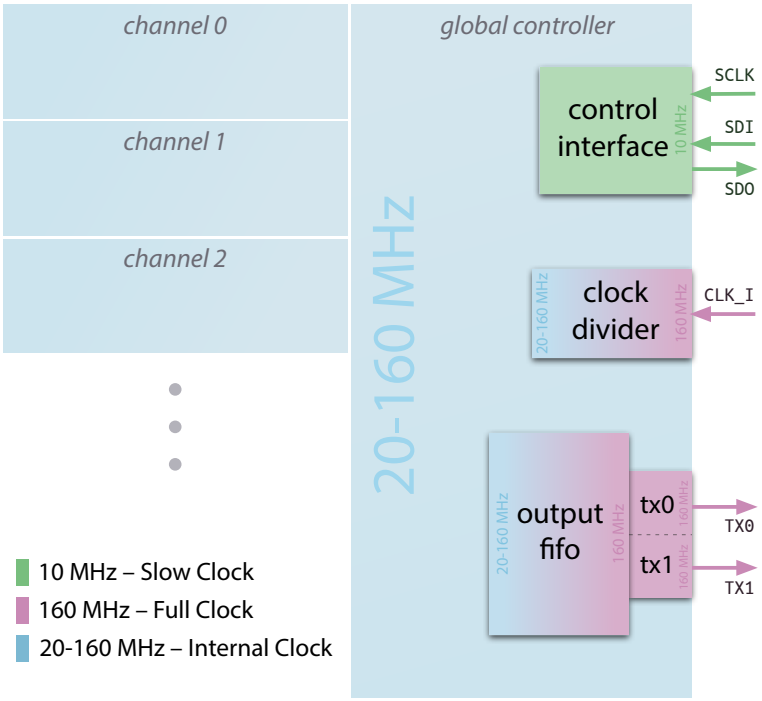

Figure 5.21: The clock domains used in PASTA. Everything apart from the highlighted parts use the internal clock (light blue), adjusted through the clock divider.

more time. In this time, the SDO line is set to 0. Because no data is transmitted, the state TX_CRC is skipped.

The last state in the line of processing is the SLEEP state where the internal CRC is reset to the initial value 0x8A. The FSM automatically continues to the IDLE state to await new data.

5.6.3 Clock Distribution

5.6.3.1 Clocking Domains

Digital circuits employing sequential circuits determine the rate buffered data is updated and states are changed by a clock. In PASTA, three different clock domains are used with different clock speeds. For a better visualization, they are also depicted in Figure 5.21.

Slow Clock The *slow clock* is used for the ASIC's control link, involving configuration handling and reading of ASIC-internal counters. The clock speed is given by SCLK and is designed to be 10 MHz. This is slower than the operational clock to ensure data consistency more easily and reduce power consumption.

Full Clock For data taking, the clock mentioned above would be too slow, thus a second, primary clock is provided through CLK_I which is optimized for 160 MHz. This matches the main clock distributed to all sub-detectors in $\bar{\text{P}}$ANDA. The *full clock* also drives the output transfer lines including the reading of their buffers.

Internal Clock Finally, the *internal clock* for all other operations can be the 160 MHz from the full clock, but might also be a reduced one. A dedicated and configurable module, the clock divider (see next section), distributes this internal clock.

5.6.3.2 Clock Divider

The module responsible for reducing the clock was implemented as a part of this thesis and uses an internal counter with 3 bit, increasing with every rising edge of the clock and wrapping around after reaching the maximum value. The least significant bit (LSB) of this counter is then changing its state with every clock cycle. Using this signal as a clock would result in a reduction factor of 2 for the clock speed. The next bit changes with every wrap-around of the LSB, leading to a further reduction of clock speed by a factor 2, or 4 in total. Finally, the most significant bit (MSB) changes state every four clock cycles, leading to a reduction factor of 8. Depending on the setting (Section B.2.2.2), a multiplexer uses either the original clock or one of the counter bits to feed the clock for the main operation, called the *internal clock*.

5.6.3.3 TDC Clock Enable Signals

In the TDC controller, the transition rate of the state machines that handle write and read operations can be reduced by means of TDC clock enable signals. Only when this clock enable signal is high, the FFs included in the FSM logic are scanning their input. For the read logic, this signal's rate determines the time of transferring charges between the TAC and TDC capacitors and also for resetting (details in Section 5.5.1.1). The concept of enabling signals was implemented before the description of write and read logics were finalized, thus both parts have their individual enable signals. Currently, the TDC controller disregards the write logic[27].

Depending on the setting, the clock enable signals are either activated all the time, i.e. their output is 1, or they are connected to a simple circuit: Falling edge FFs scan the global time counter and set the output high only when the last 4 bits of the counter are all high. Because this counter is driven by the internal clock[28], this is true every 16 clock cycles, leading to a clock enable strobe every 16 clock cycles. The FFs scan on the falling edge of the clock to simplify timing by making sure that the enable signals are already high when the rising edge of the clock arrives[29].

5.6.4 Event Data Handling

5.6.4.1 Stored Data

Internally, a 42 bit wide clock counter is the base to all timestamps. Because an event is processed within a certain time, the difference between the first and the last timestamp is limited. To avoid transmitting redundant information, events are grouped together to frames. One frame contains all the events that fall in a time window of 1024 clock cycles. Consequently, the timestamps are split into a global frame counter (frame ID, 32 bit) and the five timestamps

[27] In case the logic has to be altered for future versions, the enable signal for the write logic's FSM may be reintroduced quickly.

[28] In other words after passing the clock divider.

[29] All relevant digital circuits that are affected by the clock enable are rising edge triggered.

stored by the TDC controller (each 10 bit). The wrap-around of the frame ID happens after 2^{42} clock cycles, resulting in a repetition of frame IDs after around 7 hours and 38 minutes using the 160 MHz internal clock speed.

5.6.4.2 Gray Encoded Channel Timestamps

While the overall clock counter uses natural binary codes to represent its values, the 10 bit channel timestamps use Gray encoded values. The reason for that are the asynchronous buffer flags initiating the channel timestamp to be copied into a register and the high rate with which the timestamp changes its value.

Considering an example with a 3 bit counter, the consecutive numbers 3 and 4 would be represented as `011` and `100` in natural binary representation with all counter bits being flipped. Due to realistic signal propagation, not all bit flips would occur at exactly the same time, so the latching process could catch one of the intermediate steps (`110` for instance, translating to 6). To circumvent this problem, GRAY proposed an encoding scheme only switching one bit for each sequential state [148]. This was later named after him as the *Gray code*. In Table 5.7, the Gray code representation for all 3 bit counter states is given.

Table 5.7: The translation table of a 3 bit counter from natural to Gray encoded binary values.

Decimal	Natural	Gray
0	`000`	`000`
1	`001`	`001`
2	`010`	`011`
3	`011`	`010`
4	`100`	`110`
5	`101`	`111`
6	`110`	`101`
7	`111`	`100`

To translate a normal binary encoding into Gray encoded states, one only has to apply a series of `XOR` operations. Each of the counter bits is compared with a shifted counter vector by one to the right, prepended by a `0`. So for $x = \texttt{010}$ (3 in decimal), this leads to a shifted (and truncated) $x' = \texttt{\_01}$ where a `0` is inserted at the empty space, leading to $x_s = \texttt{001}$. The following logical operation is then performed bitwise:

$$x \texttt{ XOR } x_s = \texttt{010 XOR 001} = \texttt{011} \ .$$

5.6.4.3 Data Collection and Transfer

Event data is continuously taken on a channel level if TAC buffers are available. While processing an event, the TDC controller sends five different strobes to latch timestamps. The buffers responsible for storing these timestamps have been moved from the TDC controller to the global controller in the course of this thesis. To get the data formatted in a readable structure which can be transmitted, several steps and modules are involved.

The procedure starts on a local level with a timestamp buffer module for each channel. Buffers are present here for each of the five timestamps: $t_{\text{coarse,T}}$, $t_{\text{coarse,E}}$, t_{soc}, $t_{\text{eoc,E}}$, and $t_{\text{eoc,E}}$. If one of these strobes arrives, the buffer will be connected to the global time counter and the last 10 bits are latched. When the event is completed and valid, an event valid flag is set and the data is ready to be transmitted. After the data is read from global controller, the valid flag is set back to `0`, prohibiting a second transfer of the same data. As soon as new latch strobes arrive from the TDC controller, the old data will be overwritten.

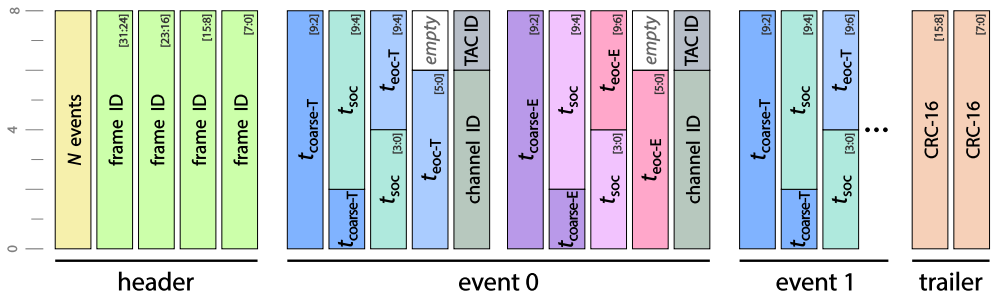

Figure 5.22: Data structure of the output stream in *full mode* shown in 8 bit blocks.

The sequence of data transfer from the channel to global buffers is decided by a multiplexer. It selects channels in an increasing order[30], jumping to the next set valid flag. If the multiplexer reaches the last channel, it starts again with the first one. Transfer of data from the channel takes one clock cycle and the next rotation is initiated after four clock cycles.

The first module the data arrives to after the channel is a formatting module. Depending on the selected data format (compact or full event mode) a corresponding module is activated and formats the data accordingly into 40 bit words. In case of the compact mode some calculations are made while the full mode needs to append two words (details on the data format itself are given in Section 5.6.4.4). Therefore, both modules buffer the incoming data for a short time.

The formatted data words are then transferred into the frame buffers. Two frame buffers, each dimensioned for 128 words, are used alternately with only one collecting new data while the other is being read out. This is switched by the LSB of the frame ID, making sure that one full frame is in one buffer. Before the frame data is transferred to the next stage, it is formatted into a proper frame. This includes prefixing the header information of frame ID and the number of events in this frame as well as attaching the CRC-16 word at the end. It also splits up the data into 16 bit words.

In the last step, data is transferred to the transceiver lines. Depending on the setting, the main logic might use a slower clock than the transceiver, thus an asynchronous first in, first out buffer (FIFO) sits in between. If both transceiver lines are activated, the 16 bit word is split up and sent simultaneously by both lines. Otherwise, both octets of the word are transmitted sequentially. Each line converts the 8 bit input from the FIFO into a 10 bit word, encoded with 8b/10b encoding to ensure a DC-balanced line.

5.6.4.4 Data Format for Transmission

The transmitted information is bundled together into words of 40 bit. One frame consists of one header word, N data words, and one trailer word. The header contains the number of events (8 bit) in this frame and the global frame counter of 32 bit. In the following data words the information is encoded dependent on the event mode. At the end, a trailer closes the frame with a 16 bit long CRC-16.

[30] That means from channel 0 to 1 ... until channel 63.

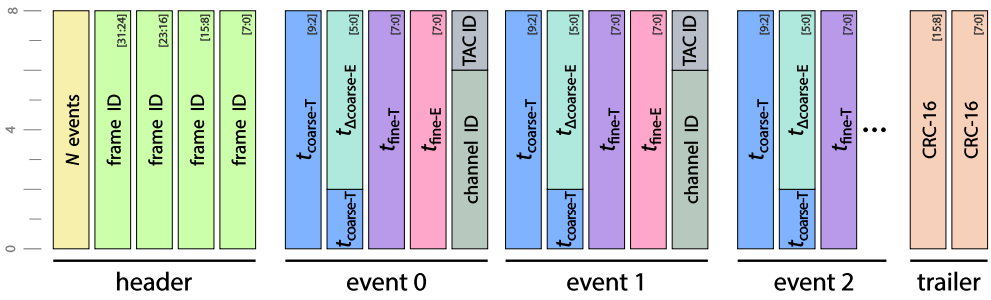

Figure 5.23: Data structure of the output stream in *compact mode* shown in 8 bit blocks.

Full Mode Intended for debug operations, the full mode contains all information the ASIC stores internally. This also means, that the channel counter values are untouched and transmitted in Gray code. It requires two words to transmit, therefore the output data rate shrinks by a factor of two compared to the compact event mode. The arrangement of the data is visualized in Figure 5.22

Compact Mode In contrast to the full mode, the compact event mode transfers normal binary representation of counter values, and takes advantage of the dynamic range of some values and reduces redundancy by not transmitting certain bits twice (like TAC and channel IDs).

The first reduced value is the energy coarse counter. It is expected that the distance between the time and energy coarse counter values is limited due to the possible signal shapes. Therefore, not the full energy coarse counter is transmitted but the distance in 6 bit to the time coarse counter ($t_{\Delta\text{coarse,E}} = t_{\text{coarse,E}} - t_{\text{coarse,T}}$), limiting the dynamic range of the pulse length to $2^6 = 32$ clock cycles.

Additionally, the fine time values are also compressed. Because of the dynamic charging range to the TAC and fixed time interpolation factor, the recharging time in the TDC is limited. Therefore, start and end of conversion are not transmitted individually but as their difference and without a constant offset:

$$t_{\text{fine}} = t_{\text{eoc}} - t_{\text{soc}} - t_{\text{offset}} \ .$$

The data formats and stream encoding are described in more detail in Section B.1.3.

5.6.4.5 Achievable Data Rates

Three main bottlenecks limit the data rate of measuring signals: the front-end's preamplifier, the event processing in the TDC, and the data storage and transmission.

Preamplifier Recovery The first bottleneck affects every incoming signal. After the sensor's current reaches the preamplifier, it generates a pulse shape depending on the input which involves capacitances. These take some time to recover back to their base level in which a following signal would be overlaid with the previous one, the so called *pileup effect*. The recovery time is $\mathcal{O}(100\,\text{ns})$, but is strongly dependent on the signal amplitude. Simulations show that this is well below 1 µs even for very high amplitude signals [143].

Event Processing in the TDC For the event processing, the event has to be detected first, then TAC capacitors are discharged, charges transferred, recharged, and finally reset. Out of this list, the recharging process takes most of the time because here the interpolation is applied. Depending on the fine time setting[31], the initial time of up to 3 clock cycles is stretched with a factor of 128. With a clock speed of 160 MHz this leads to

$$3\,\mathrm{clk} \cdot 128 \cdot \frac{1}{160\,\mathrm{MHz}} \;=\; 384 \cdot 6.25\,\mathrm{ns} \;=\; 2.4\,\mu\mathrm{s}\,.$$

The other subprocesses need significantly fewer clock cycles so that the total time stays below 3 µs. An average input rate exceeding this limit will lead to event loss because the channel's processing cannot keep up. Short bursts can be handled by using four TAC branches in a round-robin scheme.

Data Transmission Many factors influence the data transmission rate. To get an upper limit of the rate, it is assumed here that both transceiver lines are used in double data rate (DDR) mode. The data format of PASTA has to be revised for future prototypes, until then the full event mode will be the de facto standard, hence it is used for this estimation as well.

PASTA's data stream is split into frames of 1024 clock cycles. With two transceiver lines in DDR mode this enables transmission of 4096 bits per frame. Only 3272 bits per frame are actually usable due to the 8b/10b encoding. Header and trailer words reduce the space for data to 3208 bits which is enough for 40 events in full event mode with 80 bits each.

The 40 events per frame are transmitted in a time of $6.25\,\mathrm{ns} \cdot 4096\,\mathrm{clk} = 6.4\,\mu\mathrm{s}$. This is equivalent to 6.25×10^6 events per second for the whole chip. That means, each channel can produce on average 97.7×10^3 events per second.

Even though many parameters influence the rate capability of PASTA, one can expect the front-end to cope with a maximum rate of 100,000 ev/(s ch) for full clock speed and maximum transmission throughput. All three limiting factors are also summarized in Table 5.8.

5.6.4.6 Buffer Size

The buffer size, i.e. the maximum amount of storable data, of PASTA is given by the size of the frame buffer. Two buffers are included into the design that are used alternately and with a capacity of 128 words each. A word holds 40 bits of information, leading to a capacity of 128 events in compact and 64 for full format. The buffers collect data for the duration of a frame, i.e. 1024 clock cycles.

Two transmission lines are foreseen for the first prototype, as already done for PASTA's predecessor ASIC. This limits the transmittable data to 40 or 80 events per frame for full or compact mode, respectively (see last part in Section 5.6.4.5). More stored events in the frame buffer will get discarded. In case future simulations show this as a critical limitation, the VHDL basis holds the option to increase the output to four transceiver lines for a future prototype, effectively doubling the output rate. Because the header and trailer words only have to be

[31] All settings and their effect on the charging time are given in Table B.9.

Table 5.8: The dead time and maximum rate caused by the three bottlenecks in PASTA. Each influences a different aspect of event rate, hence a comment clarifies the impact. The numbers are given for full clock speed (160 MHz) and maximum transmission speed (combined 640 Mbit/s).

Bottleneck	Time / µs	Rate / kHz	Comment
Preamplifier	< 1	> 1000	Minimal time between two consecutive events in a channel (*burst rate*). This strongly depends on the signal amplitude.
TDC operation	$2-3$	$300-500$	Maximum continuous event rate for a single channel, depending on the fine time setting. A burst of up to four events is dealt with buffering in four TAC branches.
Data output	10	100	Maximum continuous event rate per channel for all 64 channels. Higher rates lead to event loss due to output bandwidth limitations.

transmitted once, four output lines result in a maximum of 81 and 162 events for full and compact mode, respectively[32].

5.7 Final PASTA Design

As of beginning of 2015, a first final design of PASTA has been completed, as depicted in Figure 5.24. This involved extended studies in three different domains.

Digital Simulation For the digital layout, simulations were done in parallel to the development process, investigating the behavior of the control logic for different configuration settings and input conditions. It also involved testing the effects of SEUs by altering operation critical registers at random moments. Some of the tests revealed flaws in logic or problems with the automatic synthesis and place and route algorithms[33], which could be solved.

Analog Simulation Similarly, simulations for the analog parts where conducted by the analog design team, checking if the calculated parameters lead to the expected behavior. This is especially important since many circuits rely on a proper input from others to work as desired. An example is the circuit supplying the channels with a reference voltage. This circuit needs to deliver a stable voltage level[34], otherwise the measurement based on the discriminator outputs gets corrupted.

Mixed Simulation Finally, after combining the analog circuits with their digital control, simulations have been performed to inspect a proper connection and interaction. Testing the

[32] To fully exploit this range the buffer size would have to be adjusted to 162 words.

[33] As an example, one major issue was the placement of the well tap cells, which could be solved by modifying the cell itself, see Section 5.3.2

[34] Actually, a simulation revealed an unexpected oscillation that only occurred when all channels were included into the simulation. The oscillations had a big amplitude and would have made the ASIC unusable.

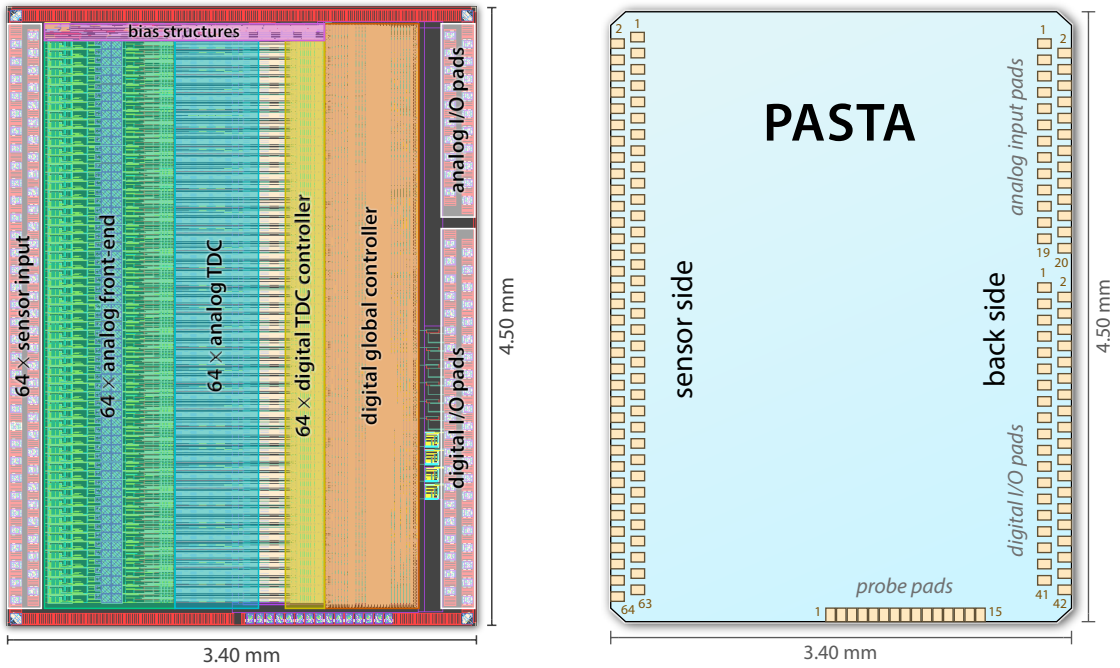

(a) Screenshot of the design with major sections.

(b) Sketch of the floor plan with I/O pads.

Figure 5.24: The final design of the PASTA ASIC as it was sent to the foundry for fabrication.

latter is a necessary step to verify that the designers understood the intentions of the others correctly and produced circuits that match the planned operation.

In conclusion, PASTA underwent thorough tests to verify the design towards a successful fabrication. The 64-channel ASIC was submitted in spring of 2015 and will return in summer 2015.

Readout System for ASIC Prototypes

6

6.1 Motivation and Overview

Readout components are the first stage of transforming the sensor signals to data files stored on disk. Very often, their location and performance requirements make it necessary to custom tailor front-ends for the specific application. The typical development cycle for new versions of ASICs is on the order of one year. So, thoroughly testing these electronic devices is a crucial part of the development process towards a functional detector system.

The MVD requires custom ASICs, both for pixel and strip sections. Therefore, an evaluation system has been developed to examine different prototypes. Originally intended for the pixel readout solution, ToPix ASIC, it is also planned to be used for PASTA measurements. This is possible because the basic requirements to access a readout front-end are relatively similar across different versions. Fundamentally, it converges to writing global and local[1] configurations to the ASIC and reading the data stream from it.

To accomplish access to a variety of front-ends and thus being reusable, the Jülich Digital Readout System (JDRS)'s structure is kept as modular as possible. Exploiting the full potential of the devices under test (DUTs) in terms of data throughput, the JDRS is optimized for high performance by utilizing an FPGA as the central control unit. The system is a compact, table-top setup including the following components:

- A custom **readout board** hosting the DUT,
- the central FPGA on a commercially available **evaluation board**,
- and a connected **readout PC** running the control software
- using a **software framework** to access the DUT's functions.

[1] *Local* refers to configuration valid for one channel.

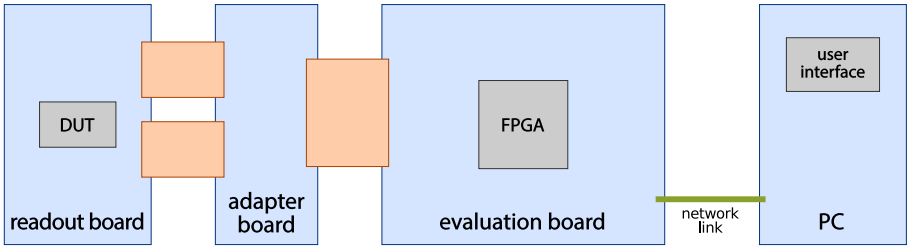

Figure 6.1: The structure of the Jülich Digital Readout System, containing three boards to access the DUT and a connected PC for configuration and data handling. Adapted from [149].

The initial development of the system has been conducted by MERTENS [51] and has been continuously enhanced. Some of these enhancements were done in the course of this thesis and are described in the following sections after an introduction of the system's structure and components.

Besides the mentioned thesis [51], the basic description of the system has also been published as an appendix in the »Technical Design Report for the: PANDA Micro Vertex Detector« [98] and was also covered in the thesis of ESCH [149].

6.2 Basic Components of the System

The system is constructed around an evaluation board featuring an FPGA handling the data conversion and communication with the PC (see also Figure 6.1). In the following, the evaluation board itself (Section 6.2.1) and the software framework for the PC (Section 6.2.3) are explained. An aspect touching both subjects is the connection between the evaluation board and PC, which is described in Section 6.3.

This leaves the components relevant to connect the DUT to the evaluation board. It involves a custom-tailored readout board hosting the ASIC and connectors for data lines and voltage supply. To achieve maximum flexibility for laboratory setups, especially in radiation-intense environments like tests with particle beams, a simple adapter board is also produced to detach the DUT from the evaluation board. These components have been produced for setups with the ToPix ASICs, described for example in [149]. For PASTA, new board designs have to be done, which are still pending.

6.2.1 ML605 Evaluation Board

The key component of the JDRS is the ML605 evaluation board with a Virtex-6 FPGA. It is part of an off-the-shelf evaluation kit available from Xilinx and is depicted in Figure 6.2. Using such a commercial product is more cost-efficient than a custom development. The big advantage of this kit is its inherent flexibility by using a variety of connection possibilities and offering a collection of useful items for electronics development like clock generators or memory buffers. The most relevant technical details are collected in Table 6.1.

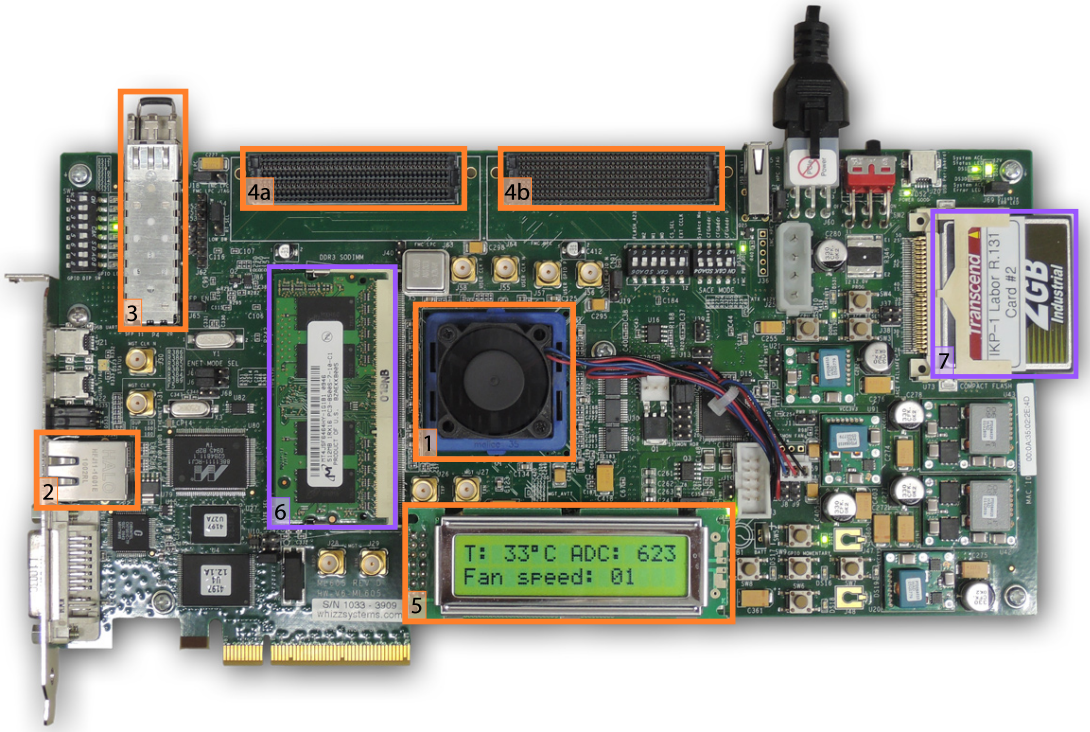

Figure 6.2: The central component of the Jülich Digital Readout System: the ML605 evaluation board. The highlighted structures are: 1 Virtex-6 FPGA with cooling fan, 2 Ethernet connector, 3 SFP connector, 4a and 4b low and high pin count FMC connectors, respectively, 5 LCD, 6 512 MB DDR3 RAM, and 7 CF card slot.

Besides these central items, several small components help to make life of a developer easier. This includes easy-to-access[2] input buttons and switches, status light emitting diodes (LEDs), a liquid-crystal display (LCD) for displaying more verbose information, and coaxial SubMiniature version C (SMC) connectors for signal I/O.

6.2.2 FPGA Firmware

A field programmable gate array (FPGA) is a programmable logic device offering fast performance for a dedicated task. The performance arises from exploiting parallelizable logic connections which can execute a set of fixed operations in one clock cycle. This processing concept is in contrast to general purpose processors like CPUs in computers which need to call a sequence of generalized functions to achieve the same result. Especially for processing a stream of data, FPGAs are predestined. Therefore, the additional effort of developing the software or logic scheme for an FPGA, called *firmware*, is worthwhile.

The firmware for the JDRS is based on the original developments described in [51, 149] and has been refined since. It is written in VHDL, a hardware description language, using assignments as they are available in the gates of the FPGA. Even though the software tools for

[2]Easy-to-access from inside the firmware.

Table 6.1: Selected technical details on the ML605 evaluation board with a short comment on their purpose.

Type	Version / Description	Purpose
FPGA	Virtex-6 XC6VLX240T	Central unit for logic operations
Memory	512 MB DDR3 SDRAM SO-DIMM	Large temporary data storage
	CompactFlash card slot	Firmware transfer from PC
I/O	2× FMC connectors (LPC and HPC)	Direct connection to daughter boards
	10/100/1000 Tri-Speed Ethernet	Network communication to PC via copper cable; current data transfer mode
	1× SFP connector	Modular I/O interface, e.g., via an optical link; former data transfer mode

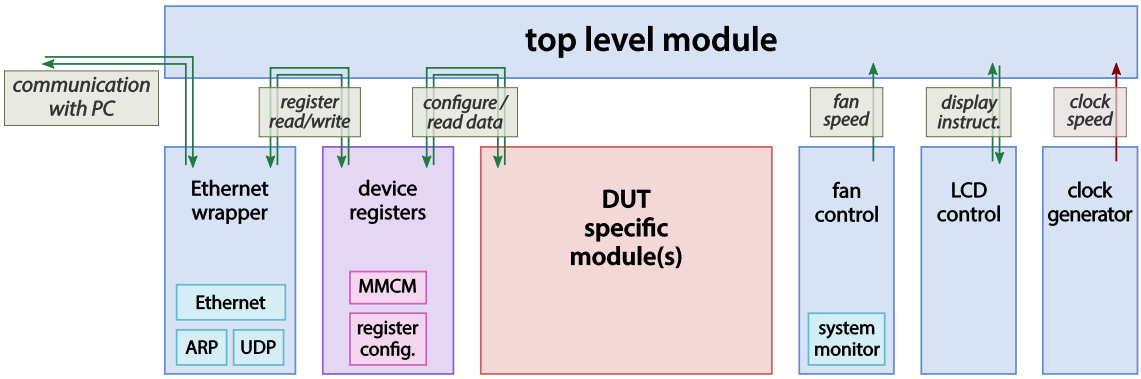

Figure 6.3: The modular structure of the FPGA's firmware visualized with a top level module combining all sub-modules. The most important ones are the Ethernet wrapper, device register module, and the specific modules for the DUT. Two clock generators are included: one providing the main Ethernet clock and other general speeds if needed, and one adjustable during runtime feeding the DUT. The shown arrows indicate the main connection.

the developer are different from ASIC tools, the conceptional workflow is comparable to the one described in Section 5.1.1.3, and thus is not repeated here.

Internally, the firmware is divided into modules taking on different tasks. The modular structure makes a transition towards new ASICs or measurement campaigns uncomplicated. The main modules are visualized in Figure 6.3 and described below.

6.2.2.1 Top Level with Clock Generator

The top level module builds the foundation of the firmware. It bridges internal signals to output lines of the FPGA which connect it to other components on the evaluation board. A user constraint file (UCF) links the names chosen in the top level description with physical pins and assigning constraints, especially for timing of signals or their type[3].

[3] Inputs and outputs can be single ended or part of a differential line. The used standard for the signal type and desired voltage levels is chosen in the UCF.

Besides the outward connections, the top level also connects sub-modules internally. This involves clock and data lines, the latter are particularly relevant for the central register module (see Section 6.2.2.3) and the DUT module(s). The central clock is generated by a 200 MHz oscillator[4] soldered onto the board and connected to the FPGA via a differential line pair using the low-voltage differential signaling (LVDS) standard. After reaching the top level module, the clock feeds a clock generator converting it to a 50 MHz, a 125 MHz, and optionally other clocks. The rate of 125 MHz is determined by the desired transmission speed of data over Gigabit Ethernet, which transfers 8 bits per clock cycle, and acts as a de facto main clock of the JDRS firmware.

6.2.2.2 Ethernet Wrapper

The Ethernet block of the firmware was introduced as an alternative way of connecting the board to a PC. Previously, a connection was established by a proprietary optical connection (SIS1100 [151]), requiring a dedicated receiver card in the PC.

A wrapping module serves as the firmware's interface to the Ethernet packages. Here, the incoming data is processed with a finite-state machine, which connects the received content with the central device register (see Section 6.2.2.3 and Section 6.3.3.3). Depending on the request issued by the PC, an appropriate response is also prepared by the state machine, again by using the buffered data in the device register.

A more general discussion on the Ethernet implementation into the system including the available functions for communicating is given in Section 6.3.

6.2.2.3 Device Register Control

A register is a placeholder for information and is composed of an address and a value. In the JDRS, information from several modules has to be accessible from the outside, therefore a central module collects the data and provides a unified interface for access. Internally, it enables reading and writing of single data words as well as a bulk data transfer including data buffering from the DUT to the readout PC. The register module also includes an MMCM clock generator as a submodule, which provides the clock for the DUT and is configurable during runtime by overwriting a set of registers.

A more in-detail description of this module is provided in Section 6.3.3.3 as a part of the Ethernet implementation.

6.2.2.4 Auxiliary Modules

Two auxiliary sub-modules provide control over the built-in fan and access to the LCD module. They are described in Chapter C in the appendix.

6.2.3 MVD Readout Framework for PC Software

Similarly to the firmware, the software for the PC is also developed with the paradigm for maximum modularity in mind. It is called MVD Readout Framework (MRF) because it was

[4]The oscillator is a SiTime SiT9102AI-243N25E200.00000 with a frequency stability of 50×10^{-6} [150].

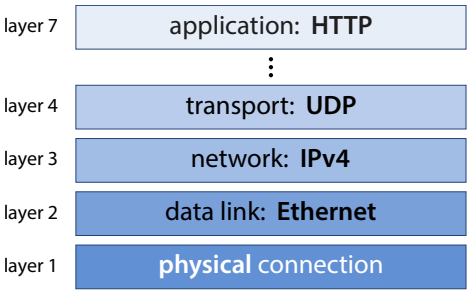

Figure 6.4: The original OSI model as defined in [152], applied to Ethernet communication with data encapsulated in UDP packages.

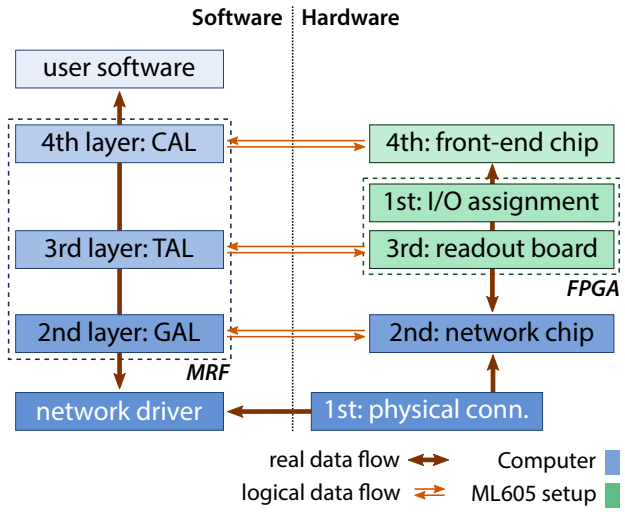

Figure 6.5: The OSI model applied to the MRF's structure. On the left side, software relevant layers are shown while hardware components are grouped on the right. Adapted from [51].

originally developed for front-ends used in the MVD but its general design makes it applicable for other front-ends as well. The framework delivers prepared functions to use in a user application, be it a graphical user interface (GUI) with direct user interaction or a program executed in a terminal and running in the background. The framework itself is also kept modular to enable an easy exchange of components. Incorporating an additional ASIC into the system would only require adding a new module in the framework, leaving the other components unchanged.

Being a framework with its focus on communication between PC and DUT, the MRF uses a model originating from a standard developed by ISO in the 1970s [152, 153]. This Reference Model for Open Systems Interconnection (OSI) uses abstraction layers to isolate lower level functions from higher level ones. Starting from the physical connection, the first layer above defines the most basic structure in the software that is required to transmit any kind of data over the selected communication channel. Higher layers offer more and more functionality and services to accomplish more complicated tasks but are always enclosed in their corresponding lower levels. The scheme as defined in [152] with an example for Ethernet communication is shown in Figure 6.4.

The OSI model's idea has been applied to the MRF, defining four layers:

1st layer The physical layer between the ML605 readout board and the PC is the lowest layer. This has been done with an optical connection in the past and now uses an Ethernet connection.

2nd layer The Generic Access Layer (GAL) takes care of the data transport and encapsulating it into proper formatted data packages. This is the first layer implemented in the MRF, offering the option to open a connection and send and receive generic data packages.

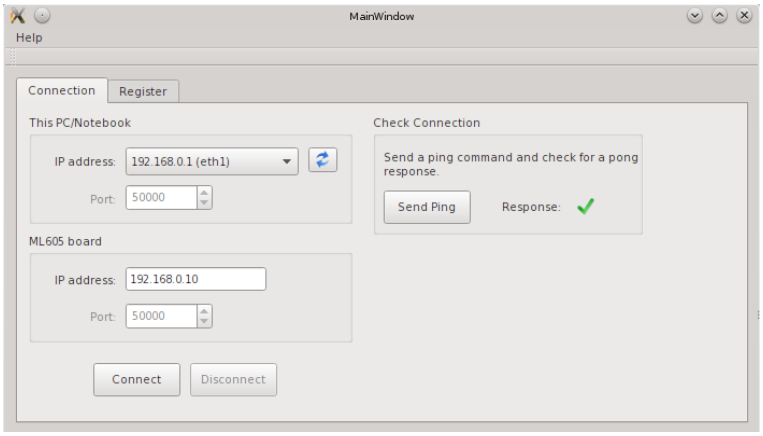

Figure 6.6: A screenshot of the bare GUI without any modifications for a DUT. The connection tab is activated, showing the input fields for configuring the network connection to the ML605.

3rd layer The Transport Access Layer (TAL) manages board-specific functions like the clock generator, flushing data buffers, setting the LED states, etc.

4th layer Finally, the Chip Access Layer (CAL) handles all DUT-specific functions like configuration settings and data readout. This is the layer where most adaptations for the PASTA front-end have to be done.

This structure enables logical data connections, for instance to the DUT. An adaptation for a different configuration structure has to be applied only on the CAL level by creating a different configuration data container. The required communication for configuring is handled by lower level functions. A schematic view of the physical and logical data flow is shown in Figure 6.5.

The implementation of the MRF is done in C++, only requiring the C++ Standard Template Library – a set of commonly used functions and objects. This way, the package is easy to implement into user applications.

6.2.4 Graphical User Interface

One exemplary application is the graphical user interface (GUI). It is motivated by giving the developer an easily usable front-end to access the various configuration settings of a DUT. It also provides the possibility to automate measurements and display results.

The basis of the graphical interface is two-fold: The MRF handles connection and data management, while the C++ framework Qt [154] undertakes the display of the interface and the user's interaction with it. A big advantage of Qt is the cross-platform usability, enabling the user to use it on stationary PCs or mobile laptops without much effort[5]. To prevent overloading the user with information, the interaction possibilities are grouped logically together and separated by tabs. They are ordered based on the sequence they are commonly used: first the connection, then board settings, and finally DUT specific functions.

[5]While the transition between Linux and OS X has been tested, running the GUI and MRF on Windows would need some extended work.

6.3 Ethernet Implementation into JDRS

6.3.1 Motivation for the Change

The task of the communication link is bidirectional, sending from the PC to the ML605 and vice versa. It should offer reliable transmission and a high data throughput so as not to limit the DUT data output. Therefore, the SIS1100 system was originally chosen, enabling the connection with an optical link. For this purpose, the system uses an optical transmitter in the Small Form-factor Pluggable (SFP) slot of the ML605, a Peripheral Component Interconnect (PCI) card for the PC, and an optical fiber inbetween. The system is a shared development of the ZEA-2 department of the Forschungszentrum Jülich with a company that commercially distributes it [155]. As a ready-to-use system, the only work required was the setup of the system like installing the Linux kernel driver[6].

While this was a reasonable choice at first, installing the needed driver on newer Linux systems was increasingly difficult and required additional maintenance work. Eventually, this would limit the JDRS to a small set of carefully set up machines. Additionally, a PCI slot was required, which is getting rarer in more recent PCs and is non-existent in laptops.

This has been addressed by the change to a common Ethernet connection over copper cables. The additional development time is outweighed by the advantages, mainly the gained flexibility of a readout machine using standard drivers and widely-used hardware. As a side product, a network system is also possible with one PC reading out several ML605s connected with an Ethernet switch.

6.3.2 Connection Protocols

To be able to use functions provided by the operating system (OS), one has to format the data in a certain structure which was already introduced by the OSI model in Section 6.2.3. Out of feasibility reasons of the VHDL implementation it was chosen to encapsulate the JDRS data into User Datagram Protocol (UDP) packages. The UDP data itself is included in the Internet Protocol (IP) and Ethernet formatted packages to comply with common OS standards. Otherwise, administrator privileges would be required, which would limit the available set of machines again. The following sections describe the packaging structure used.

6.3.2.1 Ethernet

The first layer used is the Ethernet link layer. It is closest to the hardware transmission of bits, hence containing hardware media access control addresses (MAC addresss) unique to the devices to guide the packages. Generally, packages are sent to every participant, independent of their intended destination. Hardware receivers only have to compare the first 48 bits – or 6 octets with 1 octet containing 8 bits[7] – to detect the package's relevance.

[6] The Linux kernel is the core of the system, handling all interactions of software with the connected hardware. A special software called *driver* includes necessary functions to address the hardware properly.

[7] Historically, the byte defined the amount of bits required to define a character [156]. Therefore, the length of a byte is not fixed, despite having a de facto standard today of using 8 bits for a byte. Octets are used instead to clarify the length when describing network protocol parameters.

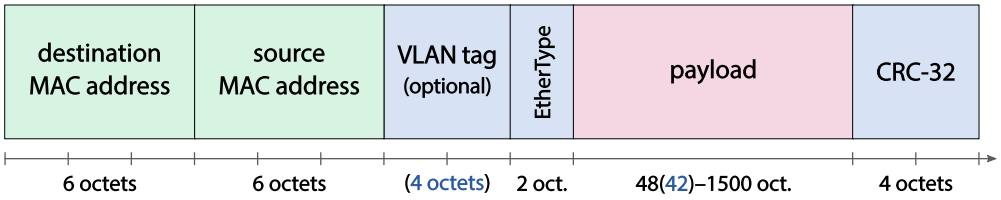

Figure 6.7: The structure of an Ethernet frame. It contains the hardware destination and source address as well as information of the content in the payload (VLAN tag and EtherType). Overall, an Ethernet frame has a total length of 64 byte to 1518 byte (with VLAN tag up to 1522 byte).

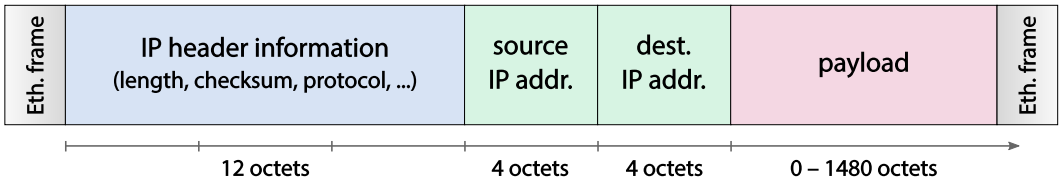

Figure 6.8: The structure of an IP frame. It starts with some header information to define the version (IPv4 is shown here), type and length of the payload as well as IP addresses of source and destination.

Besides the addresses for sender and receiver, it also contains a defined section of 2 octets (*EtherType*) for the type of payload the receiver has to decode. Data encoded as IPv4 has the EtherType of 0x0800, for instance. After the payload, a checksum using a 32 bit CRC code is appended to detect transmission errors. The full length of an Ethernet frame is 1518 byte, with an option to include an additional 4 octets for virtual local area networks (LANs) but this is not relevant for the JDRS. Figure 6.7 shows a sketch of the structure described prior, based on the definition in [157].

In between two Ethernet frames, the line has to be silent for a gap of 12 octets before initializing a new frame with a preamble (7 octets, each 0x55) and a start of frame delimiter (1 octet, 0xD5). This makes sure that the package boundaries are well defined in a stream of data.

6.3.2.2 Internet Protocol

The Internet Protocol was developed to transport data packets across one or more networks, independent on their physical structure. Today, the fourth version, IPv4, is still the main transport mechanism for data on the Internet, even though its limited address range makes many workarounds necessary and efforts are made to migrate to the most recent version 6. For closed LANs, like it is used for the JDRS, IPv4's capabilities are sufficient besides having less complexity regarding the implementation. While the Ethernet protocol defined the communication between hardware devices, IP operates on the software system level.

The simplified protocol structure[8] is shown in Figure 6.8, which is defined in »RFC 791: Internet Protocol« [158]. Before the payload block with a maximum of 1480 octets is transmitted, two fields of 4 octets each are reserved for the IP addresses. The source is automatically inserted by the sending device's driver and the destination is chosen by the user.

[8]The 12 octets comprising the header are combined as they are quite technical and only specify details about the following content and transmission instructions.

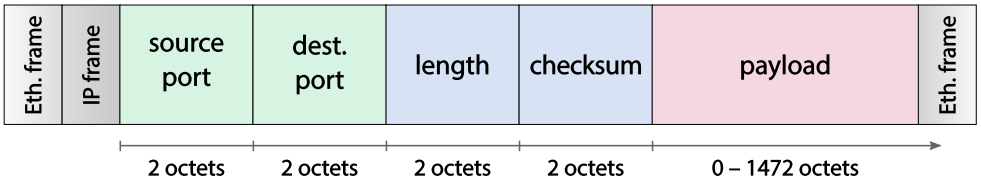

Figure 6.9: The structure of an UDP frame. It contains only 8 octets in the header, half of it is used for source and destination identifiers. Everything else is left for payload.

In case a communication channel is started to an unknown device, the destination's MAC address required for a valid Ethernet frame is not available at the start and needs to be converted from the IP address. Therefore, a special request is generated and broadcasted over the network to acquire this address, formatted as an Address Resolution Protocol (ARP) packet. Its response is then buffered for a while in a memory to speed up further interaction. On the OS level, this is done automatically by the driver, in the FPGA firmware the UDP IP core takes care of appropriate responses. So far, communication in the JDRS is always initiated by the PC, therefore the firmware is not required to start the procedure of address resolution and buffering.

6.3.2.3 User Datagram Protocol

Finally, to reach the application running on the OS, data is put into the User Datagram Protocol (UDP), a message-based transfer protocol. It provides datagram transmission, i.e. it does not rely on previous communication. This connectionless interaction has a low lag and is performant, especially in unidirectional communication as it occurs for ASIC readout in the JDRS[9]. This outweighs the downside of not recognizing package loss intrinsically, despite the good implementability in FPGAs with VHDL.

The simplicity mentioned above is represented in the protocol structure (Figure 6.9), as it was defined in »RFC 768: User Datagram Protocol« [159]. In addition to the two port addresses, just the length and a checksum are present in the UDP header, each field with 2 octets. After that, the payload follows, theoretically allowing up to 65,507 bytes[10]. Due to the enclosing in Ethernet and IP frames, the UDP packages used in the JDRS are limited to 1472 bytes length.

The protocol itself allows splitting of datagrams into multiple IP packages, but this was not pursued on the level of UDP. Being a connectionless communication, package loss is not recognizable intrinsically, which in case of a large UDP frame would lead to a large continuous section of lost information. Alternatively, an automatic generation of packages has been introduced inside the JDRS firmware, achieving a similar effect with a finer granularity of independent data blocks.

[9] The few additional packages for configuration which have to be sent bidirectional do not have a significant effect.

[10] The length field holds 2^{16} states, allowing UDP packages with up to 65,535 bytes. The header with 32 bytes needs to be substracted from that.

6.3.3 Implementation as a VHDL Module

The task of using the Ethernet interface of the ML605 is a common one, hence IP cores are provided by Xilinx, accessing the physical Ethernet chip. An open source core from [160] implements the basic functionality of accessing the Ethernet IP core and formatting data according to afore-mentioned protocol definitions. As a consequence of this, the raw connection was already prepared, albeit the implementation into the firmware at hand still had to be done.

6.3.3.1 Ethernet Wrapper

The focus of this implementation is laid onto the module that wraps around the Ethernet and UDP blocks and connects it to other components in the firmware. This *Ethernet wrapper*'s main item is a finite-state machine which is driven by the 125 MHz Ethernet clock and is thus synchronized with 8 bit blocks of data. It has the following states:

`IDLE` After startup and each processed request, the state machine is set to this state and awaits instructions from incoming data. If data is available, the first byte determines the type of request.

`WAIT_RX_DONE` Depending on the incoming request, more data than just the first byte has to be gathered. This state initializes storing of the incoming data blocks into the proper buffers.

`WAIT_DATA_OUT_RDY` To be independent of the register processing backend, the Ethernet wrapper waits up to 20 clock cycles for the reply data words to be ready. After that, a timeout will be sent as a response.

`DATA_OUT` The largest part of the state machine takes care of composing the requested data or just sending an acknowledgement flag.

`FINISH_SEND` Finally, some signals needed in the process are set to their initial values and the state machine is made ready for new data.

Packages that are transmitted in the JDRS follow an internal structure to instruct firmware and software what the data is about. They are based on 32 bit words because this is the default container length in the MRF and register value length of the firmware. The first of these words is always associated as a header word with the first 8 bits of it as a command or type indicator (see Table 6.2 for a list of possibilities). Further data in the header word is ignored from the firmware. After the header, data in 32 bit words follows, like register addresses and values.

Replies from the firmware use additional information in the header. On the third and fourth bytes sent, the current number of the sent packages for the bulk transfer is transmitted (see Figure 6.10). This has been introduced to enable the MRF the detection of package loss during data taking. Even though a retransmission is not possible, the user is at least informed about the loss. Similar to receiving packages, the following word size is also 32 bit for single register data but might differ from that for bulk data transfer. For the implementation of ToPix 4 for instance, a word size of 40 bit was chosen to match the ASIC's data stream.

Table 6.2: The command words defined in the JDRS. They are placed at the first byte in every transported UDP package within the system and instruct the firmware for the following data structure or just provide short-hands.

Command	Name	Comment
0x00	`nothing`	A void command word to use as a fall back.
0x01	`ping`	Request a pong reply to test the connection.
0x02	`pong`	The response to the `ping` request.
0x03	`confirm`	A short-hand to confirm an operation, like a `write_reg`.
0x04	`error`	The opposite of `confirm`, something went wrong.
0x05	`timeout`	Sent in case the requested data could not be prepared in time (issued by the `WAIT_DATA_OUT_RDY` state).
0x11	`read_reg`	Read a register, followed by the address to read.
0x12	`write_reg`	Write a value to a register, followed by address and value.
0x13	`pkg_count`	Return the number of received packages by the wrapper.
0x14	`pkg_count_rst`	Reset the package counter.
0x21	`bulk_read`	Bulk data read, followed by the number of requested words.

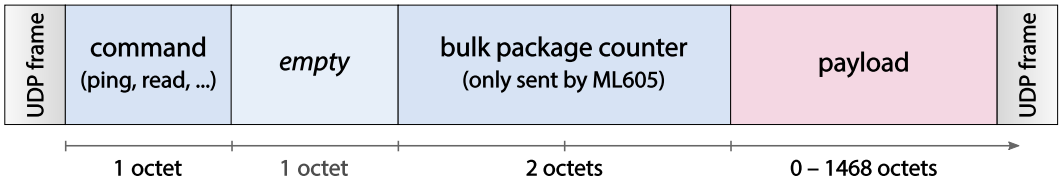

Figure 6.10: The first word, or 4 octets, of the JDRS frame is the header of the package. Its first octet determines the command and type of data, this package is transporting. After that, there is room for up to 1468 octets, which translates into 367 32 bit words.

6.3.3.2 Bulk Data Transfer

One particular task emerging from working with ASICs is transferring the produced data to a storage device, a PC in the case of the JDRS. The data typically comes with a high rate, therefore an effective transport method has to be available. While writing a single register continuously would not cause problems within the FPGA, the procedure of requesting it, building a response package, sending it to the PC, and extracting it there introduces a strong bottleneck[11].

Consequently, ASIC data is processed differently and transferred in bunches. The bunch size is limited by the UDP payload length, resulting in 1468 bytes[12] available for this bulk transfer. Assuming a 32 bit word size, this can bundle 367 data words into one single response (or up to 293 ToPix 4 words).

As of now, the request for such a bulk transfer will be cut off after filling one response packet. A future improvement possibility would be to automatically send additional packages if the

[11] Measurements of transmission and response times are given in Section 6.3.5.
[12] 4 bytes of the 1472 bytes for UDP payload are required for the JDRS header.

requested number has not been reached yet. This would reduce the influence of sending and receiving a request even further, hence increasing the data throughput. However, actual beam test measurements with high hit rates of the ToPix 4 prototype show that the achieved maximum throughput of the ToPix 4 is an order of magnitude below the current maximum of the JDRS system (see Section 6.4.1).

6.3.3.3 Device Register Handling

Experience with the existing system concerning the register handling and its flexibility for new environments showed room for improvement. With the change to Ethernet communication, many functions became obsolete and made the corresponding module more difficult to maintain. Therefore, the register handling has been rewritten.

Single Registers The new module groups certain types of registers based on their application, basically if they belong to either board or device functions. The latter refers to device specific information which changes in between DUTs and sometimes even for new measurements. On the other hand, the first group represents the range of capabilities the JDRS offers, which ideally is not required to change.

As a consequence, board registers have fixed addresses set in a central configuration file and their access has to be added manually. This is acceptable, because enhancing the systems capabilities requires wider modifications anyways. However, device registers change often while developing the readout interface, hence a flexible system has been integrated. An array of registers is provided to be directed to the DUT module(s) and intended to be used therein if required. Unused slots in the array will be automatically removed during the synthesis optimization (refer to Section 5.1.1.3), therefore no unwanted overhead is introduced into the FPGA's utilization.

The array is split into two groups: *status registers* are written by the DUT module(s) and contain information from the ASIC; *configuration registers* are written by the Ethernet wrapper or other board inputs and control functions and states of the DUT module(s). This strict separation prevents invalid signal states because two processes are trying to write their information.

Finally, all device relevant registers are available twice, preparing the system to integrate two DUTs simultaneously by using both FPGA Mezzanine Card (FMC) connectors. In Table 6.3 the ranges for the different register groups are given.

Bulk Data Register As mentioned before, single registers are not suitable for the continuous stream of data coming from an ASIC. Therefore, this stream is buffered in a FIFO memory and read out by a stimulus from the Ethernet wrapper. It takes care of the proper timing when a new word is required and composes the output of the FIFO together into a full response. With the FIFO buffer, the system can cope with the introduced latency in the communication flow without data loss.

Adjustable Clock Generator The JDRS also offers the possibility to drive the DUT with a clock speed configurable at runtime. This is achieved by a Mixed-Mode Clock Manager

Table 6.3: The predefined ranges of register addresses used in the central register control.

Address range	Intended area of usage
	Board features
0x000 to 0x00f	General registers for system inherit functions like control register or version information.
0x010 to 0x01f	Board-specific features, using available components.
0x020 to 0x03f	Registers used to configure the MMCM clock generator.
0x040 to 0x04f	Bulk transfer relevant registers. Bulk data itself is available at 0x040.
	First device
0x100 to 0x17f	Configure registers writing data to the device module, first DUT.
0x180 to 0x1ff	Status registers written by the device module, first DUT.
	Second device
0x200 to 0x27f	Configure registers writing data to the device module, second DUT.
0x280 to 0x2ff	Status registers written by the device module, second DUT.

(MMCM), which was inherited by the previous register handling module. The MMCM is one of two managers included in the Virtex-6 for clock generation based on phase-locked loop (PLL) architectures [161]. It gets accessed through a wrapping module storing the initial configuration values in a read-only memory (ROM)[13] and providing a possibility to dynamically overwrite the current configuration.

A peculiarity arises from the two clock domains that are in use by this. The ASIC uses a variable clock which a priori is not equal to the Ethernet clock speed. This is resolved by using an asynchronous FIFO for the bulk data register.

All of the components mentioned above are bundled in the register control module placed hierarchically beside the DUT module instead of using it as a mother. Because of this, a user conducting tests with a new device ideally only has to change the device specific module and can leave the surrounding ones untouched.

6.3.4 Modifications to the MRF

Getting the MVD Readout Framework to work with an Ethernet connection means addressing two tasks: first open a socket to gain access to the hardware device and second use this access to send and receive data. The main objective was to not rely on additional external packages to keep the MRF's requirements minimal. Using an operating system based on Unix, many Ethernet functions are accessible through standard C libraries.

6.3.4.1 Socket Creation

The lowest level in the MRF's abstraction layer model is the GAL, which was extended by the `TMrfGal_Udp()` class to implement the Ethernet connection. Upon initialization, it creates a *socket*, an endpoint of a communication over a computer network. For that it needs information

[13] If a change in the initial configuration is desired, it has to be changed during firmware compilation.

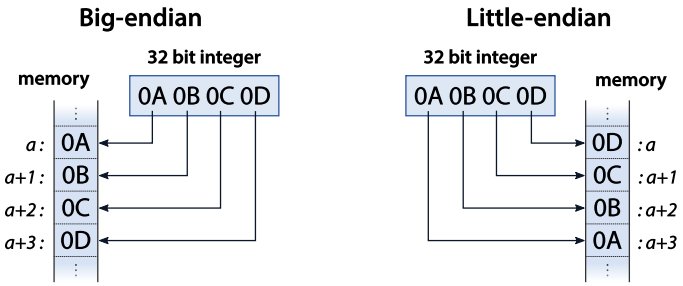

Figure 6.12: Endianness describes the different storing principles by starting with the first (*big-endian*) or last (*little-endian*) byte. This becomes important when directly accessing objects from the memory or a data stream. Adapted from [162, 163].

about the domain (in this case IPv4), socket type (datagram), and used protocol (UDP). The socket is now able to format and read packages according to the defined standards, but is not yet linked to a hardware component. Therefore, the socket gets *bound* to an address, in this case the assigned IP address of the network card. As a result, the OS is now able to assign data to the physical network.

The UDP definition does not foresee an active connection that is kept alive but merely sends data and concludes the transmission with that. The function `TMrfGal_Udp::deviceIsOnline()` is introduced to check if a transmitted *ping* gets the expected *pong* reply from the ML605 board. In the GUI, this is implemented with a button and icon as seen in Figure 6.11 to enable a fast check.

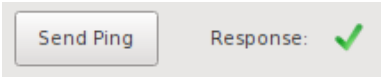

Figure 6.11: A screenshot of a small button-icon pair that is available in the GUI to check the connection with the ML605.

6.3.4.2 Read and Send Data

All data transmissions through the socket, including this online check, are handled by provided system functions, namely `sendto` and `recvfrom`. As parameters they expect address objects containing the source/destination addresses and ports, a pointer to the memory address where to write to or read from, the length of data to send/receive, and finally the socket which should be used. With that information, the OS is able to transmit data from the memory or receive into it. Since these operations operate directly on the memory, special care has to be taken not to access wrong sections and overwrite data from other processes.

One particularity arising from directly transferring data from the memory over network is the impact of *endianness*: the convention of interpreting bytes in memory to more complex objects like 32 bit integers. The least significant byte might be stored first (called *little-endian*) or the most significant one (*big-endian*), depending on the definition adopted. See Figure 6.12 for a graphical representation. In contrast to the MSB/LSB sequence definition of bits, endianness refers to block-wise ordered data. The architecture of the central processing unit (CPU) defines which of the two definitions is applied to the system. Physical data transmission over Ethernet is bunched in bytes too, using big-endian ordering which is also referred to as the *network byte order*.

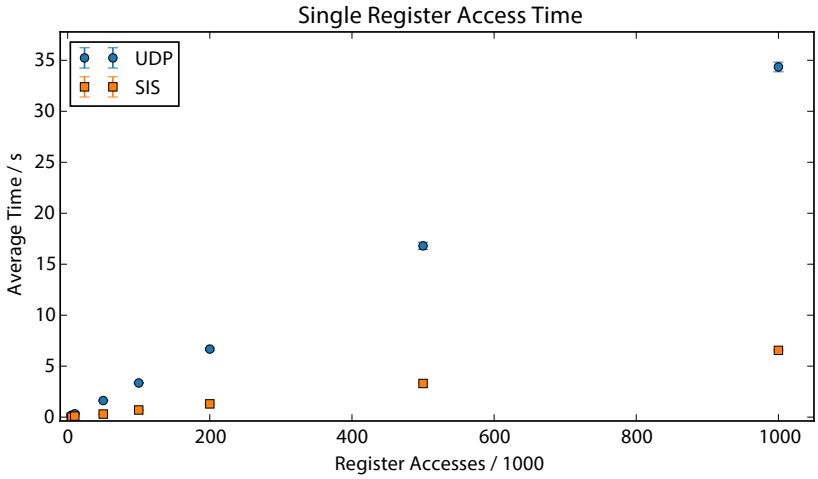

Figure 6.13: Comparison of the time it takes for a series of single register reads with the old SIS1100 interface and the new Ethernet connection. Each measurement was conducted four times, shown here are the mean values including their RMS (which is mostly invisible).

As long, as data is only accessed on one device, the endianness does not play a significant role in the programs. However, Ethernet communication is now a feature of the MRF, which uses direct memory access to optimize for high data throughput. Therefore, the read and send functions accessing the socket need to apply a potential conversion. They utilize the C functions `htonl(uint32_t)` and `ntohl(uint32_t)` to convert between host and network byte order.

6.3.5 Performance Measurements

Some performance measurements have been done to quantify the speed of the system before and after the implementation of the Ethernet connection. First, the single register performance has been obtained by repeatedly requesting to read a register, both with the existing link of the SIS1100 system and with the Ethernet connection. The results are shown in Figure 6.13. Based on this, it takes $t_{\text{eth}} = (34.4 \pm 0.5)\,\text{s}$ with Ethernet and $t_{\text{SIS}} = (6.55 \pm 0.05)\,\text{s}$ with SIS1100 to read one million register values. Using a register word size of 32 bit, this translates into the rates of

$$R_{\text{single,eth}} = 0.87\,\text{Mbit/s} \qquad \text{and} \qquad R_{\text{single,SIS}} = 4.70\,\text{Mbit/s}\,. \tag{6.1}$$

The reduction in rate results from the overhead Ethernet communication introduces in order to be versatile and robust. Therefore, it takes some time for the OS to generate packages, pass them to the involved physical components, and receive the answer. The approach of SIS1100 is more tailored for a direct connection, explaining the speedup with the downside of requiring dedicated hardware. Since single register access is mainly used for control and configuration operations, the raw rate is not critical.

For the bulk transfer, a similar measurement has been done with the Ethernet connection. 10^7 words of 32 bit each have been transmitted in 6.8 s by requesting the maximum for one

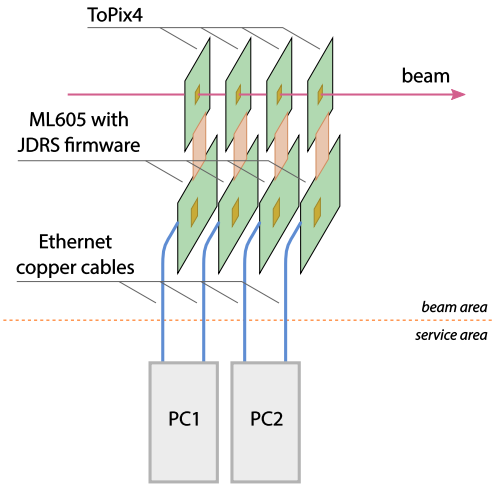

Figure 6.14: A sketch of the JDRS readout setup that was used to acquire data from 4 ToPix 4 prototypes, each connected to a PC via an Ethernet link.

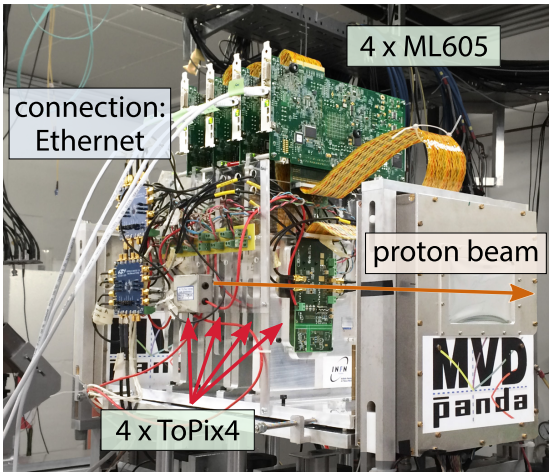

Figure 6.15: The setup used to investigate 4 ToPix 4 sensor prototypes with a proton beam. Adapted from [164].

transmission of 368 words per package. A comparable measurement is not possible with the firmware of SIS1100 but a lower limit from a beam time with ToPix 3 can be obtained. During highest beam intensity, 2.7×10^7 hits were collected in a spill of around 90 s [149]. One hit consists of 8 bytes, thus an average rate from at least 2.4 MB/s was reached.

Comparing the rates of both systems with bulk mode

$$R_{\text{bulk,eth}} = 44.9\,\text{Mbit/s} \qquad \text{and} \qquad R_{\text{bulk,SIS}} > 19.2\,\text{Mbit/s} \tag{6.2}$$

reveals that at this stage the Ethernet based system is in the same ballpark as the optical link of SIS1100. Implementing transmission of multiple UDP packages with one request promises a significant speedup.

6.4 Applications with the Ethernet Connection

6.4.1 Readout for Measurements with Beam

A first application of the JDRS with Ethernet communication was a beam test measurement with the ToPix 4 in October 2014. Four ToPix 4 prototypes were installed simultaneously to measure a proton beam. Even though it was not designed to measure the exact data throughput, one can estimate the achieved rates from the data recording.

6.4.1.1 Setup

The setup of the four ToPix 4 prototypes was done with the goal to limit the readout as little as possible. Each ToPix chip was connected to a ML605 board, which itself had a direct connection to a PC via Ethernet copper cable (see also Figure 6.14). The data presented here was taken with a clock rate for the ToPix ASIC of 50 MHz. The array of ToPix 4 sensors was setup in an

Table 6.4: Measured frame and hit count numbers as well as average data rates for two different intensities, each taken for 10 spills with the first ToPix reached by the proton beam.

	Frames		Hits	
	Counts	Data rate	Counts	Data rate
Low intensity:	6,423,911	1.03 Mbit/s	2,377,694	0.53 Mbit/s
High intensity:	5,854,190	0.94 Mbit/s	28,412,946	6.31 Mbit/s

experimental area at the Cooler Synchrotron (COSY) of the Forschungszentrum Jülich. Its beam consisted of protons with a momentum of 2.9 GeV/c. Extraction of the protons was not continuous but concentrated on a period called a *spill* of around

$$t_{\text{spill}} \approx 18\,\text{s} \quad \text{with a repetition cycle of} \quad T \approx 50\,\text{s}\,. \tag{6.3}$$

Absolute numbers of protons hitting the sensors were not available but the beam intensity could be varied providing a qualitative change in the hit rate.

To investigate the achieved rates in this measurement, one has to understand the ToPix 4's behavior regarding its data output. Hits are bundled into frames, much like the concept of PASTA. All hits taken in the time window of 4096 clock cycles will be associated and transmitted with one frame. A transmitted frame consists of at least one header and one trailer word and the hits recorded within[14]. All words, regardless of being a header, trailer, or hit data, have a length of 40 bit [98].

6.4.1.2 Achieved Data Rates

One representative example of numbers for frames and hits for a recorded data set is given in Table 6.4. The data has been taken with two intensities and over 10 spills to lower the statistical fluctuations of the beam.

Frame Statistics Over the whole period of 10 cycles, a continuous stream of frames has been collected. This should not be related to the intensity because a frame might be full, empty, or anything in between – it is always transmitted after 4096 clock cycles have been reached. This tendency is visible in the first data column of Table 6.4, even though a slight decrease towards high intensities is recognizable due to the ASIC itself.

The average rate contribution from the frames is calculated by

$$R_{\text{frame}} = \frac{2 \cdot w \cdot N_{\text{frame}}}{n \cdot T}\,, \tag{6.4}$$

with the data word size $w = 40\,\text{bit}$, the number of frames N_{frame}, the number of spills recorded $n = 10$, and the repetition cycle $T = 50\,\text{s}$ from Equation 6.3. This resolves in roughly 1 Mbit/s for both low and high intensities. Expected is a rate of 0.97 Mbit/s for a clock rate of 50 MHz.

[14] If no hits occur, only header and trailer will be transmitted.

Hit Count Statistics A similar calculation can be done for the rate during spill, just exchanging the repetition cycle time T with the active time of beam $t_{\text{beam}} = 18\,\text{s}$. This yields to varying data rates from 0.5 Mbit/s up to 6.3 Mbit/s, as it was expected qualitatively.

Together with the base data rate given by the frame headers and trailers, this is still well below the expected capabilities of $R_{\text{bulk,eth}} = 44.9\,\text{Mbit/s}$ conducted in Equation 6.2. This shows that the system in the current state is capable of taking data in measurements of realistic prototypes even without the mentioned possible enhancements integrated yet.

6.4.2 Preparations for PASTA Readout

Besides the application for ToPix, the JDRS is also intended to be used for the upcoming PASTA prototype. Work on a first basic implementation has been started [165] in order to speed up the setup of the system when the ASIC will arrive.

A major part addressed in this work is the communication to the DUT itself. While the configuration is sent directly over a dedicated line, data comes 8b/10b encoded over a separate one. Even though this data coming from the chip is just forwarded to the PC, it needs to be decoded first. The reason for that is that a decoding in logic gates is more efficient than trying to achieve the same with high level functions of C++, thus this step is included into the firmware.

To validate the function of this decoding module, a stream of data from the PASTA simulation test bench was extracted and transferred into a FIFO on the FPGA. By a user initiated command, the FPGA's firmware then pushed the bit stream to the decoding module and further to the internal data buffer where the Ethernet modules can access and transfer it to the PC.

Additionally, the work on a configuration interface has been started. The motivation for this is the efficient packaging of configuration values, which is just a stream of bits. Updating the configuration by changing the bits manually would be possible but is more difficult and prone to errors. Therefore, a GUI displays appropriate options for all values and it labels their purpose with more verbose tooltips appearing while hovering over the fields. In the program's core, the given values are then combined into the proper configuration word which is sent to the ASIC. A screenshot of the GUI is shown in Figure 6.16.

This work has been done before the PASTA design has been frozen, hence the configuration values differ, especially in the analog section. This is not a critical issue because it effects only the labels and placements in the GUI and the internal C++ values, respectively. The communication process will stay the same.

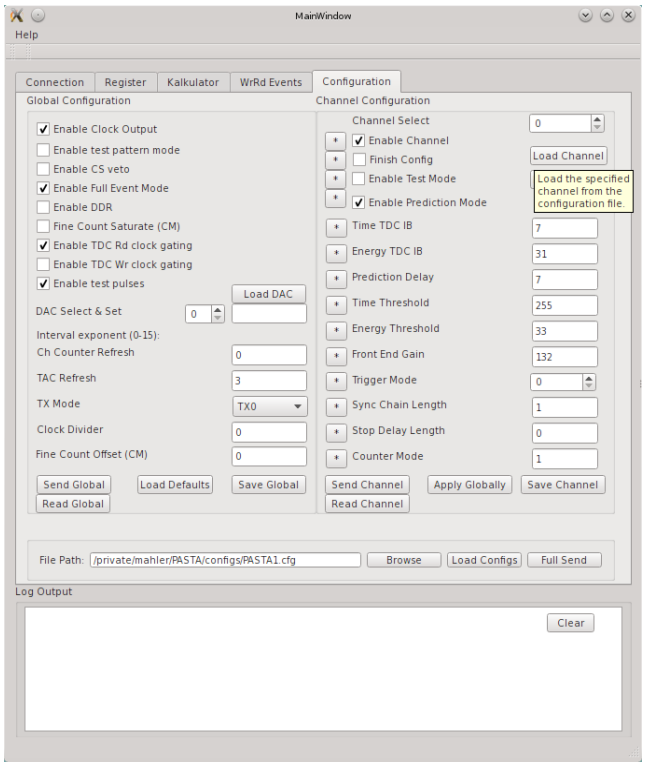

Figure 6.16: A screenshot showing the configuration section of the GUI for the JDRS with a PASTA chip. The light-yellow box on the top-right is an example and appears over elements where additional information is available. Some of the shown configuration values are not in the submitted ASIC design because the exact definition was made after the initial work for reading out PASTA with the JDRS has been completed.

Exploratory Simulation to Reconstruct the $\Xi^-(1690)$

7

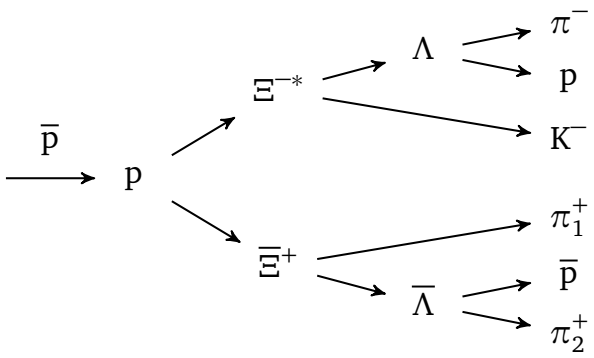

Figure 7.1: The decay tree of the process analyzed in this thesis. Ξ^{-*} refers to the state $\Xi^-(1690)$. The two π^+ in the final state are distinguished by indices: π_1^+ and π_2^+.

In this chapter, the simulation and reconstruction of the reaction $\bar{p}p \to \bar{\Xi}^+\Xi^-(1690)$ with the PandaRoot framework is presented. The full decay tree, as shown in Figure 7.1, includes long-living hyperons (Λ, $\bar{\Lambda}$, and Ξ^+) with decay lengths of $\mathcal{O}(\text{cm})$. The contribution of the MVD for the reconstruction of these particles with displaced vertices is studied as well. The symbol Ξ^{-*} is used as an abbreviation for the $\Xi^-(1690)$ hyperon in this chapter. To distinguish the two positively charged pions in the final state, indices are used: π_1^+ and π_2^+. The contribution of the MVD for this decay with displaced vertices is studied as well an

7.1 Motivation to Study $\bar{p}p \to \bar{\Xi}^+\Xi^{-*}$

As discussed in Section 2.2.3, the measured baryon spectra cannot be explained solely by the quark model. Experimental input is required to find and validate models that describe meson and baryon excitations accurately. In case of the baryons, the spectrum for strange-containing hyperons is extremely sparse, for instance for the Ξ^- states. Thus, measuring excitations like the $\Xi^-(1690)$ provides a good probe for structures in the baryon spectra. Even though the production cross section of cascade-anticascade pairs in $\bar{p}p$ annihilations is not yet known with

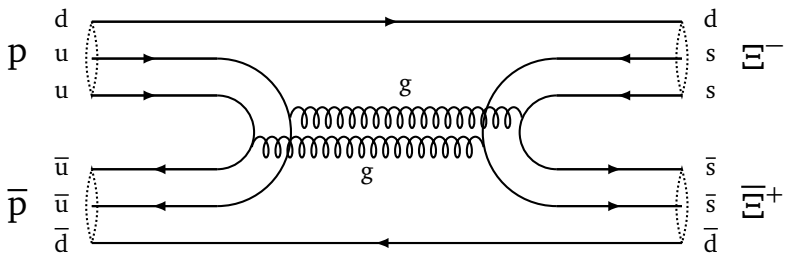

Figure 7.2: A Feynman diagram for the reaction $\bar{p}p \to \bar{\Xi}^+\Xi^-$ in the quark model, with two gluons exchanged.

good precision, sparse experimental data and theoretical models indicate a value of $\sim 2\,\mu b$. In HESR's high luminosity mode of $\mathcal{L} = 2 \times 10^{32}/(cm^2\,s)$ this is equivalent to a production rate of around 1×10^6 $\bar{\Xi}^+\Xi^-$ pairs per hour. Combined with their distinct event topology this makes Ξ studies an attractive channel for investigations of the strong interaction with $\bar{P}$ANDA.

In addition to the spectroscopy measurements, the production itself is another important aspect in understanding the underlying processes. As shown in Figure 2.6 in Section 2.2.3, various models exist to describe the Ξ production in $\bar{p}p$ annihilation but require experimental input. One particularly interesting aspect is the polar angle distribution in the $\bar{p}p$ center-of-mass (CM) frame. This can be illustrated with the Feynman diagram in Figure 7.2, which shows a possible production mode in the quark model with two-gluon exchange. The $\bar{d}$ antiquark of the $\bar{\Xi}^+$ is originating from the antiproton directly, thus it carries part of the antiproton's initial momentum. A production favoring more forward boosted $\bar{\Xi}^+$ baryons is expected and would be visible in the polar angle distribution. Hence, a precise measurement of the angular distribution will constrain the models attempting to describe $\bar{\Xi}^+\Xi^-$ production in $\bar{p}p$ annihilation.

In the following sections, the analysis of the production and reconstruction of $\bar{p}p \to \bar{\Xi}^+\Xi^{-*}$ is investigated. Since neither experimental data nor theoretical predictions for the angular distribution are available, a homogeneous phase space production is used as a first approach. The systematic effects of a forward peaked angular distribution are investigated in Section 7.4.6. For estimations of the achievable statistical accuracy, a production cross section of $1\,\mu b$ is assumed. It is based on the ground state estimations that are discussed in Section 2.2.4. Finally, background studies are carried out to estimate the signal purity.

7.2 Event Generation

7.2.1 Input Parameters

The event generation is based on a set of input parameters. The most relevant parameters are summarized in Table 7.1. Furthermore, the software versions used to generate and analyze the data of the $\bar{p}p \to \bar{\Xi}^+\Xi^{-*}$ reaction are collected in Table 7.2 to make the presented steps reproducible.

A total of 499,750 signal events has been generated with the PandaRoot simulation framework. After the generation, the particles are propagated through the full detector setup and digitized

Table 7.1: Most relevant parameters used in the simulation procedure.

Parameter	Value	Comment
Beam Momentum	4.1 GeV/c	Selected above $\bar{p}p \to \overline{\Xi}^{+}\Xi^{-*}$ threshold to allow population of the $\Xi^{-}(1690)$ state; slightly above resonant formation of J/ψ to combine measurements.
Production	PHSP	Homogeneous phase space production (ref. to Section 7.1).
Decay Chain	fixed	Refer to Section 7.2.1.2 for details.
Tracking	Ideal	Used class: `PndMCIdealTrackFinderNewLinks`
Particle ID	Ideal	Used algorithm: `PidAlgoIdealCharged`

Table 7.2: The software versions used to generate and analyze the data presented in this thesis.

Software	Version	Comment
PandaRoot	r27694	Software framework for $\bar{P}$ANDA, trunk branch with the most recent developments.
FairRoot	v-15.03	Software framework for high-energy physics experiments with common functions, latest release.
FairSoft	mar15	Software collection (including ROOT, GEANT, etc.) used by FairRoot and PandaRoot, latest release.
GEANT	GEANT-3	Framework for realistic particle propagation through matter.
Genfit	2	Framework for track reconstruction and error propagation.

according to the implemented sensor and readout characteristics. The following reconstruction consists of track finding, particle identification, and the event analysis.

For track finding and particle identification it has been necessary to use ideal algorithms that use the input data from the Monte Carlo (MC) generation to perform these tasks. The realistic algorithms are not yet in a stage to be used for this analysis. Clearly, the ideal particle reconstruction overestimates the performance of a realistic reconstruction and can only be used to obtain an upper limit.

The development version (called *trunk*) of PandaRoot is used with revision r27694 because a new cross-referencing system to the data's origin is employed in this version. This system enables the new ideal track finding algorithm `PndMCIdealTrackFinderNewLinks`, which solves some problems in assigning hits to a track candidate compared to the established version. Since some errors in the software were found in the course of this analysis, the class for ideal track finding was updated to the SVN revision r27911.

Other input parameters are described more extensively in the following paragraphs.

7.2.1.1 Beam Momentum and Energy

The antiproton beam momentum is an essential parameter for event generation. Based on this value, the dynamics of the reaction and subsequent decays are determined. One particular

momentum is the threshold which is the lowest beam momentum enabling the production of the initial states.

The basic inputs for calculating the required antiproton beam momentum are the masses of the particles involved in this initial process. For the proton and antiproton masses, a value of $M_\mathrm{p} = 938\,\mathrm{MeV}/c^2$ is used and for the produced states the central values (without error) are taken

$$M_{\overline{\Xi}^+} = 1322\,\mathrm{MeV}/c^2 \qquad M_{\Xi^{-*}} = (1690 \pm 10)\,\mathrm{MeV}/c^2\,.$$

The Ξ^{-*} is an excited state and decays almost instantaneously, thus it has a large width of $\Gamma_{\Xi^{-*}} = 30\,\mathrm{MeV}/c^2$. All values are taken from the current report of the Particle Data Group (PDG) [1].

The threshold energy for production is obtained by summing the masses of all produced particles:

$$\sqrt{s_\mathrm{thr}} = M_{\overline{\Xi}^+} + M_{\Xi^{-*}} = 3012\,\mathrm{MeV}/c^2.$$

The threshold beam momentum for an antiproton beam incident on a proton target at rest is given by:

$$p_\mathrm{beam,thr} = \sqrt{s_\mathrm{thr} \cdot \left(\frac{s_\mathrm{thr}}{4\,m_\mathrm{p}^2} - 1 \right)}\,.$$

Applying this to the cascade production in this thesis results in a threshold beam momentum of $p_\mathrm{beam,thr} = 3.78\,\mathrm{GeV}/c$. The actual beam momentum chosen for this study is

$$p_\mathrm{beam} = 4.1\,\mathrm{GeV}/c \tag{7.1}$$

in order to have an excess energy of around 100 MeV in the CM frame. With this excess energy, the phase space is expected to be large enough for a sufficient production cross section for this reaction channel. A beneficial side effect of this choice is that it is slightly above the $\overline{\mathrm{p}}$ momentum for $\overline{\mathrm{p}}\mathrm{p} \to \mathrm{J}/\psi$ formation[1] ($p_\mathrm{beam} = 4.068\,\mathrm{GeV}/c$). This enables simultaneous measurements of $\overline{\Xi}^+\Xi^-(1690)$ during J/ψ measurement campaigns.

7.2.1.2 Particle Definitions

For the event generation with EvtGen, the desired particles need to be defined in a particle database. A large set of known particles is already included in the program. However, the $\Xi^-(1690)$ needed to be introduced to the database for this analysis. The mass and width are chosen according to the values given above. A value of $^1/_2$ is chosen for the unknown spin. This leads to s-wave production, i.e. with an orbital angular momentum quantum number of $L = 0$. The angular distribution is set to phase space (PHSP).

[1] The J/ψ meson has a mass of $M_{\mathrm{J}/\psi} = (3096.916 \pm 0.011)\,\mathrm{MeV}/c^2$ [1].

Table 7.3: The particle decays used in this analysis and their branching ratio of all possible decays. No measurements exist for the Ξ^{-*} branching ratio, the decay has merely been seen. Data from [1].

Particle	Decay Daughters	Branching Ratio
$\overline{\Xi}^{+}$	$\overline{\Lambda}\ \pi^{+}$	$(99.887 \pm 0.035)\,\%$
$\overline{\Lambda}$	$\overline{\mathrm{p}}\ \pi^{+}$	$(63.9 \pm 0.5)\,\%$
$\Xi^{-}(1690)$	$\Lambda\ \mathrm{K}^{-}$	*seen*
Λ	$\mathrm{p}\ \pi^{-}$	$(63.9 \pm 0.5)\,\%$

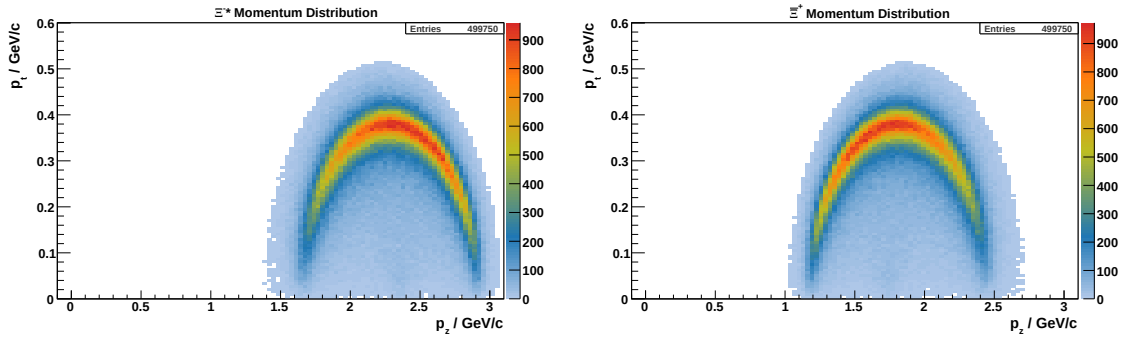

(a) Momentum distribution of Ξ^{-*}.

(b) Momentum distribution of $\overline{\Xi}^{+}$.

Figure 7.3: The transverse momentum p_t versus longitudinal momentum p_z distributions of the initial state particles in the reaction $\overline{\mathrm{p}}\mathrm{p} \rightarrow \overline{\Xi}^{+}\Xi^{-*}$.

The decay of the initial state has been fixed in a decay file according to Figure 7.1. By fixing the decay, the analysis can be optimized to this topology without generating unnecessary events. For the particles $\overline{\Xi}^{+}$, $\overline{\Lambda}$, and Λ, the most probable decays are chosen with a combined branching ratio of 40.8 %. The branching ratio of $\Xi^{-*} \rightarrow \Lambda\mathrm{K}^{-}$ is not known, however the K^{-} provides a good tagging possibility for the event selection. All fixed decays and their branching ratios are summarized in Table 7.3.

7.2.2 Generated Kinematics

7.2.2.1 Initial State

The initial state of $\overline{\Xi}^{+}\Xi^{-*}$ is produced with an antiproton beam momentum of $p_{\mathrm{beam}} = 4.1\,\mathrm{GeV}/c$. The transverse versus longitudinal momentum distributions of the cascade states are shown in Figure 7.3. The distributions generally show a higher longitudinal momentum for the Ξ^{-*} than for its partner $\overline{\Xi}^{+}$, as a consequence of their mass difference. The available phase space of this two-body production would be a thin ellipse in the p_t-p_z plane but is smeared out due to the Ξ^{-*} particle's width. The transverse momentum peaks at about $0.35\,\mathrm{GeV}/c$, which is at around 20 % of the longitudinal momentum, due to the forward boost of the system.

The mass distribution of the Ξ^{-*} is shown in Figure 7.4 with a nominal value for the mass of $M_{\Xi^{-*}} = 1690\,\mathrm{MeV}/c^2$. The distribution is slightly asymmetric because higher masses of the Ξ^{-*}

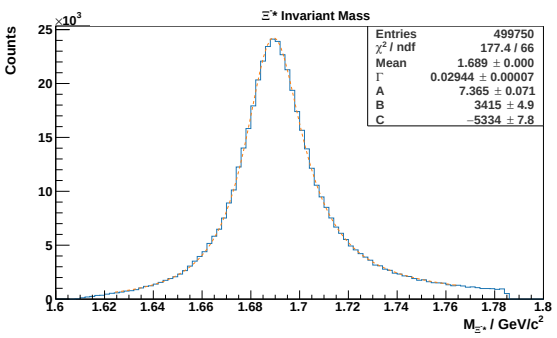

Figure 7.4: The invariant mass distribution of the **Ξ⁻(1690)**. The applied fit is a Breit-Wigner function, multiplied by a linear function from the decay's phase space (refer to Equation 7.2).

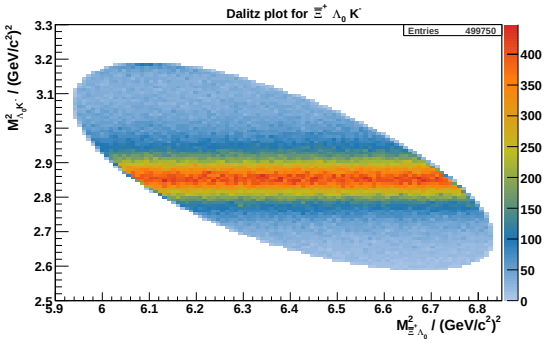

Figure 7.5: The Dalitz plot for the pairs of squared invariant masses of $\overline{\Xi}^+\Lambda$ on the x-axis and $\overline{\Xi}^+K^-$ on the y-axis. The Ξ^{-*} resonance is visible as a horizontal band.

enlarge the phase space of the daughter particles and thus increase the decay cross section. According to [1], the decay rate for two-particle decays is

$$\mathrm{d}\Gamma \propto \frac{|\vec{p}_1|}{M^2},$$

with the momentum of the first daughter particle[2] $\vec{p}_1$ in the CM frame of the Ξ^{-*}. Therefore, the Breit-Wigner distribution is adjusted linearly for higher masses. The complete function the fit uses for the mass distribution is:

$$f(M) = A \cdot \frac{\Gamma}{(M-\langle M\rangle)^2 + \frac{1}{4}\Gamma^2} \cdot \frac{B\cdot M + C}{M^2}. \tag{7.2}$$

Γ is the width and $\langle M\rangle$ the mean of the Breit-Wigner distribution. The weight factor A scales the distribution to fit the number of entries in the histogram. For the phase space influence, a linear term is multiplied with the parameters B for the slope and C for the offset. The full motivation for the linear term is given in Section A.2. Applying Equation 7.2 to the invariant mass distribution yields an invariant mass value of $M^{\mathrm{MC}}_{\Xi^{-*}} = 1.689\,\mathrm{GeV}/c^2$ and a width of $\Gamma^{\mathrm{MC}}_{\Xi^{-*}} = 29.4\,\mathrm{MeV}/c^2$.

The available phase space for the $\Xi^-(1690)$ production can be seen in a Dalitz plot. Since the $\Xi^-(1690)$ decays only in the two particles Λ and K^-, the $\overline{\Xi}^+$ is taken as the third one. The resulting Dalitz plot is shown in Figure 7.5, where the resonance is clearly visible as a horizontal band. The angular distribution of the production in the $\bar{p}p$ CM frame is shown in Figure 7.6, matching the input of a phase space production. A constant has been fit to the distribution, highlighting its uniform structure.

7.2.2.2 Daughter Particles

The $\Xi^-(1690)$ nearly instantaneously decays into a Λ baryon and a K^- meson. The Λ then decays after a long mean decay time of $c\tau = 7.89\,\mathrm{cm}$ into a proton and π^-. All momentum

[2] Due to momentum conservation $|\vec{p}_1| = |\vec{p}_2|$.

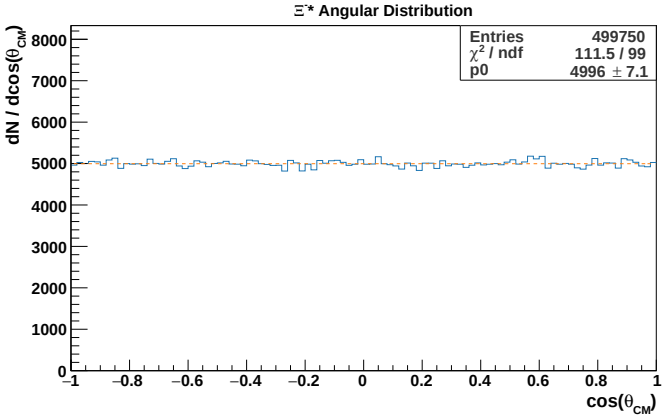

Figure 7.6: The angular distribution of the $\overline{\Xi}^{-*}$ in the $\overline{\mathrm{p}}\mathrm{p}$ CM frame.

distributions are collected in Figure 7.7. While the protons' distribution shows high longitudinal momenta with a peak between 1 GeV/c and 1.5 GeV/c, the K^- and π^- distributions have much lower values in the beam direction. Especially the π^- distribution has a large contribution of very low momenta below 100 MeV/c in both longitudinal and transverse directions.

Similarly, the momenta of the $\overline{\Xi}^+$ decay products are shown in Figure 7.8. From the decay into $\overline{\Lambda}$ baryons and π_1^+ mesons, the $\overline{\Lambda}$s carry the larger momentum fraction from the two daughters. The $\overline{\Lambda}$ particle's momentum is largely passed to the antiproton, which also shows high momenta in its distribution. Again, the momentum distribution of the π^+ from the $\overline{\Lambda}$ decay has a similarly low momentum as the π^- momentum distribution from the Ξ^{-*} branch.

7.2.3 Proper Time Distributions

Three particles in the decay chain have a significant delay length of $c\tau = \mathcal{O}(\mathrm{cm})$: the $\overline{\Xi}^+$, Λ, and $\overline{\Lambda}$. The proper decay lengths l' are obtained by

$$l' = \frac{\left|\vec{x}_{\mathrm{decay}} - \vec{x}_{\mathrm{prod.}}\right|}{\left|\vec{p}\right|/m}$$

and their distributions are plotted in Figure 7.9. As expected, the distributions show an exponential decrease with the decay constants λ extracted by exponential fits. The proper decay times are obtained via $\tau = \frac{1}{c\lambda}$ and yield the values collected in Table 7.4. All proper decay times including their errors lay within the nominal values from the PDG.

Table 7.4: Reconstructed mean proper decay times (τ) in comparison to the literature values (τ^{PDG}) [1].

Particle	$\tau/10^{10}$ s	$\tau^{\mathrm{PDG}}/10^{10}$ s
Λ	2.624 ± 0.006	2.632 ± 0.020
$\overline{\Lambda}$	2.627 ± 0.006	2.632 ± 0.020
$\overline{\Xi}^+$	1.636 ± 0.004	1.639 ± 0.015

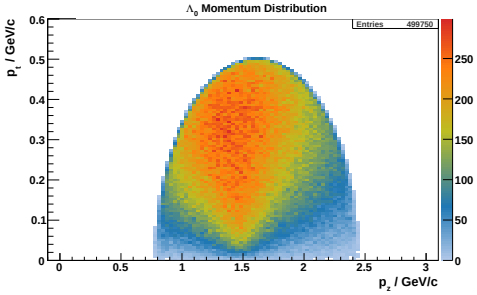

(a) Momentum distribution of the **Λ**.

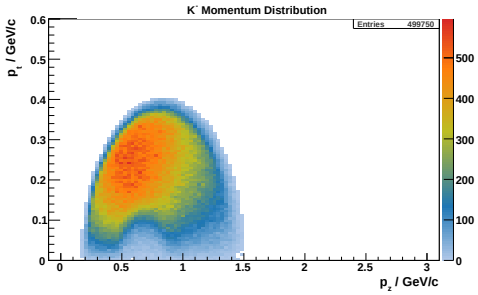

(b) Momentum distribution of the $\mathbf{K^-}$.

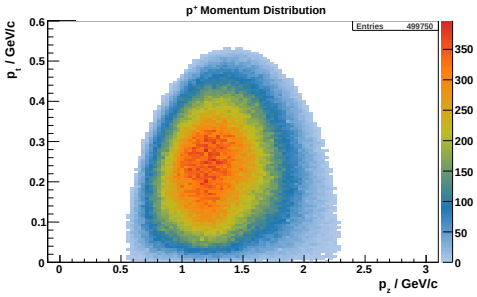

(c) Momentum distribution of the **p**, daughter of the Λ.

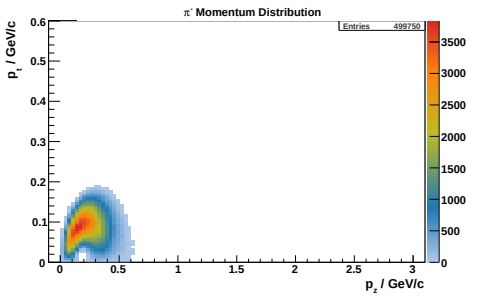

(d) Momentum distribution of the π^-, daughter of the Λ.

Figure 7.7: The momentum distributions of the daughter particles in the $\bar{\Xi}^{-*}$ branch. The transverse momenta p_t are plotted versus the longitudinal momenta p_z.

7.2.4 Decay Vertex Positions

Especially for the $\overline{\Lambda}$ baryons, the decay vertex positions are interesting because they originate from an already delayed vertex instead of originating from the interaction point. Combined, they create a distant vertex for final state particles as shown in Figure 7.10. The distribution of decay distances rises to a peak at around 8 cm and then falls off in an exponential-like shape. Four regions (DecReg1-DecReg4) have been defined with limits at 10 cm, 20 cm, and 30 cm to investigate the effect of the vertex position on the detector response later on.

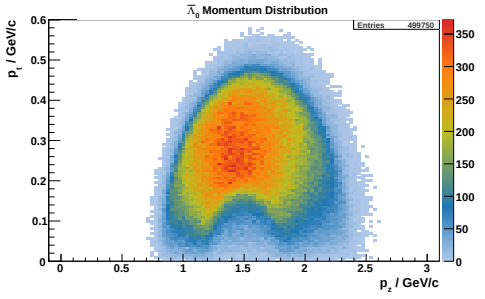

(a) Momentum distribution of the $\overline{\Lambda}$.

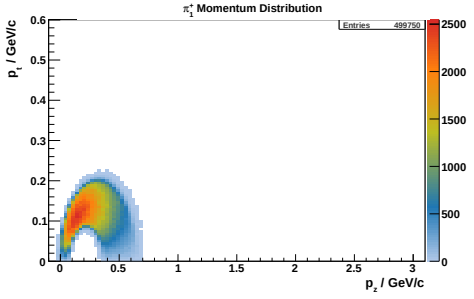

(b) Momentum distribution of the π_1^+.

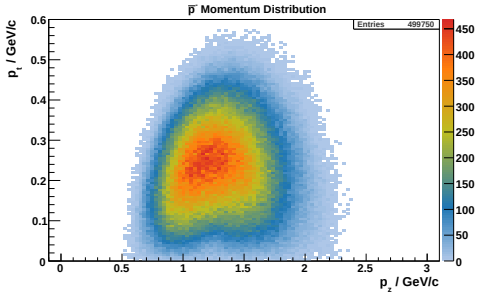

(c) Momentum distribution of the $\overline{\mathbf{p}}$, daughter of the $\overline{\Lambda}$.

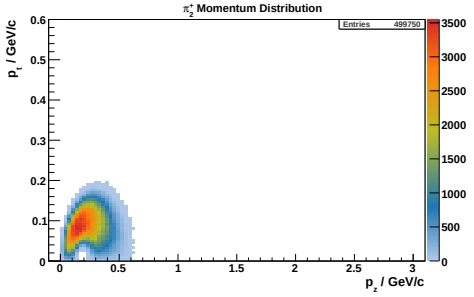

(d) Momentum distribution of the π_2^+, daughter of the $\overline{\Lambda}$.

Figure 7.8: The momentum distributions of the daughter particles in the $\overline{\Xi}^+$ branch. The transverse momenta p_t are plotted versus the longitudinal momenta p_z

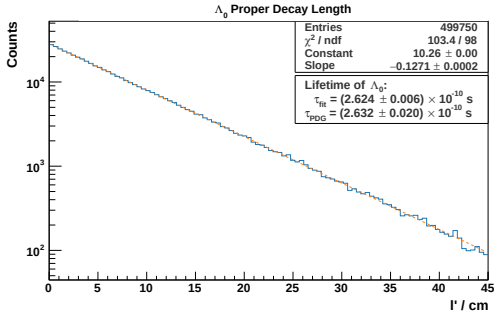

(a) Proper decay length distribution for Λ.

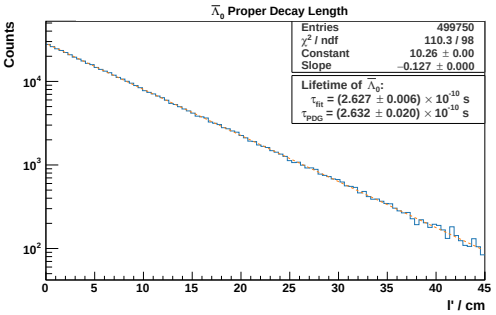

(b) Proper decay length distribution for $\overline{\Lambda}$.

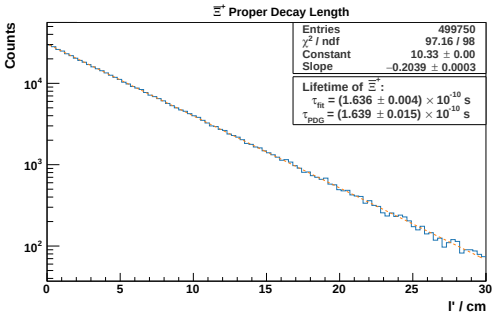

(c) Proper decay length distribution for $\overline{\Xi}^+$.

Figure 7.9: Proper decay length ($c\tau$) distributions for the three baryons $\overline{\Xi}^+$, Λ, and $\overline{\Lambda}$. All distributions are displayed with a logarithmic y-axis and an exponential fit applied to them (orange dashed line). From this, the lifetime of the particles is calculated and given in the boxes, together with the reference from [1].

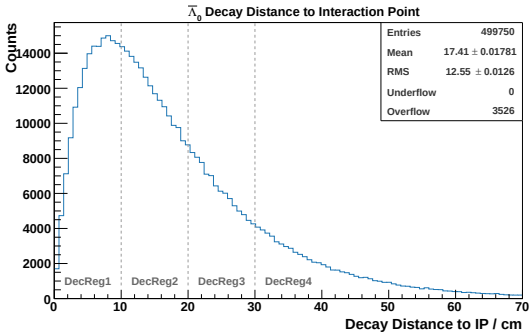

(a) Distance distribution of the $\overline{\Lambda}$ decay position to the IP.

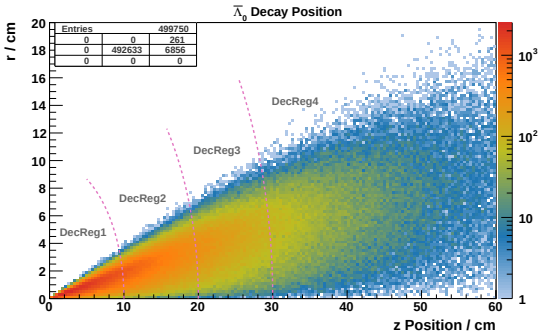

(b) Decay position distribution of the $\overline{\Lambda}$.

Figure 7.10: Distribution of the decay vertex positions of the $\overline{\Lambda}$, as the distance to the IP and the position in $r = \sqrt{x^2 + y^2}$ vs. z. Also marked are four different regions with separations at 10 cm, 20 cm, and 30 cm from the IP for later detector response studies.

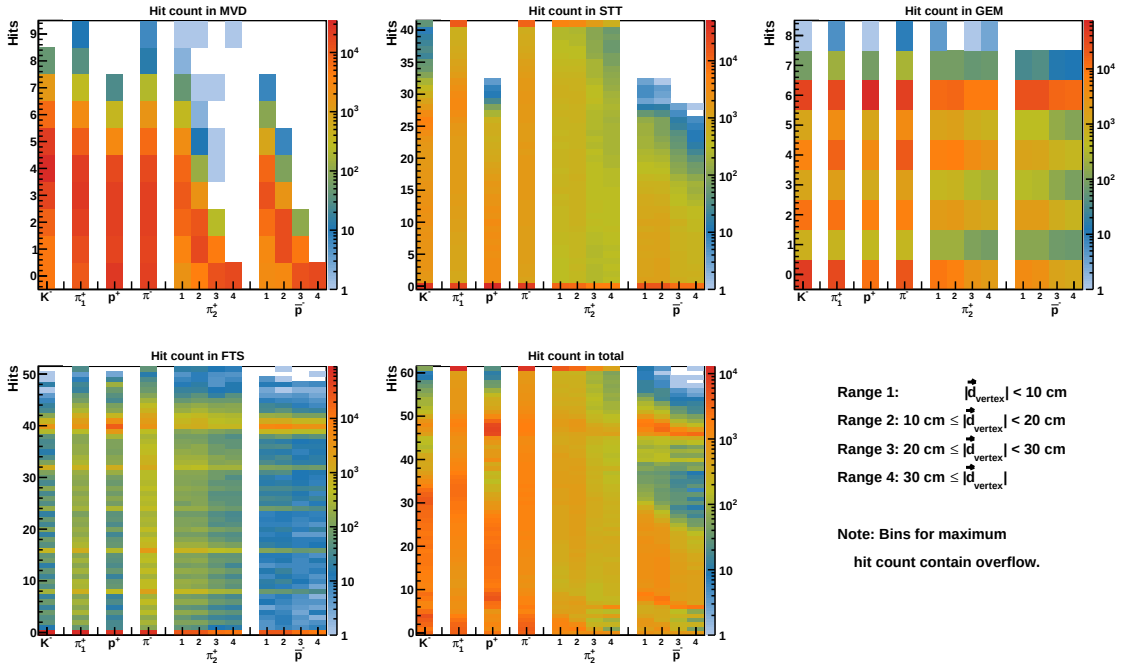

Figure 7.11: The hit multiplicity distributions in the four tracking detectors (MVD, STT, GEM, and FTS) per particle on the y-axis. The different daughter particles are specified on the x-axis. For the daughter particles in the $\overline{\Xi}^+$ chain (π_2^+, $\overline{\mathrm{p}}$) the hit multiplicity is shown separately for the different decay regions 1 to 4 as described in Section 7.2.4.

7.3 Detector Response

The next step in the simulation procedure is the propagation of all final state particles through the sub-detectors. In the following, the detector response to the simulated channel is investigated.

7.3.1 Hit Count Studies

The basis of the reconstruction are the generated detector hits. In Figure 7.11, a comprehensive overview of the number of generated hits for all four tracking systems and their sum is shown. The detector overviews are split up for the final state particles and in case of the $\overline{\Lambda}$ daughters (π_2^+ and $\overline{\mathrm{p}}$) also for the decay vertex region of the $\overline{\Lambda}$ as defined in Section 7.2.4. Especially for the π_2^+ and $\overline{\mathrm{p}}$ the impact of the displaced vertex is clearly visible in the hit counts of the MVD which drops towards decay positions of the $\overline{\Lambda}$ further away from the IP. 26 % of the $\overline{\Lambda}$ baryons decay after the last MVD disc. Consequently, their daughter particles will not deliver any tracking information in the MVD.

Due to the forward boost of the system, the GEM stations play a significant role in providing position information. If they are hit, they most probably produce 6 hit points. For tracking of the proton and antiproton, the STT plays a less important role since they are dominantly distributed at shallow polar angles. Consequently, the FTS shows a pronounced response with a peak at 40 hits per track for those particles.

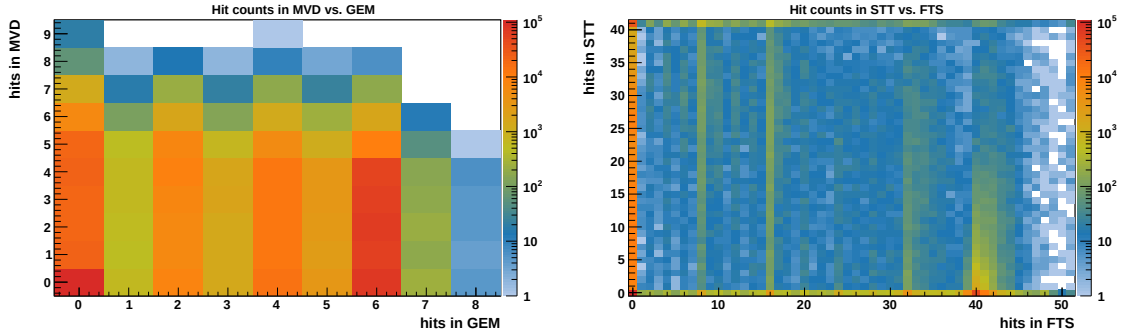

(a) MVD and GEM.

(b) STT and FTS.

Figure 7.12: Correlation of the number of hits in the central and forward oriented detectors, both with logarithmic color scale. The topmost and rightmost line of bins contains the overflow in that direction.

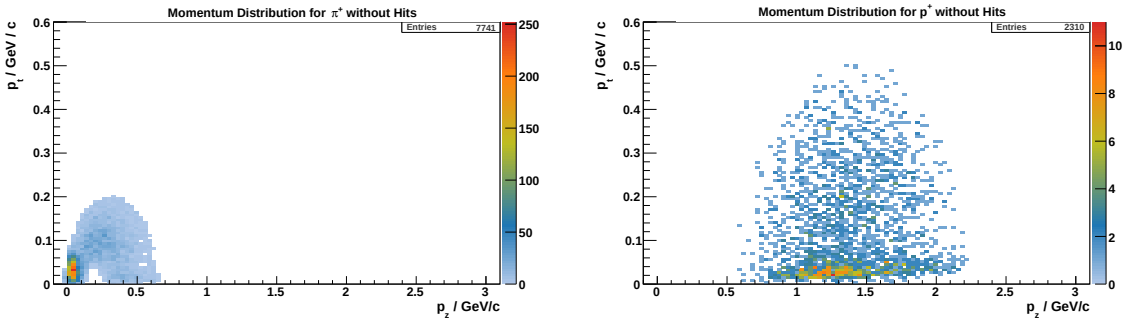

(a) Momentum distribution of tracks that generate no hits from π^+.

(b) Momentum distribution of tracks that generate no hits from **p**.

Figure 7.13: The transverse versus longitudinal momentum distributions for tracks that generate no hits in any tracking detector.

The relation between the central and forward oriented tracking detectors is shown in Figure 7.12. Also here, the importance of the GEM stations is visible: regardless of how many hits in the MVD, 6 hits in the GEM are most probable. Comparing the STT and FTS detectors reveals a more distinct separation of tracks: either a track leaves many hits in the STT or in the FTS but seldom in both. This matches the expected behavior due to the geometrical design of these two detectors, which is complementary in the polar angle.

For a successful reconstruction, the particles need to leave hit points in the tracking detectors. In Figure 7.13, the momentum distributions of protons and π^+ that did not generate any detector hits are shown. For π^+, the distribution shows a peak at $\mathcal{O}\left(10\,\mathrm{MeV}/c\right)$ while the protons at very shallow angles are suppressed. Around these maxima, only a few particles leave no hits with a homogeneous momentum distribution in the allowed phase space. The π^- distribution is comparable to the π^+ one and antiproton and K^- distributions also show a higher probability for no hits at low transverse momenta. They are shown in Figure A.5.

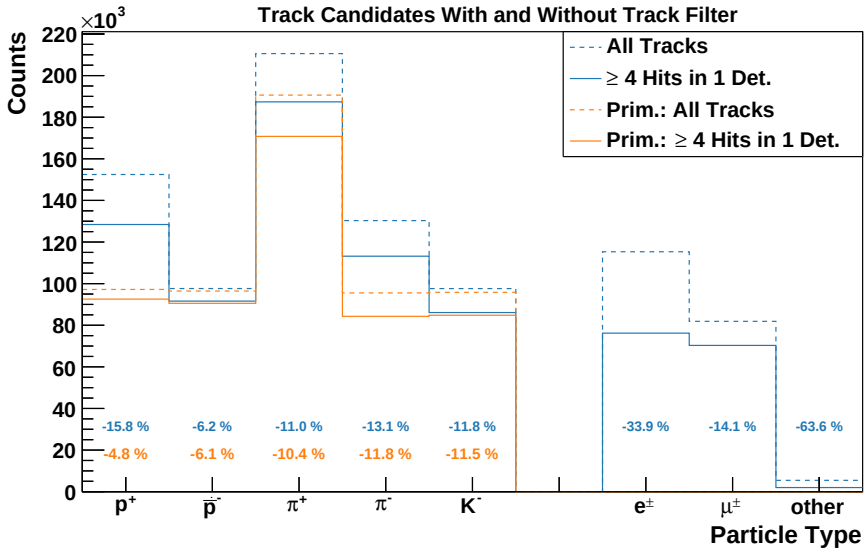

Figure 7.14: Effect of the applied track filter that only accepts tracks with at least 4 hits in any of the tracking detectors. Shown are the number of track candidates for all (blue) and only primary particles (orange), grouped by their particle species. The dashed lines represent all track candidates, i.e. with at least 1 hit, and the solid line the tracks with at least 4 hits.

7.3.2 Track Filtering

To group detector hits into track candidates, an ideal track finder is used because a realistic track finding algorithm for particles produced far from the IP is still incomplete in PandaRoot. The ideal track finder creates track candidates even from tracks which only leave one hit point in the detector. These tracks will not be reconstructible in the experiment. Therefore, a track filter is used with the requirement that a track leaves at least four hit points in a single sub-detector.

The chosen lower limit to find tracks is motivated by the trajectories of charged particles in a solenoidal magnetic field. In first approximation, neglecting energy loss and multiple scattering, the trajectories are helices. They form circles in a projection onto the the x-y plane, which need at least three space points to be defined. Combining all three hit combinations into track candidates would create an enormous number of wrong combinations. Therefore, at least one additional hit is needed to suppress false combinations. This is assumed to be a lower limit as realistic algorithms will likely require more hits.

Applying this criterion on the track candidates leaves a set of tracks which reasonably may be found by a realistic pattern recognition algorithm. The effect of the filter for different particle species is shown in Figure 7.14, both for primary particles generated by the event generator (orange) and all particles including those created from the propagation step (blue). Since this is applied to track candidates, particles leaving no hits at all are excluded from this. The amount of rejected tracks is $\mathcal{O}(5\,\%)$ for protons and antiproton, and $\mathcal{O}(10\,\%)$ for the K^- and $\pi^\pm$ mesons.

The filter effect study is done only on a subset of 99,250 generated events. Among these, 891,247 track candidates are found, 575,641 (64.6 %) of them produced by primary particles.

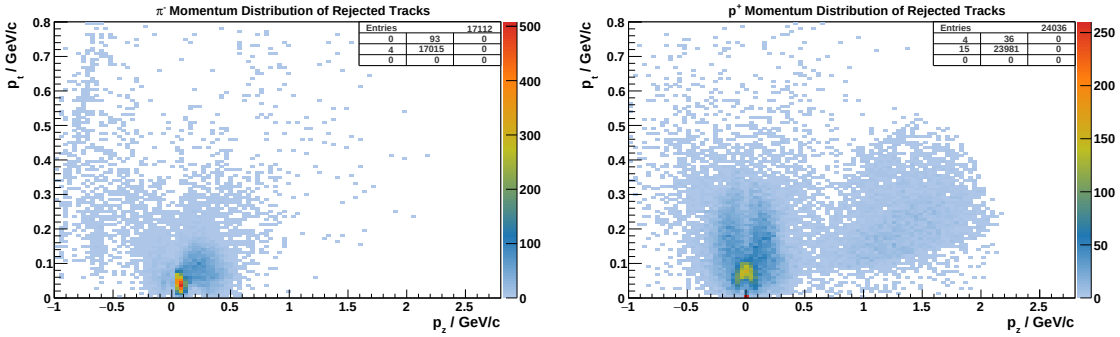

(a) Rejected tracks from π^-.

(b) Rejected tracks from **p**.

Figure 7.15: The momentum distributions of rejected tracks from π^- **(a)** and protons **(b)**, each leaving less than 4 but at least 1 hit in any tracking detector. The distribution of the rejected protons shows a maximum at $(0, 0)$.

From these candidates, 136,084 (15.3 %) and 52,666 (9.1 %) are rejected for all and primary particles, respectively. The momentum distributions for rejected π^- and protons are shown as an example in Figure 7.15, while the momentum distributions of other rejected particle are collected in Figure A.6. For the π^-, the majority of rejected tracks has a momentum of less than 100 MeV/c, both in the transverse and the longitudinal direction. Also low momentum protons are the most likely candidates to not leave enough hit points for the filter. Furthermore, different behaviors can be observed between secondary protons generated from material interaction (below $p_z \approx 0.5\,\mathrm{GeV}/c$) and primary protons (above $p_z \approx 0.5\,\mathrm{GeV}/c$).

All track candidates passing the selection are then used for further tracking. Here, a Kalman filter, included in the GENFIT package, follows a track pre-fit and propagates the particle from hit to hit. The pre-fit in a realistic scenario would originate from the track finding algorithm with an intrinsic uncertainty. For the used ideal tracking, a Gaussian smearing of vertices and momenta is applied with values of 0.5 mm and 5 %, respectively. The Kalman filter also calculates the error on the track based on the hit uncertainties, which is important for the fitting algorithms that is applied in the following analysis.

7.4 Event Analysis

After simulating the detector response, particle identification algorithms are applied to the reconstructed tracks, grouping the particles into lists of common type. Again, ideal particle identification is used to be independent from the current development of realistic algorithms. The following analysis is based on the particle candidates in these lists and proceeds step-wise backward along the decay tree (Figure 7.1) towards the initial $\overline{\Xi}^+\Xi^-(1690)$ system.

7.4.1 Final State Particle Reconstruction

At the first stage, final state particles which are measured and identified by the detector are reconstructed. Based on the particle identification, five particle candidate lists are generated, containing protons, antiprotons, π^+, π^-, and K^- mesons.

Table 7.5: Summary of reconstruction efficiencies and momentum resolutions for the particles in the final state. The resolution values are the σs from Gaussian fits to the corresponding distributions.

Mother Particles		Final State	N / %	$\frac{\sigma_p}{p}$ / %
$\Xi^-(1690)$	Λ	π^-	67.1	1.43
		p	90.7	1.49
		K^-	83.6	1.66
$\overline{\Xi}^+$	$\overline{\Lambda}$	π_2^+	64.6	1.44
		$\overline{p}$	85.4	1.47
		π_1^+	68.1	1.35

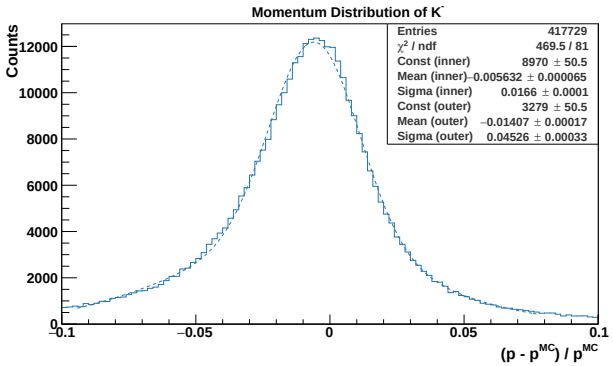

Figure 7.16: The relative momentum distribution for the $\mathbf{K^-}$ with a double-Gaussian fit.

The reconstruction efficiency for all final state particles is summarized in Table 7.5. p, $\overline{p}$, and K^- are found with efficiencies between 83 % and 91 %. Reconstructing the $\pi^\pm$ is more challenging and only 64 % to 68 % can be found because of their low momenta. This can also be seen in the rejection plots in Figure 7.13(a) and Figure 7.15(a) in Section 7.3 that peak at very low momenta. Combining the reconstruction efficiencies of the final state particles for the two main branches yields probabilities of 50.8 % and 37.5 % to find all particles required to reconstruct the Ξ^{-*} and $\overline{\Xi}^+$, respectively. Even though the $\overline{\Xi}^+$ branch has two displayed vertices, the lower reconstruction efficiency is dominated by the two low momentum π^+ in the branch. In total, an overall probability to find all six final state particles in one event is 19.1 %.

To obtain a relative momentum resolution, the difference of the reconstructed to the simulator input (MC truth) is determined according to

$$\frac{\Delta p}{p} = \frac{p - p^{\mathrm{MC}}}{p^{\mathrm{MC}}}$$

and then collected in a histogram. The resulting distribution is shown for the K^- as an example in Figure 7.16 while the others are collected in Figure A.7. Double-Gaussian fits are then applied to the distributions and the σ from the inner Gaussian is taken as the relative momentum resolution. The resolutions are around 1.4 % with the K^- as the worst ($\sigma_p/p = 1.66\,\%$) and

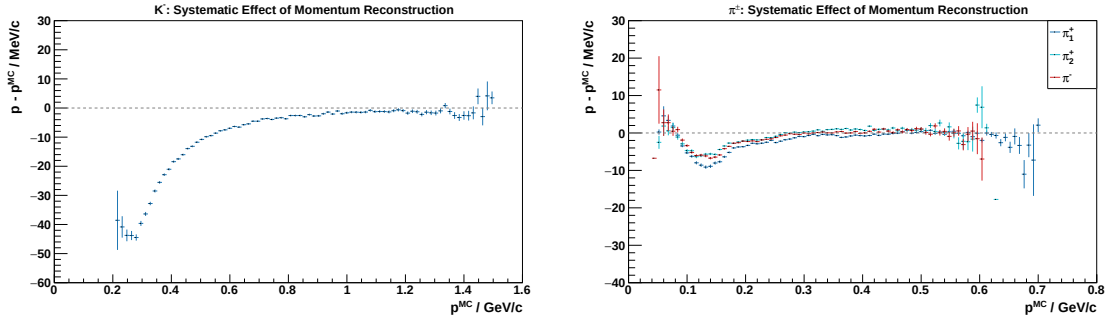

(a) Distribution for the K^-.

(b) Distributions for the $\pi^\pm$.

Figure 7.17: The systematic effect of the momentum reconstruction of final state particles K^-, π^-, π_1^+, and π_2^+ as a function of their momentum. The distributions are displayed as profile plots, where each point represents the vertical mean of this column.

the π_1^+ as the best ($\sigma_p/p = 1.35\,\%$). The values for all final state particles are collected in Table 7.5.

A feature already visible in the relative momentum distribution histogram is a shift to lower momenta with a mean of $-0.5\,\%$. This effect gets more apparent if the momentum difference is plotted as a function of the absolute momentum. It is done with a profile plot that reduces a two-dimensional histogram to show only the mean of each column instead of the full matrix. In Figure 7.17(a), a drop towards low momenta can be seen where the reconstructed momentum is significantly lower than the input. A likely explanation for this phenomenon is the passage of the particle through matter and its correction in the Kalman filter of the GENFIT package. The Kalman assumes the particle to be a pion in order to reconstruct the track, since it is applied before the information from particle identification is available. For low-energy kaons, the difference to a pion in terms of energy deposit is largest due to their higher mass[3], hence the Kalman underestimates these effects. In Figure 7.17(b), the same plot is displayed for the pions (π^-, π_1^+, and π_2^+) which have a much better matching. The profile plots for protons and antiprotons is in Figure A.8 and shows a distribution similar to that of the kaons.

7.4.2 Reconstruction of Λ and $\overline{\Lambda}$

7.4.2.1 Particle Combination

The procedure to obtain Λ and $\overline{\Lambda}$ candidates is essentially identical. First, the corresponding daughter candidates (π^- and p for Λ; π^+ and $\overline{p}$ for $\overline{\Lambda}$) are combined to $\Lambda/\overline{\Lambda}$ candidates (refer to the decay overview in Figure 7.1). The combination is only done for daughter particles that combine to an invariant mass of $< 50\,\mathrm{MeV}/c^2$ around the nominal Λ mass. Candidates lying outside of this window are discarded. This mass window already removes the most unreasonable combinations, for instance from protons generated in secondary interactions. As a result, the Λ multiplicity is most probable for one candidate per event, which can be seen in

[3]The energy loss is inversely proportional to the particle's velocity squared as shown in Figure 4.28. Therefore, for two particles with the same momentum the more massive one deposits more energy.

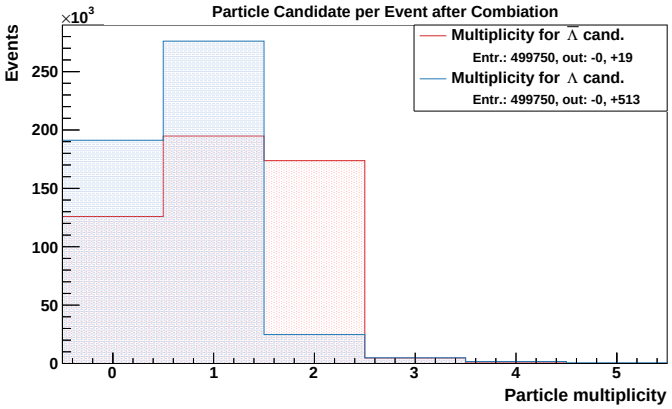

Figure 7.18: The multiplicity distribution of Λ (blue) and $\overline{\Lambda}$ (red) candidates from combining all p and π^- candidates and $\overline{p}$ and π^+ candidates, respectively.

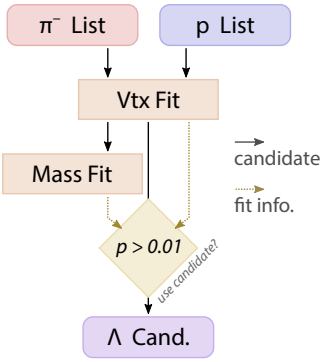

Figure 7.19: The scheme to filter the best Λ candidates and sort out the most unreasonable ones. This is done for $\overline{\Lambda}$ using the corresponding $\overline{p}$ and π^+ lists.

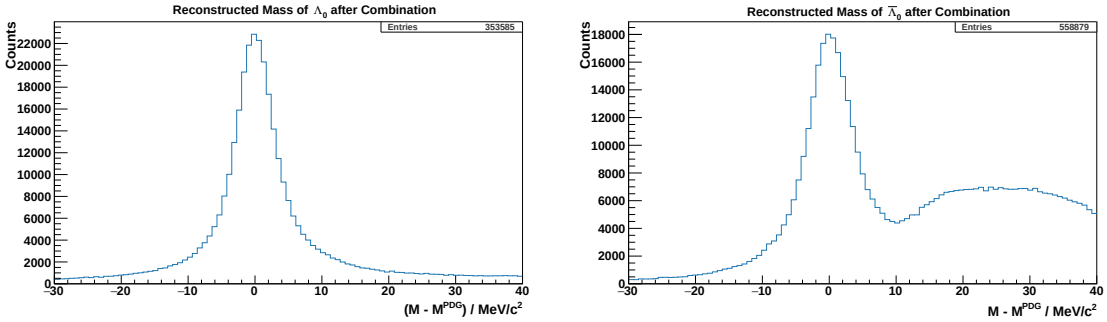

(a) Invariant mass distribution for Λ.

(b) Invariant mass distribution for $\overline{\Lambda}$.

Figure 7.20: The invariant mass distributions of the Λ and $\overline{\Lambda}$ candidates as differences to the nominal value of $M^{\mathrm{PDG}}(\Lambda/\overline{\Lambda}) = 1115.7\,\mathrm{MeV}/c^2$ [1]. All candidates are shown without further selection. The excess at high $M - M^{\mathrm{PDG}}$ for the $\overline{\Lambda}$ distribution arises from wrong daughter particle combinations.

Figure 7.18. However, the $\overline{\Lambda}$ is often found twice per event because two π^+ are in the final state but only one comes from the $\overline{\Lambda}$ decay.

The effect of wrongly combined final state particles can also be seen in the Λ and $\overline{\Lambda}$ invariant mass distributions in Figure 7.20. The invariant mass distributions are displayed as differences of the reconstructed to the nominal mass: $M - M^{\mathrm{PDG}}$. While the Λ mass difference distribution shows the expected peak around zero, the $\overline{\Lambda}$ distribution has an excess besides the main peak towards higher masses. Wrong combinations with the π^+ originating from the $\overline{\Xi}^+$ decay explains this asymmetry, because these pions have slightly higher momenta (see Figure 7.8).

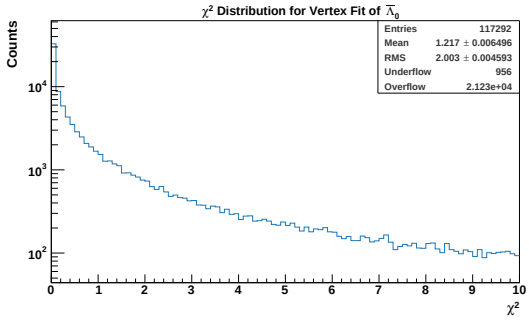

(a) Vertex fit, χ^2 distribution.

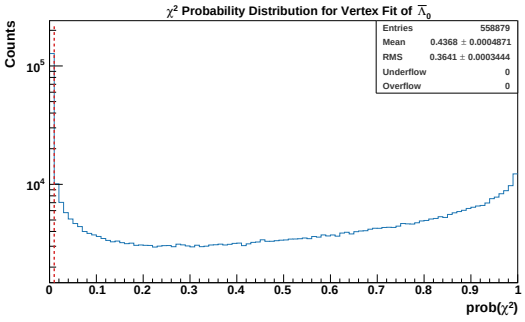

(b) Vertex fit, probability distribution.

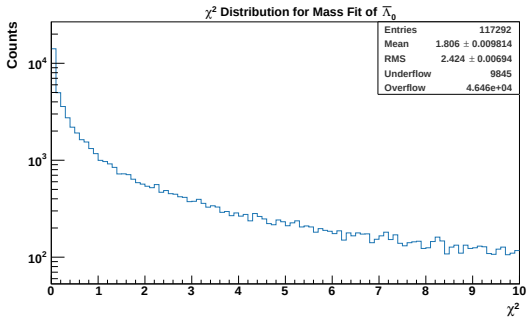

(c) Mass fit, χ^2 distribution.

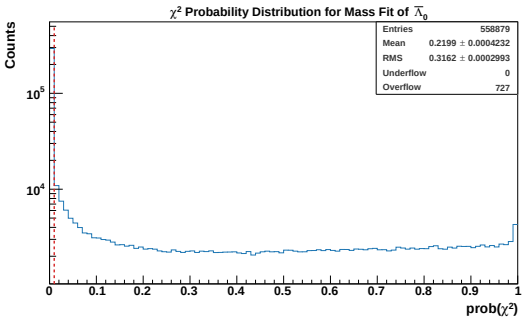

(d) Mass fit, probability distribution.

Figure 7.21: The vertex (top) and mass (bottom) fit qualities for $\overline{\Lambda}$ candidates, shown as χ^2 and prob(χ^2) distributions, all displayed with a logarithmic y-axis. Only candidates with a probability > 0.01 are considered.

7.4.2.2 Vertex and Mass Constraint Fitting

With the following steps, the best candidates are selected. The decision, which is graphically outlined in Figure 7.19, is based on two kinematic fitters: a vertex fit and a mass constraint fit. In case of the vertex fit, the requirement is that the two daughter particles have to come from a common origin, i.e. the Λ or $\overline{\Lambda}$ particles' decay vertex. To achieve this, the fitter varies the daughter's tracks but keeps their deviations from the original hits to a minimum, using the inverse hit uncertainties as weights. The fit class `PndKinVtxFit` of the PandaRoot framework is used for the vertex fitting.

The resulting quality of the fits for $\overline{\Lambda}$ candidates is depicted in the upper half of Figure 7.21. The χ^2 distribution in Figure 7.21(a) shows a high peak close to zero and falls off to higher χ^2 values. An even more pronounced peak at zero is visible for the probability distribution prob(χ^2) in Figure 7.21(b), which represents entries with very unlikely fit results. Consequently, a cut is applied here to leave out probabilities with prob(χ^2) ≤ 0.01. Otherwise this distribution is expected to be rather flat, but a rise towards values of prob(χ^2) $= 1$ is visible. A possible explanation is the overestimation of hit uncertainties in the detector descriptions.

A mass constraint fit is then applied to all candidates remaining after the vertex fit. The algorithm used (`PndKinFitter` of PandaRoot) adjusts the four-vectors of the daughter candidates

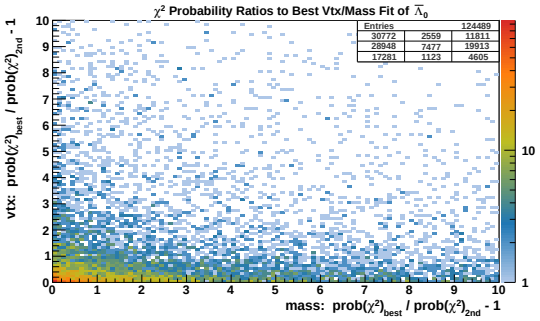

Figure 7.22: $\overline{\Lambda}$: The ratios of the best to the second best probability for both vertex (y-axis) and mass constraint (x-axis) fits. Second best probabilities of $<1\times10^{-10}$ are fixed to a ratio of $R=-1$, hence they are displayed in the underflows of the histogram.

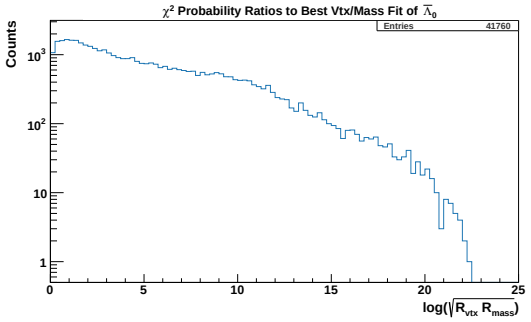

Figure 7.23: $\overline{\Lambda}$: The distribution of the geometric mean values of the probability ratios from both fits. The closer the value is to 0, the more equal the first and second best candidates are.

to match the invariant mass of the combined candidate with a given mass. Also for this fit, the quality is shown in Figure 7.21 with the χ^2 distribution in Figure 7.21(c) and the probability distribution in Figure 7.21(d). Both distributions show similarities to the vertex fit results but the probability distribution is flatter for higher probabilities. The same requirement that $\text{prob}(\chi^2) > 0.01$ is applied. The corresponding distributions for the Λ can be found in Figure A.9.

For both particles, the best candidate is defined as the one with the lowest χ^2 values under the condition it has a probability of $\text{prob}(\chi^2) > 0.01$. The candidate used for the further reconstruction contains the vertex and momentum vectors after the vertex fit. After applying these cuts, 194,907 $\overline{\Lambda}$ and 224,435 Λ candidates remain. 9.4 % of the $\overline{\Lambda}$ candidates and 1.9 % of the Λ candidates cannot be matched to the simulation input (MC truth).

In case two or more candidates pass the probability selection, an additional quality criterion is investigated that shows the similarity between the two best candidates. The motivation is to ensure that the selected candidate is not mistakenly originating from a wrong combination. The ratio of the second best to best is calculated by

$$R = \frac{\text{prob}(\chi^2)_{\text{best}}}{\text{prob}(\chi^2)_{\text{2nd}}} - 1$$

for both the vertex and mass fit probabilities. The closer the ratio is to 0, the more similar are the two candidates' fit probabilities. Thus, bigger values show a better separation from the first to the second best candidate. The ratios for the $\overline{\Lambda}$ candidates are displayed in a two-dimensional histogram in Figure 7.22. Often, the second best probability becomes very low so that the division can cause problems due to the limited floating-point accuracy in the program[4]. Therefore, probabilities $<1\times10^{-10}$ are manually set to -1. Candidates where this happens are represented in the underflow bins of the histogram.

[4]For a division, both exponents are set to the same value. If one value is too small, the significand of the floating-point number will round to 0. This leads to a division by 0, hence a result of NaN and problems when filling this into the histogram.

From a total of 373,862 events with a $\overline{\Lambda}$ candidate, 124,489 (33.3 %) have two candidates that satisfy both fit probability selection criteria. Most of them lie in the underflow of the histogram, i.e. have a big distance between first and second best probability. For those candidates, where a ratio could be calculated, a peak can be seen at $(0,0)$. However, it only contains 18 entries. The abundance of ratios close to $(0,0)$ drops quickly so that only 3882 or 3.1 % of the candidates with two $\overline{\Lambda}$ candidates have $\sqrt{R_{\text{vtx}} \cdot R_{\text{mass}}} < 1$. In other words, for 96.9 % of the $\overline{\Lambda}$ candidates with a two-fold multiplicity the probability of the second best fit is smaller than half of the best candidate's probability.

Since there is a much lower probability to have more than one Λ candidate per event, a probability ratio can be determined only for 19,578 events. Here, 1314 or 6.7 % of the ratios have a distance of less than 1 from $(0,0)$. The corresponding plots are given in Figures A.10 and A.11. For both Λ and $\overline{\Lambda}$ candidates, no significant structures indicating a separation to false selections are visible. Therefore, no further selection is done here.

7.4.2.3 Point of Closest Approach Method

Alternatively, the decay vertex position can be determined by the point of closest approach (POCA) method. Here, the daughter particles' track information is used to parameterize helices[5]. The algorithm `PndVtxPoca` then determines the closest distance of the two helices and uses the midpoint of this distance as the POCA (see Figure 7.24). Ideally, this is the vertex where the daughter particles are originating from but due to reconstruction inaccuracies the tracks always have a gap between them. The closest distance is also referred to as pocaQA since it indicates the quality of the extrapolation. This pocaQA is displayed in Figure 7.25(a) for Λ and $\overline{\Lambda}$ candidates after vertex and mass constraint selection. The distance values peak at 0 cm and fall off rapidly for both candidates.

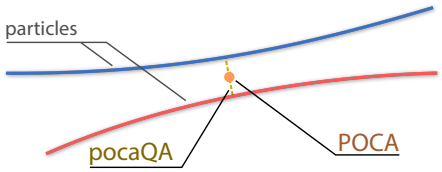

Figure 7.24: The POCA is the midpoint of the closest distance (pocaQA) between two particle tracks.

The distance distribution of the found POCA to the IP is shown in Figure 7.25(b). Here, the Λ candidate's distance decreases roughly exponentially, as expected, since it is produced at the IP. However, the $\overline{\Lambda}$ originates from the $\overline{\Xi}^+$, which has a decay length in the cm range, and therefore the distance distribution is biased towards higher values. The efficiency drops after the MVD's forward discs at 16 cm and 23 cm are visible as well.

7.4.2.4 Λ Reconstruction

From the 353,585 Λ candidates available from the combination of daughter particles, the selection with the vertex fit reduces this to 286,713. After the mass constraint fit, a total of 224,435 Λ baryons remain.

Decay Vertex Resolution The effect of the selection on the decay vertex resolution for x and z-direction is shown in Figure 7.26. In the y-direction, the behavior is comparable to x. The values are obtained by comparing them to the simulation input (MC truth). The vertex

[5] Assuming the solenoid field is homogeneous, charged particles will follow helix trajectories.

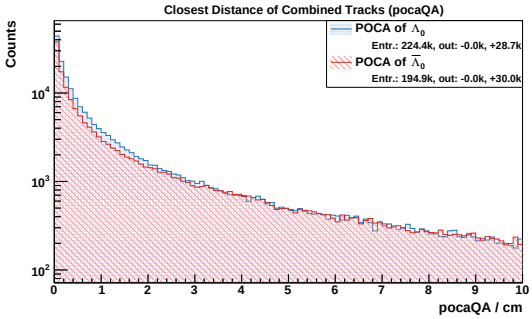

(a) Distance distributions of the closest approach (pocaQA).

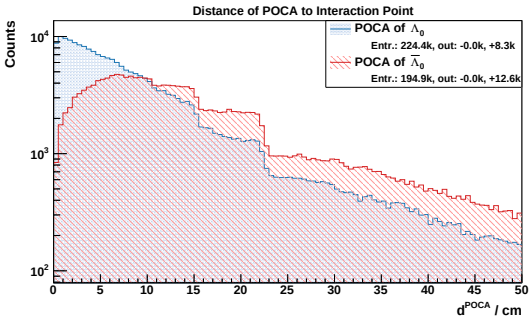

(b) Distance distributions of the POCA to the IP.

Figure 7.25: The result of calculating the POCA for Λ candidates in blue and $\overline{\Lambda}$ candidates in red. Only the best candidates after vertex and mass constraint fits are used.

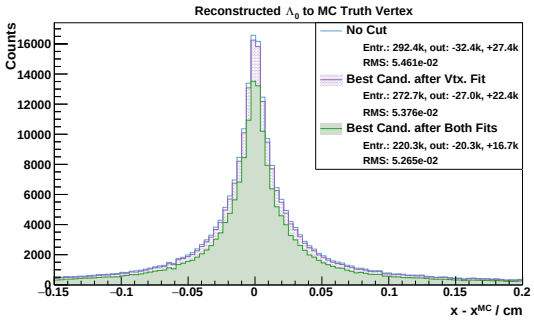

(a) x-vertex position difference distribution.

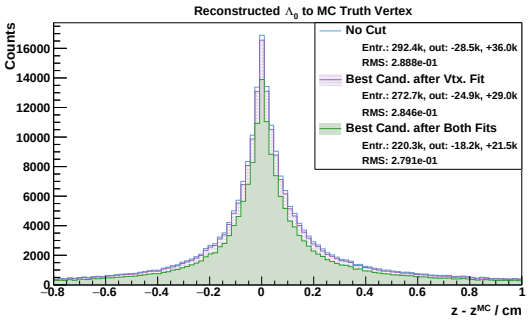

(b) z-vertex position difference distribution.

Figure 7.26: The vertex position difference distributions of the Λ candidates at the three mentioned steps: after combination (blue), best candidate after vertex fit (purple), and best candidate after vertex and mass fits (green). The difference between reconstructed position and MC truth is shown.

difference distributions peak around 0 and have a RMS of $\Delta x = 0.55\,\text{mm}$ in the transverse direction and $\Delta z = 2.9\,\text{mm}$ in the longitudinal direction after the combination. Applying the vertex and mass constraint fits does not change this value significantly; only a decrease of around 1 % to $\Delta x^{\text{best}} = 0.53\,\text{mm}$ and $\Delta z^{\text{best}} = 2.8\,\text{mm}$ RMS is achieved. In order to calculate the difference, a matching MC truth candidate has to be found.

Using the same method, the influence of the MVD on the vertex resolution can be investigated. In Figure 7.27, the difference of the reconstructed Λ decay vertex to the simulation input is shown, for all best candidates after the fits and with the condition that all daughter particles have at least one hit from the MVD in their tracks. One can see that an additional MVD hit suppresses the tails of the distributions and improves the RMS values from $\Delta x^{\text{best}} = 0.53\,\text{mm}$ to $\Delta x^{\text{MVD}} = 0.45\,\text{mm}$ and from $\Delta z^{\text{best}} = 2.8\,\text{mm}$ to $\Delta z^{\text{MVD}} = 2.4\,\text{mm}$.

Decay Vertex Position The Λ is produced directly in the decay of the short-living, excited Ξ^{-*} state, thus only its own decay time contributes to its decay position. This can be seen in Figure

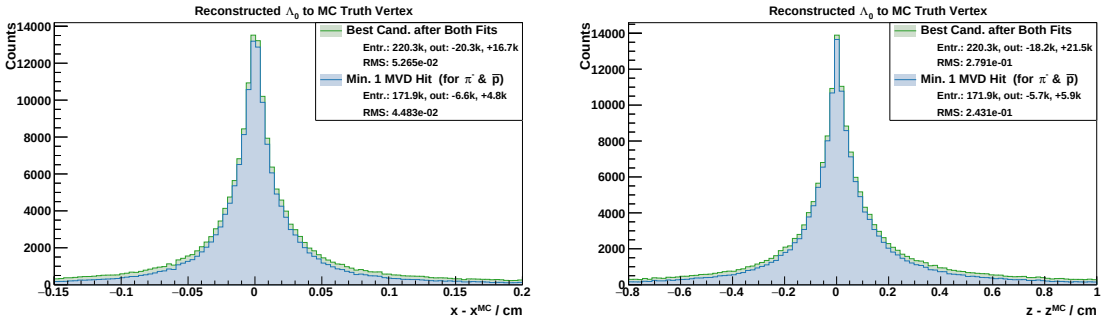

(a) x-vertex position difference distribution. **(b)** z-vertex position difference distribution.

Figure 7.27: The vertex position difference distributions of the **Λ** candidates for the best candidates after both fits (green) and requiring at least one MVD hit in all of the daughters tracks (blue).

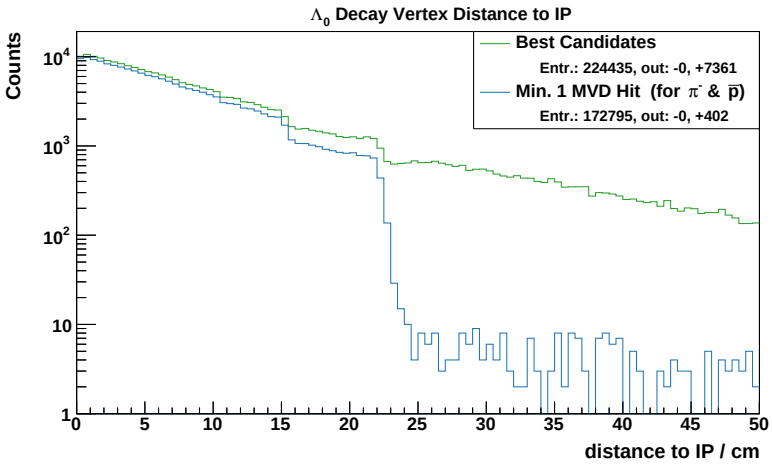

Figure 7.28: The distance distribution of the reconstructed vertex positions of the best **Λ** candidates to the IP. All best candidates are shown in green, in blue only those that have at least one hit provided by the MVD for both daughter candidate.

7.28, showing the distance of the reconstructed decay vertex position to the IP. Requiring the MVD in the reconstruction has two effects on this distribution: firstly, a relative constant decrease of the number of events over the distance and, secondly, a sharp drop between 22 cm and 23 cm, indicating the position of the last forward disk of the MVD.

Momentum Resolution The momentum resolution after the fits is shown in Figure 7.29, using the relative momentum difference

$$\frac{\Delta p}{p} = \frac{p - p^{\mathrm{MC}}}{p^{\mathrm{MC}}} \,.$$

Both directions, transverse and longitudinal, are given, each using the Λ candidate 4-vector after the vertex fit but using the selection based on both fits. The distributions both peak at 0 and fall off in a Gaussian-like shape. Thus, double-Gaussian fits are applied. The inner

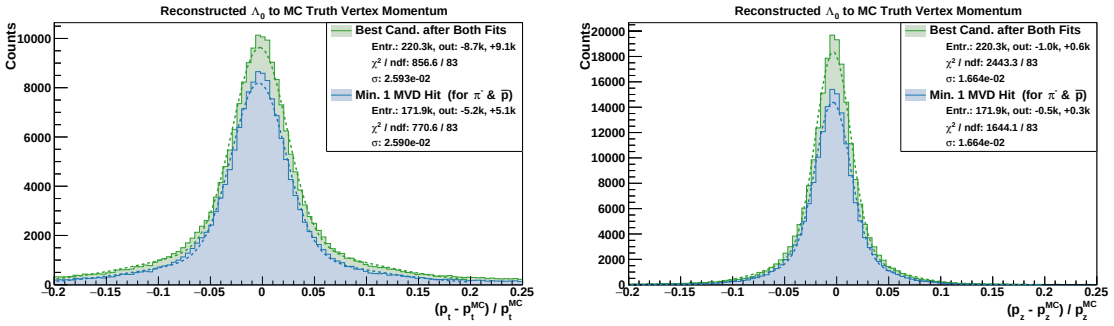

(a) Transverse momentum difference distribution. **(b)** Longitudinal momentum difference distribution.

Figure 7.29: The relative momentum difference distributions for the transverse (p_t) and the longitudinal (p_z) directions of the **Λ** candidates, comparing the effect of requiring at least one MVD hit for each daughter particle. Double-Gaussian fits are applied to all distributions, their inner σs are given in the histograms' legends.

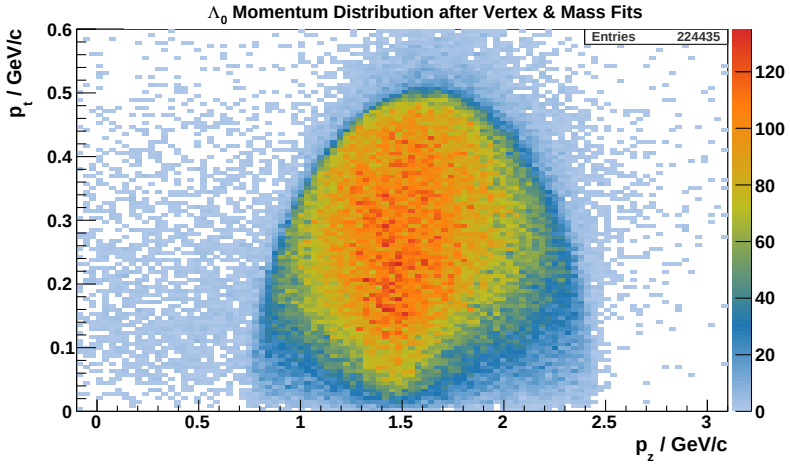

Figure 7.30: The transverse versus the longitudinal momentum distribution of the best **Λ** candidates after both fits.

Gauss parameters result in resolutions of $\sigma_{p_t}/p_t = 2.59\,\%$ and $\sigma_{p_z}/p_z = 1.66\,\%$. Additionally, the influence of the MVD is shown again with the second (blue) distribution. This time, the resolutions do not change and only the number of events is reduced by about 22 %.

In Figure 7.30, the reconstructed absolute values of the longitudinal and the transverse momentum are depicted. The distribution shows Λ candidates after the vertex fit but with the selection based on both vertex and mass fits. The Λ phase space distribution is clearly visible with only a few entries outside the main area. Comparing this reconstructed distribution with the generated distribution in Figure 7.7(a) demonstrates the agreement.

Invariant Mass Distribution Finally, the invariant mass distribution of the Λ candidates is depicted in Figure 7.31. The spectra are overlaid and show the candidates after the vertex fit without any cut (blue), with the vertex selection of requiring at least 1 % fit probability (green),

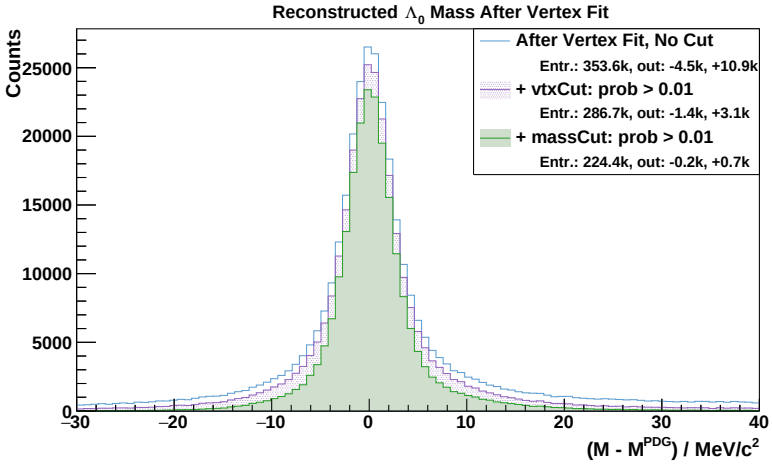

Figure 7.31: The invariant mass difference distributions of **Λ** candidates showing the effect of the vertex and mass constraint fitting. The blue line refers to all candidates after the fit, the purple one includes only those after the vertex cut, and the green distribution shows the additionally applied mass cut.

and with both vertex and mass cuts applied (pink). All distributions are based on the candidates after the vertex fit[6] and show the difference $M - M^{\mathrm{PDG}}$ between the reconstructed and the nominal mass of $M^{\mathrm{PDG}} = 1115.7\,\mathrm{MeV}/c^2$. The original spectrum has low tails, indicating a low contribution from wrong combinations. Applying both cuts significantly reduces the outliers which produces a cleaner invariant mass spectrum.

To obtain the mass resolution values for all distributions, double-Gaussian fits are applied and the inner one's σ is taken as the resolution. After the fit, the resolution is $\sigma_M = 2.72\,\mathrm{MeV}/c^2$ and improves to $\sigma_M = 2.37\,\mathrm{MeV}/c^2$ after both cuts are applied.

7.4.2.5 $\overline{\Lambda}$ Reconstruction

The same procedure as for Λ can be applied for the $\overline{\Lambda}$ which is produced by the $\overline{\Xi}^+$ decay. Initially, 373,862 events have at least one $\overline{\Lambda}$ candidate. Due to the observed multiplicity, this sums up to 558,879 $\overline{\Lambda}$ candidates, of which 324,337 pass the vertex fit. The additional requirement of the mass constraint fit probability to be larger than 1 % reduces the number of $\overline{\Lambda}$ candidates to 194,907.

Decay Vertex Resolution In Figure 7.32, the effect of the vertex fit on the $\overline{\Lambda}$ candidate is shown. Again, only the x coordinate is shown for the transverse direction as the y coordinate results in a similar distribution. The difference to the simulation input peaks at 0 and has only slight differences in the RMS values: from $\Delta x = 0.58\,\mathrm{mm}$ in the transverse direction and $\Delta z = 3.1\,\mathrm{mm}$ in the longitudinal direction after the fit the resolution improves to $\Delta x^{\mathrm{best}} = 0.55\,\mathrm{mm}$ and $\Delta z^{\mathrm{best}} = 2.9\,\mathrm{mm}$, respectively. In the overflow and underflow tails, the probability cut removes around 45 % to 50 % compared to an overall statistical reduction of 34 %.

[6] The mass fit constraints the mass to the nominal mass, thus a sharp peak is the result of taking these candidates as an input.

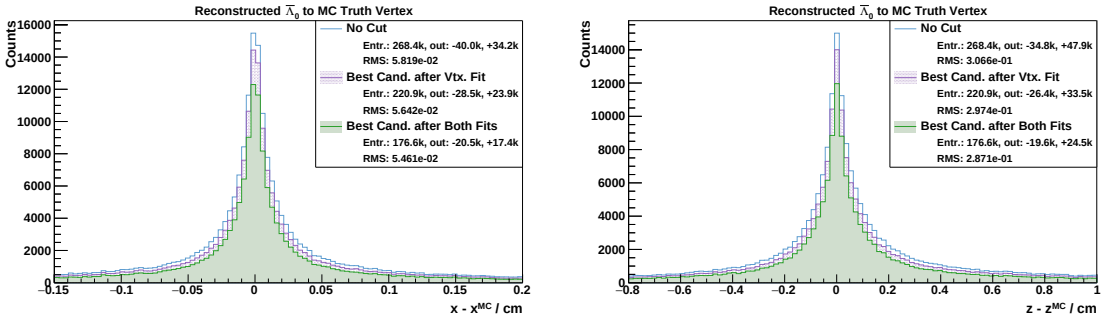

(a) x-vertex position difference distribution. **(b)** z-vertex position difference distribution.

Figure 7.32: The vertex position difference distributions of the $\overline{\Lambda}$ candidates at three steps: after combination (blue), best candidate after vertex fit (purple), and best candidate after vertex and mass fits (green). The difference between reconstructed position and MC truth is shown.

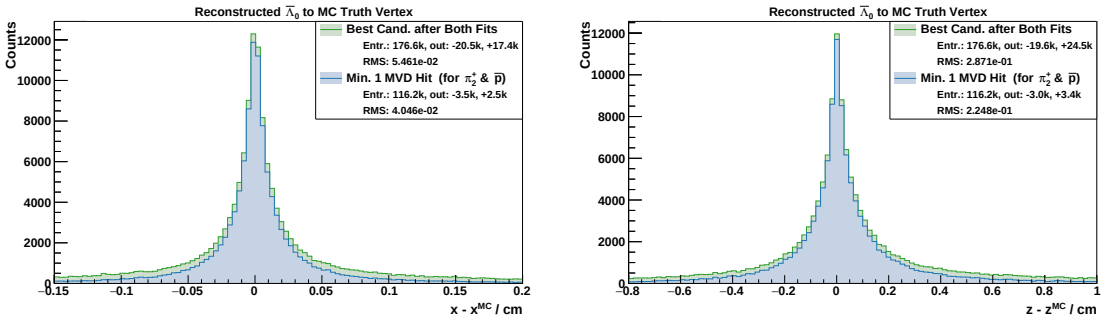

(a) x-vertex position difference distribution. **(b)** z-vertex position difference distribution.

Figure 7.33: The vertex position difference distributions of the $\overline{\Lambda}$ candidates. Shown for the best candidates after both fits (green) and after additionally requiring at least one MVD hit in all of the daughters tracks (blue).

The rejecting of entries in the tails is even more pronounced when including the MVD in the reconstruction, which can be seen in Figure 7.33. Requiring at least one hit point of the π_2^+ and $\overline{\mathrm{p}}$ daughters in the MVD improves the vertex position resolution to $\Delta x^{\mathrm{MVD}} = 0.40\,\mathrm{mm}$ in the transverse direction and $\Delta z^{\mathrm{MVD}} = 2.4\,\mathrm{mm}$ in the longitudinal direction. At the same time, this further reduces the statistics by 34 % rejected candidates.

Decay Vertex Position The reason for this reduction is visualized in Figure 7.34, showing the reconstructed vertex positions, once for all best candidates after both fits (Figure 7.34(a)) and once additionally requiring hit points from the MVD for the $\overline{\Lambda}$'s daughter particles. In the latter, a sharp drop after 23 cm can be seen, indicating the position of the last sensor disc of the MVD.

Momentum Resolution The relative momentum resolution is depicted in Figure 7.35 for all best candidates after the fits in green and the additional condition of MVD hits for all daughters in blue. In both cases, the distributions peak at 0 and have only a few outliers in the

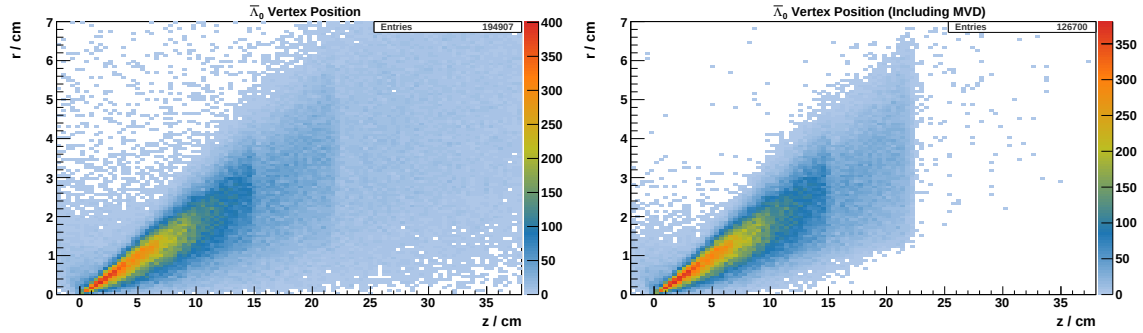

(a) Vertex position distribution for best candidates. **(b)** Vertex position distribution with MVD involvement.

Figure 7.34: The reconstructed vertex position distributions of the best $\overline{\Lambda}$ candidates in $r = \sqrt{x^2 + y^2}$ and z space. The right plot additionally requires at least one MVD hit for each daughter particle. The end of the MVD's range to the right is clearly visible.

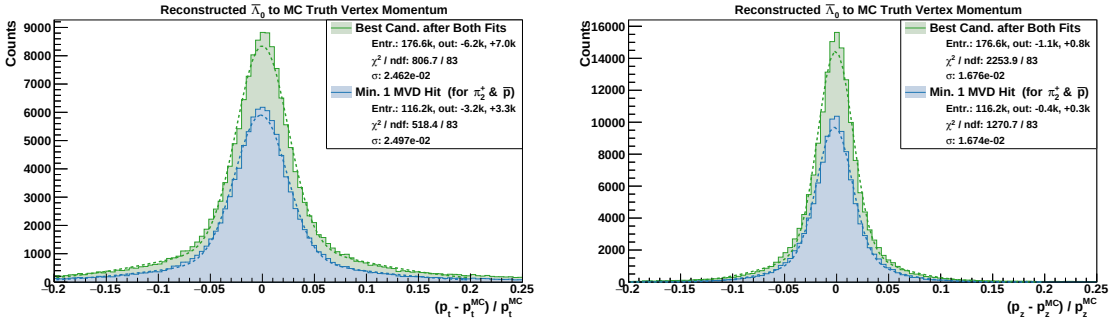

(a) Transverse momentum difference distribution. **(b)** Longitudinal momentum difference distribution.

Figure 7.35: The relative momentum difference distributions for the transverse (p_t) and longitudinal (p_z) directions of the $\overline{\Lambda}$ candidates, comparing the effect of requiring at least one MVD hit for each daughter particle.

overflow and underflow, especially for the longitudinal direction. The resolutions are extracted from double-Gaussian fits with $\sigma_{p_t}/p_t = 2.46\,\%$ and $\sigma_{p_z}/p_z = 1.68\,\%$ for the transverse and longitudinal directions, respectively. Including the MVD does not change these values appreciably, in the transverse direction it even worsens it a bit to $\sigma^{\mathrm{MVD}}_{p_t}/p_t = 2.50\,\%$. This can be explained considering the low particle momenta in the transverse direction which is affected more markedly by the material in the particles' path.

The reconstructed momentum distribution of the $\overline{\Lambda}$ can be seen in a two-dimensional display in Figure 7.36. It resembles the simulation's input (Figure 7.8) with transverse momentum values in the range of around 150 MeV/c and 450 MeV/c and a gap below 150 MeV/c. This is caused by the decay kinematics and is observed in event generator output. In the longitudinal direction, the most probable value lies at around 1.5 GeV/c.

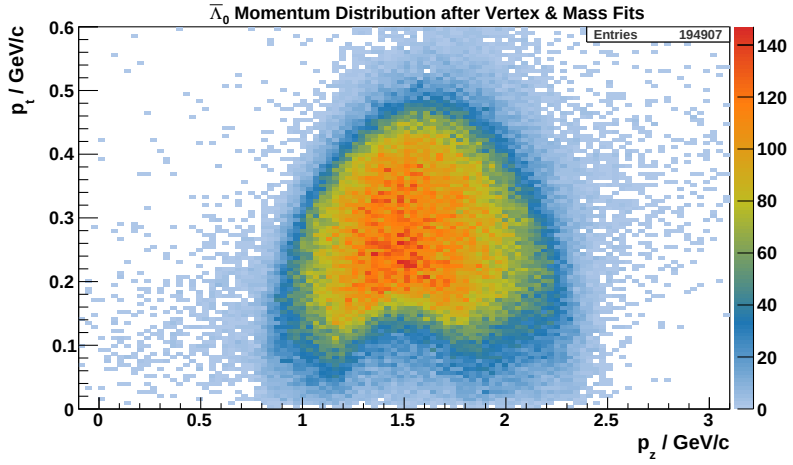

Figure 7.36: The transverse versus the longitudinal momentum distribution of the best $\overline{\Lambda}$ candidates after both fits.

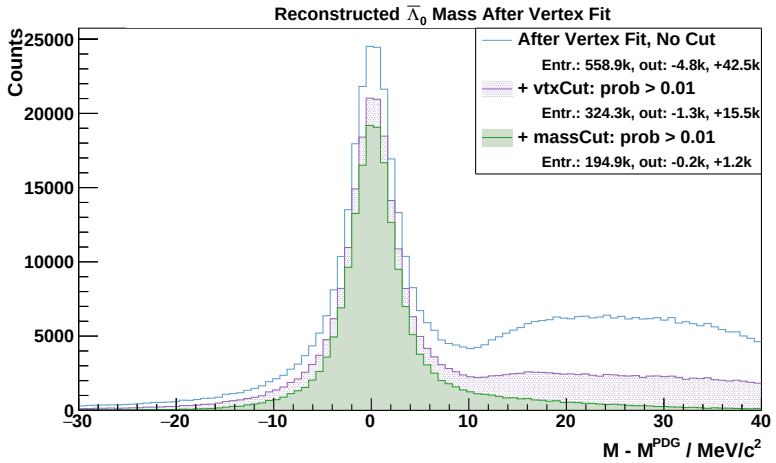

Figure 7.37: The invariant mass distributions of $\overline{\Lambda}$ candidates showing the effect of the vertex fitting. From the full spectrum after the fit (blue), many wrong combinatorial candidates are rejected by vertex (purple) and mass cuts (green), leaving a much cleaner sample.

Invariant Mass Distribution A clear excess from wrong combinations is visible in the initial invariant mass distribution (Figure 7.20(b)) which displays the differences between reconstructed and nominal $\overline{\Lambda}$ masses. Applying the vertex fit and mass constraint fit and selecting only the best candidates significantly suppresses the wrong combinations, as seen in Figure 7.37. It shows the distributions after the vertex fit without cuts as well as with the requirement of a minimum probability of 0.01 for vertex fit and both fits. Each time, the vertex fit's candidate is used for the mass value. From the inner part of double-Gaussian fits one can extract resolution values of $\sigma_M = 2.5\,\mathrm{MeV}/c^2$ before and $\sigma_M^{\mathrm{best}} = 2.4\,\mathrm{MeV}/c^2$ after the cuts. This shows, that the cuts do not modify the signal itself but mostly affect the tails.

Table 7.6: Reconstruction results of the Λ and $\overline{\Lambda}$ baryons in the different stages of analysis: after combination, after vertex fit with applied probability cut, additional mass cut, and with MVD involvement for all daughters. N is the ratio of events having a candidate with the matching criteria. All σ values are taken from the inner one of double-Gaussian fits.

	Λ				$\overline{\Lambda}$			
	N %	σ_{p_t}/p_t %	σ_{p_z}/p_z %	σ_M MeV/c^2	N %	σ_{p_t}/p_t %	σ_{p_z}/p_z %	σ_M MeV/c^2
Combination	61.7	3.44	1.78	3.14	74.8	4.09	1.82	3.26
Vertex Fit	57.4	2.61	1.77	2.60	64.9	2.52	1.81	2.56
Mass Fit	44.9	2.59	1.66	2.37	39.0	2.46	1.68	2.43
Include MVD	34.6	2.59	1.66	2.28	25.4	2.50	1.67	2.37

7.4.2.6 Λ and $\overline{\Lambda}$ Reconstruction Summary

An overview of the efficiencies and resolution results obtained for the $\overline{\Lambda}$ and Λ reconstruction is shown in Table 7.6. Combining both vertex and mass fit successfully reduces the amount of wrong combinations and thus increases momentum and mass resolutions. With the conservative cuts of prob(χ^2) > 0.01 the efficiency for Λ reconstruction is 44.9 % and 39.0 % for $\overline{\Lambda}$. The influence of the MVD on this reconstruction with delayed vertices is merely a slight increase in resolution, if any, but a good tool to reduce outliers in the distributions. However, it significantly reduces statistics, especially for the $\overline{\Lambda}$ by roughly a third.

7.4.3 Reconstruction of $\overline{\Xi}^+$

7.4.3.1 Particle Combination

A total of 124,554 $\overline{\Xi}^+$ candidates are combined out of the 194,907 $\overline{\Lambda}$ candidates that remain after vertex and mass constraint cuts (discussed in Section 7.4.2.5) and the π^+ candidates that have not been assigned to the $\overline{\Lambda}$. Similar to the Λ and $\overline{\Lambda}$ combinations, a mass window is set to eliminate unreasonable combinations. Its full width is 300 MeV/c^2. The combination yields mostly just one candidate per event. However, for 4607 events more than one $\overline{\Xi}^+$ candidate has been found, thus a selection needs to be done here as well.

7.4.3.2 Vertex Reconstruction

The chosen approach of kinematic fitting for the Λ reconstruction constraining the vertex and mass does not work for the $\overline{\Xi}^+$ because PandaRoot cannot fit vertices of neutral daughter particles at the moment. The Λ does not have a net charge, hence the algorithms abort immediately and return an error flag.

An alternative is the calculation of the closest approach of the two daughters' tracks, as explained in Section 7.4.2.3. The distribution of the closest distance, or pocaQA, of the daughter particles' track can be seen in Figure 7.38(a). From a peak close to a distance of 0 a rapid decrease follows. This is comparable with the pocaQA distribution obtained for the Λ candidates (Figure 7.25(a)). In case more than one $\overline{\Xi}^+$ candidate is found in one event, the

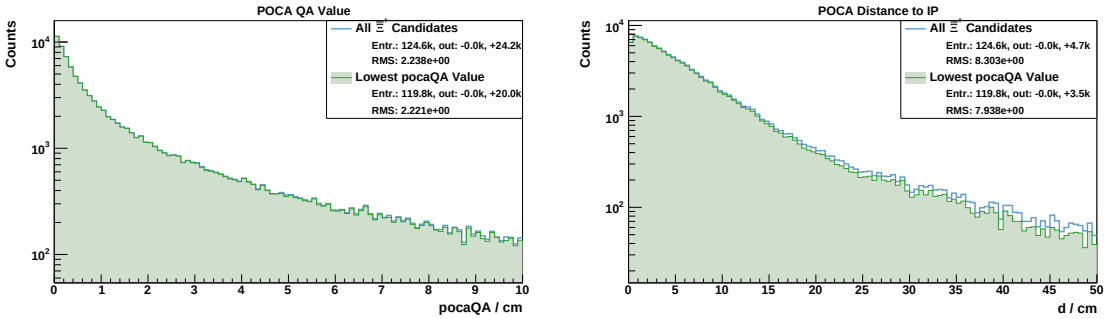

(a) Distance distributions of the closest approach (pocaQA).

(b) Distance distributions of the POCA to the IP.

Figure 7.38: $\overline{\Xi}^{+}$: The result of the point of closest approach (POCA) calculation. The closest distance between the two tracks (also referred to as pocaQA) is shown on the left and the distance of the POCA to $(0,0)$ on the right. The blue line represents all candidates and the green distribution shows only those with the smallest pocaQA in case more than one candidate is available per event.

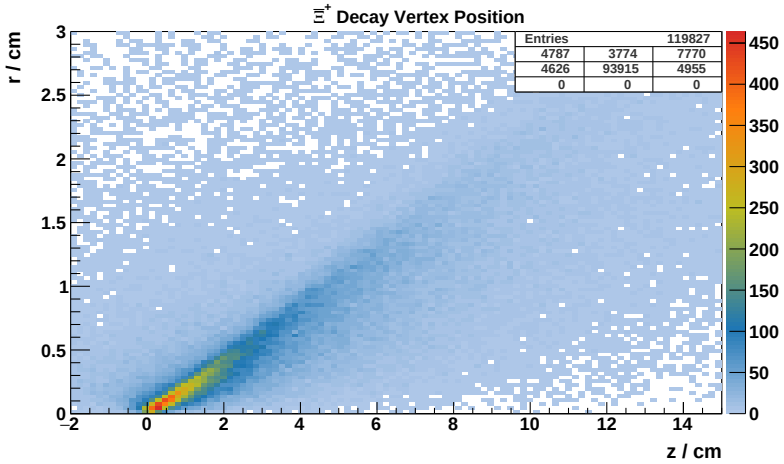

Figure 7.39: The position distribution of the POCA for the $\overline{\Xi}^{+}$ candidates' daughters in the r-z projection.

one with the smallest pocaQA value is taken for further analysis. Since not many events with multiplicities larger 1 are in the data sample, the effect is not very strong, as the two overlaid distributions in Figure 7.38 show. The blue one contains all candidates and the green one those with the applied pocaQA filter. In the case of the pocaQA distributions they are practically the same for the displayed range.

The location of the POCA is depicted as the distance to the interaction point in Figure 7.38(b). Since the POCA is a reconstruction of the $\overline{\Xi}^{+}$ baryon's decay vertex, an exponential decline from the IP is expected, which is true for the first $\approx 25\,\text{cm}$. Here, a slight effect on the minimum pocaQA condition is visible for larger distances. In a two-dimensional display of the decay vertex position, the distribution shows a narrow cone in the $r-z$ projection (Figure 7.39) but also a spread over the shown region with a few entries per bin.

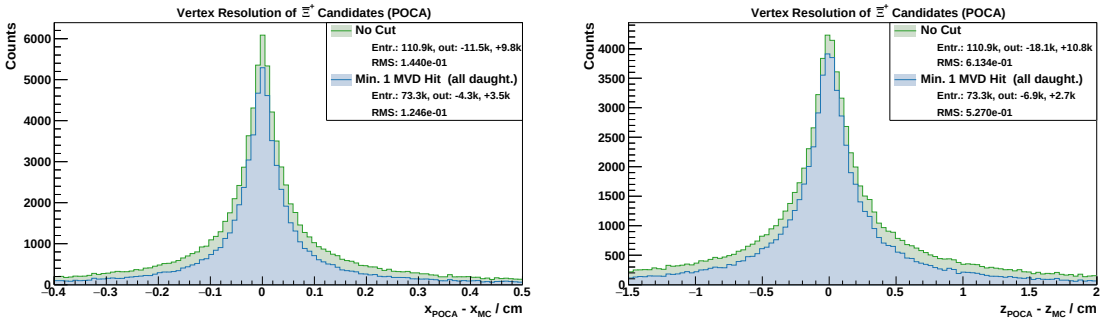

(a) Vertex difference distribution of the POCA in x.

(b) Vertex difference distribution of the POCA in z.

Figure 7.40: The decay vertex difference distribution of the $\bar{\Xi}^+$ candidates by comparing the result from the POCA method with the MC truth position. The green distributions contain all candidates, the blue ones additionally require MVD involvement for all daughters (π_1^+, π_2^+, $\bar{p}$).

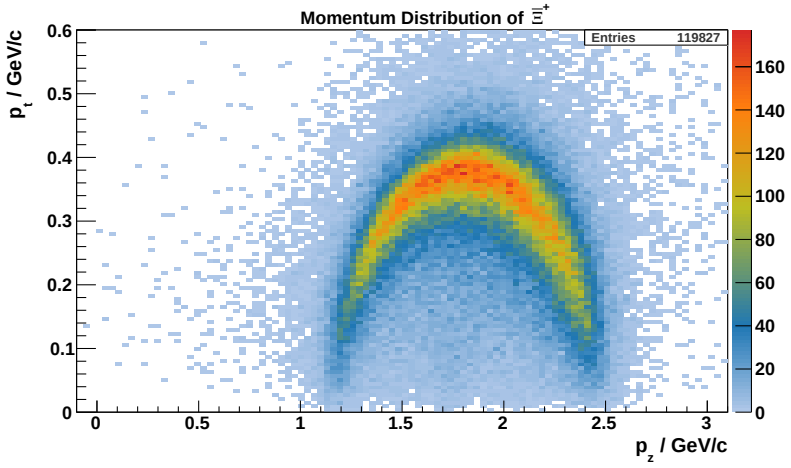

Figure 7.41: The transverse versus the longitudinal momentum distribution of the $\bar{\Xi}^+$ candidates.

The accuracy of the decay vertex reconstruction is obtained by comparing it with the generated input (Figure 7.40). Based on this, RMS values of $\Delta x = 1.4\,\text{mm}$ and $\Delta z = 6.1\,\text{mm}$ are reached. This can be improved by additionally requiring MVD hit points for all daughter particles (π_1^+, π_2^+, and $\bar{p}$) to $\Delta x^{\text{MVD}} = 1.2\,\text{mm}$ and $\Delta z = 5.2\,\text{mm}$. While this also reduces the statistics by 34 %, it dominantly suppresses the tails of the distribution by a factor of 3 to 4.

7.4.3.3 Momentum Distribution

From the combination of the π_1^+ and $\overline{\Lambda}$ candidates, a net momentum is determined. The distribution of these momenta in the longitudinal (p_z) and transverse (p_t) direction is presented in Figure 7.41. A smeared out ellipse is formed, caused by the kinematics of the initial reaction with longitudinal momenta in the range of 1.2 GeV/c to 2.5 GeV/c and transverse values of 0.1 GeV/c to 0.45 GeV/c. This resembles the input from the event generator as shown in Figure 7.3(b).

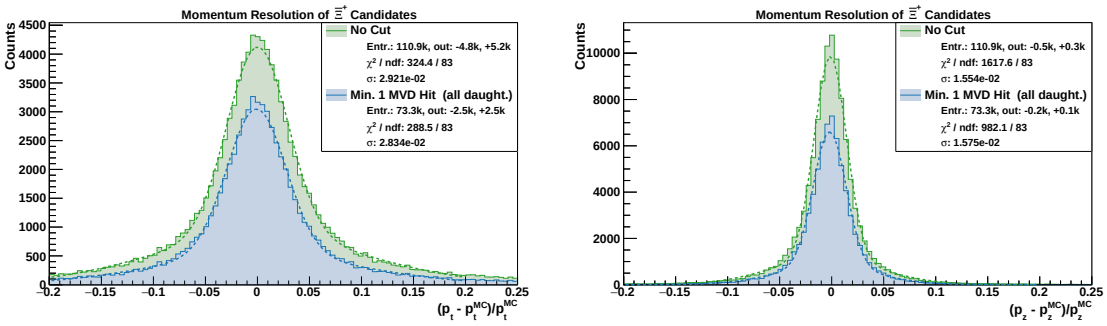

(a) Transverse momentum difference distribution. **(b)** Longitudinal momentum difference distribution.

Figure 7.42: The momentum difference distributions for the $\bar{\Xi}^+$ in transverse **(a)** and longitudinal **(b)** direction. The distributions for all candidates (green) are shown, overlaid with the distribution that requires MVD hits for all daughter particles (π_1^+, π_2^+, $\bar{p}$) (blue).

Comparing the reconstructed momentum values with the simulation input results in the distributions in Figure 7.42 which are based on the relative difference $\Delta p/p^{MC}$. Besides the distribution for all $\bar{\Xi}^+$ candidates in green the effect of the MVD is shown in blue. Double-Gaussian fits are applied to all distributions to obtain the resolution values. In longitudinal direction this is $\sigma_{p_z}/p_z = 1.6\,\%$ and in transverse direction $\sigma_{p_t}/p_t = 2.9\,\%$. As already seen with the Λ and $\bar{\Lambda}$ reconstruction, the MVD has a negligible influence on the momentum resolution.

7.4.3.4 Back-Propagation of $\bar{\Xi}^+$

Propagation to IP With the decay vertex information and the combined momentum, the $\bar{\Xi}^+$ candidate can be back-propagated through PANDA and its magnetic field towards the production location. This is done by utilizing the GEANE framework with the propagator class `FairGeanePro` and the option `BackTrackToVertex()`. The algorithm propagates the particle to the IP and stops when the closest distance to this point is achieved. The midpoint is then given as the POCA, much like for the POCA method discussed in Section 7.4.2.3.

The results of this back-propagation are shown in Figure 7.43 for the 87.4 % of the $\bar{\Xi}^+$ candidates where the propagation was successful. First, the distributions of the absolute coordinates in the x and z directions are depicted in Figure 7.43(a) and Figure 7.43(b), respectively. They show a symmetric peak around 0 with RMS values of $\Delta x = 1.6\,\text{mm}$ and $\Delta z = 0.3\,\text{mm}$. The smaller uncertainty on the longitudinal propagation result is caused by the forward boost of the system. This results in shallow tracks and the distance vector to the IP at the POCA will be almost perpendicular to the beam axis. Combining the transverse coordinates with $r = \sqrt{x^2 + y^2}$ and plotting the z position result leads to Figure 7.43(c). The peak near $(0, 0)$ is clearly visible and falls off rapidly towards higher distances. This is also resembled in Figure 7.43(d) where the distance to the IP is calculated. The peak of this distribution is at $\approx 0.35\,\text{mm}$.

POCA Between $\bar{\Xi}^+$ and K^- In the actual experiment, the annihilation reaction will not be at exactly $(0, 0, 0)$ but rather spread out due to the finite overlap volume of the beam and target.

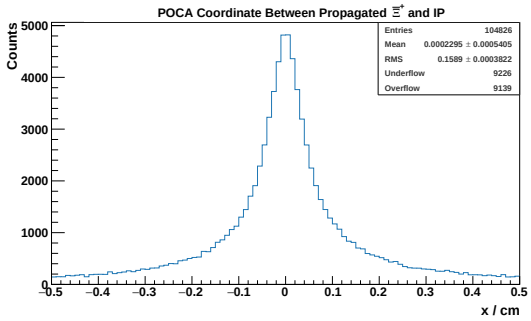

(a) POCA distribution of the back-propagation, x coordinate.

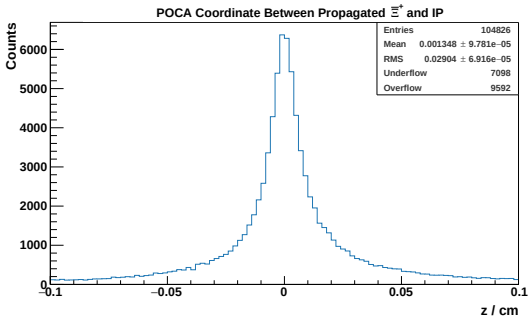

(b) POCA distribution of the back-propagation, z coordinate.

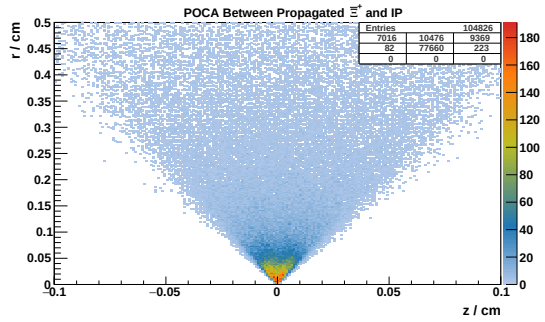

(c) Location distribution of the POCA of the back-propagation.

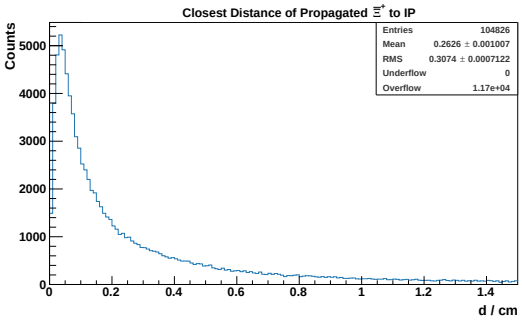

(d) Distance distribution from the POCA to the IP.

Figure 7.43: Results of the $\overline{\Xi}^+$ back-propagation to the minimal distance to the IP, called POCA.

However, the K^- is a decay product of the Ξ^{-*} and thus originates from the primary vertex. Therefore, a combination of the K^- particles with the $\overline{\Xi}^+$ candidate is done and the POCA method applied. If more than one K^- candidate is available, the one with the lowest pocaQA value is taken.

In Figure 7.44(a), the quality of this approach as the distance between the two particle tracks is displayed. This pocaQA distribution has the same trend as other POCA determinations (like in Figure 7.38(a)) but decreases significantly faster. The position of the POCA between the $\overline{\Xi}^+$ and K^- in Figure 7.44(b) is most probable around the IP – as expected – and falls off rapidly towards further distances. Evaluating the x and z coordinates individually determines RMS values of $\Delta x = 0.3\,\text{mm}$ and $\Delta z = 1.6\,\text{mm}$, verifying the good match with the nominal IP. The distributions of the POCA coordinates between $\overline{\Xi}^+$ and K^- are given in Figure A.12 in the appendix. This shows that involving the K^- improves the primary vertex reconstruction, independent on its actual location. The good tracking possibility of the K^- supports this reconstruction with many hit points from the MVD (see Figure 7.11).

7.4.3.5 Invariant Mass Distribution

The invariant mass distribution as a difference to the nominal value is shown in Figure 7.45. The nominal mass of $M^{\text{PDG}} = 1.314\,\text{GeV}/c^2$ is used [1]. The mass distribution is symmetric

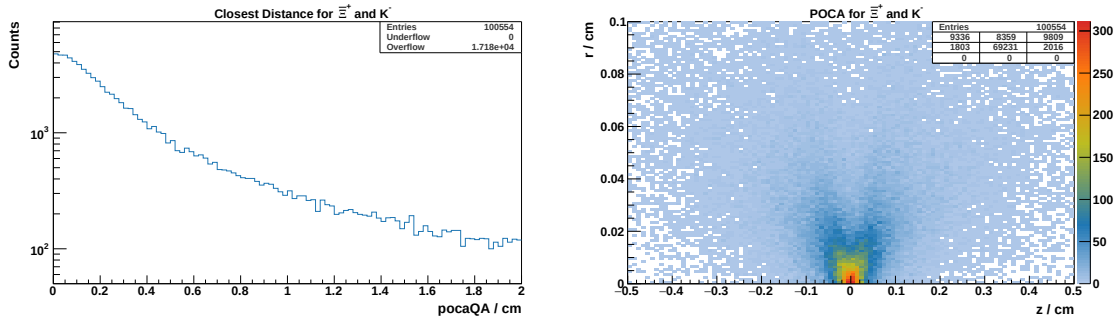

(a) Distance distribution of closest approach (pocaQA). **(b)** Position distribution of the POCA in the r-z plane.

Figure 7.44: The results of combining the $\bar{\Xi}^+$ with a K^- from the same event and determining their POCA. Only the combination with the lowest pocaQA value is shown.

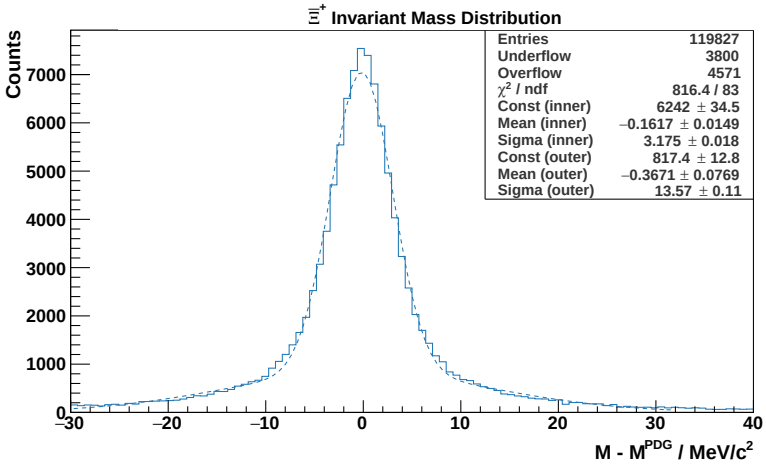

Figure 7.45: The invariant mass distribution of the $\bar{\Xi}^+$ with a double-Gaussian fit applied.

around zero with low tails, indicating a good suppression of wrongly combined candidates. Except for filtering the $\bar{\Xi}^+$ candidate with the best pocaQA, no additional cuts are applied here. A double-Gaussian function is fitted to the resulting distribution with an inner width of $\sigma_M = 3.2\,\mathrm{MeV}/c^2$.

7.4.4 Reconstruction of $\Xi^-(1690)$

7.4.4.1 Particle Combination

The Ξ^{-*} candidates are combined from 420,947 found K^- mesons and the 224,435 reconstructed Λ baryons as discussed in Section 7.4.2.4. Only those within a mass window of $\pm 150\,\mathrm{MeV}/c^2$ around the nominal mass of $1690\,\mathrm{MeV}/c^2$ are considered for the further analysis. This yields 188,112 Ξ^{-*} candidates. For 597 events or 0.3 %, two candidates are found per event. More than two Ξ^{-*} candidates per event are not present in the used data sample.

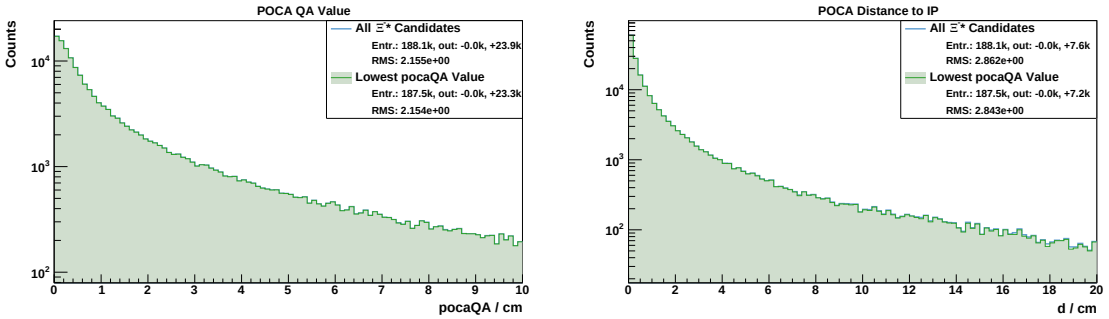

(a) Distance distribution of closest approach (pocaQA). **(b)** Distance distribution of the POCA to the IP.

Figure 7.46: The minimum distance between daughter tracks (pocaQA) and distance distribution to the IP from the POCA determination for the Ξ^{-*}. The green distribution shows only Ξ^{-*}s with the smallest pocaQA in case more than one candidate is available per event. A blue line is also drawn, containing all Ξ^{-*} candidates, but it follows the green distribution and thus is barely visible.

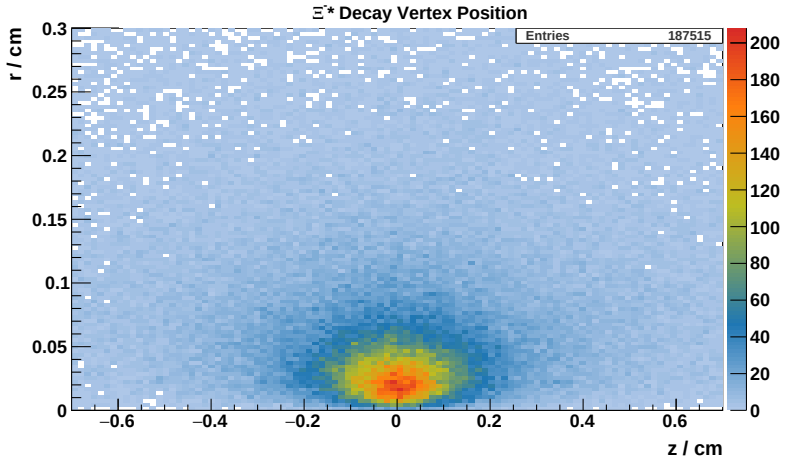

Figure 7.47: The POCA location distribution of the combined daughters from the Ξ^{-*}.

7.4.4.2 Vertex Reconstruction

Like with the $\overline{\Xi}^+$ reconstruction, a vertex fitting is not possible due to the neutral Λ as a daughter particle. Therefore, the POCA is calculated, based on helix and straight line hypotheses of the daughter particles' tracks. The results are shown in Figure 7.46 with the closest distance between the track extrapolations, i.e. the pocaQA value, in Figure 7.46(a) and the distance of the resulting POCA to the IP in Figure 7.46(b). Both distributions show the same trend as for the other particle's in earlier steps. In case more than one Ξ^{-*} candidate is found per event, the one with the smallest pocaQA value is taken. However, this only occurs in 0.3 %, thus the difference is not visible in the distribution. Most of the difference is in the long tails, indicated by the overflow values.

The position of this POCA is a representation of the decay vertex of the Ξ^{-*}. Figure 7.47 shows a two-dimensional projection of this location in the r-z coordinates. It is most probable

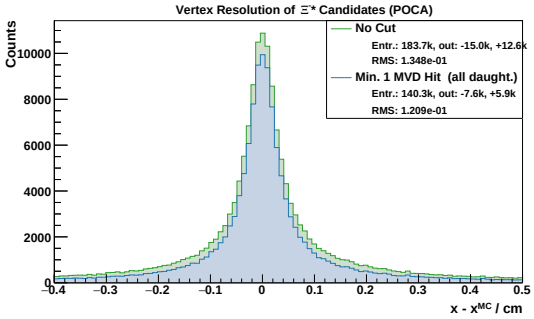

(a) Vertex difference distribution of the POCA in x.

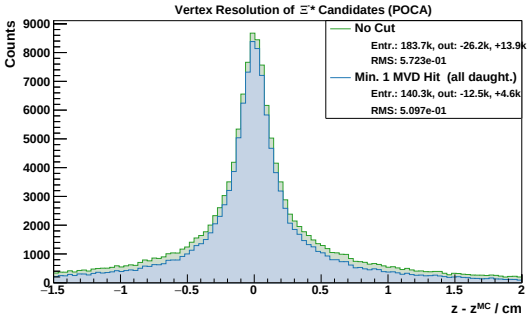

(b) Vertex difference distribution of the POCA in in z.

Figure 7.48: The difference distributions of the reconstructed decay vertex to the MC truth for the $\bar{\Xi}^{-*}$. In green, all candidates are shown while the blue distribution additionally requires MVD hits for all daughters (π^-, K, and p).

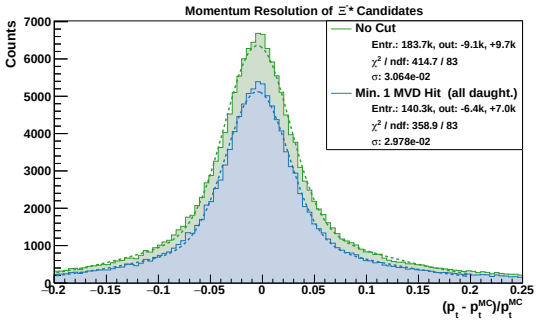

(a) Transverse momentum difference distribution.

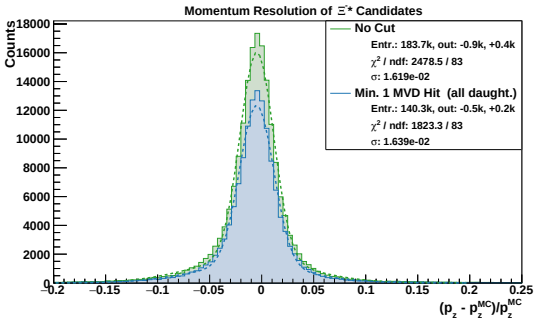

(b) Longitudinal momentum difference distribution.

Figure 7.49: The relative momentum differences for the $\bar{\Xi}^{-*}$ in transverse and longitudinal direction. The green distribution contains all Ξ^{-*} candidates and the blue one only those with MVD hits for all daughter particles (π^-, K, and p). In both cases, double-Gaussian functions are fitted.

around the nominal IP. By subtracting the MC truth value in the x and z positions, a value for the resolution is obtained. The distributions in Figure 7.48 reveal a symmetric arrangement around zero with RMS values of $\Delta x = 1.3\,\text{mm}$ for the transverse direction and $\Delta z = 5.7\,\text{mm}$ for the longitudinal direction. Both values slightly improve when MVD involvement for all daughter particles (π^-, K^-, and p) is required as well. The RMS values are then $\Delta x = 1.2\,\text{mm}$ and $\Delta z = 5.1\,\text{mm}$, respectively.

7.4.4.3 Momentum Distribution

The difference of the reconstructed momentum with the generator input is shown in Figure 7.49 as relative values. Again, the green curve comprises all Ξ^{-*} candidates and the blue one requires MVD involvement for all daughter particles. Double-Gaussian functions are fitted to both distributions to obtain the resolution values. In the transverse direction this is $\sigma_{p_t}/p_t = 3.1\,\%$ for all and $\sigma_{p_t}^{\text{MVD}}/p_t = 3.0\,\%$ with the MVD. For the resolution in the longitudinal direction the MVD does not influence the momentum resolution, both values are $\sigma_{p_z}/p_z = 1.6\,\%$.

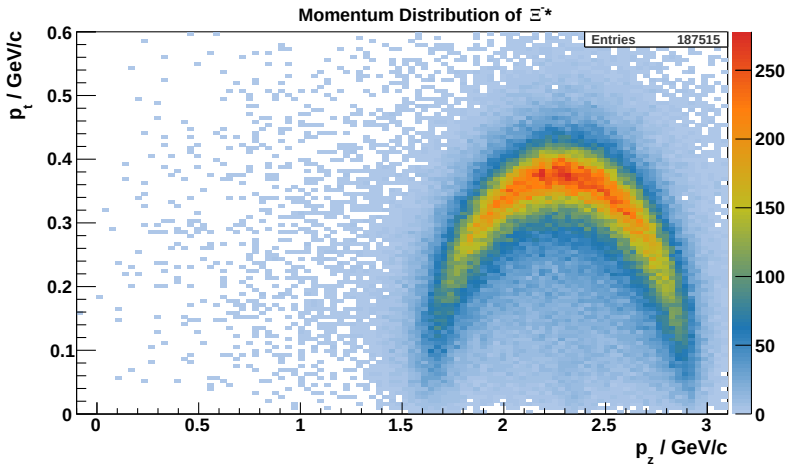

Figure 7.50: The transverse versus the longitudinal momentum distribution of Ξ^{-*} candidates.

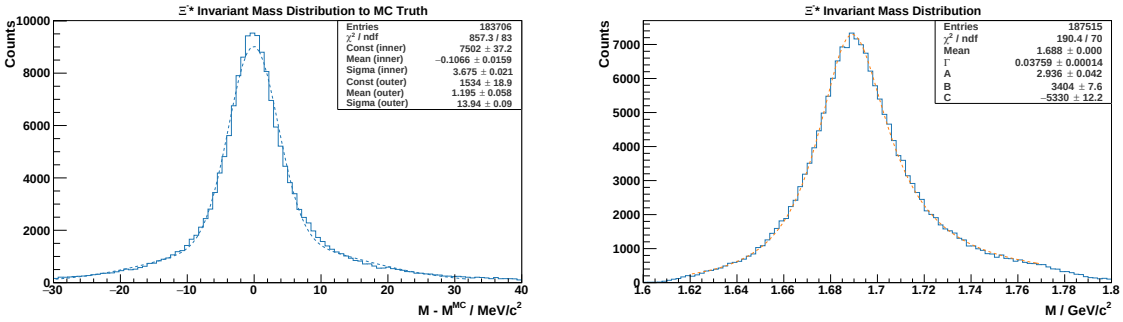

(a) Difference distribution of the reconstructed mass to the MC truth value.

(b) Reconstructed invariant mass distribution.

Figure 7.51: The invariant mass distributions of the Ξ^{-*}. The distribution on the left shows the difference of the reconstructed to the generated value with a double-Gaussian fit applied. On the right, the reconstructed invariant mass distribution is given, together with a Breit-Wigner fit according to Equation 7.2.

The momentum distribution of the Ξ^{-*}, which is determined from the sum of the daughter's momenta, is displayed in Figure 7.50. The ellipse from the initial production is clearly visible, along with the smearing caused by the width of the Ξ^{-*}. Only a few candidates lie outside the allowed phase space. Comparing this with the event generator output in Figure 7.3(a) indicates a good agreement.

7.4.4.4 Invariant Mass Distribution

In Figure 7.51, the invariant mass distributions of the $\Xi^-(1690)$ are given. On the left, the difference to the generated input is given in Figure 7.51(a). This distribution represents the detector resolution for this reconstruction and consequently, a double-Gaussian function is applied to extract a resolution value. The inner Gaussian reveals $\sigma_M = 3.7\,\mathrm{MeV}/c^2$. However, this input is not available in the real experiment, thus the distribution will more likely look

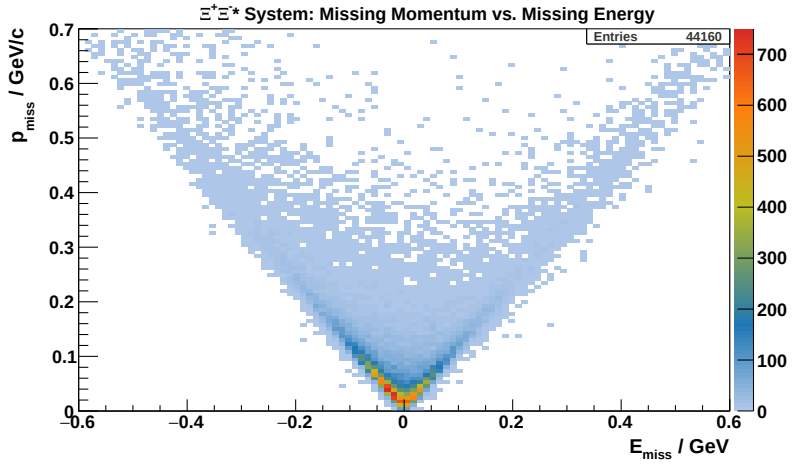

Figure 7.52: The missing energy and missing momentum distribution of the combined $\overline{\Xi}^{+}\Xi^{-*}$ system without any cuts.

as shown in Figure 7.51(b). Here, the reconstructed invariant mass distribution is given. The resulting distribution resembles the production as shown in Figure 7.4, overlaid with the finite resolution making it wider. A Breit-Wigner function with a linear part from the phase space influence is applied (Equation 7.2), resulting in a width of $\Gamma = 37.6\,\mathrm{MeV}/c^2$. The mean of the Breit-Wigner function is at $M = 1.688\,\mathrm{GeV}/c^2$, which is close to the fit result from the generated distribution $M^{\mathrm{MC}} = 1.689\,\mathrm{GeV}/c^2$.

7.4.5 Reconstruction of the $\overline{\Xi}^{+}\Xi^{-*}$ System

7.4.5.1 Particle Combination

In the final step of the event reconstruction, the exclusive $\overline{\Xi}^{+}\Xi^{-*}$ system is reassembled. First, for those events containing both Ξ particles, a system candidate is build. This reduces the statistics from 119,827 $\overline{\Xi}^{+}$ and 187,515 Ξ^{-*} to 44,160 system candidates. Since both are produced directly from the $\bar{\mathrm{p}}\mathrm{p}$ annihilation and the $\bar{\mathrm{p}}$ beam momentum is given, the initial momentum and energy parameters are known. The missing momentum and missing energy are given by the two equations

$$p_{\mathrm{miss}} = \sqrt{p_t^2 + (p_z - p_{z,\mathrm{beam}})^2} \qquad \text{and} \qquad E_{\mathrm{miss}} = E - E_{\bar{\mathrm{p}}\mathrm{p}}\ .$$

$E_{\bar{\mathrm{p}}\mathrm{p}} = 5.14\,\mathrm{GeV}$ is the total energy of the beam and target system and $p_{z,\mathrm{beam}} = 4.1\,\mathrm{GeV}/c$ beam momentum, as defined in Section 7.2.1.1. Filling both missing momentum and energy in a two dimensional histogram results in Figure 7.52. The distribution peaks near vanishing missing energy and momentum values but also has long tails. The main fraction of events lie in a range of roughly $E_{\mathrm{miss}} = \pm 0.1\,\mathrm{GeV}$ and $p_{\mathrm{miss}} < 0.1\,\mathrm{GeV}/c$.

7.4.5.2 Four-Constraint Fitting

Knowing the input parameters of the production also enables a so-called four-constraint (4C) fit. Here, the daughter particles' four-vectors are modified so that their net momentum and

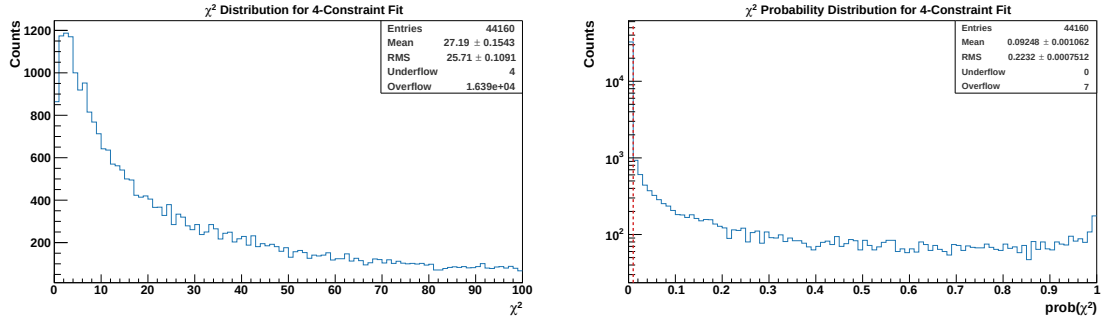

(a) χ^2 distribution.

(b) Probability distribution with marker for cut.

Figure 7.53: The fit quality emerging from the four-constraint fit of the $\overline{\Xi}^+\Xi^{-*}$ system. Shown are the χ^2 and prob(χ^2) distributions with the minimum probability of > 0.01 marked in the probability distribution.

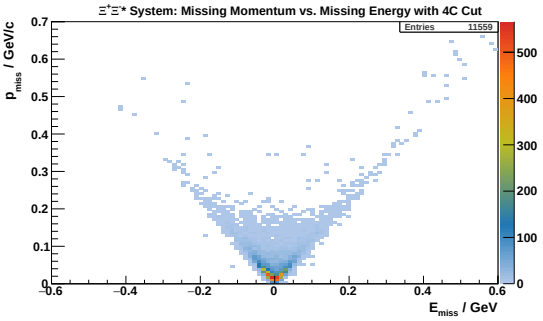

Figure 7.54: The missing momentum and missing energy distribution requiring prob(χ^2) > 0.01 from the four-constraint fit.

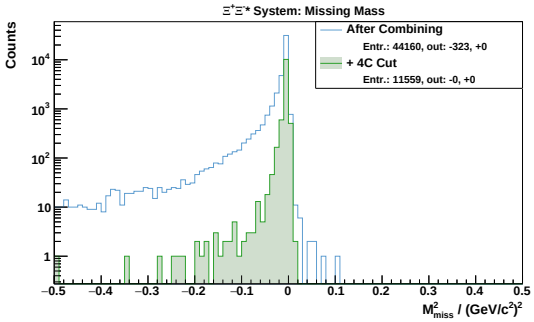

Figure 7.55: The missing mass distribution for all system candidates (blue) and with the selection based on the four-constraint fit probability (green).

energy matches the $\overline{\text{p}}\text{p}$ system. In PandaRoot, the class `Pnd4CFitter` handles this operation. The χ^2 and probability distributions of the fits are given in Figure 7.53. Similarly to the fitting done for the Λ and $\overline{\Lambda}$ candidates, a cut is applied on the probability to reject the most unreasonable combinations. By selecting only system candidates above 1 % probability, the number of reconstructed $\overline{\Xi}^+\Xi^{-*}$ systems shrinks by 73.8 % to 11,559, corresponding to an exclusive reconstruction efficiency of 2.3 %.

The effect of the cut on the pre-fit values of missing momentum and energy is shown in Figure 7.54. The distribution still peaks close to $(0, 0)$ but the tails are strongly suppressed compared to the initial distribution (Figure 7.52). A similar effect can be seen in the spectrum of the missing mass in Figure 7.55. The squared missing mass is calculated with

$$M^2_{\text{miss}} = \left(E_{\overline{\text{p}}\text{p}} - E\right)^2 - \left(p_{\text{beam}} - p\right)^2 .$$

The resulting spectrum has a long tail after the combination of $\overline{\Xi}^+\Xi^{-*}$ candidates but is cut to a narrow peak after applying the probability condition.

7.4.5.3 Momentum Distribution

In Figure 7.56, the two-dimensional distribution for longitudinal and transverse momenta after the 4C fit is displayed, once before and once after the cut. The production ellipse is clearly visible and is comparable to the reconstructed distributions in Figure 7.41 and Figure 7.50. Applying the cut increases the statistical fluctuations but also suppresses the outliers in the distribution.

Concerning the momentum resolution, the 4C fit improves the accuracy. This is shown in Figure 7.57 for longitudinal and transverse momentum differences to the MC truth values of the Ξ^{-*}. The distributions of the $\overline{\Xi}^{+}$ are in Figure A.13 in the appendix. Due to the significant difference in statistics of roughly a factor 4, the distributions are displayed in relative units to their corresponding maximum bins. From double-Gaussian fits, the resolution can be extracted and is at $\sigma_{p_t}/p_t = 2.6\,\%$ before the cut (blue distribution) and $\sigma^{4C}_{p_t}/p_t = 2.2\,\%$ after requesting a minimum of 1 % for the fit probability (green distribution). Both values are the same for both initial states due to momentum conservation. However, in longitudinal direction the resolution is slightly different for the two Ξ baryons. For the $\overline{\Xi}^{+}$, the resolution improves from $\sigma_{p_z}/p_z = 1.5\,\%$ before to $\sigma^{4C}_{p_z}/p_z = 1.1\,\%$ after the 4C cut. A similar improvement is observable for the Ξ^{-*} from $\sigma_{p_z}/p_z = 1.2\,\%$ to $\sigma^{4C}_{p_z}/p_z = 0.9\,\%$.

7.4.5.4 Invariant Mass Distribution

The invariant mass distributions of Ξ^{-*} and $\overline{\Xi}^{+}$ are given in Figure 7.58. For the Ξ^{-*} particles, the difference to the event generator input is given to see a spectrum independent of the particle's natural width. This is not required for the $\overline{\Xi}^{+}$, hence it shows the difference to the nominal value of $M^{\mathrm{PDG}}(\overline{\Xi}^{+}) = 1321.7\,\mathrm{MeV}/c^2$ [1]. Using the reconstructed invariant mass value after the 4C fit with the probability cut results in the green distributions. They have resolutions of $\sigma_{M,\Xi^{-*}} = 5.9\,\mathrm{MeV}/c^2$ and $\sigma_{M,\overline{\Xi}^{+}} = 5.5\,\mathrm{MeV}/c^2$, which is a factor 1.6 to 1.7 worse than the inclusive reconstructions. Therefore, also the distributions of the pre-fit invariant mass values are given but with the 4C cut applied. This leads to narrower distributions with $\sigma^{\text{pre-fit}}_{M,\Xi^{-*}} = 3.4\,\mathrm{MeV}/c^2$ and $\sigma^{\text{pre-fit}}_{M,\overline{\Xi}^{+}} = 2.9\,\mathrm{MeV}/c^2$. For comparison, the invariant mass resolutions after the inclusive reconstruction are $\sigma^{\text{incl}}_{M,\Xi^{-*}} = 3.7\,\mathrm{MeV}/c^2$ and $\sigma^{\text{incl}}_{M,\overline{\Xi}^{+}} = 3.2\,\mathrm{MeV}/c^2$.

The reason for this worsening of the resolution after the 4C is not known and needs further investigation. A probable explanation is the presence of neutral particles in the reconstruction chain. As already seen for the Ξ reconstruction in Section 7.4.3.2 and Section 7.4.4.2, the vertex fitting algorithm in PandaRoot fails for neutral daughter particles. Hence, it stands to reason that also the 4C fitter is not processing neutral candidates as expected. Alternatively, if the events are not correctly accounted for by the 4C fitter, then the large natural width of the Ξ^{-*} could worse the results for the $\overline{\Xi}^{+}$ after the fit. However, the momentum resolution is not negatively affected by the 4C fit but rather improves, as discussed in Section 7.4.5.3.

7.4.5.5 Dalitz Plot

With the Dalitz plot, the kinematics of the initial production can be displayed. This is done for the event generator data in Figure 7.5 and after the reconstruction of the full system in Figure

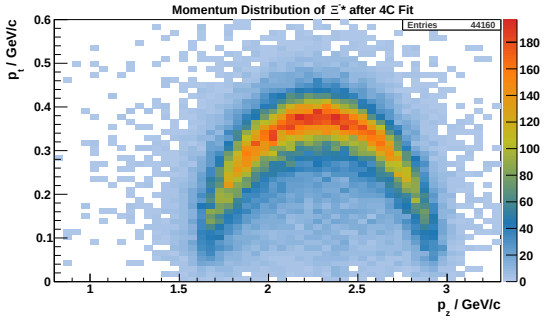

(a) All Ξ^{-*} after the 4C fit.

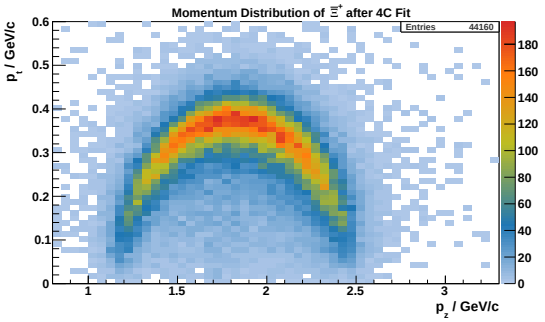

(b) All $\overline{\Xi}^{+}$ after the 4C fit.

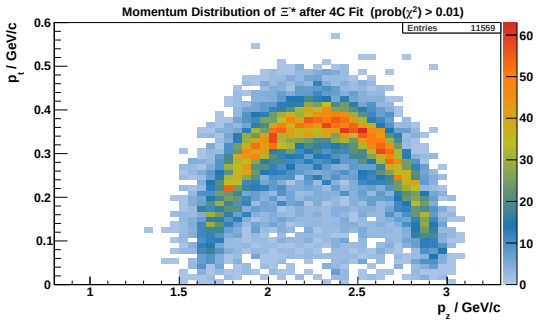

(c) Only Ξ^{-*} with 4C probability larger 1 %.

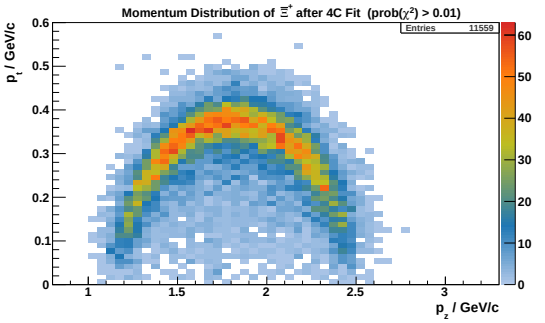

(d) Only $\overline{\Xi}^{+}$ with 4C probability larger 1 %.

Figure 7.56: The transverse versus the longitudinal momentum distributions for Ξ^{-*} and $\overline{\Xi}^{+}$ baryons after the four-constraint (4C) fit. For the distributions in the lower row the χ^2 probability was required to be > 0.01.

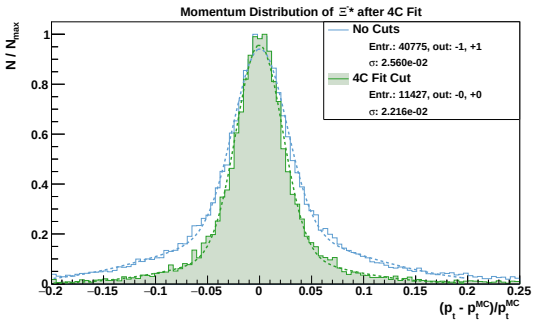

(a) Transverse momentum difference distribution after the 4C fit.

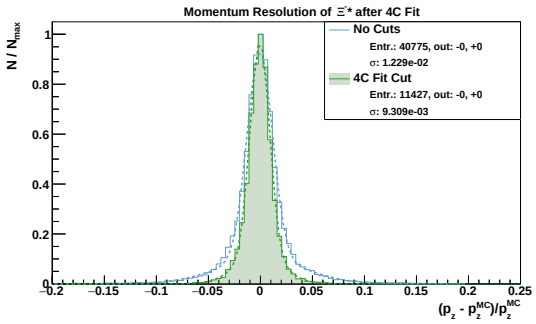

(b) Longitudinal momentum difference distribution after the 4C fit.

Figure 7.57: Ξ^{-*}: The relative momentum difference distributions to the generator input after the four-constraint (4C) fit. The blue distribution shows the difference after the fit but without cuts, the green one with the applied probability cut. The histograms are each normalized to their maximum bin.

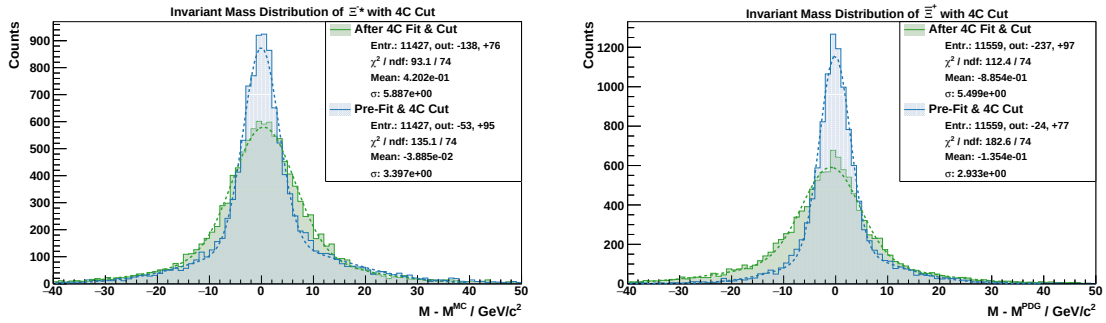

(a) Invariant mass distribution of Ξ^{-*}.

(b) Invariant mass distribution of $\overline{\Xi}^{+}$.

Figure 7.58: The invariant mass distributions as difference to the input values for both initial state particles after the probability cut was applied. The distribution of the pre-fit masses is shown in blue, the one after the fit in green. All distributions have double-Gaussian fits applied.

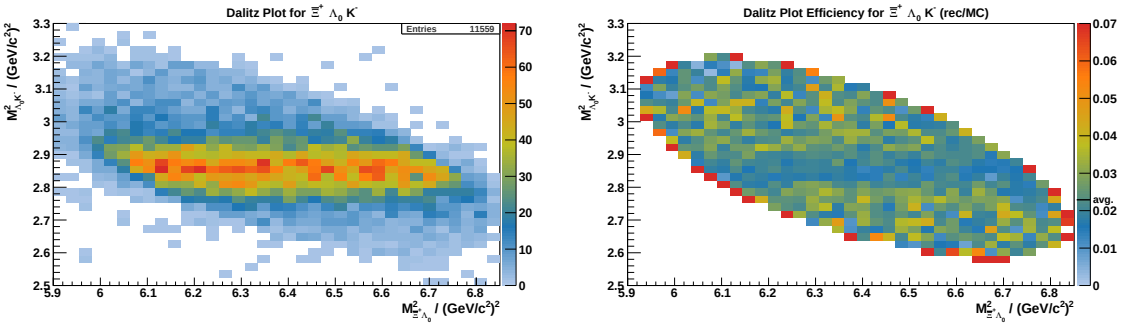

(a) Dalitz plot after reconstruction.

(b) Reconstructed Dalitz plot divided by the event generator input.

Figure 7.59: The $\overline{\Xi}^{+}$, K^{-}, Λ Dalitz plot after full reconstruction. The reconstructed distribution is shown on the left and the efficiency on the right (average: 0.023).

7.59(a). The resonance of the Ξ^{-*} is highlighted as a horizontal band and the ellipse shape of the allowed phase space is recognizable. Besides the main resonance band, no other structures are visible that could be misinterpreted as resonances.

Dividing this Dalitz plot by the generator input gives an indication for the homogeneity of the reconstruction efficiency. The corresponding distribution is shown in Figure 7.59(b). Besides the statistical fluctuation due to the low number of entries in the bins besides the main band, a dip is seen where the resonance band lies. It is slightly below the average efficiency of 0.023. This is an effect of the invariant mass distribution widening after the 4C: Events which were generated within the resonance band are reconstructed further outwards, thus decreasing the entries in the band.

Table 7.7: Summary of the reconstructed $\Xi^-(1690)$ and $\overline{\Xi}^+$ hyperons for the inclusive and exclusive analysis stages. The stage »4C Cut« has the probability criterion from the 4C fit applied but uses the pre-fit value. All σ values are taken from the inner Gaussian of the double-Gaussian fits.

	$\Xi^-(1690)$				$\overline{\Xi}^+$			
	N %	σ_{p_t}/p_t %	σ_{p_z}/p_z %	σ_M MeV/c^2	N %	σ_{p_t}/p_t %	σ_{p_z}/p_z %	σ_M MeV/c^2
	Inclusive							
Combination	37.5	3.06	1.62	3.67	24.0	2.92	1.55	3.17
Include MVD	28.3	2.98	1.64	3.58	15.3	2.83	1.58	3.07
	Exclusive							
Combination	8.8	3.04	1.61	3.65	8.8	2.94	1.57	3.17
4C Cut	2.3	2.75	1.23	3.29	2.3	2.50	1.16	2.88
4C Fit & Cut	2.3	2.22	0.93	5.58	2.3	2.22	1.08	5.14

7.4.5.6 $\overline{\Xi}^+\Xi^{-*}$ Reconstruction Summary

The efficiencies and resolution effects of the presented steps for the $\overline{\Xi}^+$ and Ξ^{-*} reconstruction are collected in Table 7.7. Two aspects stand out: First, the statistics for the full exclusive reconstruction is strongly reduced by requiring a successful reconstruction of all intermediate states of the decay chain. Only in 2.3 % of all events could the full $\overline{\Xi}^+\Xi^{-*}$system be combined and properly fitted with a 4C fit. Secondly, the invariant mass resolution becomes worse after the 4C fit. Quite likely, it is either related to the improper handling of neutral daughter particles in the decay tree or from the defined energy resolution in combination with the large natural width of the Ξ^{-*}. However, this is topic for subsequent investigations.

7.4.6 Angular Distribution Reconstruction

A precise measurement of the angular distribution provides essential insight to help distinguish between production models. Hence, an analysis of $\overline{\text{P}}$ANDA's reconstruction efficiency for the polar angle distribution is done. First with the flat input from a phase space production, then with a modified input to estimate systematic effects.

7.4.6.1 Phase Space Production

Exclusive Reconstruction Based on the previously analyzed data set one can use the reconstructed momentum and energy information after the 4C fit to assemble the particles' four-vectors. Boosting these to the beam and target system's center of mass frame (CM) gives rise to the angular distribution of the production. With the input of phase-space production, a flat distribution of $\cos(\theta_{\text{CM}})$ is expected. In Figure 7.60(a) the reconstructed angular distribution of the Ξ^{-*} is shown, indicating an almost flat distribution with statistical fluctuations due to the limited amount of data.

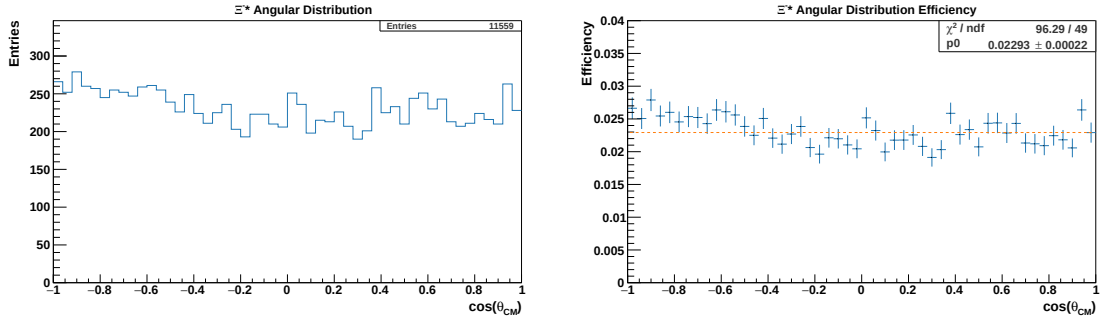

(a) Reconstructed $\cos(\theta_{\mathrm{CM}})$ distribution. **(b)** Reconstruction efficiency as a function of $\cos(\theta_{\mathrm{CM}})$.

Figure 7.60: Ξ^{-*}: The exclusive reconstructed angular distribution of the polar angle in the CM frame (left) and divided by the MC truth input (right). An overall constant function has been fit to the distribution on the right, as shown in orange.

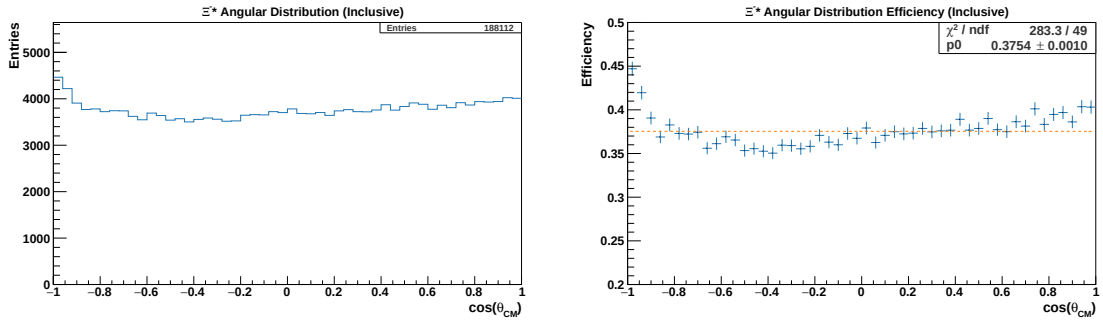

(a) Reconstructed $\cos(\theta_{\mathrm{CM}})$ distribution. **(b)** Reconstruction efficiency as a function of $\cos(\theta_{\mathrm{CM}})$.

Figure 7.61: The inclusive reconstructed angular distribution for the Ξ^{-*} in the CM frame (left). On the right, the distribution is divided by the MC truth input and an overall constant has been fit, as shown in orange.

This is also confirmed by the efficiency distribution in Figure 7.60(b), which is obtained by dividing by the MC truth input. Since a flat distribution is expected, a constant is fit to the efficiency distribution. It results in 2.3 % mean efficiency and follows reasonably well the distribution. However, a small systematic excess by ~ 0.3 percent points towards low polar angles is recognizable. Consequently, the $\overline{\Xi}^{+}$ is slightly more likely to be reconstructed for shallow forward angles.

Inclusive Reconstruction In case of a clear event signal, the inclusive reconstruction of just one branch provides valuable input. The inclusive signal reconstruction efficiency for the $\Xi^{-}(1690)$ is with 37.5 % much higher than the exclusive one with 2.3 %. The same procedure as for the exclusive reconstruction can be applied to obtain the polar angle distribution in the CM system. Now, the values originate from the combined Ξ^{-*} candidate without the 4C fit.

The resulting distributions are shown in Figure 7.61. The absolute distribution in Figure 7.61(a) has lower fluctuations due to the higher statistics but shows a minor structure. In

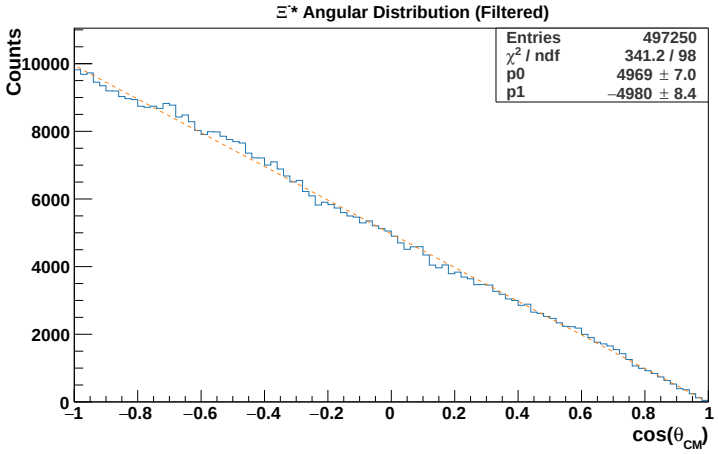

Figure 7.62: The filtered angular distribution of the $\bar{\Xi}^{-*}$ in the $\bar{p}p$ CM system as an output of the event generator. A linear function is fit to the distribution and shown in orange, resembling the input.

the backwards direction a swift increase is notable between $\cos(\theta_{CM})$ values of -0.8 rad and -1 rad. Also, a slight rising slope can be seen from -0.4 rad until 1 rad. This is also present in the efficiency distribution in Figure 7.61(b).

Both the exclusive as well as the inclusive reconstruction efficiency distributions show minor systematical features that differ from a flat distribution.

7.4.6.2 Modified Production Distribution

To account for the expected forward boost of the $\bar{\Xi}^+$, a modified angular distribution is simulated as well. It is realized by a rejection method from the initially homogeneous distribution. The probability is determined by a predefined probability function for a particular parameter. In this case, a linear function is applied to the polar angle distribution of the $\bar{\Xi}^+$, preferring forward emitted $\bar{\Xi}^+$ baryons. Consequently, the distribution is inverted for the Ξ^{-*} with the highest probability for backwards directed particles, as shown in Figure 7.62. This case provides an uncomplicated base for the analysis of possible systematic effects in the reconstruction efficiency.

In total, 497,250 events have been simulated with the modified input. After the same reconstruction procedure as presented with the flat phase space distribution, 11,465 events are left over in the exclusive reconstruction. This corresponds to an overall efficiency of 2.3 % in signal reconstruction and is the same as with the unfiltered, flat phase-space distributed input.

The reconstructed angular distribution of the Ξ^{-*} is shown in Figure 7.63(a) and resembles the input. This becomes even clearer in the efficiency distribution over $\cos(\theta_{CM})$ which is given in Figure 7.63(b). The values mostly fluctuate around the mean value shown as a horizontal fit to the distribution. Again, an excess towards backwards angles starting at -0.7 rad can be observed. This is loosely consistent with the reconstruction efficiencies for flat input distributions in Section 7.4.6.1. However, the statistical fluctuations make it difficult for a more detailed comparison.

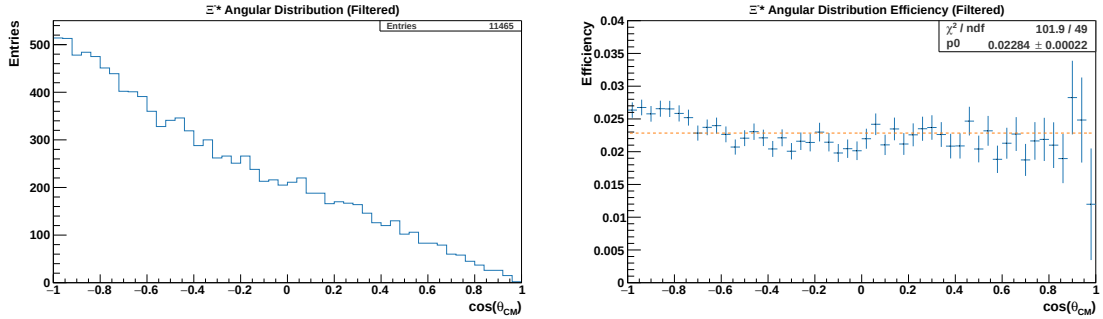

(a) Reconstructed $\cos(\theta_{\mathrm{CM}})$ distribution.

(b) Reconstruction efficiency over $\cos(\theta_{\mathrm{CM}})$.

Figure 7.63: The reconstructed angular distribution for the filtered $\bar{\Xi}^{+*}$ in the $\bar{\mathrm{p}}\mathrm{p}$ CM frame (left) and divided by the generator input (right). An overall constant function has been fit ot the distribution on the right, as shown in orange.

7.5 Background Studies

7.5.1 Introductory Remarks

The $\bar{\mathrm{p}}\mathrm{p}$ reaction creates many more reactions in addition to the investigated signal events which might also create topologies similar enough to the signal that they are falsely interpreted as signal events. To simulate the influence of this non-resonant background, 47.4×10^6 events have been generated using the DPM model as implemented in the `PndDpmDirect` class of PandaRoot. The total cross section at the antiproton beam momentum of $p_{\bar{\mathrm{p}}} = 4.1\,\mathrm{GeV}/c$ is estimated to be $\sigma_{\mathrm{bkg}} = 50\,\mathrm{mb}$. Compared to the signal's production cross section, this is a factor of 5×10^4 higher. To make the background comparable with the signal, the following scaling factor $\mathcal{B}$ is applied to the reconstructed background events:

$$\mathcal{B} = \frac{N_{\mathrm{sig,gen}} \,/\, (\sigma_{\mathrm{sig}} \times \mathrm{BR})}{N_{\mathrm{bkg}} \,/\, \sigma_{\mathrm{bkg}}} \,. \tag{7.3}$$

This formula includes the numbers of generated signal ($N_{\mathrm{sig,gen}}$) and background ($N_{\mathrm{bkg,gen}}$) events as well as their corresponding production cross sections σ_{sig} and σ_{bkg}, respectively. The decay tree has been fixed, neglecting decays into other final states. This overestimation of the signal is corrected in Equation 7.3 by the factor BR. Depending on the currently investigated portion of the decay tree, BR is obtained by the product of all relevant branching ratios. All background distributions presented in this analysis are scaled according to Equation 7.3.

The cut optimizations discussed in this chapter generally aim for a high background suppression while reducing the signal as little as possible. This is quantified by the signal-to-background ratio, or the significance $\mathcal{S}$:

$$\mathcal{S} = \frac{N_{\mathrm{sig}}^2}{N_{\mathrm{sig}} + N_{\mathrm{bkg}}} \,. \tag{7.4}$$

The condition under investigation is applied to both data sets, changing the remaining number of events and thus the significance. The condition is modified until a maximum for $\mathcal{S}$ is found,

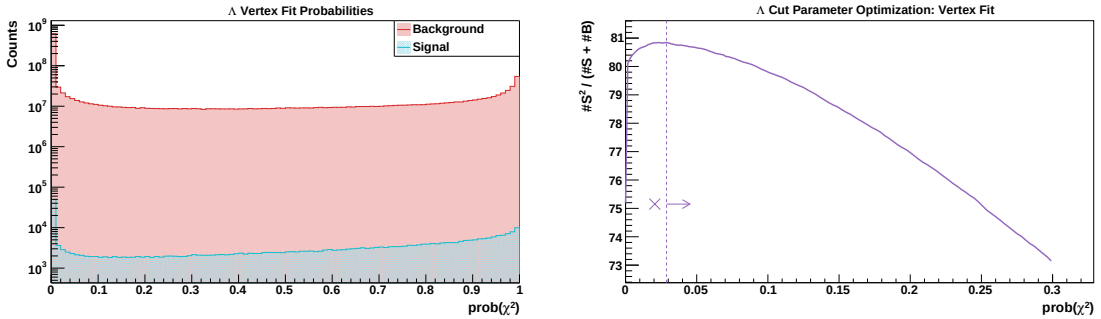

(a) Probability distributions.

(b) Significance $\mathcal{S}$ for varying probability cuts.

Figure 7.64: Cut optimization for the **Λ** vertex fit probability prob(χ^2). The distribution on the left superimposes the probability distributions of signal (turquoise) and scaled background (red) data. On the right, the significance behavior is given for varying probability limits. The optimal cut position is indicated by the dashed line, the arrow indicates the direction of accepted events.

providing an optimal operating point. This value is then assigned to a cut which is represented by the symbol $\mathcal{C}$, accompanied by the type of cut in the subscript, for instance $\mathcal{C}_{\Lambda,\text{vtx}}$ for the vertex fit of the Λ.

7.5.2 Λ and $\overline{\Lambda}$ Fit Optimization

The Λ candidates are combined from the list of π^- and p particles, the $\overline{\Lambda}$ candidates from the π^+ and $\overline{\text{p}}$ lists. Two kinematic fits are then performed to the Λ and $\overline{\Lambda}$ reconstruction: a vertex fit and a mass constraint fit. The preliminary cuts applied in the event reconstruction in Section 7.4.2.2 require a fit probability of more than 1 % to reduce unreasonable candidates from wrong combinations. The position of this cut is investigated in the following. Before applying any cut, a total of $N_{\Lambda,\text{sig}} = 353{,}585$ Λ candidates are found in the signal data set and $N_{\Lambda,\text{bkg}} = 2{,}132{,}407 \times \mathcal{B}_\Lambda$ Λ candidates in the background data set. For the $\overline{\Lambda}$, the numbers are $N_{\overline{\Lambda},\text{sig}} = 558{,}879$ and $N_{\overline{\Lambda},\text{bkg}} = 868{,}695 \times \mathcal{B}_\Lambda$, respectively. The background scaling factor for both Λ particles is

$$\mathcal{B}_\Lambda = 825.6\,, \tag{7.5}$$

calculated with Equation 7.3 and a branching fraction of BR = 0.639 for the decay $\Lambda \to \text{p}\pi^-$.

The probability distributions of the Λ vertex fit is given in Figure 7.64(a) for signal and background events. The applied cut requires a minimum probability and is optimized to achieve a maximum significance $\mathcal{S}$. To calculate $\mathcal{S}$, the background is scaled according to Equation 7.5. The resulting dependance of $\mathcal{S}$ for varying the cut value is shown in Figure 7.64(b). This indicates a slightly higher cut value than conservatively assumed. The maximum significance can be obtained for $\mathcal{C}_{\Lambda,\text{vtx}} = \text{prob}(\chi^2)_{\text{vtx}} > 0.029$.

Optimizing the mass constraint fit of the Λ is done in the same way. Based on the signal and background distributions (Figure 7.65(a)), a minimum probability is required. The significance that results from the events left after applying the cut is shown in Figure 7.65(b). Also here,

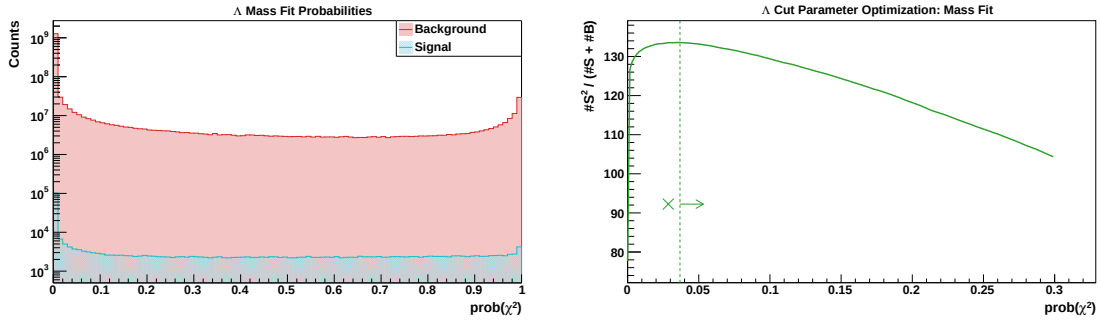

(a) Probability distributions. **(b)** Significance $\mathcal{S}$ for varying probability cuts.

Figure 7.65: Cut optimization for the **Λ** mass constraint fit probability prob(χ^2). The plots have the same format as in Figure 7.64.

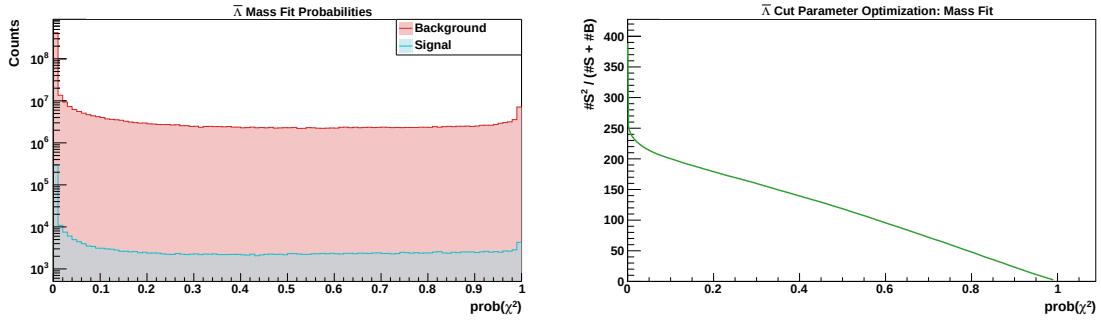

(a) Probability distributions. **(b)** Significance $\mathcal{S}$ for varying probability cuts.

Figure 7.66: Cut optimization for the $\overline{\mathbf{\Lambda}}$ mass constraint fit probability prob(χ^2). The plots have the same format as in Figure 7.65.

the maximum is close to the preliminary cut and yields a value $\mathcal{C}_{\Lambda,\text{mass}} = \text{prob}(\chi^2)_{\text{mass}} > 0.037$. After applying both cuts, the number of events is reduced to $N_{\Lambda,\text{sig,cut}} = 220{,}593$ (62.4 %) for signal and $N_{\Lambda,\text{bkg,cut}} = 367{,}609$ (17.2 %) for background data.

The probability distributions of the $\overline{\Lambda}$ candidates show a strong similarity between signal and background data as shown in Figure 7.66(a) for the mass constraint fit. The vertex fit can be found in Figure A.14 in the appendix. Using the same method for scanning the cut parameter and calculating the significance reveals a continuously falling distribution of $\mathcal{S}$. The reason lies in the similarity of the probability distributions itself. Hence, increasing the cut value not only reduces the background but with a similar rate also the number of signal events. In terms of significance, the best cut parameter would be none at all but this would certainly include unreasonable combinations from wrong reconstructions. Therefore, the already mentioned conservative cut of $\mathcal{C}_{\overline{\Lambda},\text{vtx}} = \mathcal{C}_{\overline{\Lambda},\text{mass}} = \text{prob}(\chi^2) > 0.01$ is used for the $\overline{\Lambda}$ reconstruction. As it is shown in the following sections, other parameters are more effective in suppressing the background in the decay branch of the $\overline{\Xi}^+$.

The statistics after the obtained probability cuts on the $\overline{\Lambda}$ and Λ candidates are summarized in Table 7.8.

Table 7.8: Overview of the optimized cut parameters for kinematic fits of the Λ and $\overline{\Lambda}$ candidates. The cuts are optimized individually and the best (lowest χ^2) of both is used for the further reconstruction. The number of background events are scaled with $\mathcal{B}_\Lambda = 825.6$ for the calculation of $\mathcal{S}$.

	Cut Parameter	Signal $\Lambda/\overline{\Lambda}$		Background $\Lambda/\overline{\Lambda}$		$\mathcal{S}$
	No cut	353,585	(100 %)	2,132,407	(100 %)	71
Λ	Vertex fit: prob(χ^2) > 0.029	297,962	(84.3 %)	1,329,868	(62.4 %)	81
	Mass fit: prob(χ^2) > 0.037	236,003	(66.7 %)	504,802	(23.7 %)	134
	Best after both fits	210,761	(59.6 %)	270,433	(12.7 %)	199
	No cut	558,879	(100 %)	868,695	(100 %)	435
$\overline{\Lambda}$	Vertex fit: prob(χ^2) > 0.01	431,575	(77.2 %)	758,350	(87.3 %)	297
	Mass fit: prob(χ^2) > 0.01	264,658	(47.4 %)	356,967	(41.1 %)	237
	Best after both fits	194,907	(34.9 %)	317,156	(36.5 %)	145

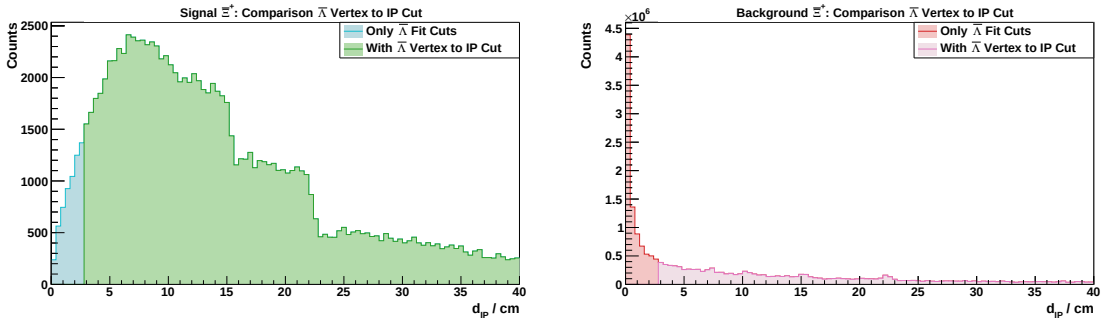

(a) Signal data.

(b) Background data.

Figure 7.67: The distance distributions of the $\overline{\Lambda}$ decay vertex to the nominal IP. The distributions are shown without cuts (turquoise, red) and superimposed with the distributions resulting from the applied cut (green, pink).

7.5.3 Inclusive $\overline{\Xi}^+$ Background Suppression

$\overline{\Xi}^+$ candidates are combined by using the discussed cuts on the $\overline{\Lambda}$ and requiring an additional π^+ in the event. This leads to $N_{\overline{\Xi}^+,\text{sig}} = 119{,}827$ signal candidates and $N_{\overline{\Xi}^+,\text{bkg}} = 32{,}674 \times \mathcal{B}_{\overline{\Xi}^+}$ background candidates. Since the decay $\overline{\Xi}^+ \to \overline{\Lambda}\pi^+$ is fixed, an additional factor BR = 0.9989 is needed for the background scaling factor, which is now $\mathcal{B}_{\overline{\Xi}^+} = 826.5$, according to Equation 7.3.

7.5.3.1 Cut Parameter Optimization

In the following, a series of cut parameters is investigated. For all, the background is scaled according to $\mathcal{B}_{\overline{\Xi}^+}$ and the optimizations use the data set of the $\overline{\Xi}^+$ combination as an input. All optimizations are done individually, a cross-check for interdependent influences is presented in Section 7.5.3.2.

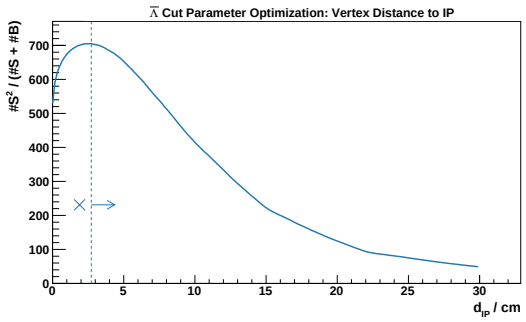

Figure 7.68: The significance distribution for a cut on the distance of the $\overline{\Lambda}$ decay vertex to the IP. The dashed line marks the optimal operation point, the arrow indicates the direction of accepted events.

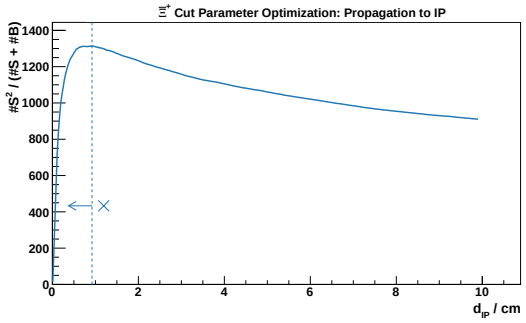

Figure 7.69: The significance distribution for a cut on the distance of the back-propagated $\overline{\Xi}^+$ track to the IP. The dashed line marks the optimal operation point, the arrow indicates the direction of accepted events.

The first cut parameter investigated makes use of the decay channel's particular topology with delayed vertices. The $\overline{\Lambda}$ baryon's decay distribution is shown in Figure 7.67(a), resembling the generated distribution of Figure 7.10(a) albeit with the efficiency drops resulting from decays beyond the MVD discs. This spectrum is significantly different from the background distribution (Figure 7.67(b)). Hence, this parameter is a good candidate for rejecting fake $\overline{\Xi}^+$ candidates.

In Figure 7.68, the cut optimization of $\mathcal{C}_{\overline{\Lambda},d}$ is depicted. The maximum of $\mathcal{S}$ is constrained by a distinct peak, leading to a value of $\mathcal{C}_{\overline{\Lambda},d} = d_{\mathrm{IP}}(\overline{\Lambda}) > 2.8\,\mathrm{cm}$. This is highlighted by a dashed line in the plot, accompanied by an arrow indicating the direction of the accepted signals. The maximum significance is $\mathcal{S}_{\overline{\Lambda},d} = 705$ and reduces the background to 67.5 % while leaving 94.9 % of the signal events.

The back-propagation to the IP, as presented in Section 7.4.3.4, can also be used to distinguish background since properly reconstructed $\overline{\Xi}^+$ signal candidates are expected to originate from the IP. Optimizing the maximum distance to the nominal IP at $(0,0,0)$ yields in the significance behavior shown in Figure 7.69. The most efficent background suppression is at $\mathcal{C}_{\overline{\Xi}^+,\mathrm{propIP}} = d_{\mathrm{IP}} < 0.92\,\mathrm{cm}$. This cut reduces the signal to 73.0 % and the background to 21.3 %. The distributions of signal and background distances with and without applied $\mathcal{C}_{\overline{\Xi}^+,\mathrm{propIP}}$ cut are displayed in Figure A.15 in the appendix. The assumption that particles originate from $(0,0,0)$ is only true for simulation. Indeed, in the real experiment the IP distribution will be spread out due to the finite beam and target profiles of $\varnothing_{\overline{\mathrm{p}}\ \mathrm{beam}} \approx 100\,\mu\mathrm{m}$ and $\varnothing_{\mathrm{cluster\ beam}} \approx 1\,\mathrm{cm}$, respectively. This is in the same order as the cut value, therefore the cut on the back-propagation only makes sense when target tracking is introduced to $\overline{\mathrm{P}}$ANDA later with the pellet target and a resolution of $\sigma_{\mathrm{pellet}}(x,y,z) < 0.2\,\mathrm{mm}$.

The determination of the point of closest approach (POCA) can be used to quantify the combination quality of two particles, for instance when kinematic fitters are not available. This POCA method is described in Section 7.4.2.3 and provides the closest distance between the two particle's trajectories as the pocaQA value. Evaluating this for the $\overline{\Xi}^+$ candidate's

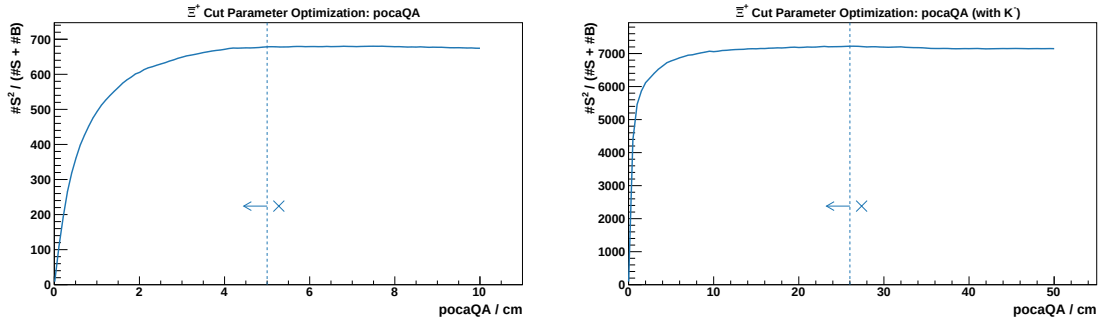

(a) POCA of $\bar{\Xi}^+$ daughters. **(b)** POCA of $\bar{\Xi}^+$ with K^- from Ξ^{-*} branch.

Figure 7.70: The significance optimization distributions for pocaQA values. In the left figure the combination of $\bar{\Xi}^+$ daughters is shown and the combination of $\bar{\Xi}^+$ with K^- in the right one.

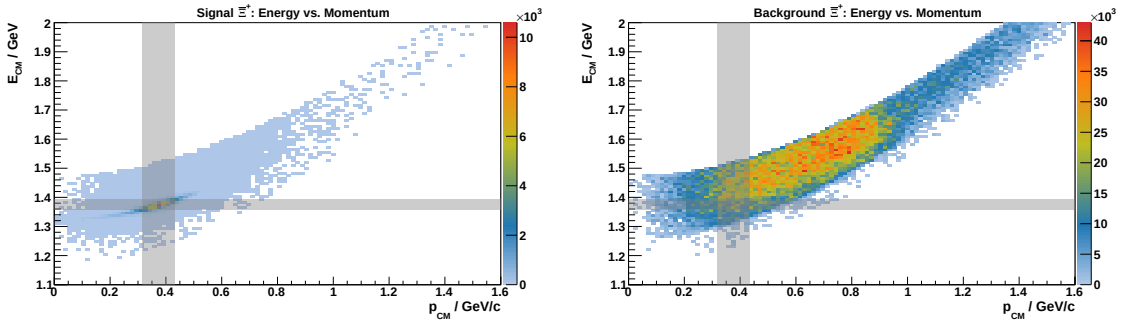

(a) Signal distribution. **(b)** Background distribution.

Figure 7.71: The distributions of energy and momentum in the center of mass frame for signal events (left) and scaled background data (right). The gray bands indicate the cut positions, their overlap is the area of accepted events.

daughters ($\bar{\Lambda}$ and π^+) gives the significance distribution in Figure 7.70(a). The distribution shows a rise until distances of $\sim 5\,\text{cm}$ and then passes into a plateau. Thus, the cut is set there: $\mathcal{C}_{\bar{\Xi}^+,\text{POCA}} = \text{pocaQA} < 5\,\text{cm}$.

Similarly, the pocaQA value of the combination of the $\bar{\Xi}^+$ with a K^- candidate can be investigated. In a signal event, both originate from the same point since the K^- particle's mother, the Ξ^{-*}, is short-living. The significance distribution for varying the corresponding pocaQA cut parameter $\mathcal{C}_{\bar{\Xi}^+,\text{POCA},K^-}$ is shown in Figure 7.70(b). A similar behavior like in Figure 7.70(a) is observable since both parameters originate from the same method. With a maximum significance of $\mathcal{S}_{\bar{\Xi}^+,\text{POCA},K^-} = 7222$ for a cut at $\text{pocaQA}_{K^-} < 26\,\text{cm}$ this cut provides a very beneficial background suppression. If applied, the $\mathcal{C}_{\bar{\Xi}^+,\text{POCA},K^-}$ cut reduces the signal only to 82.1 %, while the background gets suppressed to 4.6 %. However, it is not completely inclusive since it needs the K^- from the Ξ^{-*} decay branch. Therefore, the actual position of the cut is less important but rather the possibility of combining a $\bar{\Xi}^+$ with a K^-. Nevertheless, this cut is reasonable to reconstruct the Ξ^{-*}.

Table 7.9: Overview of the optimized cut parameters for the $\overline{\Xi}^+$ reconstruction. Each cut is optimized individually. The number of events without cuts are $N_{\overline{\Xi}^+,\mathrm{sig}} = 119{,}827$ (24.0 % of all events) and $N_{\overline{\Xi}^+,\mathrm{bkg}} = 32{,}674 \times \mathcal{B}_{\overline{\Xi}^+}$ (0.07 % of all). The background scaling factor is $\mathcal{B}_{\overline{\Xi}^+} = 826.5$.

Cut Parameter	Unit	Condition	$N_{\overline{\Xi}^+,\mathrm{sig}}$ / % (119,827)	$N_{\overline{\Xi}^+,\mathrm{bkg}}$ / % ($32{,}674 \times \mathcal{B}$)	$\mathcal{S}$
$\overline{\Lambda}$ *kinematic cuts*			*100.0*	*100.0*	529
$\overline{\Lambda}$ Decay Vertex: d_{IP}	cm	$x > 2.80$	94.9	67.5	705
POCA($\overline{\Lambda}\pi_1^+$): pocaQA	cm	$7.70 < x$	80.3	50.0	680
POCA($\overline{\Xi}^+\mathrm{K}^-$): pocaQA	cm	$26.0 < x$	82.1	4.6	7222
Prop. to IP: d_{IP}	cm	$0.92 < x$	73.0	21.3	1314
ΔE_{CM}	GeV	$1.357 < x < 1.393$	65.0	4.9	4357
ΔP_{CM}	GeV/c	$0.316 < x < 0.434$	68.3	11.0	2196
Inclusive (no K^-, no back-propagation)			49.9	0.58	16,497
Inclusive (no K^-)			45.5	0.22	26,250
Semi-inclusive (no back-propagation)			41.2	0.10	31,831
Semi-inclusive (all)			37.6	0.05	34,790

Finally, the energy and momentum distributions in the overall CM system are analyzed. Their uncut distribution is shown in Figure 7.71(a). It shows a clear peak at $p_{\mathrm{CM}} = 0.375\,\mathrm{GeV}/c$ and $E_{\mathrm{CM}} = 1.375\,\mathrm{GeV}/c$. In comparison, the background sample is much more spread out and has only a few entries in the signal region. A similar cut optimization is done for E_{CM} and p_{CM} individually as discussed before but now by increasing a symmetric window around the central value of the signal. The so found optimal values are

$$\begin{aligned} \mathcal{C}_{\overline{\Xi}^+,E} &= 1.357\,\mathrm{GeV} < E_{\mathrm{CM}} < 1.393\,\mathrm{GeV} \\ \mathcal{C}_{\overline{\Xi}^+,p} &= 0.316\,\mathrm{GeV}/c < p_{\mathrm{CM}} < 1.434\,\mathrm{GeV}/c \end{aligned}$$

and have a significance of $\mathcal{S}_{\overline{\Xi}^+,E} = 4357$ and $\mathcal{S}_{\overline{\Xi}^+,p} = 2196$, respectively. The cut windows are also shown as gray bands superimposed to the distributions in Figure 7.71. The underlying significance optimization plots are presented in Figure A.16 in the appendix.

The overview of all presented cuts is given in Table 7.9. There, the cut values are given as well as their effect on signal and background events and the significance. Since all cut parameters have been optimized individually, also the effects are displayed independently of other cuts. Combining all cuts together yields in a significance of $\mathcal{S}_{\overline{\Xi}^+,\mathrm{all}} = 34{,}790$. However, this includes the cut on the back-propagation ($\mathcal{C}_{\overline{\Xi}^+,\mathrm{propIP}}$). The distance result from the propagation is obtained under the assumption that the $\overline{\Xi}^+$ hyperon's origin is at exactly $(0,0,0)$. This is true only in simulation, the vertex positions of a realistic experiment will be smeared by beam and target profiles. Leaving this cut out reduces the significance only a little to $\mathcal{S}_{\overline{\Xi}^+,\mathrm{no\ propIP}} = 31{,}831$. With this cut combination, the background is reduced to 0.1 % while 41.2 % of the signal events survive. In total event numbers, 46,491 signal events and $30 \times \mathcal{B}_{\overline{\Xi}^+}$ fake candidates survive all

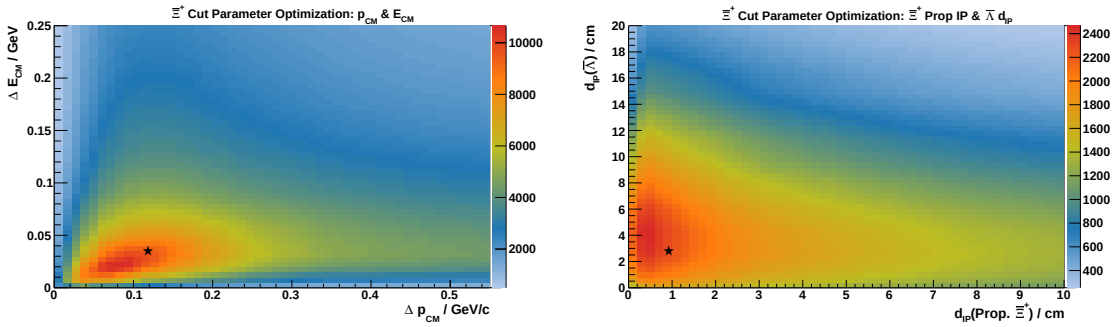

(a) 2D significance scan of $\mathcal{C}_{\overline{\Xi}^+,E}$ and $\mathcal{C}_{\overline{\Xi}^+,p}$.

(b) 2D significance scan of the two distance-to-IP cuts.

Figure 7.72: Two-dimensional cut optimizations for possibly related cuts. The left shows the scan for the center of mass energy (ΔE_{CM}) and momentum (Δp_{CM}) windows. In the right plot, the scan of the $\overline{\Lambda}$ decay vertex distance cut ($\mathcal{C}_{\overline{\Xi}^+,\mathrm{propIP}}$) versus the cut on the back-propagation ($\mathcal{C}_{\overline{\Lambda},d}$) is displayed. In both cases, the black star denotes the individually found optimum.

but the propagation cut. After scaling, the amount of background is roughly half of the signal. The semi-inclusive $\overline{\Xi}^+$ reconstruction with the presented cuts results in 9.3 % efficiency.

7.5.3.2 Cut Interdependence Studies

The investigated cuts are not necessarily independent of each other. That means, an individually optimized cut might change its optimal point when introducing a second cut. Therefore, an n dimensional analysis would be needed for n cuts, simultaneously varying all cuts. This is computational very intensive, so only selected pairs of cut parameters are optimized together. The approach is similar to the one-dimensional process, except that the scan space is now two-dimensional.

Two results of such scans are shown in Figure 7.72. The left comparison is done between the center of mass energy and momentum cuts and the right one for the distance-to-IP cuts ($\mathcal{C}_{\overline{\Xi}^+,\mathrm{propIP}}$ and $\mathcal{C}_{\overline{\Lambda},d}$). A third scan of the pocaQA cuts can be found in Figure A.17 in the appendix. All plots have smooth distributions with no apparent structure apart from the peak. This means that for the investigated combinations, no strong correlations exists that can lead to a significantly worse cut position than the individually found ones. The optimization of the pocaQA cuts does not lead to different values. However, in both cases of Figure 7.72, the previously found best cut value lies slightly outside the peak so that more events are accepted.

The so found significance optima are collected in Table 7.10. Generally, they lead to tighter cuts. This slightly worsens the significance for all individually applied cuts as well as for the combination of all. However, the cuts make a cleaner sample with only 5 background events left (0.02 % of the original candidates). After scaling, this is roughly an eighth of the number of signal events (33,169 or 27.7 % of the original candidates). The reconstruction efficiency of this semi-inclusive channel is then 6.6 %. However, this includes a tight cut on the propagated distance to the IP. Leaving this out leads to $20 \times \mathcal{B}_{\overline{\Xi}^+}$ background and 41,875 signal events, the latter corresponding to an efficiency of 8.4 %.

Table 7.10: Overview of the two-dimensionally optimized cut parameters for the $\overline{\Xi}^+$ reconstruction. The pocaQA values are the same as for the individual optimization presented in Table 7.9.

Cut Parameter	Unit	Condition	$N_{\overline{\Xi}^+,\mathrm{sig}}$ / % (119,827)	$N_{\overline{\Xi}^+,\mathrm{bkg}}$ / % (32,674 × $\mathcal{B}$)	$\mathcal{S}$
$\overline{\Lambda}$ *kinematic cuts*			*100.0*	*100.0*	529
$\overline{\Lambda}$ Decay Vertex: d_{IP}	cm	$x > 4.40$	89.2	62.3	674
POCA($\overline{\Lambda}\pi_1^+$): pocaQA	cm	$7.70 < x$	80.3	50.0	680
POCA($\overline{\Xi}^+\mathrm{K}^-$): pocaQA	cm	$26.0 < x$	82.1	4.6	7222
Prop. to IP: d_{IP}	cm	$0.60 < x$	67.6	18.4	1301
ΔE_{CM}	GeV	$1.363 < x < 1.387$	53.1	3.5	3980
ΔP_{CM}	GeV/c	$0.331 < x < 0.419$	57.7	8.2	2084
Semi-inclusive (no back-propagation)			34.9	0.06	30,023
Semi-inclusive (all)			27.7	0.02	29,494

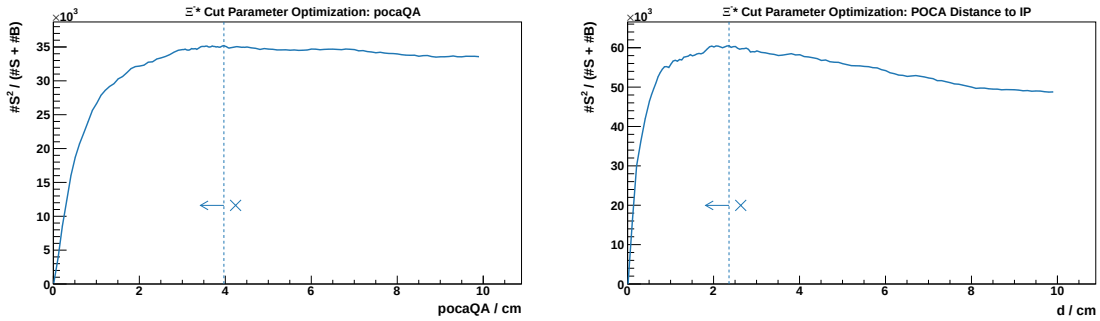

(a) pocaQA. **(b)** Distance to IP.

Figure 7.73: The cut optimizations on the POCA method results of Ξ^{-*} daughters (Λ and K^-).

7.5.4 Inclusive Ξ^{-*} Background Suppression

The Ξ^{-*} candidates are combined from K^- mesons and the Λ baryons remaining from the cuts discussed in Section 7.5.2. This results in $N_{\Xi^{-*},\mathrm{sig}} = 176{,}885$ signal Ξ^{-*} and $N_{\Xi^{-*},\mathrm{bkg}} = 1441 \times \mathcal{B}_{\Xi^{-*}}$ background events. Since the branching ratio is not known for the decay $\Xi^-(1690) \to \Lambda\mathrm{K}^-$, they are scaled with the same factor as for the Λ investigation: $\mathcal{B}_{\Xi^{-*}} = 825.6$. Already the candidate abundance indicates a much better inclusive background suppression for the Ξ^{-*} branch than for the $\overline{\Xi}^+$ branch. This is also represented in the signal's significance of $\mathcal{S}_{\Xi^{-*}} = 22{,}897$.

The Ξ^{-*} decays immediately, hence the event topology is not significantly different from other decay reactions starting from the IP. Nevertheless, the POCA method can be applied to investigate the quality of the daughter particle's combination. The optimization of the cuts on the pocaQA values and the distance of the POCA to the nominal IP are shown in Figure 7.73. Again, the significance values are maximized, leading to cut values of $\mathcal{C}_{\Xi^{-*},\mathrm{pocaQA}} = \mathrm{pocaQA} < 4.0\,\mathrm{cm}$ and $\mathcal{C}_{\Xi^{-*},d} = d_{\mathrm{IP}} < 2.4\,\mathrm{cm}$. The pocaQA has a lower significance with $\mathcal{S}_{\Xi^{-*},\mathrm{pocaQA}} = 35{,}188$

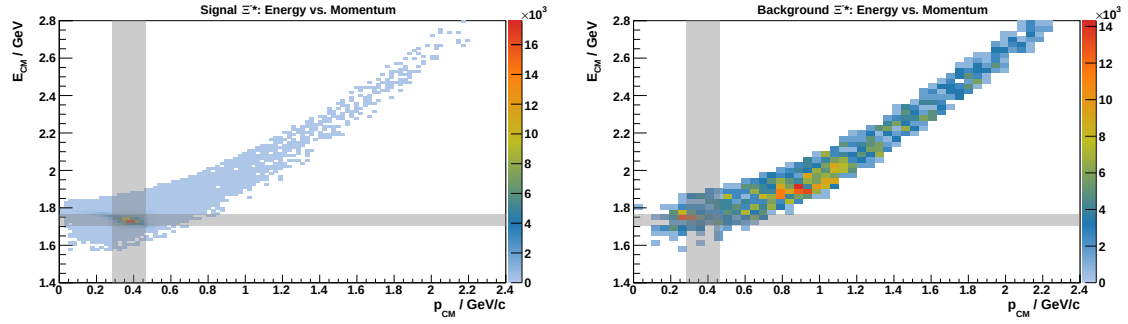

(a) Signal distribution.

(b) Background distribution.

Figure 7.74: The center of mass energy and momentum distributions for signal (left) and scaled background (right). The cut areas are superimposed as gray bands. Due to the low statistics in the background distribution, the bin width is increased.

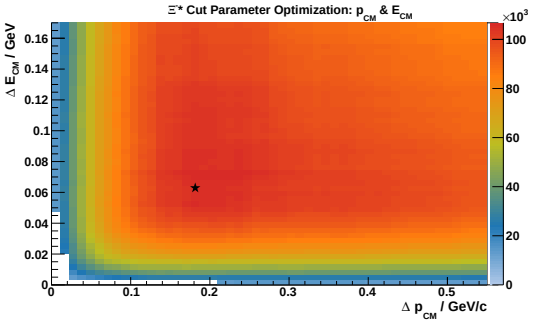

Figure 7.75: The parallel optimization of center of mass energy and momentum cuts. The star indicates the best value from the individual optimizations.

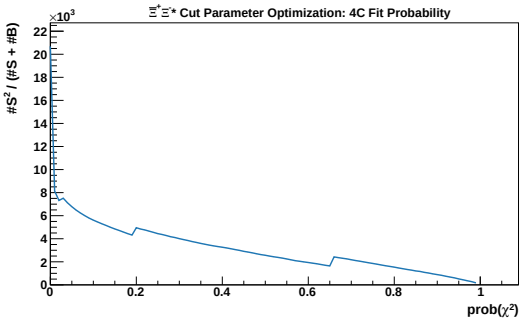

Figure 7.76: The 4C fit optimization of the full system for highest significance $\mathcal{S}$.

compared to the distance cut's significance $\mathcal{S}_{\Xi^{-*},d} = 60{,}499$. However, the latter assumes the production at exactly $(0,0,0)$.

Similar to the $\overline{\Xi}^+$ filtering, the center of mass energy and momentum selection can be applied here as well. First, the two figures of merit are optimized individually by selecting the window around the expected value which provides the highest significance. The plots showing the optimization are in Figure A.18 in the appendix. The resulting cuts are at $\mathcal{C}_{\Xi^{-*},E} = 1.704\,\text{GeV} < E_\text{CM} < 1.766\,\text{GeV}$ for the energy and $\mathcal{C}_{\Xi^{-*},p} = 0.284\,\text{GeV}/c < p_\text{CM} < 0.466\,\text{GeV}$ for the momentum. They both reduce the background drastically to less than 8 % while keeping the signal at 85.5 % (energy) and 82.5 % (momentum), respectively. The good separation is also visible in Figure 7.74 which compares the signal and background distributions. While the signal has a distinct peak within the cut area (gray band), the background data is mostly outside the cut.

Optimizing the two cuts in parallel yields the distribution shown in Figure 7.75. The procedure for obtaining this distribution is the same as described in Section 7.5.3.2. The significance

Table 7.11: Overview of the optimized cut parameters for the Ξ^{-*} reconstruction. Each line shows the efficiency of one parameter individually. The number of events without cuts are $N_{\Xi^{-*},\mathrm{sig}} = 176{,}885$ (35.4 % of all events) and $N_{\Xi^{-*},\mathrm{bkg}} = 1441 \times \mathcal{B}$ (3×10^{-3} % of all). The background scaling factor is $\mathcal{B}_{\Xi^{-*}} = 825.6$.

Cut Parameter	Unit	Condition	$N_{\Xi^{-*},\mathrm{sig}}$ / % (176,885)	$N_{\Xi^{-*},\mathrm{bkg}}$ / % ($1441 \times \mathcal{B}$)	$\mathcal{S}$
Only Λ kinematic cuts			*100.0*	*100.0*	22,897
POCA($\Lambda\pi^-$): pocaQA	cm	$3.97 < x$	75.8	31.6	35,188
POCA($\Lambda\pi^-$): d_{IP}	cm	$2.36 < x$	80.3	16.1	60,499
ΔE_{CM}	GeV	$1.704 < x < 1.766$	85.5	7.8	93,920
ΔP_{CM}	GeV/c	$0.284 < x < 0.466$	82.5	7.7	89,656
Inclusive (no distance to IP)			61.0	1.80	89,990
Inclusive (all)			58.9	1.67	87,560

$\mathcal{S}$ of the two-dimensional scan rises fast to a plateau-like structure. The shallow peak is at roughly $\Delta E_{\mathrm{CM}} \approx 0.06\,\mathrm{GeV}$ and $\Delta p_{\mathrm{CM}} \approx 0.2\,\mathrm{GeV}/c$, so just near the window determined by the individual optimizations (black star in the figure).

All results of the inclusive Ξ^{-*} cut parameter optimization are collected in Table 7.11. It becomes apparent that the cuts on center of mass energy and momentum are the most effective. Combined with the pocaQA cut, they reach a signal-to-background ratio of $\mathcal{S}_{\Xi^{-*},\mathrm{no\ dist}} = 89{,}990$. In absolute numbers, 107,893 signal and $26 \times \mathcal{B}_{\Xi^{-*}}$ background candidates remain in the sample after these cuts. Of the initial Ξ^{-*} candidates, these are 61 % and 1.8 %, respectively. The number of signal events is roughly five times bigger than the scaled background events in the inclusive reconstruction. The inclusive reconstruction efficiency of the Ξ^{-*} signal is at 21.6 % after the mentioned cuts. Including the last condition of $\mathcal{C}_{\Xi^{-*},d}$ as well does not change the result significantly, as seen in Table 7.11.

7.5.5 Exclusive $\overline{\Xi}^{+}\Xi^{-*}$ Background Suppression

The last step of the reconstruction is the exclusive combination of both branches to the full $\overline{\Xi}^{+}\Xi^{-*}$ system. This has an inherently good background suppression because of the low background contribution in the Ξ^{-*} branch. Therefore, only $N_{\overline{\Xi}^{+}\Xi^{-*},\mathrm{bkg}} = 20 \times \mathcal{B}_{\mathrm{all}}$ background signals are available at this last step. Compared with the number of $N_{\overline{\Xi}^{+}\Xi^{-*},\mathrm{sig}} = 41{,}614$ signal events and a scaling factor of $\mathcal{B}_{\mathrm{all}} = 1293$ for the full system, the background is already suppressed by a factor of 1.6 just from the combination.

A four-constraint (4C) fit is applied to the full system to match it with the $\bar{\mathrm{p}}\mathrm{p}$ system's momentum and energy. As already done with the kinematic fits for the Λ, a conservative cut of $\mathcal{C}_{4\mathrm{C}} = \mathrm{prob}(\chi^2) > 0.01$ is applied to remove the most unreasonable combinations. However, optimizing this further fails with the significance method, as it can be seen in Figure 7.76. Due to the low statistics, it is most efficient to leave the cut at this conservative level. This limits the background events to $3 \times \mathcal{B}_{\mathrm{all}}$ and achieves a significance of $\mathcal{S}_{4\mathrm{C}} = 8142$.

Table 7.12: Overview of the cut parameter effects for the $\overline{\Xi}^+\Xi^{-*}$ system reconstruction. The number of events without cuts are $N_{\overline{\Xi}^+\Xi^{-*},\mathrm{sig}} = 41{,}614$ (8.3 % of all events) and $N_{\overline{\Xi}^+\Xi^{-*},\mathrm{bkg}} = 20 \times \mathcal{B}_{\mathrm{all}}$ (4×10^{-5} % of all). The background scaling factor is $\mathcal{B}_{\mathrm{all}} = 1293$.

Cut Parameter	N_{sig} / % (41,614)	N_{bkg} / % ($20 \times \mathcal{B}$)	$\mathcal{S}$
Only $\Lambda,\overline{\Lambda}$ kinematic cuts	*100.0*	*100.0*	25,662
4C cut: $\mathrm{prob}(\chi^2)_{4\mathrm{C}} > 0.01$	26.5	15.00	8142
4C cut + cuts on Ξ^{-*}	17.7	10.00	5441
4C cut + cuts on $\overline{\Xi}^+$	12.1	5.00	4019
All cuts	9.6	5.00	3034

Including the cuts discussed in Section 7.5.4 for the Ξ^{-*} branch reduces the background by one event, a third, and the signal by a third as well. Consequently, the significance shrinks from 8142 to 5441. A similar effect can be seen when including the cuts discussed in Section 7.5.3.2 for the $\overline{\Xi}^+$ without $\mathcal{C}_{\overline{\Xi}^+,\mathrm{propIP}}$: The background is reduced by two down to one remaining event and the signal is roughly halved. Combining all cuts together leaves only $1 \times \mathcal{B}_{\mathrm{all}}$ background event and 4012 signal events, corresponding to a significance of 3034. All numbers are also summarized in Table 7.12.

The exclusive reconstruction efficiency is 2.2 % for the adapted kinematic cuts of the Λ reconstruction and the conservative cuts on the $\overline{\Lambda}$ reconstruction as well as the 4C fit. Additionally including the cuts on the $\overline{\Xi}^+$ branch reduces the efficiency to 1.15 % but also the background by a factor 3. Due to the low number of events remaining after all cuts, it is not clear whether stricter criteria provide a cleaner signal sample. The significance is higher with more conservative cuts, so without the Ξ^{-*} and $\overline{\Xi}^+$ cuts applied, but the amount of signal compared to background stays roughly the same with three times more signal events than background events.

7.6 Summary and Discussion

7.6.1 Summary

This chapter covers the possibility to reconstruct the channel $\overline{\mathrm{p}}\mathrm{p} \to \overline{\Xi}^+\Xi^-(1690)$ with further decays of $\Xi^{-*} \to \Lambda\mathrm{K}^- \to \mathrm{p}\pi^-\mathrm{K}^-$ and $\overline{\Xi}^+ \to \overline{\Lambda}\pi^+ \to \overline{\mathrm{p}}\pi^+\pi^+$. The reaction is investigated for an antiproton beam momentum of 4.1 GeV/c and with a phase space production assumption since no verified model exists, yet. A modified angular distribution was generated as well to test the systematic effects on the reconstruction.

The event generator output is studied to understand the generated event topology. Based on this the expected phase space coverage can be determined and the momentum distributions are obtained. They reveal low momenta for pions, partially below 100 MeV/c. To verify the generation procedure, the Ξ^{-*} invariant mass distribution and the proper decay time distributions of $\overline{\Xi}^+$, $\overline{\Lambda}$, and Λ are produced. They match with the input parameters.

After that, the detector's response is investigated and shows that some of the final state particles are not reconstructible because they leave too few hits for track reconstruction. Since an ideal pattern recognition is used, a filter is applied to continue only with those tracks leaving more than 4 hits in any of the four tracking detectors MVD, STT, GEM, or FTS. The strongest effect of this condition is recognizable for secondary protons and primary pions, both with low momenta. Combining the acceptance for all final state particles reveals an overall probability of 19 % to reconstruct all necessary particles of the full event.

Based on the final state particle candidates, the decay chain is reconstructed until the initially produced $\overline{\Xi}^{+}\Xi^{-}(1690)$ system. For the combination of the Λ and $\overline{\Lambda}$ baryons, kinematic constraints are applied to the daughter particles, rearranging them to originate from a common vertex and have a mass matching the nominal Λ mass. Using a minimal probability of at least 1 % from these fits, a selection of the best Λ and $\overline{\Lambda}$ candidates in terms of the lowest χ^2 can be done. This reduces the data set to 45 % of the events with a good Λ candidate and 39 % with a good $\overline{\Lambda}$ candidate. The selection is crucial for the $\overline{\Lambda}$ reconstruction since a multiplicity of two π^+ mesons in the final state leads to a wrong combination roughly every third event. The momentum resolutions after the cuts are around 2.5 % in transverse and 1.6 % in longitudinal direction.

For the $\overline{\Xi}^{+}$ and Ξ^{-*}, the kinematic fitters are not applicable because the current algorithms cannot combine neutral daughter particles. Therefore only a mass filter of $\pm 150\,\mathrm{MeV}/c^2$ around the mean nominal mass is applied. Several observables are investigated, among others the quality of a point of closest approach (POCA) determination for the daughter particles and for the $\overline{\Xi}^{+}$ the back-propagation to the interaction point (IP). Especially the combination of the $\overline{\Xi}^{+}$ with the K^- provides a good tool to reconstruct the real IP. This inclusive reconstruction works in 38 % of the events for the Ξ^{-*} and in 24 % for the $\overline{\Xi}^{+}$.

Combining both Ξ hyperons to the initial system is possible in 9 % of the events. With the known input parameters, a four-constraint (4C) fit becomes possible. Selecting again only those candidates with a fit probability of more than 1 % leaves 2.3 % of the events for a full exclusive reconstruction. Applying the 4C fit improves the momentum resolution of the full system from 3.0 % to 2.2 % in transverse and from 1.6 % to 1.0 % in longitudinal direction. However, the mass resolution worsens by a factor of around 1.6 from $3.3\,\mathrm{MeV}/c^2$ to $5.6\,\mathrm{MeV}/c^2$ for the Ξ^{-*}.

The MVD's involvement on the reconstruction of this decay channel with delayed vertices can be concluded to a negligible improvement to the momentum resolution but a better vertex resolution due to the hit points close to the decay vertices. Also the purity of the shown distributions is increased by suppressing outliers in the tails of the distributions significantly. Overall, requiring a contribution from the MVD reduces the statistics. Especially the number of $\overline{\Lambda}$ baryons are reduced by a third, mainly because 26 % decay outside the MVD's functional volume.

The reconstruction efficiency is investigated for systematic effects in the polar angle distribution. This is done for the exclusive and inclusive Ξ^{-*} reconstruction. Both show a relatively flat distribution around the average values of 2.3 % and 38 %, respectively. However, small structures are visible, especially in backwards direction of the Ξ^{-*} for the inclusive distribution

Table 7.13: Overview of the reconstruction efficiencies of the different stages of the reconstruction after applying the presented cuts.

Particle	N_{sig} (ϵ_{sig})	N_{bkg} (ϵ_{bkg})	$\mathcal{S}$
Generated	499,750 (100 %)	47,367,000 (100 %)	
Λ	210,761 (42.2 %)	270,433 (0.6 %)	199
$\overline{\Lambda}$	194,907 (39.0 %)	317,156 (0.7 %)	145
Ξ^{-*}	107,893 (21.6 %)	26 (5.5×10^{-7})	89,990
$\overline{\Xi}^+$	41,875 (8.4 %)	20 (4.2×10^{-7})	30,023
$\overline{\Xi}^+\Xi^{-*}$, only 4C cut	11,011 (2.2 %)	3 (0.6×10^{-7})	8142
$\overline{\Xi}^+\Xi^{-*}$, $+\overline{\Xi}^+$ cuts	4012 (0.8 %)	1 (0.2×10^{-7})	3034

with higher statistics. This is confirmed with a modified input distribution with a maximum forward boost of the $\overline{\Xi}^+$. Also here, backwards emitted Ξ^{-*} show a higher reconstruction efficiency. Nevertheless, also in this case the original angular distribution can be extracted from the reconstruction.

Finally, the expected non-resonant background is analyzed. Out of 47×10^6 generated DPM events, only 3 system candidates remain by applying the conservative cuts introduced in the event analysis. After appropriate scaling, this is equivalent to 3879 background events for 11,011 reconstructed $\overline{\Xi}^+\Xi^{-*}$ events. However, an investigation on the possibilities to further suppress background, especially in the inclusive reconstruction, is carried out. Cut parameters are optimized based on their significance for a good signal-to-background ratio. Selectively, a two-dimensional cut parameter determination is done as well. The inclusive reconstruction of Ξ^{-*} achieves a background suppression of approximately a factor 5 with a reconstruction efficiency of 21.6 %. In the $\overline{\Xi}^+$ branch, the efficiency is lower with 8.4 % but still twice as much signal as background. However, this is reached by a semi-inclusive combination with a K^- from the other branch. Using this cut for the exclusive reconstruction as well reduces the number of background events to only 1 candidate which, after scaling, is roughly a third of the number of signals events. However, the significance is reduced by more than a factor two. The efficiencies and significance values of all steps of the reconstruction are collected in Table 7.13.

7.6.2 Discussion and Outlook

The reconstruction of the $\bar{p}p \to \overline{\Xi}^+\Xi^-(1690)$ channel shows to be reliable. The signal can be reconstructed cleanly even with only rudimentary cuts to reject unreasonable combinations. This analysis has revealed problems in the reconstruction including a mixture of neutral and charged particles. Not only the vertex fitting algorithms at this stage of development are incomplete but also the 4C fitter shows partially unexpected results with the worsening of the mass resolution. More thorough investigations on the origin of this behavior need to be done.

Also the cuts in this analysis can be optimized further to improve background suppression. Several observables are shown that are expected to be good candidates for signal filtering. However, more input from background data simulation would be needed.

The reconstruction's main limitation is the combined acceptance of all final state particles, limiting the efficiency already to 19 %. After the presented full reconstruction chain and the optimization of cut parameters, the efficiency shrinks to 2.2 % for the exclusive reconstruction. Since ideal pattern recognition is used in this analysis, a further reduction is expected and the efficiency can be seen as an upper limit. When algorithms for realistic pattern recognition with displaced vertices are available, a more genuine value for efficiency can be determined.

Combining the reconstruction efficiency of this channel $\epsilon_{\overline{\Xi}^+\Xi^{-*}} = 0.022$ with the known branching ratios BR = 0.408 and the assumption of a production cross section of $\sigma_{\overline{p}p\to\overline{\Xi}^+\Xi^{-*}} = 1\,\mu b$ reveals the expected signal detection ratio. The number of signals per second is given by

$$N = \mathcal{L} \cdot \sigma_{\overline{p}p\to\overline{\Xi}^+\Xi^{-*}} \cdot \mathrm{BR} \cdot \epsilon_{\overline{\Xi}^+\Xi^{-*}} \,,$$

with the luminosity $\mathcal{L} = 2 \times 10^{32}/(\mathrm{cm}^2\,\mathrm{s})$ in HESR's high luminosity mode. This results in a ratio of up to 2 detectable signal events per second or 6756 per hour. Even with the low luminosity mode of $\mathcal{L} = 1 \times 10^{31}/(\mathrm{cm}^2\,\mathrm{s})$ the number of detectable signal events can be up to 338 per hour. The efficiencies of pattern recognition, particle identification, and further reduction by background optimized cuts are not taken into account here.

Nevertheless, this channel provides a high production rate with very good intrinsic background suppression. Even inclusively it is possible to reach a two to five times higher signal than spurious background rate. Hence, data with large statistics can be taken and an accurate determination of the angular distribution becomes possible. This will aid in the verification and formulation of production models for the $\overline{p}p \to \overline{\Xi}^+\Xi^{-*}$ and ultimately improve the understanding of strong interactions in hyperons.

8 Conclusions

Three main topics are discussed in this thesis: the development of the readout ASIC PASTA for the MVD strip sensors, the preparations of the JDRS readout system to test PASTA in the laboratory, and the investigation of the reconstruction performance of the channel $\bar{p}p \rightarrow \bar{\Xi}^{+}\Xi^{-}(1690)$ with PandaRoot.

8.1 PASTA Development

The development for the MVD's microstrips readout solution, the $\bar{P}$ANDA Strip ASIC, is described in Chapter 5. The ASIC is based on a predecessor front-end, the TOFPET ASIC, and has been vastly modified for use in $\bar{P}$ANDA. This involves an adapted analog front-end to match the different sensor parameters but also many enhancements in the digital part.

In the course of this thesis, a major goal was the implementation of radiation protection measures for the operation in a radiation-intense environment. For that, operation critical flip-flops have been identified and protected with TMR or Hamming encoding, depending on the register length. The protection has been verified with randomly inserted glitches to simulate SEUs in those flip-flops. The stability of the operation with the included measures could be confirmed.

The TDC controller, as the block that autonomously controls the data taking procedure, has been completely redesigned based on the experiences gathered with the predecessor front-end. Besides shrinking the footprint to around 20 % of the original size, the detection efficiency of the circuit has been improved as well. Before, events in a window of around 6 % in one clock cycle were missed. According to simulations, the introduced synchronization circuit solves this issue in PASTA. Overall, the new design of the two digital parts, the TDC controller and the global controller, could be advanced significantly in terms of area and power consumption. The complete ASIC is expected to consume in the range of 3 mW/ch to 4 mW/ch, which is within the limits of the maximum cooling capacity of the MVD of 4 mW/ch.

After successfully submitting PASTA in spring 2015 to the foundry for production, it is expected to be delivered in the third quarter of 2015. Extensive laboratory measurements will follow to confirm its operability and verify the effectiveness of the implemented changes. The closing

of the efficiency gap can be confirmed by injecting signals with a controlled phase to the clock. Varying this phase should not affect the detection efficiency of the system. The radiation hardness will be tested with radioactive sources for SEUs and irradiation effect measurements after irradiating with controlled total ionization doses. Further optimizations for a followup prototype of PASTA can be in the area of data handling. The dynamic ranges of the transmitted data and the internal buffer capacity should be fitted to the needs of the operation in the MVD.

8.2 JDRS Advancements

The Jülich Digital Readout System is generally intended for laboratory and test beam measurements with readout ASICs and specifically planned for the PASTA characterization measurements. Therefore, the system has been optimized and prepared for the first PASTA prototype, which is the topic of Chapter 6.

The generic improvements concern the data handling of the system. The initial proprietary communication link has been replaced with a standard compliant Ethernet connection using the UDP protocol for data formatting. This makes the system more flexible and easier to setup because only standard PC hardware is required. Along with this change, a simplification of the FPGA firmware's internal buffer structure has come to make adaptations for other prototypes simpler.

The changes have been tested with the ToPix 4 prototype in a proton beam at COSY. Connection-wise, the system ran stably and performed with data rates of up to 6.3 Mbit/s, which ultimately was limited by the beam intensity and ToPix data output, and not by the connection bandwidth. A performance test without a connected readout front-end indicates that the system is able to transmit up to 45 Mbit/s of signal data.

In anticipation of the upcoming PASTA characterization measurements, a modification of the system's data structure towards PASTA has been started. This involves the implementation of an encoder for the 8b/10b-encoded data stream and an extension of the GUI for the configuration parameters. However, these adaptations are only tested in simulations as the physical ASIC and the required adapter board are not yet available. As soon as the produced PASTA prototype becomes accessible, the JDRS's adaptations will be finished to control and read out the ASIC.

In case future measurements indicate a throughput bottleneck in the readout system, an enhancement is possible in the firmware's communication structure. As of now, only one Ethernet package with data is sent back from the firmware to the PC per request. Automatically sending multiple packages is expected to significantly increase the throughput of the system.

8.3 Reconstruction of $\bar{p}p \to \bar{\Xi}^{+}\Xi^{-}(1690)$

In Chapter 7, the reconstruction performance of an excited hyperon in the reaction $\bar{p}p \to \bar{\Xi}^{+}\Xi^{-}(1690)$ with $\bar{P}$ANDA has been investigated, using the PandaRoot framework.

The signal data from the event generator for a beam momentum of $p_{z,\mathrm{beam}} = 4.1\,\mathrm{GeV}/c$ is examined and the detector response simulated. Ideal tracking and particle identification is

used because realistic algorithms are still under development. The response of the four tracking detectors MVD, STT, GEM, and FTS is investigated, revealing an essential contribution from the GEM stations for tracking. This is caused by the event topology with many delayed vertices, which is most pronounced for the $\overline{\Lambda}$ baryons of which 26 % decay outside the MVD's detector volume.

Following, the reconstruction of the full event is presented. It starts with the combination of final state particles to Λ and $\overline{\Lambda}$ candidates. Vertex and mass constraint fits are applied to reject wrong combinations. The vertex fitting of the next stage towards Ξ^{-*} and $\overline{\Xi}^{+}$ candidates fails because the algorithms employed in PandaRoot do not yet work with neutral daughter particles. Hence, other parameters are investigated that provide potentially good selection criteria for background suppression, like the back-propagation to the nominal IP or the combination quality of the $\overline{\Xi}^{+}$ with a K^{-}. Finally, the Ξ^{-*} and $\overline{\Xi}^{+}$ are combined and a four-constraint fit is applied to match the combined system with the initial beam-target system. The signal reconstruction efficiency for the whole procedure is 2.3 %.

Since the production model is still to be determined, the events are generated with a uniform angular distribution according to a homogeneous phase space production. The angular distribution after the exclusive reconstruction shows an approximately flat efficiency with only a slight increase towards the backwards direction of the Ξ^{-*}. However, more statistics would be needed to better resolve the efficiency distribution. In addition to the uniform distribution, a comparison is done with a modified input distribution that prefers forward boosted $\overline{\Xi}^{+}$ hyperons. Again, the reconstructed angular distribution reasonably well resembles the input but shows a slight excess towards backwards emitted Ξ^{-*}.

Methods to suppress the non-resonant background are investigated. With a DPM data sample, different cut parameters are discussed both for inclusive and exclusive reconstruction. The exclusive signal reconstruction efficiency is 2.2 % by requesting only conservative conditions on the performed fit qualities. This already reduces the 47.4×10^{6} simulated DPM events to 3. After including the optimized cuts, this is further suppressed to 1 event, albeit keeping the ratio of threefold more signal events compared to background events. Further optimization on the cuts can be done by simultaneously optimizing multiple cut parameters. However, this would require more background data. Moreover, the algorithms and detector description are still under development and more accurate predictions will be possible in the future. The discussed parameters can provide good starting points for such optimizations.

An unexpected feature that has been discovered during the analysis is the widening of the invariant mass distribution after the 4C fit while other observables are not affected. It is likely that the presence of the neutral Λ particles in the decay tree causes the algorithms to behave unexpectedly, like it has been seen with the vertex fitter. Hence, further investigations are needed to clarify this aspect.

In conclusion, the reconstruction of the reaction $\bar{p}p \to \overline{\Xi}^{+}\Xi^{-}(1690)$ provides a good tool for probing hyperon interactions and providing new experimental data. Even though the reconstruction efficiency of the full system is quite low at 2.2 % by requiring conservative cuts, it is compensated by the high production cross section and the inherent good background suppression. This leads to an expected rate of 6756 reconstructed events per hour with a luminosity of $\mathcal{L} = 2 \times 10^{32}/(\mathrm{cm}^2\,\mathrm{s})$.

Additional Plots

A.1 Production Cross Section for $\bar{p}p \to \bar{\Xi}^{+}\Xi^{-}$

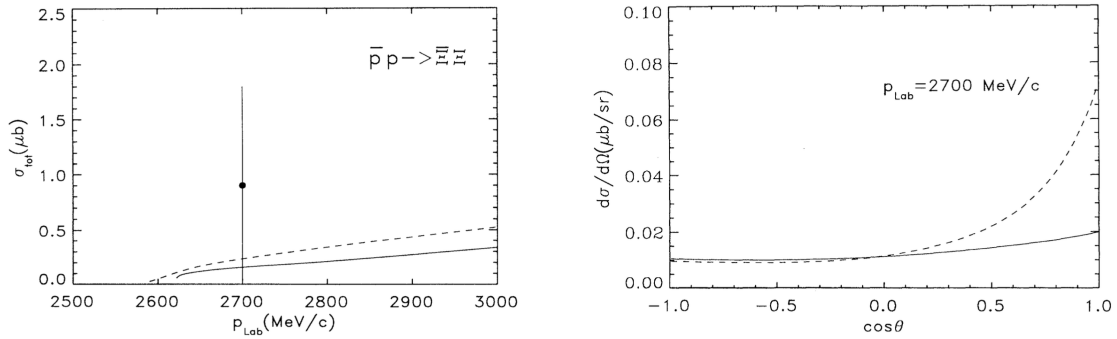

(a) Cross section for different beam momenta.

(b) Angular differential cross section.

Figure A.1: Total σ_{tot} and differential cross section $\frac{d\sigma}{d\Omega}$ predictions for cascade production in antiproton proton annihilation with a scalar meson exchange model. $\bar{p}p \to \bar{\Xi}^{+}\Xi^{-}$ shown with a solid, $\bar{p}p \to \bar{\Xi}^{0}\Xi^{0}$ with a dashed line. Images from [19].

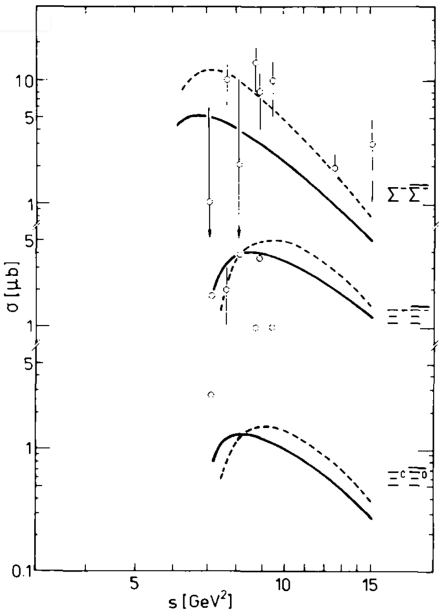

Figure A.2: Total cross section prediction with a quark model exchanging gluons. Two calculation methods are applied: using a wave function (solid) or an overlap integral parametrization (dashed). Image from [22].

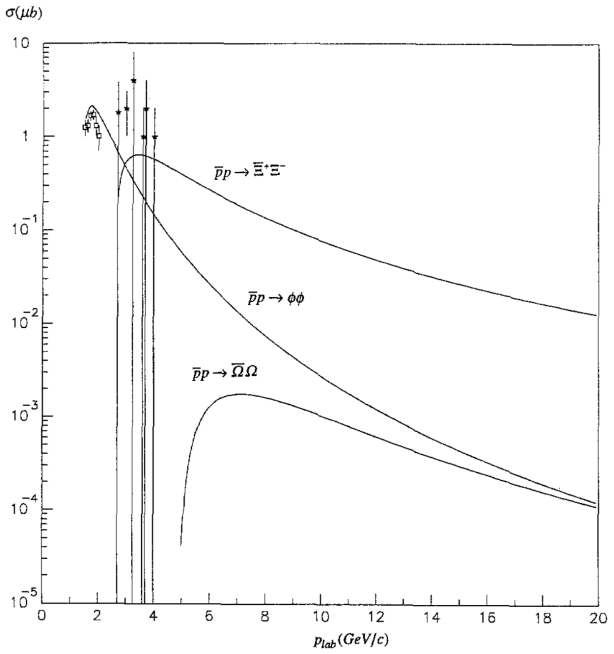

Figure A.3: Total cross section σ_{tot} prediction for hyperon production in antiproton proton annihilation with vector meson exchange. Image from [23].

A.2 Phase Space Influence on the Breit-Wigner Distribution

The invariant mass distribution of a short-living state generally follows a Breit-Wigner function

$$f(M) = \frac{\Gamma}{(M-\langle M\rangle)^2 + \frac{1}{4}\Gamma^2}\,, \tag{A.1}$$

with the invariant mass M, the mean mass $\langle M\rangle$ and the width Γ. However, the decay rate of the particle also depends on the volume of available phase space $\mathrm{d}\Phi_n$ for n daughter particles [1]:

$$\mathrm{d}\Gamma = \frac{(2\pi)^4}{2M}\,|\mathcal{M}|^2\;\mathrm{d}\Phi_n(P;p_1,\ldots,p_n)\,. \tag{A.2}$$

The factor $|\mathcal{M}|^2$ refers to the amplitude from the Lorentz-invariant matrix element.

For a two-particle decay, as it is for $\Xi^-(1690)\to\Lambda\mathrm{K}^-$, Equation A.2 can be simplified to

$$\mathrm{d}\Gamma = \frac{1}{32\pi^2}\,|\mathcal{M}|^2\,\frac{|\vec{p}_1|}{M^2}\;\mathrm{d}\Omega \quad\propto\quad \frac{|\vec{p}_1|}{M^2}\;\mathrm{d}\Omega\,, \tag{A.3}$$

with the solid angle $\mathrm{d}\Omega = \mathrm{d}\phi_1\,\mathrm{d}(\cos\theta_1)$ and the momentum $\vec{p}_1$ of the first daughter particle. Due to momentum conservation, the second daughter has the same absolute value of the momentum $|\vec{p}_1| = |\vec{p}_2|$.

The momentum of the daughter particles in the CM frame is directly dependent on the invariant mass of the mother:

$$|\vec{p}_1| = \frac{1}{2M}\sqrt{\left(M^2-(m_1+m_2)^2\right)\left(M^2-(m_1-m_2)^2\right)}\,. \tag{A.4}$$

m_1 and m_2 are the invariant masses of the daughter particles one and two, respectively. In first approximation, this relation follows a linear rise for mass values M above the sum of the daughters masses as it can be seen in Figure A.4. Therefore, it can be parameterized as $|\vec{p}_1| \approx B\cdot M + C$ in this case. The values $m_1 = m_\Lambda = 1115.7\,\mathrm{MeV}/c^2$ and $m_2 = m_{\mathrm{K}^-} = 493.7\,\mathrm{MeV}/c^2$ are used [1].

Since the decay rate is proportional to the daughter particle's momentum (Equation A.3) and shows a linear behavior for rising invariant masses, the Breit-Wigner function from Equation A.1 is extended by a linear term:

$$f(M) = A\cdot\frac{\Gamma}{(M-\langle M\rangle)^2 + \frac{1}{4}\Gamma^2}\;\cdot\;\frac{B\cdot M + C}{M^2}\,. \tag{A.5}$$

A, B and C are constants that are determined by the fit to the invariant mass distribution. This is shown in Figure 7.4 for the invariant mass distribution of the Ξ^{-*} from the event generator.

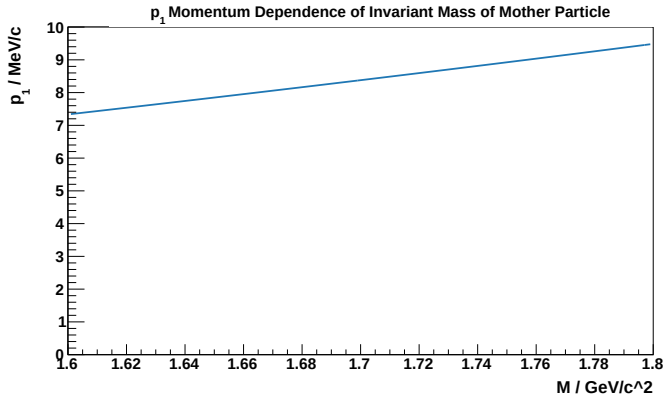

Figure A.4: The momentum of the first daughter particle $|\vec{p}_1|$ as a function of the invariant mass of the mother particle M, according to Equation A.4.

A.3 Event Analysis

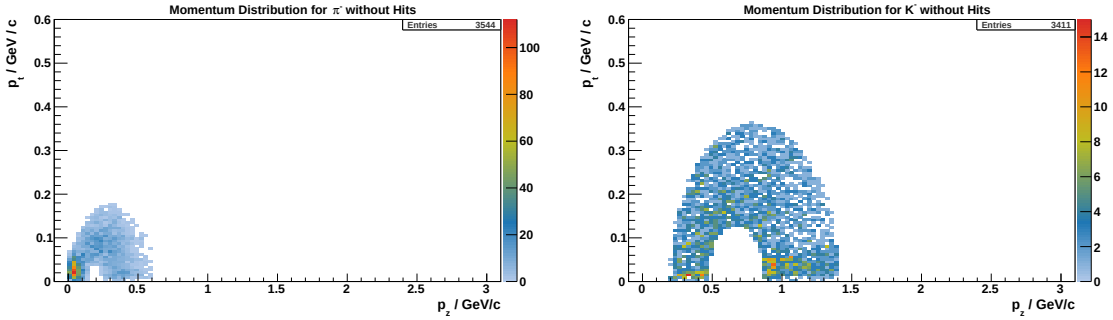

(a) π^-. **(b)** K^-.

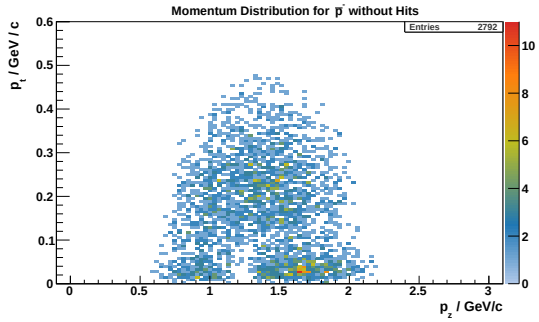

(c) Antiprotons.

Figure A.5: Detector Response: The transverse versus the longitudinal momentum distributions for tracks that generate no hits in any tracking detector.

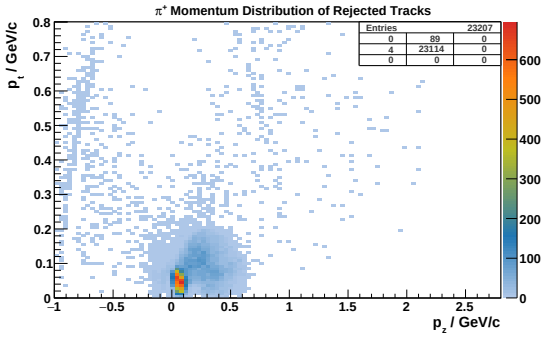

(a) Momentum distribution of rejected tracks for π^+.

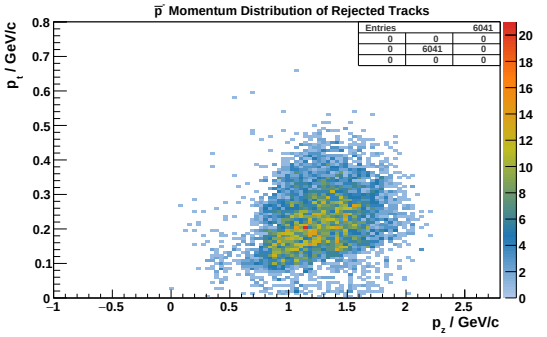

(b) Momentum distribution of rejected tracks for $\overline{\mathrm{p}}$.

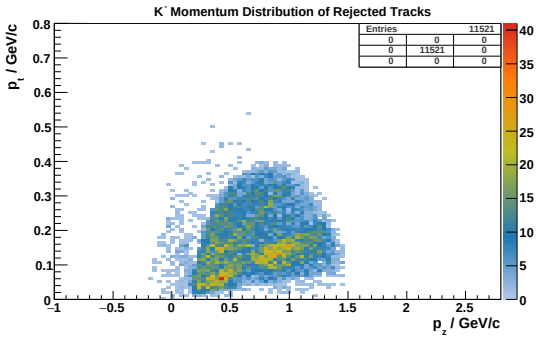

(c) Momentum distribution of rejected tracks for K^-.

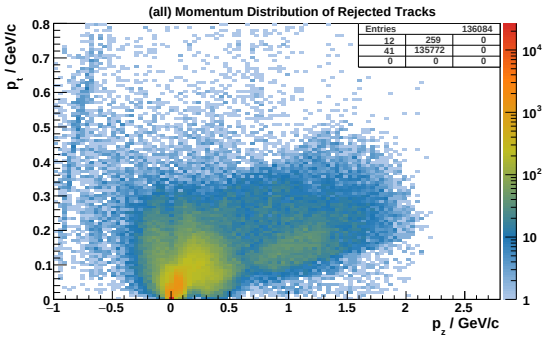

(d) Momentum distribution of rejected tracks for all particles.

Figure A.6: Track Filter: The transverse versus the longitudinal momentum distributions of rejected tracks for π^+, $\overline{\mathrm{p}}$, K^-, and all particles that generate less than 4 but at least 1 hit in any tracking detector.

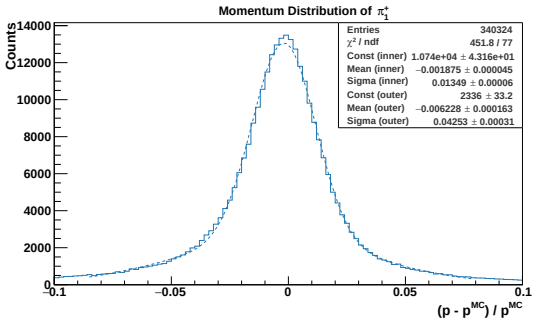

(a) π_1^+: momentum difference distribution.

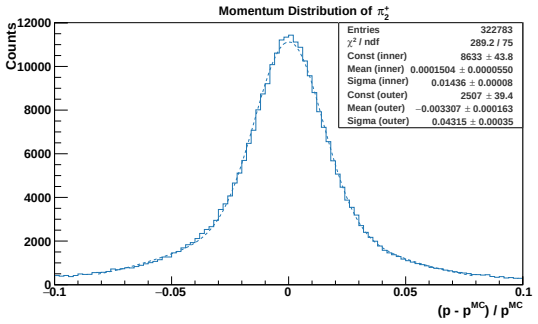

(b) π_2^+: momentum difference distribution.

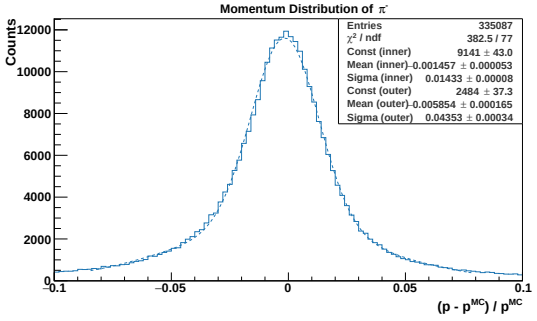

(c) π^-: momentum difference distribution.

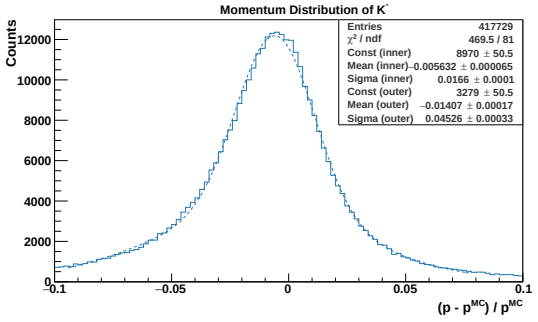

(d) K^-: momentum difference distribution.

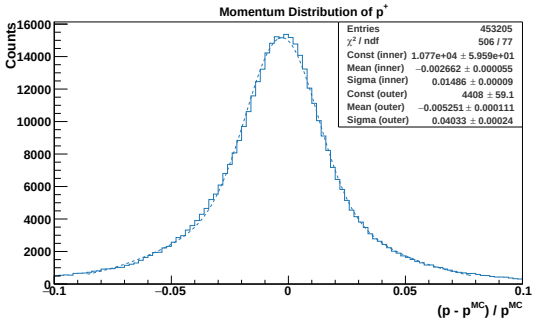

(e) $\mathbf{p}$: momentum difference distribution.

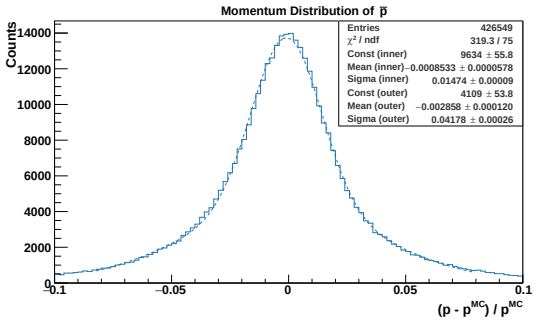

(f) $\bar{\mathbf{p}}$: momentum difference distribution.

Figure A.7: Final State Particles: The relative momentum difference distributions $\Delta p/p$ for all final state particles, each with a double-Gaussian applied.

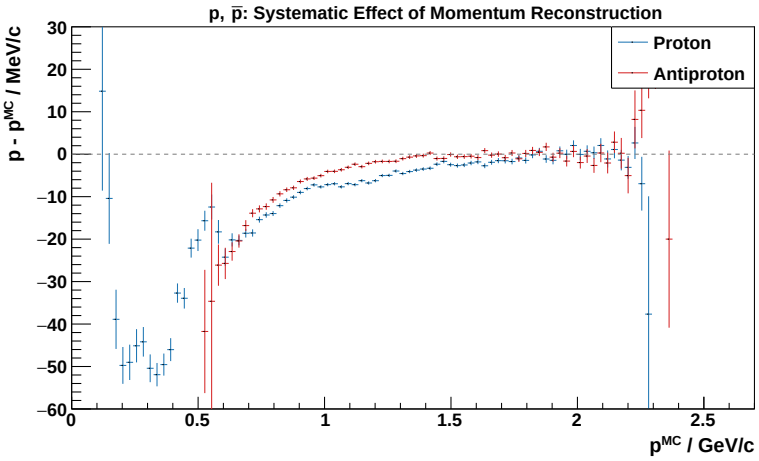

Figure A.8: Final State Particles: The systematic effect of the momentum reconstruction of the final state particles **p** and $\overline{\mathbf{p}}$ as a function of their momentum, displayed as a profile plot.

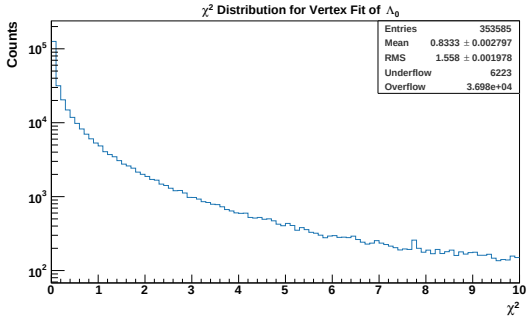

(a) Vertex fit, χ^2 distribution.

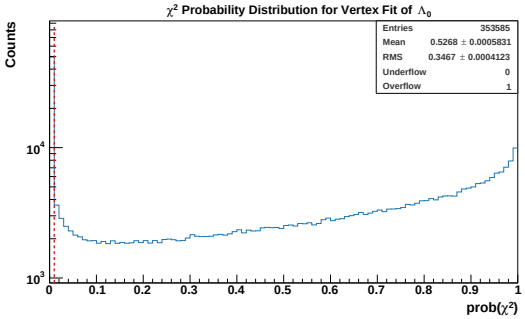

(b) Vertex fit, probability distribution.

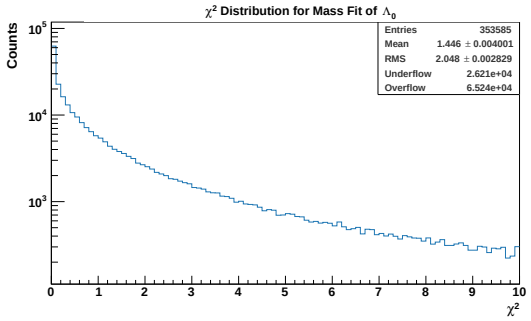

(c) Mass fit, χ^2 distribution.

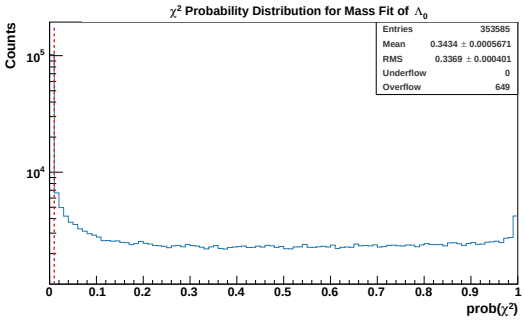

(d) Mass fit, probability distribution.

Figure A.9: Λ Reconstruction: The vertex (top) and mass (bottom) fit qualities for Λ candidates, shown as χ^2 and prob(χ^2) distributions. Only candidates with a probability > 0.01 are considered for the further analysis.

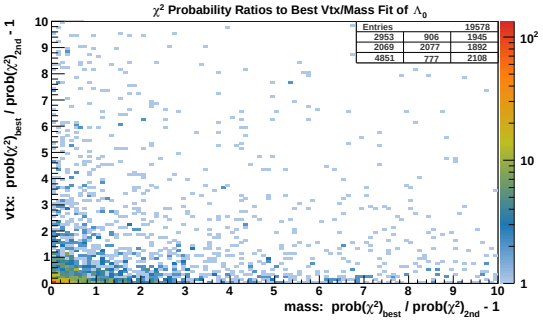

Figure A.10: Λ Reconstruction: The ratios of the best to the second best probability for both vertex (y-axis) and mass constraint (x-axis) fits. Second best probabilities of $<1 \times 10^{-10}$ are fixed to a ratio of $R = -1$, hence they are displayed in the underflows of the histogram.

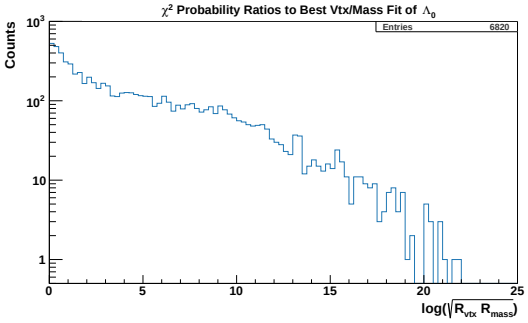

Figure A.11: Λ Reconstruction: The distribution of the geometric mean values of the probability ratios from both fits. The closer the value is to 0, the more equal the first and second best candidates are.

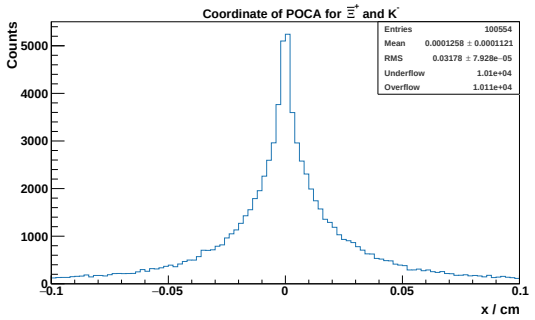

(a) Distribution of the POCA in the x coordinate.

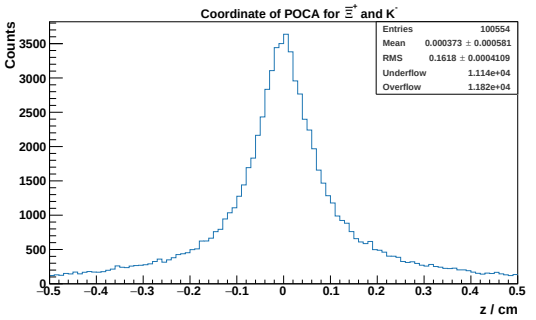

(b) Distribution of the POCA in the z coordinate.

Figure A.12: $\overline{\Xi}^+$ Reconstruction: The POCA position distributions from the combination of the $\overline{\Xi}^+$ candidate with a K^- candidate.

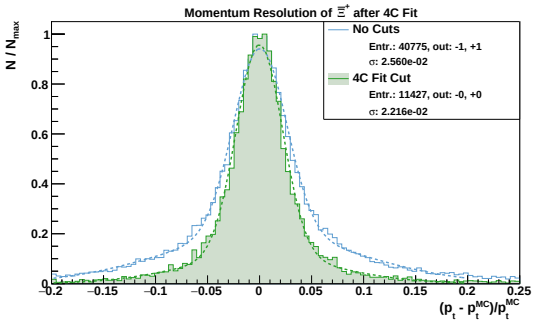

(a) Transverse momentum difference distribution after the 4C fit.

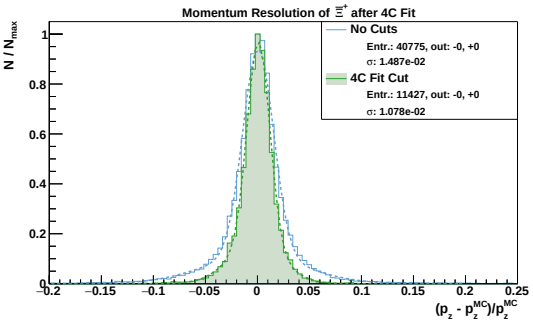

(b) Longitudinal momentum difference distribution after the 4C fit.

Figure A.13: $\overline{\Xi}^+\Xi^{-*}$ System Reconstruction: The relative momentum difference distributions to the generator input for the $\overline{\Xi}^+$ after the four-constraint (4C) fit. The blue distribution shows the difference after fit but without cuts, the green one with the applied probability cut. The histograms are normalized to their maximum bin.

A.4 Background Studies

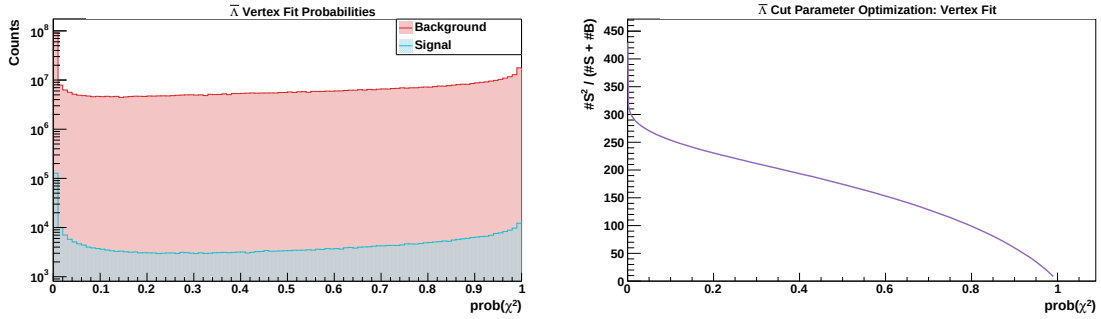

(a) $\overline{\Lambda}$: Vertex fit probability distributions. **(b)** $\overline{\Lambda}$: Vertex fit significance.

Figure A.14: $\overline{\Lambda}$ cut optimization: The vertex fit probability distributions of $\overline{\Lambda}$ candidates for signal (turquoise) and scaled background data (red) on the left and for the significance optimization on the right.

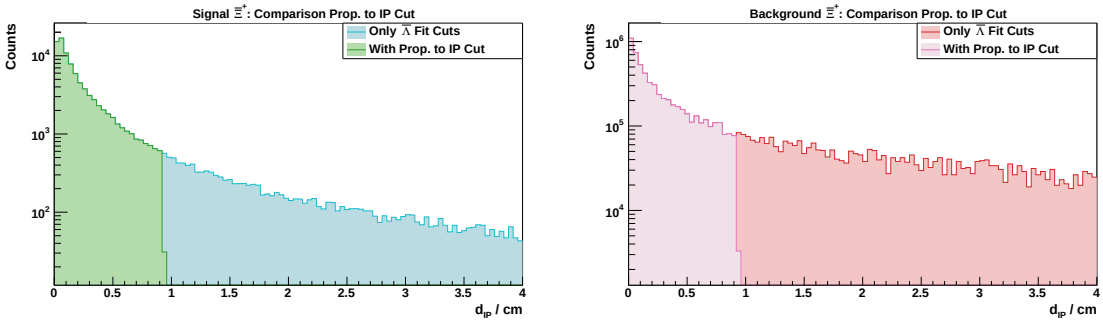

(a) Signal data. **(b)** Scaled background data.

Figure A.15: $\overline{\Xi}^+$ cut optimization: The closest distance distributions of back-propagated $\overline{\Xi}^+$ candidates to the nominal IP. The distributions are shown without cuts (turquoise, red) and superimposed with the distributions resulting from the applied cut (green, pink).

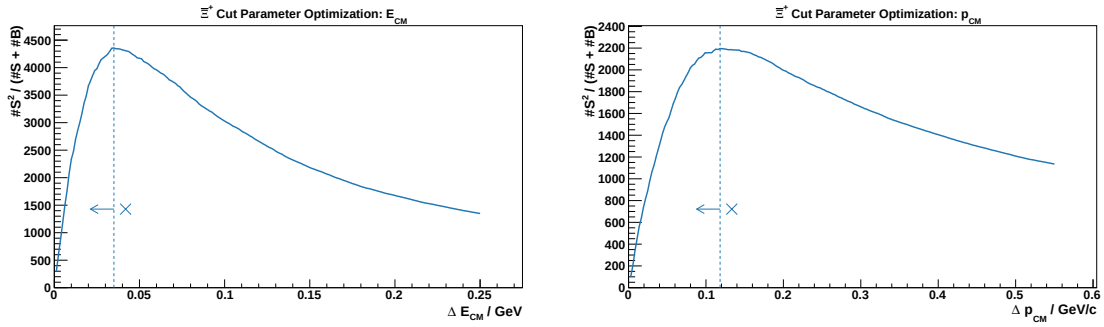

(a) ΔE_{CM} significance optimization. **(b)** Δp_{CM} significance optimization.

Figure A.16: $\overline{\Xi}^{+}$ cut optimization: The center of mass momentum and energy optimizations around the signals central values. The symmetric window's full width is given in the x-axes.

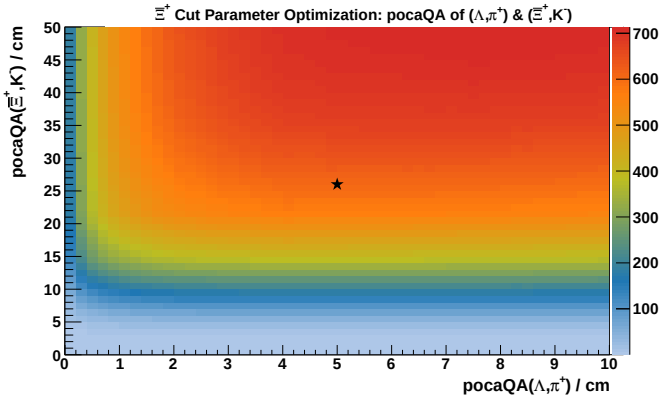

Figure A.17: $\overline{\Xi}^{+}$ cut optimization: Two-dimensional cut optimizations for possibly related cuts. In this plot, the optimization for both pocaQA cuts ($\mathcal{C}_{\overline{\Xi}^{+},\mathrm{POCA},\mathrm{K}^{-}}$ and $\mathcal{C}_{\overline{\Xi}^{+},\mathrm{POCA}}$) is shown. The black star denotes the individually found optimum.

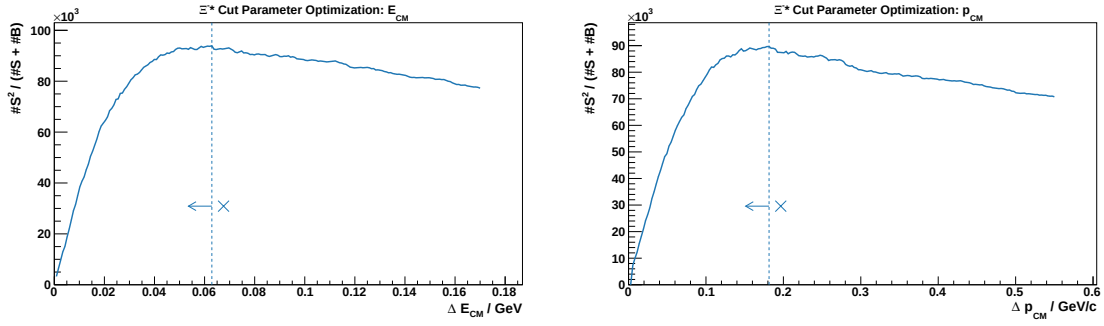

(a) ΔE_{CM} significance optimization. **(b)** Δp_{CM} significance optimization.

Figure A.18: $\overline{\Xi}^{-*}$ cut optimization: The center of mass momentum and energy optimizations around the signals central values. The symmetric window's full width is given in the x-axes.

ASIC Manual B

The functionality of the PANDA Strip ASIC (PASTA) is described in Chapter 5 as the main part of the thesis. This chapter contains additional information as an excerpt from the ASIC's manual. It focuses on the configuration and usage of PASTA.

B.1 Input and Output Connections

B.1.1 Pin Groups and Positions

The ASIC's connection pins can be classified into four categories: supply, sensor, probing, and signal. The location of the pins is shown in Figure 5.24. Differential signals use the LVDS definition.

Supply Pins These pins connect the chip with the external power supply, separated into digital and analog domain, both with ground and power pins (1.2 V). For the current prototype an additional power line with 2.5 V is needed for the LVDS driver.

Sensor Pins These single-ended pins provide connections between the sensor and the input of the channels. Consequently, 64 of these pins exist on the west side of the chip.

Probe Pins The prototype version has a set of probing pins connected to internal signals. In case something in the digital part prohibits the proper signal processing, a direct access to intermediate internal signals is possible (see Section B.1.4 for details). These 15 single-ended probing pins are located on the south side of the chip.

Signal Pins The input and output connections to the readout chain are done with the signal pins. 6 differential inputs and 4 differential outputs (20 pins in total) are located on the east side, see Table B.1 for details.

B.1.2 Reset Signal

The ASIC has a reset input line to set the chip into a defined state. The line is called `SYNC_RST` and is used for two purposes: a *partial* and a *full* reset.

Table B.1: I/O pins for the ASIC's signals on the east side. The location gives the distance from the south side edge.

Name	Location	Description
Outputs		
SDO	889 µm	serial configuration data out
TX1	1026 µm	second serial data output
TX0	1166 µm	first serial data output
CLK_O	1305 µm	main clock output to synchronize data stream
Inputs		
CS	1530 µm	chip select for configuration
SCLK	1670 µm	serial clock input, 10 MHz
SDI	1819 µm	serial configuration data input
CLK_I	1959 µm	main clock input, 160 MHz
SYNC_RST	2099 µm	synchronous reset (see Section B.1.2)
TEST_PULSE	2239 µm	test pulse input

A single clock active high strobe issues a partial reset to reset everything but the configuration. This is particularly useful during operation to synchronize the internal time counter with other chips or an external global counter.

The full reset on the other hand resets everything, including the configuration, and happens after a high strobe of two or more clock cycles. After such a full reset is released, the chip operates in default mode as described in this document.

B.1.3 Data Output

B.1.3.1 Internally Stored Values

The ASIC's event data is based on timestamps. Five timestamps with 10 bits each are needed for an event, as described in Section 5.5.1.1. Additionally, an event requires also general information: The channel number represents the position on the connected inputs and the TAC number is needed for calibration since different instances of capacitors might have slightly different parameters.

Combining this information leads to seven blocks in the internal storage of one event:

- Time coarse counter ($t_{\text{coarse,T}}$, 10 bit)
- Energy coarse counter ($t_{\text{coarse,E}}$, 10 bit)
- Start of conversion (t_{soc}, 10 bit)
- End of conversion, time ($t_{\text{eoc,E}}$, 10 bit)
- End of conversion, energy ($t_{\text{eoc,E}}$, 10 bit)

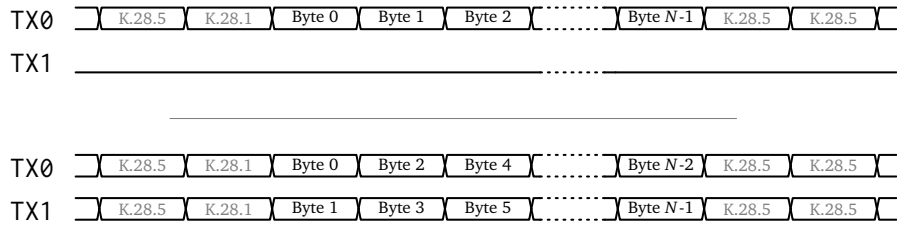

Figure B.1: The output links `tx0` and `tx1` for single (top) or double line (bottom) output.

- Channel ID (n_{ch}, 6 bit)
- TAC ID (n_{TAC}, 2 bit)

This data is embedded into frames, comprising all events across all channels within a time window of 1024 clock cycles. Two modes are employed on how the data itself is structured and compressed: a full mode with two 40 bit words per event and a compact mode with one 40 bit word per event. The format of a frame and the two data modes are described in Section 5.6.4.4.

B.1.3.2 Data Stream Encoding

The data transmitted over the LVDS lines out of the chip is encoded with 8b/10b encoding to ensure a DC-balanced output and enough state changes to enable clock recovery. This is especially useful in periods without data, when the line would be dead otherwise. One feature of this encoding is the alternating structure of transmitted symbols based on a running disparity (RD).

The additional bits of the 8b/10b encoding provide the possibility of using special patterns which do not occur in encoded data. These control symbols have a `001111 xxxx` or `110000 xxxx` sequence, depending on the RD. Of this set, two cases of comma words (K.28.1 and K.28.5) are used to fill the space between frames (see Table B.2 for their encoding).

Table B.2: Comma symbols used in 8b/10b encoding for positive and negative running disparity (RD).

Name	neg. RD	pos. RD
K.28.1	`001111 1001`	`110000 0110`
K.28.5	`001111 1010`	`110000 0101`

Just before a frame of data, the control symbol K.28.1 is transmitted. Then the encoded octets follow, each now containing 10 bit. After the frame is finished, K.28.5 symbols fill the gap until the next frame and its precursor K.28.1 arrives. This is also shown in Figure B.1.

B.1.3.3 Output Synchronization

There are two ways how a receiver is able to synchronize to the output data stream. First, the clock output (`CLK_O`) of PASTA may be used which is always synchronous to the data stream. A second method requires changing a bit in the global configuration (bit 30) to activate a repeating training pattern (`0101...`). Similarly to the comma symbols, this pattern cannot appear in the encoded data words.

B.1.4 Probe Outputs

In order to have a possibility to measure internal intermediate signals some probe outputs are available on the southbound pads. There are 14 signals from the TDC controller and one from the global controller. The exact signals are summarized in Table B.3.

Table B.3: Probe outputs available on the south pad line, counting starts on the left.

Number	Connected Signal
14	`payload_r[0]`
13	`COMP_OUT_E`
12	`COMP_OUT_T`
11 to 8	`tac_status[3:0]`
7	`ev_valid`
6	`r_eoc_e`
5	`r_eoc_t`
4	`r_soc`
3	`w_ecoarse`
2	`w_tcoarse`
1	`DOE`
0	`DOT`

B.1.4.1 Global Controller Probe Output

The probe signal from the global controller is hard wired to the last bit of the internal control link shift register (`payload_r[0]`). Incoming configuration commands store the series of bits in this register which then forwards the information to FFs. By probing this signal one is able to see if incoming data through the ASIC control link is recognized as such.

B.1.4.2 TDC Controller Probe Outputs

The probe signals related to the TDC controller on the other hand are not directly connected to internal signals but to a bus spreading over all channels. By configuring the global test configuration (see Section B.3.1) the user can activate this bus (bit 7) and select the channel which is connected to the bus (bits 13 to 8).

Some of the following comments on the selected signals include references to time and energy branches, indicated by a `T/t` or `E/e` in their name.

Discriminator Outputs The signals `DOT` and `DOE` are the outputs of the discriminator after the preamplifier stage for both branches. They are the basis for event detection and indicate if the analog front-end works.

Digital Event Processing Five signals initiate the storage of timestamps: `w_tcoarse` and `w_ecoarse` for the coarse time of both branches, `r_soc` for the start of conversion, and `r_eoc_t` and `r_eoc_e` for the stop of conversion. Additionally, the `ev_valid` signal indicates a valid processed events. If all signals are present for a given event, the channel is most probably operational.

TAC Status The four bit array `tac_status[3:0]` helps to understand the status of the different TAC capacitors. Each bit represents one of those, a `0` means the capacitor is free and ready for an event while a `1` indicates a used state.

Comparator Outputs The comparator output for the recharging stage of the TDC operation is given in `COMP_OUT_T` and `COMP_OUT_E`. They control the stop of this step.

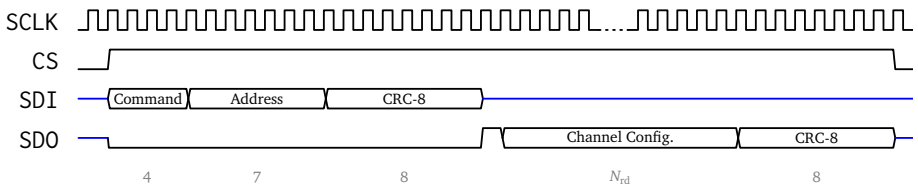

Figure B.2: ASIC control interface with the timing information to read the channel configuration.

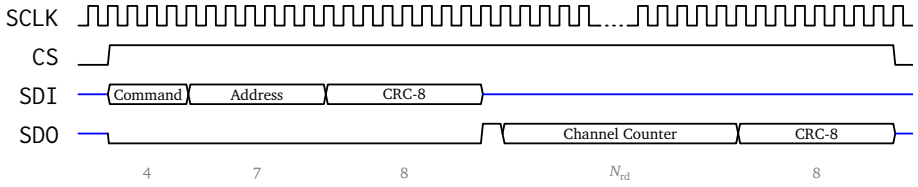

Figure B.3: ASIC control interface with the timing information to read the channel configuration.

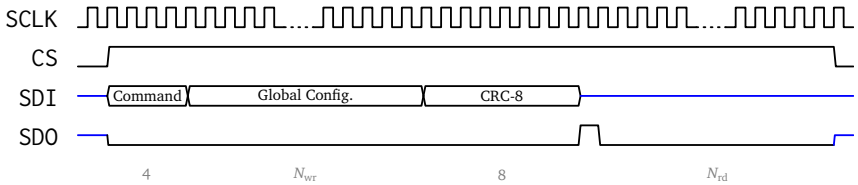

Figure B.4: ASIC control interface with the timing information to write the global configuration.

B.2 Configuration

B.2.1 ASIC Control Link

Configuring the ASIC is done via the ASIC control link. It consists of four lines (`SCLK`, `CS`, `SDI`, and `SDO`) and is independent of the data output and thus the regular operation.

The `SCLK` may be disabled but must be reactivated one clock cycle before chip select (`CS`) and must stay on for at least one clock cycle after `CS` is revoked. The `SDI` input line can be shared with other ASICs while the output `SDO` has to be connected to one receiver only.

Commands sent to the ASIC's control interface follow a general structure: 4 bit command, 7 bit channel address (if applicable), N bit command data (if applicable), CRC-8 (see also Figure B.4). The CRC's polynomial uses $x^8 + x^2 + x + 1$ for division (also used in ISDN communication for instance) and `0x8A` as the initial value. Depending on the command, the command data and sometimes even the channel address is not required and thus the are omitted. An example is requesting the global counter value which only requires the command word itself. The commands are collected in Table B.4.

B.2.2 Global Configuration

The configuration of the ASIC is split into a global and a local channel configuration (the latter is documented in the next section). As the name suggests, the global configuration influences the operation for the whole chip.

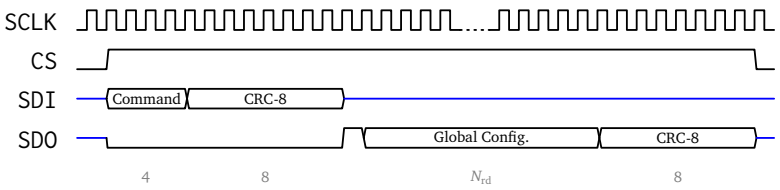

Figure B.5: ASIC control interface with the timing information to read the global configuration.

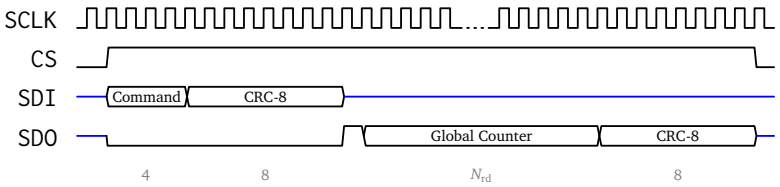

Figure B.6: ASIC control interface with the timing information to read the global counter.

Table B.4: Possible commands to use with the ASIC's control interface.

	Command	Description	Data length N_{wr}	Data length N_{rd}	More Information	Timing
Local	0000	Write channel configuration	41	41	Section B.2.3	Figure 5.19
	0001	Read channel configuration		41		Figure B.2
	0010	Write channel test config.	1	1	Section B.3.2	
	0011	Read channel test config.		1		
	0100	Read channel counter	10	10	Section B.2.2.1	Figure B.3
Global	1000	Write global configuration	172	1	Section B.2.2	Figure B.4
	1001	Read global configuration		172		Figure B.5
	1010	Initiate internal test pulses	26	26		
	1011	Read global counter	10	10	Section B.2.3.4	Figure B.6
	1100	Write global test config.	14	1	Section B.3.1	
	1101	Read global test config.		14		

It consists of two fields, the analog (Table B.5) and the digital settings (Table B.6). While most digital settings switch on or of a certain function, the configuration concerning the analog part controls mostly DACs handling current or voltage levels in a given range. The description together with the default values of the individual settings is done in the mentioned tables.

Table B.5: Overview of the analog global configuration settings (from MSB to LSB), mostly handling DAC settings.

Bit(s)	Default	Description
		analog configuration (TDC)
171 to 167	01001	ILSB: Sets the LSB of the current ratio set locally (Iref_ratio).
166 to 162	01101	Iref_cs: Reference current for the current generator.
161 to 157	10010	Vcas_p: Cascode voltage for the pMOS transistors in the TACs.
156 to 152	10000	Vcas_n: Cascode voltage for the nMOS transistors in the TACs.
151 to 147	11001	Comp_Vcas: Cascode voltage for the latched comparator.
146 to 142	01011	Comp_Vb: Bias voltage for the latched comparator.
		analog configuration (front-end)
141 to 137	11110	BLR_Ib: Bias current for baseline restorer.
136 to 132	10110	BLR_Vcas: Cascode voltage for baseline restorer.
131 to 127	01110	CB_Ib1: Bias current for the input stage of the current buffer.
126 to 122	10101	CB_Ib2: Bias current for the output stage of the current buffer.
121 to 117	01010	CB_Vbias: Bias voltage for the input stage of the current buffer.
116 to 112	01101	CSA_Ib1: First bias current for the charge sensitive amplifier's input stage.
111 to 107	10111	CSA_IbSF: Bias current for the source follower at the output stage of the charge sensitive amplifier.
106 to 103	1001	HCGDAC−: Reference voltage for neg. input to the hystersis comparator.
102 to 99	1111	HCGDAC+: Reference voltage for pos. input to the hystersis comparator.
98 to 94	01000	HC_Ib1: Bias current for the first stage of the hysteresis comparator.
93 to 89	01110	HC_Ib2: Bias current for the second stage of the hysteresis comparator.
88 to 84	10011	HC_Ib3: Bias current for the third stage of the hysteresis comparator.
83 to 89	01101	IfDAC_Ilsb: Current of the LSB for the local feedback current DAC.
78 to 74	10101	IfDAC_Ilsb: Reference current for the local feedback current DAC.
73 to 69	01110	PREAMP_Ifn: Feedback current (n-strip).
68 to 64	01110	PREAMP_Ifp: Feedback current (p-strip).
63 to 59	10001	PREAMP_Ishift: Shift of the preamplifier's output voltage (only n-strip).
58 to 54	01110	PTA_Ibn: Bias current for peaking time adjuster stage (n-strip).
53 to 49	01110	PTA_Ibp: Bias current for peaking time adjuster stage (p-strip).
48 to 44	10101	PTA_Ibuf: Add. buffer current for peaking time adjuster (only n-strip).
43 to 39	01110	ToT_Ib: Bias current for the ToT amplifier.
38 to 33	01111	Vbl: Baseline voltage value.
32	0	FSWITCH: Input signal polarity: '0' for n-strip configuration, '1' for p-strip.
		digital configuration
31 to 0	-	See Table B.6 for details.

Table B.6: Overview of the digital global configuration settings (from MSB to LSB).

Bit(s)	Default	Description
		analog configuration
171 to 32	-	See Table B.5 for details.
		digital configuration
31	1	Enable the clock output `clk_o`.
30	0	Enable the test pattern mode for data output lines.
29	0	When set to '1' a high `CS` acts as a veto and will disable all channels.
28	1	Transmit data in full ('1') or compact event mode ('0').
27	0	Enable counting of SEUs in the global controller.
26	0	Enable counting of truncated events due to a full frame buffer.
25	0	Enable counting of missed events due to a full event buffer.
24 to 21	0000	Counting interval for the channel counter, ranges from 2^{10} ('0000') to 2^{25} ('1111') clock cycles.
20 to 13	x"00"	Subtraction value t_{offset} for the fine counter in compact event mode.
12	0	If set to '1' and in compact event mode, the fine time counter will saturate, if set to '0' it will wrap around.
11	1	Enables clock gating for TDC read logic
10	0	Enables clock gating for TDC write logic
9 to 8	00	Clock divider
7 to 4	0011	Sets the TAC refresh period in a range from 2^{12} ('0001') to 2^{26} ('1111') clock cycles. '0000' deactivates the refresh.
3	1	When set to '1', test pulses from `test_pulse_i` are distributed to all channels, with '0' this input is ignored.
2	0	'0': TX in single data rate (SDR) mode, '1': DDR
1 to 0	00	Sets the TX mode. '00' sends out data only on `tx0_o`, '01' sends also on `tx1_o`, '11' sends a training pattern.

B.2.2.1 Counter Information

The ASIC has a global counter which can count different events that are combined with a logical OR. With the bits 25 to 27 one or more of the following events can be activated:

25: Missed Events By setting this bit to '1', an overflow in the frame buffer is increasing the global counter. The frame buffer is collecting all events in raw format within a frame from the channel buffers.

26: Truncated Events With this bit set to '1', an overflow in the fifo buffer is increasing the global counter. After the data is collected in the frame buffer, it is formatted into the selected data format and transferred to the fifo buffer from where it is sent out eventually.

27: Detected SEU If this bit is set to '1', a detected SEU in one of the protected registers will increase the counter by one. Registers crucial to a stable operation are protected either by Hamming encoding or TMR, both being able to indicate an upset. This pulse can be registered by the counter.

B.2.2.2 Clock Divider and Clock Gating

PASTA's digital timing precision, provided by the clock, can be artificially decreased by an internal clock divider. The benefit of a reduced frequency is less switching activities of FFs and consequently less power consumption. The bits 9 to 8 control this divider, the effect of the possible settings can be seen in Table B.7.

Table B.7: Effect of the clock divider setting (bits 9 to 8) for the achievable digital precision.

Setting	Div.	Digital Precision for 160 MHz
00	1	50 ns
01	$1/2$	100 ns
10	$1/4$	200 ns
11	$1/8$	400 ns

This divided clock doesn't affect the data output, this will always run with the provided external clock to maximize throughput.

The clock enable signals are also handled by the clock divider. They are either high all the time (bit 10/11 set to 0) or they are activated every 16 clock cycles (bit 10/11 set to 1). More details on the effect of the clock enable is described in Section 5.6.3.3.

B.2.2.3 TAC Refresh Period

A refresh is a reset of a TAC capacitor after a set time without an event. The time is given by the configuration bits 7 to 4. If everything is set to zero (0000), the refresh logic is deactivated, otherwise it sets the interval, increasing exponentially. To get the interval length, convert the binary setting to decimal, add 11 and use the result as the exponent of 2.

Examples after how many clock cycles without an event a refresh is issued to a TAC:

- Setting 0001 $\rightarrow 2^{11+1} = 4096$ clock cycles (25.6 µs at 160 MHz)
- Setting 0011 $\rightarrow 2^{11+3} = 16{,}384$ clock cycles (102 µs at 160 MHz)

- Setting `1000` $\rightarrow 2^{11+8} \approx 524$ thousand clock cycles (3.3 ms at 160 MHz)
- Setting `1111` $\rightarrow 2^{11+15} \approx 67.1$ million clock cycles (419 ms at 160 MHz)

B.2.2.4 Data Transfer Modes

The ASIC supports several options for data transmission. All of them affect the throughput of data but on different aspects.

Data Rate The most basic setting is just changing the speed data is being transmitted. If the corresponding bit 2 is set to `0`, a bit is set with the rising edge of the clock, i.e. it lasts for one clock cycle. If however it is set to `1`, the bit is set with each clock edge, i.e. half a clock cycle per bit.

Transceiver Modes The ASIC contains two transceiver lines. The first one (`tx0`) is always active while the second one (`tx1`) is activated with TX mode `01` and deactivated with `00`. The relevant bits for TX mode are 1 to 0. If the mode is set to `11`, a training pattern of `K28.5` words is sent continuously. A more in-depth description on the data transfer can be found in Section 5.6.4.3.

Data Format Finally, the data format itself can be changed. Two modes exist, the compact event mode (bit 28 set to `0`) and the full event mode (`1`). While the full mode aims to send information untouched from the ASIC's internal storage, the compact event mode is making use of dynamic range of the information and removes unnecessary bits. Details on the data format and bit pattern are described in Section B.1.3.

B.2.3 Channel Configuration

Similarly to the global configuration, the local channel configuration consists of digital and analog parts. Information about the effect and default values is in Table B.8.

B.2.3.1 Trigger Modes

Each channel measures timestamps independently from an external trigger source. This requires conditions to match, when a time mark should be stored. In the default operation mode this is controlled by the discriminator output from time and energy branch, hence the name *time trigger* for the first timestamp and *energy trigger* for the second.

By setting the bits 2 to 3, other modes can be selected to store timestamps with other conditions. An overview of this is given in Table 5.5. Common for all is that two values are stored to keep the output data format consistent.

The trigger modes can be grouped into two groups. The first one takes the discriminator output of time and energy branch (`DOT` and `DOE`) as an input[1]. Depending on the mode, it can trigger on the rising or falling edge of each signal. Similarly, the second group uses the external `TEST_PULSE` input. The test mode bit (bit 1) of the channel configuration switches between the two groups.

[1] In other words they use the analog front-end circuitry.

Table B.8: Overview of the channel specific configuration settings (from MSB to LSB).

Bit(s)	Default	Description
		analog configuration
40 to 37	1010	Iref_ratio_e: Fine tuning the TDC's recharging current, energy br.
36 to 33	1010	Iref_ratio_t: Fine tuning the TDC's recharging current, time br.
32 to 28	00000	HCLDAC_e: Differential threshold, energy branch.
27 to 23	00000	HCLDAC_t: Differential threshold, time branch.
22	x	*unused*
21 to 18	1000	If: Fine tuning of the feedback current of the ToT stage.
17	1	Use the delay line for the DOT signal.
		digital configuration
16	0	Enable counting of SEUs.
15	0	Enable counting of refresh signals.
14	0	Enable counting of missed signals.
13	0	Enable counting of discarded events.
12	0	Enable counting of dark events.
11	1	Enable counting of valid events.
10 to 9	00	Delay for the »stop charging« signal in clock cycles.
8 to 7	01	Length of the synchronization chain (# of cascaded FFs). '00': first FF with next rising *or* falling edge of the clock; '01': two FFs, next rising edge after first stage; '10': three FFs, next falling edge after second stage; '11': four FFs, next rising edge after third stage.
6	1	Use the parallel, falling edge triggered FF in the first stage.
5	1	Use hit validation with energy branch in prediction mode.
4	1	Use prediction mode if set to '1' or synchronous mode otherwise.
3 to 2	00	Set the trigger mode, see Section B.2.3.1 for details.
1	0	Enable test mode to use test pulses instead of discriminator outputs.
		channel enable
0	1	Enable this channel

B.2.3.2 Hit Validation

In order to store time stamps from the trigger condition, the event itself has to be classified as valid. There are four different possibilities for a event to be valid, ordered by the sequence of checking.

Test Mode If the test mode (bit 1) is activated, a hit is considered valid when the TEST_PULSE signal is high.

Validation Off In case the validation is turned off (bit 5 set to 0) it does not depend on which of the two discriminator outputs (DOT or DOE) are high, both validate the event.

Prediction Mode This is the default operation mode. By setting bit 4 to 1, an event is valid if both discriminator outputs (DOT and DOE) are high. The delay line has to be activated for this mode to work (bit 17 set to 1).

Synchronous Mode This mode is based on synchronized discriminator output signals. A signal is valid if the synchronous DOT is high and the synchronous DOE is followed not later than two clock cycles. It is seen as an alternative mode to the prediction mode.

More details and background information to these settings can be found in Section 5.5.2.1.

B.2.3.3 Synchronization Chain

The synchronization chain is a construct to prevent signal loss due to timing constraint violations between asynchronous and synchronous circuits. The details are described in Section 5.5.2.3. Setting the bits 7 to 8 selects the length of this chain.

This has two effects: By increasing the amount of involved flip-flops the probability for event loss decreases. The exact dependence has to be determined with the first prototype. The second effect is increasing the fixed time for discharging the TAC capacitor. The fine time is obtained from the time it takes to recharge a capacitor to a known reference voltage. Since the stop signal is obtained by a logical path after the synchronization circuit, the fine time value does not only contain the phase to the clock but also the offset coming from the chain.

The minimum offset is achieved by using the output after the first flip-flop stage (bit setting 00). If both flip-flops in the first stage are active (bit 6 set to 1), the stop signal comes with the next clock edge, independent of rising or falling. Otherwise[2], only the next rising edge is used. The next stages (selected with 01, 10, and 11) use additional flip-flops triggering on the rising, falling, and rising edge respectively, each increasing the offset by half a clock cycle.

The offset does not have to be corrected from the final fine time value because it still gives the distance from the coarse time to the real trigger edge. It just increases the range, the fine time might lay in. The possible ideal[3] ranges for different settings are given in Table B.9.

B.2.3.4 Counter Information

Same as for the global counter configuration, some bits (here bits 10 to 15) control which events are being counted, combined with an OR. The possible settings are:

10: Valid Events In case this bit is '1', a validly processed event in the TDC will increase the counter by one. This doesn't take into account if this event gets lost due to a buffer overflow at a later stage.

11: Dark Events Signals which cross only the lower threshold are called dark events. If the validation (bit 5) is turned on or synchronous mode is selected (bit 4), a dark event triggers the channel counter to increase.

[2] Configuration bit set to 0

[3] Disregarding effects due to latencies.

Table B.9: Possible ranges for fine time values in clock cycles, disregarding latencies. Depending on configuration bit 6, the falling edge triggered flip-flop in the first stage is deactivated which influences the range.

(a) Use parallel FF, bit 6 is **1**.

Sync. Chain	Fine Time Range min		max
00	0.0	...	0.5
01	0.5	...	1.5
10	1.0	...	2.0
11	1.5	...	2.5

(b) do not use parallel FF, bit 6 is **0**.

Sync. Chain	Fine Time Range min		max
00	0.0	...	1.0
01	1.0	...	2.0
10	1.5	...	2.5
11	2.0	...	3.0

12: Discarded Events Setting this bit to '1' a discarded event will increase the counter. Discarding events is a feature from the global controller which is not in use for the first prototype, so this bit has no effect.

13: Missed Events If this bit is set to '1', missed events due to a full event buffer will increase the counter by one. The event buffer is sitting right behind the TDC controller and thus once per channel. It is the first to store the event's timestamps. If this buffer is not read out by the global controller before the next event arrives, the event will get lost.

14: Refresh Signals Each refresh increases the counter by one if this bit is set to '1'. A refresh resets a TAC if it was inactive for a long time.

15: SEUs Same as the SEU counting flag for the global counter, this bit enables counting of upsets in the protected registers specific to the channel. Registers crucial to a stable operation are protected either by Hamming encoding or TMR, both being able to indicate an upset. In case bit 15 is high, such a pulse is then registered by the counter.

B.3 Test Circuits

Additionally to the configuration for regular operation, a set of bits is foreseen for calibrating and testing the channels. Like the regular operation settings, it is divided into a global and local section. Additionally, a command to generate test pulses is available.

B.3.1 Global Configuration

The global configuration refers to a DAC setting regulating the calibration pulse's amplitude and a selection which channel test outputs are forwarded to the test pads on the south side. All bits are described in Table B.10.

B.3.2 Channel Configuration

The channel test configuration consists of just one bit which switches the input of the front-end from the connections to the pads ('0') to using the pulse generated by the calibration circuit ('1').

Table B.10: Overview of global test configuration (from MSB to LSB).

Bit(s)	Default	Description
13 to 8	`000000`	Channel address which should be probed by the southbound pads.
7	`0`	Enable the probing of certain signals from one channel to output pads.
6 to 1	`xxxxxx`	DAC setting for pulse amplitude.
0	`0`	Enable calibration circuitry.

B.3.3 Digital Test Pulse Generator

When the test pulse command is sent to the ASIC (command word `1010`, see Table B.4 in Section B.2.1), a number of digital test pulses are generated internally. After acknowledging the command, the module will generate $N + 1$ pulses, each having a length of $L + 1$ clock cycles and separated by $128 \times (S + 1)$. These three parameters that have to be included into the command are summarized in Table B.11.

Table B.11: The parameter used in the digital test pulse generator. The interval and length is given in clock cycles.

Bit(s)	Par.	Description
25 to 18	S	Pulse spacing ($\times 128$)
17 to 10	L	Pulse length
9 to 0	N	Number of pulses

These test pulses can initiate the data taking process with two different approaches: The digital pulse may be used directly for the event trigger when the test mode is activated (see Section B.2.3.2). Alternatively, the digital pulse will be used to generate by an analog test pulse circuit which is then fed to the input of selected channels.

JDRS Modules

C

C.1 Fan Controller

Being an active electronic component, the FPGA produces heat as a side product. To cool it, a rotating fan is mounted by the vendor (visible in Figure 6.2). In its default setting, the fan is active at full speed as soon as the board is switched on. To reduce the amount of noise, a small regulating module has been introduced.

It exploits a system monitor IP core measuring the temperature close to the FPGA. The output voltage is digitized linearly by an ADC, which is available from the monitor module. It can be transferred to a temperature by Equation C.1 [166]

$$T\,/\,^{\circ}\mathrm{C} = \frac{\mathrm{ADC} \times 503.975}{1024} - 273.15\ . \tag{C.1}$$

Based on this, the fan controller sets the rotation speed with a pulse-duration modulated signal. If the temperature is below 40 °C, the fan's power supply gets a duty cycle of roughly 29 %[1]. As the temperature rises, the speed is increased until it reaches full speed or 100 % duty cycle at 50 °C. Even on hot summer days, the temperature did not exceed 44 °C. According to the data sheet [167], the Virtex-6 FPGA has a maximum junction temperature for operation of 125 °C, therefore well above the chosen temperature limits.

C.2 LCD Controller

Accessing information of the board or connected components is easily achievable via the Ethernet connection. However, sometimes it is necessary to get a more direct response of the system. A module in the firmware provides access to the built-in LCD by initializing it and setting cells to display predefined character patterns. Figure C.1 shows two implemented examples: the

[1] More precisely, the fan gets power for 8 out of 28 clock cycles. The fan needs at least around 25 % duty cycle to start spinning.

(a) Temperature and fan speed. **(b)** IP and MAC addresss. **(c)** Startup bug.

Figure C.1: Two examples of using the LCD which is mounted on the ML605 board. Figure C.1(c) shows the startup bug of improperly addressed cells resulting in character noise.

display of the current FPGA temperature and fan speed, and the current setting of IP and MAC adresses[2].

The current implementation incorporates a so far unsolved bug affecting the startup. Initializing the LCD requires a strict sequence of signals, as documented in [168]. Even though the documented sequence is applied, the first initialization fails and a soft reset (reloading the firmware) has to be performed. After that, the display works as expected.

[2]This is especially handy when initializing a multi-board setup with the readout PCs in a different room as it occurs during beam tests. As long as the connection is not established, no information can be retrieved by the Ethernet connection.

Bibliography

[1] K. A. Olive, K. Agashe, C. Amsler, *et al.*: **Review of Particle Physics**. In: *Chinese Physics C*, **C38**:9 (2014), p. 090001. DOI: 10.1088/1674-1137/38/9/090001 (see pp. 4–7, 9–11, 25, 27, 43, 46–47, 118–121, 124, 131, 146, 153, 181).

[2] Andreas Herten: **GPU-based Online Track Reconstruction for $\bar{\text{P}}$ANDA and Application to the Analysis of D→Kππ**. PhD Thesis. Ruhr-Universität Bochum, Apr. 2015 (see pp. 5, 8–9, 14, 18–19, 21, 24–27, 29–30, 32–33, 38, 42, 52).

[3] **The Nobel Prize in Physics 2004**. Nobel Media AB 2014, Oct. 2004. URL: http://www.nobelprize.org/nobel_prizes/physics/laureates/2004/advanced.html (see pp. 3, 5).

[4] Sheldon L. Glashow: **Partial-Symmetries of Weak Interactions**. In: *Nuclear Physics*, **22**:4 (Feb. 1961), pp. 579–588. DOI: 10.1016/0029-5582(61)90469-2 (see p. 4).

[5] Peter W. Higgs: **Broken Symmetries and the Masses of Gauge Bosons**. In: *Physical Review Letters*, **13**:16 (Oct. 1964), pp. 508–509. DOI: 10.1103/PhysRevLett.13.508 (see p. 4).

[6] **The Nobel Prize in Physics 2013**. Nobel Media AB 2014, Oct. 2013. URL: http://www.nobelprize.org/nobel_prizes/physics/laureates/2013/advanced.html (see p. 4).

[7] Tom W. B. Kibble: **Englert-Brout-Higgs-Guralnik-Hagen-Kibble mechanism**. In: *Scholarpedia*, **4**:1 (Jan. 2009). Revision #91222, p. 6441. DOI: doi:10.4249/scholarpedia.6441 (see p. 4).

[8] ATLAS Collaboration: **Observation of a new particle in the search for the Standard Model Higgs boson with the ATLAS detector at the LHC**. In: *Physics Letters B*, **716**:1 (Sept. 2012), pp. 1–29. DOI: doi:10.1016/j.physletb.2012.08.020. arXiv: 1207.7214v2 [hep-ex] (see p. 5).

[9] CMS Collaboration: **Observation of a new boson at a mass of 125 GeV with the CMS experiment at the LHC**. In: *Physics Letters B*, **716**:1 (Sept. 2012), pp. 30–61. DOI: doi:10.1016/j.physletb.2012.08.021. arXiv: 1207.7235v2 [hep-ex] (see p. 5).

[10] **The Nobel Prize in Physics 1969**. Nobel Media AB 2014, 1969. URL: http://www.nobelprize.org/nobel_prizes/physics/laureates/1969/ (see p. 5).

[11] Francis Halzen and Alan D. Martin: **Quarks and Leptons: An Introductory Course in Modern Particle Physics**. John Wiley & Sons, Inc., 1984 (see p. 6).

[12] KARIN SCHÖNNING, ERIK THOMÉ, and THE PANDA COLLABORATION: **Spin observables in antihyperon-hyperon production with $\bar{\text{P}}$ANDA**. In: *XI International Conference on Hyperons, Charm and Beauty Hadrons (BEACH 2014)*. Vol. 556. 1. 2014. DOI: doi:10.1088/1742-6596/556/1/012007 (see pp. 7, 11).

[13] STEVEN WEINBERG: **Nuclear forces from chiral lagrangians**. In: *Physics Letters B*, **251**:2 (1990), pp. 288–292. DOI: http://dx.doi.org/10.1016/0370-2693(90)90938-3 (see p. 7).

[14] USER E2M: **Meson nonet for spin 0**. Wikimedia Commons, Apr. 2008. URL: https://commons.wikimedia.org/wiki/File:Meson_nonet_-_spin_0.svg (see p. 8).

[15] USER E2M: **Meson nonet for spin 1**. Wikimedia Commons, Apr. 2008. URL: https://commons.wikimedia.org/wiki/File:Meson_nonet_-_spin_1.svg (see p. 8).

[16] USER E2M: **Baryon octet**. Wikimedia Commons, Apr. 2008. URL: https://commons.wikimedia.org/wiki/File:Baryon_octet.svg (see p. 9).

[17] USER WIERDW123: **Baryon decuplet**. Wikimedia Commons, Feb. 2008. URL: https://commons.wikimedia.org/wiki/File:Baryon_decuplet.svg (see p. 9).

[18] T. MELDE, W. PLESSAS, and B. SENGL: **Quark-model identification of baryon ground and resonant states**. In: *Physical Review D*, **77**:11 (June 2008), p. 114002. DOI: 10.1103/PhysRevD.77.114002 (see p. 10).

[19] J. HAIDENBAUER, K. HOLINDE, and J. SPETH: **$p\bar{p} \to \Xi\bar{\Xi}$ reaction in the meson exchange picture**. In: *Physical Review C*, **47**:6 (June 1993), pp. 2982–2985. DOI: 10.1103/PhysRevC.47.2982 (see pp. 10–11, 179).

[20] B. MUSGRAVE, G. PETMEZAS, L. RIDDIFORD, *et al.*: **Study of YY production in two, three and four body final states by 3.0, 3.6 and 4.0 GeV/c antiprotons in hydrogen**. In: *Il Nuovo Cimento Series 10*, **35**:3 (1965), pp. 735–758. DOI: 10.1007/BF02739338 (see pp. 10–11).

[21] HENNING GENZ, MAREK NOWAKOWSKI, and DIANE WOITSCHITZKY: **Proton-antiproton reactions via double annihilation of quarks**. In: *Physics Letters B*, **260**:1–2 (May 1991), pp. 179–185. DOI: http://dx.doi.org/10.1016/0370-2693(91)90988-3 (see pp. 10–11).

[22] P. KROLL, B. QUADDER, and W. SCHWEIGER: **Exclusive production of heavy flavours in proton-antiproton annihilation**. In: *Nuclear Physics B*, **316**:2 (Apr. 1989), pp. 373–390. DOI: http://dx.doi.org/10.1016/0550-3213(89)90036-9 (see pp. 10–11, 180).

[23] A. B. KAIDALOV and P. E. VOLKOVITSKY: **Binary reactions in $p\bar{p}$ collisions at intermediate energies**. In: *Zeitschrift für Physik C Particles and Fields*, **63**:3 (Sept. 1994), pp. 517–524. DOI: 10.1007/BF01580332 (see pp. 10–11, 180).

[24] V. FLAMINIO, W. G. MOORHEAD, D. R. O. MORRISON, and N. RIVOIRE: **Compilation of Cross-Sections III: p and $\bar{p}$ Induced Reactions**. Vol. 3. Updated version of CERN HERA 79-03; contains all data published up to the beginning of 1982. Geneva: CERN, Apr. 1984. URL: https://cds.cern.ch/record/101631 (see p. 11).

[25] BIOMAT PROJECT GROUP: **Technical Proposal for the Design, Construction, Commissioning and Operation of the High-Energy Irradiation Facility for Biophysics and Materials Research**. Tech. Rep. *FAIR-PAC*, Apr. 2005. URL: https://www-alt.gsi.de/forschung/fair_experiments/biomat/TP_BIOMAT_final.pdf (see p. 13).

[26] THE FLAIR COLLABORATION: **Technical Proposal for the Design, Construction, Commissioning and Operation of FLAIR**. Tech. Rep. *FAIR-PAC*, Jan. 2005. URL: http://www.flairatfair.eu/typo3/fileadmin/files/documents/reports/Technical_Report_FLAIR_2005-01-21-final.pdf (see p. 14).

[27] THE HEDGEHOB COLLABORATION: **Technical Proposal for the Design, Construction, Commissioning and Operation of the: HEDgeHOB (High Energy Density Matter Generated by Heavy Ion Beams)**. Tech. Rep. *FAIR-PAC*, Jan. 2005. URL: http://hedgehob.physik.tu-darmstadt.de/Docs/HEDgeHOB-TP2005.pdf (see p. 14).

[28] THE SPARC COLLABORATION: **Technical Proposal for the Design, Construction, Commissioning and Operation of the SPARC Project: Stored Particle Atomic Physics Collaboration at the FAIR Facility**. Tech. Rep. *FAIR-PAC*, Dec. 2005. URL: https://www.gsi.de/fileadmin/SPARC/documents/06_01_06_SPARC_TR.pdf (see p. 15).

[29] FAIR: **FAIR Baseline Technical Report**. Tech. Rep. Sept. 2006. URL: http://www.fair-center.eu/for-users/publications/fair-publications.html (see pp. 15, 18).

[30] THE NUSTAR COLLABORATION SUPER-FRS WORKING GROUP: **Technical Design Report on the Super-FRS**. Tech. Rep. *FAIR-PAC*, Mar. 2009. URL: https://edms.cern.ch/document/994387/1 (see p. 16).

[31] THE HISPEC AND DESPEC COLLABORATIONS: **Technical Proposal for the Design, Construction, Commissioning and Operation of the HISPEC/DESPEC experiment at the Low-Energy Branch of the Super-FRS facility**. Tech. Rep. *FAIR-PAC*, Jan. 2005. URL: http://personal.ph.surrey.ac.uk/~phs1zp/Tech_Proposal_HISPEC_DESPEC-nocost.pdf (see p. 16).

[32] THE ELISE COLLABORATION: **Technical Proposal for the Design, Construction, Commissioning, and Operation of the ELISe setup**. Tech. Rep. *FAIR-PAC*, Jan. 2005. URL: http://www-alt.gsi.de/documents/DOC-2005-Oct-93-1.pdf (see p. 16).

[33] THE EXL COLLABORATION: **Update of the Technical Proposal for the Design, Construction, Commissioning and Operation of the EXL Project (Exotic nuclei studied in light-ion induced reactions at the NESR storage ring)**. Tech. Rep. Jan. 2006. URL: http://www.rug.nl/kvi-cart/research/hnp/research/exl/tech_proposal_exl_update_080106.pdf (see p. 16).

[34] THE ILIMA COLLABORATION: **Technical Proposal for the ILIMA Project**. Tech. Rep. *FAIR-PAC*, Jan. 2005. URL: http://www.fair-center.eu/fileadmin/fair/experiments/NUSTAR/Pdf/ILIMA_tp_20050120-printed.pdf (see p. 16).

[35] THE LASPEC COLLABORATION: **Technical Proposal for the Design, Construction, Commissioning and Operation of LaSpec**. Tech. Rep. *FAIR-PAC*, Jan. 2005. URL: http://www.fair-center.eu/fileadmin/fair/experiments/LaSpec/documents/Laspec-TP.pdf (see p. 16).

[36] D. Rodríguez, K. Blaum, W. Nörtershäuser, *et al.*: **MATS and LaSpec: High-precision experiments using ion traps and lasers at FAIR**. In: *The European Physical Journal Special Topics*, **183**:1 (2010), pp. 1–123. DOI: 10.1140/epjst/e2010-01231-2 (see p. 16).

[37] Volker Friese and Christian Sturm: **CBM Progress Report**. Tech. Rep. *GSI Helmholtz-zentrum für Schwerionenforschung GmbH*, 2013. URL: https://www-alt.gsi.de/documents/DOC-2014-Mar-16-1.pdf (see p. 17).

[38] Johann M. Heuser: **The Compressed Baryonic Matter Experiment at FAIR: Progress with feasibility studies and detector developments**. In: *Nuclear Physics A*, **830**:1–4 (2009). Quark Matter 2009 The 21st International Conference on Ultrarelativistic Nucleus-Nucleus Collisions, pp. 563c–566c. DOI: http://dx.doi.org/10.1016/j.nuclphysa.2009.09.048 (see p. 17).

[39] GSI: **Fair Conceptual Design Report - An International Accelerator Facility for Beams of Ions and Antiprotons**. Tech. Rep. *GSI Darmstadt, Germany*, Mar. 2004. Chap. Section 3. URL: https://www-alt.gsi.de/documents/DOC-2004-Mar-201-1.pdf (see p. 18).

[40] A. Lehrach, O. Boine-Frankenheim, F. Hinterberger, R. Maier, and D. Prasuhn: **Beam Performance and Luminosity Limitations in the High-Energy Storage Ring (HESR)**. In: *Nuclear Instruments and Methods in Physics Research Section A: Accelerators, Spectrometers, Detectors and Associated Equipment*, **A561**: (2006), pp. 289–296. DOI: 10.1016/j.nima.2006.01.017. eprint: 0511165v4 (physics) (see p. 20).

[41] R. Maier: **The High-Energy Storage Ring (HESR)**. In: *Proceedings of 2011 Particle Accelerator Conference*. New York, NY, USA, 2011, pp. 2104–2106. URL: https://accelconf.web.cern.ch/accelconf/PAC2011/papers/thocn2.pdf (see p. 20).

[42] FAIR Joint Core Team: **Green Paper - The Modularized Start Version**. Tech. Rep. *FAIR*, Oct. 2009. URL: http://www.fair-center.eu/fileadmin/fair/publications_FAIR/%20FAIR_GreenPaper_2009.pdf (see pp. 20–21).

[43] The $\bar{\text{P}}$ANDA Collaboration: **Technical Progress Report for: $\bar{\text{P}}$ANDA (AntiProton Annihilations at Darmstadt) Strong Interaction Studies with Antiprotons**. Technical Progress Report. Feb. 2005. URL: http://www-panda.gsi.de/archive/public/panda_tpr.pdf (see pp. 24, 26, 29–31, 37, 51).

[44] Stephen Godfrey and Nathan Isgur: **Mesons in a relativized quark model with chromodynamics**. In: *Physical Review D*, **32**: (1 July 1985), pp. 189–231. DOI: 10.1103/PhysRevD.32.189 (see pp. 24–25).

[45] M. Di Pierro and E. Eichten: **Excited heavy-light systems and hadronic transitions**. In: *Physical Review D*, **64**: (11 Oct. 2001), p. 114004. DOI: 10.1103/PhysRevD.64.114004 (see pp. 24–25).

[46] Paola Gianotti: **Results and perspectives in hadron spectroscopy**. In: *Physica Scripta*, **2012**:T150 (Oct. 2012), p. 014014. DOI: doi:10.1088/0031-8949/2012/T150/014014 (see pp. 25–26).

[47] G. Goldhaber, F. M. Pierre, G. S. Abrams, *et al.*: **Observation in e^+e^- Annihilation of a Narrow State at 1865 MeV/c^2 Decaying to $K\pi$ and $K\pi\pi\pi$**. In: *Physical Review Letters*, **37**: (5 Aug. 1976), pp. 255–259. DOI: 10.1103/PhysRevLett.37.255 (see p. 24).

[48] I. PERUZZI, M. PICCOLO, G. J. FELDMAN, *et al.*: **Observation of a Narrow Charged State at 1876 MeV/c^2 Decaying to an Exotic Combination of K$\pi\pi$.** In: *Physical Review Letters*, **37**: (10 Sept. 1976), pp. 569–571. DOI: 10.1103/PhysRevLett.37.569 (see p. 24).

[49] THE BABAR COLLABORATION: **Observation of a Narrow Meson State Decaying to $D_s^+\pi^0$ at a Mass of 2.32 GeV/c^2.** In: *Physical Review Letters*, **90**: (24 June 2003), p. 242001. DOI: 10.1103/PhysRevLett.90.242001 (see p. 25).

[50] S.-K. CHOI, S. L. OLSEN, A. ABDESSELAM, *et al.*: **Measurements of $B \to \overline{D}D_{s0}^{*+}(2317)$ decay rates and a search for isospin partners of the $D_{s0}^{*+}(2317)$.** In: *Phys. Rev. D*, **91**: (9 May 2015), p. 092011. DOI: 10.1103/PhysRevD.91.092011 (see p. 25).

[51] MARIUS C. MERTENS: **Der PANDA Mikro Vertex Detektor: Entwicklung eines Labormesssystems, Simulation der MVD-Betriebsparameter sowie Untersuchungen zur Auflösung der Breite des D*s0(2317).** PhD Thesis. Ruhr-Universität Bochum, 2010. URL: http://www-brs.ub.ruhr-uni-bochum.de/netahtml/HSS/Diss/MertensMariusC/ (see pp. 25, 62, 96–97, 100).

[52] B. RICHTER, J. -E. AUGUSTIN, A. M. BOYARSKI, *et al.*: **Discovery of a Narrow Resonance in e^+e^- Annihilation.** In: *Physical Review Letters*, **33**: (23 Dec. 1974), pp. 1406–1408. DOI: 10.1103/PhysRevLett.33.1406 (see p. 25).

[53] SAMUEL C. C. TING, J. J. AUBERT, U. BECKER, *et al.*: **Experimental Observation of a Heavy Particle J.** In: *Physical Review Letters*, **33**: (23 Dec. 1974), pp. 1404–1406. DOI: 10.1103/PhysRevLett.33.1404 (see p. 25).

[54] **The Nobel Prize in Physics 1976.** Nobel Media AB 2014, 1976. URL: http://www.nobelprize.org/nobel_prizes/physics/laureates/1976/ (see p. 25).

[55] THE BELLE COLLABORATION: **Observation of a Narrow Charmoniumlike State in Exclusive $B^\pm \to K^\pm\pi^+\pi^- J/\psi$ Decays.** In: *Physical Review Letters*, **91**: (26 Dec. 2003), p. 262001. DOI: 10.1103/PhysRevLett.91.262001 (see pp. 26–27).

[56] THE BABAR COLLABORATION: **Study of the $B^- \to J/\psi K^-\pi^+\pi^-$ decay and measurement of the $B^- \to X(3872)K^-$ branching fraction.** In: *Physical Review D*, **71**: (7 Apr. 2005), p. 071103. DOI: 10.1103/PhysRevD.71.071103 (see p. 26).

[57] THE CDF II COLLABORATION: **Observation of the Narrow State $X(3872) \to J/\psi\pi^+\pi^-$ in $\overline{p}p$ Collisions at $\sqrt{s} = 1.96$ TeV.** In: *Physical Review Letters*, **93**: (7 Aug. 2004), p. 072001. DOI: 10.1103/PhysRevLett.93.072001. arXiv: 0312021 [hep-ex] (see p. 26).

[58] THE DØ COLLABORATION: **Observation and Properties of the $X(3872)$ Decaying to $J/\psi\pi^+\pi^-$ in $p\overline{p}$ Collisions at $\sqrt{s} = 1.96$ TeV.** In: *Physical Review Letters*, **93**: (16 Oct. 2004), p. 162002. DOI: 10.1103/PhysRevLett.93.162002. arXiv: 0405004 [hep-ex] (see p. 26).

[59] THE $\bar{\text{P}}$ANDA COLLABORATION: **Physics Performance Report for $\bar{\text{P}}$ANDA: Strong Interaction Studies with Antiprotons.** In: (Mar. 2009). arXiv: 0903.3905 [hep-ex]. URL: http://arxiv.org/abs/0903.3905 (see pp. 26–27, 30–31, 61).

[60] M. ALFORD and R. L. JAFFE: **Insight into the scalar mesons from a lattice calculation.** In: *Nuclear Physics B*, **578**:1-2 (2000), pp. 367–382. DOI: http://dx.doi.org/10.1016/S0550-3213(00)00155-3 (see p. 27).

[61] L. MAIANI, F. PICCININI, A. D. POLOSA, and V. RIQUER: **Diquark-antidiquark states with hidden or open charm and the nature of $X(3872)$**. In: *Physical Review D*, **71**: (1 Jan. 2005), p. 014028. DOI: 10.1103/PhysRevD.71.014028 (see p. 27).

[62] THE BELLE COLLABORATION: **Study of $e^+e^- \to \pi^+\pi^- J/\psi$ and Observation of a Charged Charmoniumlike State at Belle**. In: *Physical Review Letters*, **110**: (25 June 2013), p. 252002. DOI: 10.1103/PhysRevLett.110.252002 (see p. 27).

[63] THE BESIII COLLABORATION: **Observation of a Charged Charmoniumlike Structure in $e^+e^- \to \pi^+\pi^- J/\psi$ at $\sqrt{s}$=4.26 GeV**. In: *Physical Review Letters*, **110**: (25 June 2013), p. 252001. DOI: 10.1103/PhysRevLett.110.252001 (see p. 27).

[64] JONATHAN M. M. HALL, WASEEM KAMLEH, DEREK B. LEINWEBER, *et al.*: **Lattice QCD Evidence that the $\Lambda(1405)$ Resonance is an Antikaon-Nucleon Molecule**. In: *Physical Review Letters*, **114**: (13 Apr. 2015), p. 132002. DOI: 10.1103/PhysRevLett.114.132002 (see p. 28).

[65] THE HADES COLLABORATION: **Baryonic resonances close to the $\overline{K}N$ threshold: The case of $\Lambda(1405)$ in pp collisions**. In: *Physical Review C*, **87**: (2 Feb. 2013), p. 025201. DOI: 10.1103/PhysRevC.87.025201 (see p. 28).

[66] A. ABELE, J. ADOMEIT, C. AMSLER, *et al.*: **Momentum dependence of the decay $\eta \to \pi^+\pi^-\pi^0$**. In: *Physics Letters B*, **417**:1–2 (1998), pp. 197–201. DOI: http://dx.doi.org/10.1016/S0370-2693(97)01376-2 (see p. 28).

[67] J. REINNARTH: **Evidence for an exotic partial wave in $\pi\eta'$**. In: *Nuclear Physics A*, **692**:1–2 (2001). Sixth Biennial Conference on Low-Energy Antiproton Physics, pp. 268–274. DOI: http://dx.doi.org/10.1016/S0375-9474(01)01186-1 (see p. 28).

[68] EBERHARD KLEMPT and ALEXANDER ZAITSEV: **Glueballs, hybrids, multiquarks: Experimental facts versus QCD inspired concepts**. In: *Physics Reports*, **454**:1–4 (2007), pp. 1–202. DOI: http://dx.doi.org/10.1016/j.physrep.2007.07.006 (see pp. 28–29).

[69] COLIN J. MORNINGSTAR and MIKE PEARDON: **Glueball spectrum from an anisotropic lattice study**. In: *Physical Review D*, **60**: (3 July 1999), p. 034509. DOI: 10.1103/PhysRevD.60.034509 (see p. 29).

[70] A. FREUND, A. V. RADYUSHKIN, A. SCHÄFER, and C. WEISS: **Exclusive Annihilation $\overline{p}p \to \gamma\gamma$ in a Generalized Parton Picture**. In: *Physical Review Letters*, **90**: (9 Mar. 2003), p. 092001. DOI: 10.1103/PhysRevLett.90.092001 (see p. 29).

[71] T. A. ARMSTRONG, D. BETTONI, V. BHARADWAJ, *et al.*: **Proton electromagnetic form factors in the timelike region from 8.9 to 13.0 GeV^2**. In: *Physical Review Letters*, **70**: (9 Mar. 1993), pp. 1212–1215. DOI: 10.1103/PhysRevLett.70.1212 (see p. 30).

[72] M. AMBROGIANI, S. BAGNASCO, W. BALDINI, *et al.*: **Measurements of the magnetic form factor of the proton in the timelike region at large momentum transfer**. In: *Physical Review D*, **60**: (3 June 1999), p. 032002. DOI: 10.1103/PhysRevD.60.032002 (see p. 30).

[73] W. WEISE: **Hadrons with charmed quarks in the nuclear medium**. In: *International Workshop XXIX on Gross Properties of Nuclei and Nuclear Excitations, Hirschegg*. Ed. by H. FELDMEIER, J. KNOLL, W. NÖRENBERG, and J. WAMBACH. Gesellschaft für Schwerionenforschung (GSI). Jan. 2001, pp. 249–258. URL: http://theory.gsi.de/hirschegg/2001/Proceedings/Weise_129.187.137.91_hadrons.pdf (see p. 31).

[74] A. SIBIRTSEV, K. TSUSHIMA, and A. W. THOMAS: **On studying charm in nuclei through antiproton annihilation**. In: *The European Physical Journal A - Hadrons and Nuclei*, **6**:3 (1999), pp. 351–359. DOI: 10.1007/s100500050353 (see p. 31).

[75] M. DANYSZ and J. PNIEWSKI: **Delayed disintegration of a heavy nuclear fragment: I**. In: *The London, Edinburgh, and Dublin Philosophical Magazine and Journal of Science*, **44**:350 (1953), pp. 348–350. DOI: 10.1080/14786440308520318 (see p. 31).

[76] M. DANYSZ, K. GARBOWSKA, J. PNIEWSKI, *et al.*: **The identification of a double hyperfragment**. In: *Nuclear Physics*, **49**: (1963), pp. 121–132. DOI: http://dx.doi.org/10.1016/0029-5582(63)90080-4 (see p. 31).

[77] D. BONAVENTURA: **CAD-Renderings of the PANDA Detector**. Jan. 2015. URL: https://panda-wiki.gsi.de/foswiki/bin/view/Detector/Pictures (see pp. 32–33).

[78] THE $\bar{\text{P}}$ANDA COLLABORATION: **Technical Design Report for the $\bar{\text{P}}$ANDA Internal Targets: The Cluster-Jet Target and Developments for the Pellet Target**. Tech. Rep. Mar. 2012. URL: http://www-panda.gsi.de/archive/TargetTDR/Targets_TDR.pdf (see pp. 32–34).

[79] ÖRJAN NORDHAGE: **On a Hydrogen Pellet Target for Antiproton Physics with $\bar{\text{P}}$ANDA**. PhD Thesis. Uppsala Universitet, Oct. 2006. URL: http://uu.diva-portal.org/smash/record.jsf?pid=diva2:168848&dswid=7281 (see p. 34).

[80] THE $\bar{\text{P}}$ANDA COLLABORATION: **Technical Design Report for the $\bar{\text{P}}$ANDA Solenoid and Dipole Spectrometer Magnets**. Tech. Rep. May 2009. arXiv: 0907.0169 [physics]. URL: http://arxiv.org/abs/0907.0169 (see pp. 34–35).

[81] THE $\bar{\text{P}}$ANDA COLLABORATION: **Technical design report for the $\bar{\text{P}}$ANDA (AntiProton Annihilations at Darmstadt) Straw Tube Tracker**. In: *The European Physical Journal A*, **49**:2, 25 (2013). DOI: 10.1140/epja/i2013-13025-8 (see p. 36).

[82] **CERN Gas Detector Development Group**. URL: http://gdd.web.cern.ch/GDD/ (see p. 37).

[83] FLC-TPC: **GEM working principle**. URL: http://www-flc.desy.de/tpc/basicsgem.php (see p. 37).

[84] MARTIN J. GALUSKA *et al.*: **Hough Transform Based Pattern Recognition for the $\bar{\text{P}}$ANDA Forward Tracking System**. In: *PoS*, **Bormio2013**: (2013), p. 023. URL: http://inspirehep.net/record/1265424/ (see p. 37).

[85] THE $\bar{\text{P}}$ANDA COLLABORATION: **Technical Design Report for the $\bar{\text{P}}$ANDA Luminosity Detector**. Tech. Rep. *In preparation*, 2015 (see p. 38).

[86] JOCHEN SCHWIENING: **Status of the PANDA Barrel DIRC**. Talk at the XLVIII. $\bar{\text{P}}$ANDA Collaboration Meeting. Mar. 2014 (see p. 39).

[87] O. MERLE, R. DZHYGADLO, A. GERHARDT, *et al.*: **Development of an Endcap DIRC for $\bar{\text{P}}$ANDA**. In: *Nuclear Instruments and Methods in Physics Research Section A: Accelerators, Spectrometers, Detectors and Associated Equipment*, **766**: (2014). RICH2013 Proceedings of the Eighth International Workshop on Ring Imaging Cherenkov Detectors Shonan, Kanagawa, Japan, December 2-6, 2013, pp. 96–100. DOI: http://dx.doi.org/10.1016/j.nima.2014.04.016 (see p. 39).

[88] C. SCHWARZ, G. AHMED, A. BRITTING, *et al.*: **Particle identification for the PANDA detector**. In: *Nuclear Instruments and Methods in Physics Research Section A: Accelerators, Spectrometers, Detectors and Associated Equipment*, **639**:1 (2011). Proceedings of the Seventh International Workshop on Ring Imaging Cherenkov Detectors, pp. 169–172. DOI: http://dx.doi.org/10.1016/j.nima.2010.10.116 (see p. 39).

[89] A. LEHMANN, R. DZHYGADLO, A. GERHARDT, *et al.*: **The DIRC Detectors at the PANDA Experiment**. In: *Proceedings of the International Conference on Technology and Instrumentation in Particle Physics (TIPP 2014)*. Proceedings of Science, June 2014. URL: http://pos.sissa.it/archive/conferences/213/112/TIPP2014_112.pdf (see p. 39).

[90] SERGEY KONONOV: **Plans for Forward RICH**. Talk at the XLVIII. PANDA Collaboration Meeting. Mar. 2014 (see p. 40).

[91] K. GOETZEN, H. ORTH, G. SCHEPERS, *et al.*: **Proposal for a Scintillator Tile Hodoscope for PANDA**. Tech. Rep. Mar. 2011. URL: https://panda-wiki.gsi.de/foswiki/pub/Tof/SciTil/scitil.pdf (see p. 40).

[92] CARSTEN SCHWARZ: **The Status of the SciTil**. Talk at the XLVIII. PANDA Collaboration Meeting. GSI, Mar. 2014 (see p. 40).

[93] S. BELOSTOTSKI: **Status of FTOF detectors**. Talk at the XLVIII. PANDA Collaboration Meeting. GSI, Mar. 2014 (see p. 41).

[94] THE PANDA COLLABORATION: **Technical Design Report for the: PANDA Muon System**. Tech. Rep. Sept. 2012. URL: http://www-panda.gsi.de/archive/MuonTDR/Muon_TDR.pdf (see pp. 41–42).

[95] THE PANDA COLLABORATION: **Technical Design Report for the PANDA Electromagnetic Calorimeter (EMC)**. Tech. Rep. Oct. 2008. arXiv: 0810.1216. URL: http://arxiv.org/abs/0810.1216 (see pp. 41, 43).

[96] THE PANDA COLLABORATION: **Technical Design Report for the PANDA Forward Spectrometer Calorimeter**. Tech. Rep. *In preparation*, 2015 (see pp. 42–43).

[97] G. MAZZA, D. CALVO, P. DE REMIGIS, *et al.*: **The ToPiX v4 prototype for the triggerless readout of the PANDA silicon pixel detector**. In: *Journal of Instrumentation*, **10**:01 (2015), p. C01042. URL: http://stacks.iop.org/1748-0221/10/i=01/a=C01042 (see pp. 44, 48).

[98] THE PANDA COLLABORATION: **Technical Design Report for the: PANDA Micro Vertex Detector**. Technical Design Report. Aug. 2012. eprint: 1207.6581. URL: http://arxiv.org/abs/1207.6581 (see pp. 43, 45–46, 48–49, 61–62, 73–74, 96, 112).

[99] P. MOREIRA, R. BALLABRIGA, S. BARON, *et al.*: **The GBT Project**. In: *Proceedings of Topical Workshop on Electronics for Particle Physics*. Ed. by EVELYNE DHO. Paris, France: CERN, Sept. 2009, pp. 342–346. DOI: 10.5170/CERN-2009-006.342 (see pp. 48, 50).

[100] TOMASSO QUAGLI: **Tests of stave cooling**. Talk at the LII. PANDA Collaboration Meeting. Gießen, Mar. 2015 (see p. 49).

[101] R. SCHNELL, K.-TH. BRINKMANN, V. DI PIETRO, *et al.*: **The readout chain for the PANDA MVD strip detector**. In: *Journal of Instrumentation*, **10**:02 (2015), p. C02003. URL: http://stacks.iop.org/1748-0221/10/i=02/a=C02003 (see p. 49).

[102] DARIUSCH DEERMANN: **Development of the $\bar{\text{P}}$ANDA MVD Trapezoidal Sensors and a Feasibility Study of the $\bar{p}p \to \bar{\Lambda}_c \Lambda_c$**. PhD Thesis. Ruhr-Universität Bochum, 2015 (see p. 49).

[103] HANS-GEORG ZAUNICK: **Developments toward a Silicon Strip Tracker for the $\bar{\text{P}}$ANDA Experiment**. PhD Thesis. Rheinische Friedrich-Wilhelms-Universität Bonn, 2012. URL: http://hss.ulb.uni-bonn.de/2013/3185/3185.htm (see p. 49).

[104] H. KLEINES, P. WÜSTNER, M. RAMM, *et al.*: **Developments for the readout of the PANDA micro vertex detector**. In: *Real Time Conference (RT), 2010 17th IEEE-NPSS*. Lisbon, May 2010, pp. 1–3. DOI: 10.1109/RTC.2010.5750459 (see p. 50).

[105] I. KONOROV, H. ANGERER, A. MANN, and S. PAUL: **SODA: Time distribution system for the PANDA experiment**. In: *Nuclear Science Symposium Conference Record (NSS/MIC), 2009 IEEE*. Orlando, FL, USA, Oct. 2009, pp. 1863–1865. DOI: 10.1109/NSSMIC.2009.5402172 (see p. 51).

[106] RENE BRUN and FONS RADEMAKERS: **ROOT — An object oriented data analysis framework**. In: *Nuclear Instruments and Methods in Physics Research Section A: Accelerators, Spectrometers, Detectors and Associated Equipment*, **389**:1–2 (1997). New Computing Techniques in Physics Research V, pp. 81–86. DOI: 10.1016/S0168-9002(97)00048-X (see p. 51).

[107] M. AL-TURANY, D. BERTINI, R. KARABOWICZ, *et al.*: **The FairRoot framework**. In: *Journal of Physics: Conference Series*, **396**:2 (2012), p. 022001. DOI: 10.1088/1742-6596/396/2/022001 (see p. 52).

[108] STEFANO SPATARO and THE PANDA COLLABORATION: **The PandaRoot framework for simulation, reconstruction and analysis**. In: *Journal of Physics: Conference Series*, **331**:3 (2011), p. 032031. DOI: 10.1088/1742-6596/331/3/032031 (see p. 52).

[109] DAVID J. LANGE: **The EvtGen particle decay simulation package**. In: *Nuclear Instruments and Methods in Physics Research Section A: Accelerators, Spectrometers, Detectors and Associated Equipment*, **462**:1–2 (2001). BEAUTY2000, Proceedings of the 7th Int. Conf. on B-Physics at Hadron Machines, pp. 152–155. DOI: 10.1016/S0168-9002(01)00089-4 (see p. 53).

[110] A. CAPELLA, U. SUKHATME, C.-I. TAN, and J. TRAN THANH VAN: **Dual parton model**. In: *Physics Reports*, **236**:4–5 (1994), pp. 225–329. DOI: http://dx.doi.org/10.1016/0370-1573(94)90064-7 (see p. 53).

[111] S. ROESLER, R. ENGEL, and J. RANFT: **The Monte Carlo Event Generator DPMJET-III**. In: *Advanced Monte Carlo for Radiation Physics, Particle Transport Simulation and Applications*. Ed. by ANDREAS KLING, FERNANDOJ.C. BARÃO, MASAYUKI NAKAGAWA, LUIS TÁVORA, and PEDRO VAZ. Springer Berlin Heidelberg, 2001, pp. 1033–1038. DOI: 10.1007/978-3-642-18211-2_166 (see p. 53).

[112] J. ALLISON, K. AMAKO, J. APOSTOLAKIS, *et al.*: **Geant4 developments and applications**. In: *Nuclear Science, IEEE Transactions on*, **53**:1 (Feb. 2006), pp. 270–278. DOI: 10.1109/TNS.2006.869826 (see p. 53).

[113] A. FONTANA, P. GENOVA, L. LAVEZZI, *et al.*: **Use of GEANE for tracking in virtual Monte Carlo**. In: *Journal of Physics: Conference Series*, **119**:3 (2008), p. 032018. URL: http://stacks.iop.org/1742-6596/119/i=3/a=032018 (see p. 53).

[114] GIANLUIGI BOCA: **Improvements with the Offline Pattern Recognition in the 20 MHz interaction rate environment**. Talk at the L. $\bar{\text{P}}$ANDA Collaboration Meeting. Sept. 2014 (see p. 53).

[115] JOHANNES RAUCH and TOBIAS SCHLÜTER: **GENFIT — a Generic Track-Fitting Toolkit**. In: *Journal of Physics: Conference Series*, **608**:1 (2015), p. 012042. DOI: 10.1088/1742-6596/608/1/012042 (see p. 54).

[116] DAVID CARRON: **Rendering of Standard Cell**. Wikimedia Commons, July 2006. URL: http://en.wikipedia.org/wiki/File:Silicon_chip_3d.png (see p. 56).

[117] P. CHU: **RTL Hardware Design Using VHDL**. John Wiley & Sons, Inc., 2006 (see pp. 56, 80).

[118] **Intel® 14nm Technology**. 2014. URL: http://www.intel.com/content/www/us/en/silicon-innovations/intel-14nm-technology.html (see p. 56).

[119] R. JACOB BAKER: **CMOS: Circuit Design, Layout, and Simulation**. 3rd ed. IEEE Press Series on Microelectronic Systems. Wiley, 2010. URL: https://books.google.de/books?id=eoXbNAEACAAJ (see p. 56).

[120] FRANK M. WANLASS: **Low stand-by power complementary field effect circuitry**. US Patent 3,356,858. Dec. 1967. URL: http://www.google.com/patents/US3356858 (see p. 56).

[121] HARRY J. LEVINSON, MARK A. MCCORD, FRANCO CERRINA, *et al.*: **SPIE Handbook of Microlithography, Micromachining, and Microfabrication**. Ed. by P. RAI-CHOUDHURY. Vol. 1: Microlithography. Society of Photo-Optical Instrumentation Engineers, Mar. 1997. Chap. 2.9. URL: http://www.cnf.cornell.edu/cnf_spie9.html (see p. 58).

[122] **GDSII™ Stream Format Manual**. Release 6.0. Calma. Feb. 1987. URL: http://bitsavers.informatik.uni-stuttgart.de/pdf/calma/GDS_II_Stream_Format_Manual_6.0_Feb87.pdf (see p. 58).

[123] J. F. ZIEGLER, H. W. CURTIS, H. P. MUHLFELD, *et al.*: **IBM experiments in soft fails in computer electronics (1978–1994)**. In: *IBM Journal of Research and Development*, **40**:1 (Jan. 1996). DOI: 10.1147/rd.401.0003 (see p. 58).

[124] TIMOTHY C. MAY and MURRAY H. WOODS: **Alpha-Particle-Induced Soft Errors in Dynamic Memories**. In: *IEEE Transaction on Electron Devices*, **26**:1 (Jan. 1979), pp. 2–9. DOI: 10.1109/T-ED.1979.19370 (see p. 58).

[125] J. F. ZIEGLER and W. A. LANFORD: **Effect of Cosmic Rays on Computer Memories**. In: *Science*, **206**:4420 (Nov. 1979), pp. 776–788. DOI: 10.1126/science.206.4420.776 (see p. 58).

[126] H. J. BARNABY: **Total-Ionizing-Dose Effects in Modern CMOS Technologies**. In: *IEEE Transactions on Nuclear Science*, **53**:6 (Dec. 2006), pp. 3103–3121. DOI: 10.1109/TNS.2006.885952 (see pp. 59, 66).

[127] C. S. GUENZER, E. A. WOLICKI, and R. G. ALLAS: **Single Event Upset of Dynamic Rams by Neutrons and Protons**. In: *IEEE Transactions on Nuclear Science*, **26**:6 (Dec. 1979), pp. 5048–5052. DOI: 10.1109/TNS.1979.4330270 (see p. 59).

[128] N. AUBRY, E. AUFFRAY, F. B. MIMOUN, *et al.*: **EndoTOFPET-US: a novel multimodal tool for endoscopy and positron emission tomography**. In: *Journal of Instrumentation*. Vol. 8. 04. 2013, p. C04002. DOI: 10.1088/1748-0221/8/04/C04002 (see pp. 59–60).

[129] THOMAS BEYER, DAVID W. TOWNSEND, JOHANNES CZERNIN, and LUTZ S. FREUDENBERG: **The future of hybrid imaging-part 2: PET/CT**. In: *Insights Imaging*, **2**:3 (June 2011), pp. 225–234. DOI: 10.1007/s13244-011-0069-4 (see pp. 59–60).

[130] JOEL S. KARP, SULEMAN SURTI, MARGARET E. DAUBE-WITHERSPOON, and GERD MUEHLLEHNER: **Benefit of time-of-flight in PET: experimental and clinical results**. In: *Journal of Nuclear Medicin*, **49**:3 (Mar. 2008), pp. 462–70. DOI: 10.2967/jnumed.107.044834 (see p. 60).

[131] M. D. ROLO, R. BUGALHO, F. GONÇALVES, *et al.*: **TOFPET ASIC for PET applications**. In: *Journal of Instrumentation*. Vol. 8. 02. 2013, p. C02050. DOI: 10.1088/1748-0221/8/02/C02050 (see pp. 60–61).

[132] MANUEL DIONISIO DA ROCHA ROLO: **Integrated Circuit Design for Time-of-Flight PET**. PhD Thesis. Università degli Studi di Torino, 2014 (see p. 61).

[133] RICARDO BUGALHO, KATAYOUN DOROUD, AGOSTINO DI FRANCESCO, *et al.*: **A Compact Detector Module for Time of Flight PET and the Associated DAQ system**. In: IEEE Nuclear Science Symposium and Medical Imaging Conference. 2014 (see pp. 61, 77).

[134] A. E. STEVENS, R. P. VAN BERG, J. VAN DER SPIEGEL, and H. H. WILLIAMS: **A time-to-voltage converter and analog memory for colliding beam detectors**. In: *IEEE Journal of Solid-State Circuits*, **24**:6 (Dec. 1989), pp. 1748–1752. DOI: 10.1109/4.45016 (see p. 64).

[135] REZA MIRHOSSEINI: **Impurity profile of a CMOS transistor pair.** Wikimedia Commons, Nov. 2008. URL: http://commons.wikimedia.org/wiki/File:Cmos_impurity_profile.PNG (see p. 67).

[136] **UMC 0.11 um Standard Cell Library Application Note**. UMC. Dec. 2011 (see p. 67).

[137] J. VON NEUMANN: **Automata Studies**. In: Princeton University Press, 1956. Chap. Probabilistic Logics and the Synthesis of Reliable Organisms from Unreliable Components, pp. 43–98 (see p. 69).

[138] R. E. LYONS and W. VANDERKULK: **The Use of Triple-Modular Redundancy to Improve Computer Reliability**. In: *IBM Journal of Research and Development*, (Apr. 1962), pp. 200–209. DOI: 10.1147/rd.62.0200 (see p. 69).

[139] R. W. HAMMING: **Error Detection and Error Correction Codes**. In: *The Bell System Technical Journal*, **XXIX**:2 (Apr. 1950). DOI: 10.1002/j.1538-7305.1950.tb00463.x (see p. 70).

[140] ANDRÉ GOERRES: **GitHub: Generic Hamming Register in VHDL**. Aug. 2014. URL: https://github.com/Nepomuk/HDL-radiation-tools#hamming-register (see p. 71).

[141] G. ANELLI, M. CAMPBELL, M. DELMASTRO, *et al.*: **Radiation tolerant VLSI circuits in standard deep submicron CMOS technologies for the LHC experiments: practical design aspects**. In: *Nuclear Science, IEEE Transactions on*, **46**:6 (Dec. 1999), pp. 1690–1696. DOI: 10.1109/23.819140 (see p. 72).

[142] W. SNOEYSA, F. FACCIO, M. BURNS, *et al.*: **Layout techniques to enhance the radiation tolerance of standard CMOS technologies demonstrated on a pixel detector readout chip**. In: *Nuclear Instruments and Methods in Physics Research Section A: Accelerators, Spectrometers, Detectors and Associated Equipment*, **439**:2-3 (Jan. 2000), pp. 349–360. DOI: 10.1016/S0168-9002(99)00899-2 (see p. 72).

[143] VALENTINO DI PIETRO: **The Front-End Amplifier for the Silicon Microstrip Sensors of the PANDA MVD**. Talk at the DPG Spring Meeting. Heidelberg, Mar. 2015 (see pp. 74, 91).

[144] STEPHAN HENZLER: **Time-to-Digital Converters**. Vol. 29. Springer Series in Advanced Microelectronics. Springer Netherlands, 2010. DOI: 10.1007/978-90-481-8628-0 (see p. 74).

[145] VALENTINO DI PIETRO: **A Low Power Front-End Amplifier for the Microstrip Sensors of the PANDA Microvertex Detector**. Master Thesis. 2012 (see p. 75).

[146] ALBERTO RICCARDI: **A time digitizer for the microstrip detectors of the PANDA MVD**. Talk at the DPG Spring Meeting. Heidelberg, Mar. 2015 (see p. 75).

[147] DUŠAN PONIKVAR: **Wilkinson-type ADC with short conversion time and low clock frequency**. In: *Nuclear Instruments and Methods in Physics Research Section A: Accelerators, Spectrometers, Detectors and Associated Equipment*, **408**:2–3 (1998), pp. 523–529. DOI: http://dx.doi.org/10.1016/S0168-9002(98)00219-8 (see p. 74).

[148] FRANK GRAY: **Pulse code communication**. US Patent 2,632,058. Mar. 1953. URL: http://www.google.com/patents/US2632058 (see p. 89).

[149] SIMONE ESCH: **Evaluation of the $\bar{\text{P}}$ANDA Silicon Pixel Front-End Electronics and Investigation of the $\bar{\Lambda}\Lambda$ Final State**. PhD Thesis. Ruhr-Universität Bochum, 2014. URL: http://www-brs.ub.ruhr-uni-bochum.de/netahtml/HSS/Diss/EschSimone/ (see pp. 96–97, 111).

[150] **ML605 Hardware User Guide (UG534)**. v1.8. Xilinx. Oct. 2012. URL: http://www.xilinx.com/support/documentation/boards_and_kits/ug534.pdf (see p. 99).

[151] M. DROCHNER, W. ERVEN, F. G. RAMM, *et al.*: **A VME controller for data acquisition with flexible gigabit data link to PCI**. In: *Proceedings of the 12th IEEE Real Time Congress on Nuclear and Plasma Science (Valencia)*. June 2001. URL: http://juser.fz-juelich.de/record/43395 (see p. 99).

[152] ISO/IEC: **Open Systems Interconnection – Basic Reference Model: The Basic Model**. Standard 7498-1:1994(E). *International Organization for Standardization*, Nov. 1994. URL: http://www.ecma-international.org/activities/Communications/TG11/s020269e.pdf (see p. 100).

[153] HUBERT ZIMMERMANN: **OSI Reference Model – The ISO Model of Architecture for Open Systems Interconnction**. In: *IEEE Transactions on Communications*, **28**:4 (Apr. 1980), pp. 425–432. DOI: 10.1109/TCOM.1980.1094702 (see p. 100).

[154] **Qt Project Website**. URL: https://www.qt.io/ (see p. 101).

[155] **SIS1100 by Struck Innovative System**. Struck Innovative Systeme GmbH. URL: http://www.struck.de/ (see p. 102).

[156] RICHARD S. BALLANCE, ROBERT W. BEMER, GERRIT A. BLAAUW, *et al.*: **Planning a Computer System**. Ed. by WERNER BUCHHOLZ. McGraw-Hill Book Company, Inc., 1962, pp. 39–40. URL: http://archive.computerhistory.org/resources/text/IBM/Stretch/pdfs/Buchholz_102636426.pdf (see p. 102).

[157] IEEE COMPUTER SOCIETY: **IEEE Standard for Ethernet**. In: *IEEE Std 802.3-2012, section one*, (Dec. 2012), p. 53. URL: http://standards.ieee.org/getieee802/download/802.3-2012_section1.pdf (see p. 103).

[158] **RFC 791: Internet Protocol**. Protocol Specification. *Darpa Internet Program*, Sept. 1981, p. 11. URL: http://tools.ietf.org/pdf/rfc791.pdf (see p. 103).

[159] J. POSTEL: **RFC 768: User Datagram Protocol**. Protocol Specification. Aug. 1980. URL: http://tools.ietf.org/pdf/rfc791.pdf (see p. 104).

[160] PETER FALL and ADRIAN FIERGOLSKI: **1G eth UDP / IP Stack**. June 2013. URL: http://opencores.org/project,udp_ip_stack (see p. 105).

[161] **Virtex-6 FPGA Clocking Resources**. v2.5. Xilinx. Jan. 2014. URL: http://www.xilinx.com/support/documentation/user_guides/ug362.pdf (see p. 108).

[162] R. S. SHAW: **Little-Endian**. Wikimedia Commons, Oct. 2007. URL: http://commons.wikimedia.org/wiki/File:Little-Endian.svg (see p. 109).

[163] R. S. SHAW: **Big-Endian**. Wikimedia Commons, Oct. 2007. URL: http://commons.wikimedia.org/wiki/File:Big-Endian.svg (see p. 109).

[164] SIMONE ESCH: **TestBeam Analysis**. Talk at the LI. P̄ANDA Collaboration Meeting. Jülich, Dec. 2014 (see p. 111).

[165] AARON L. MAHLER. Private communication. (see p. 113).

[166] **Virtex-6 FPGA System Monitor**. v1.2. Xilinx. Sept. 2014. URL: http://www.xilinx.com/support/documentation/user_guides/ug370.pdf (see p. 203).

[167] **Virtex-6 FPGA Data Sheet**. v3.6. Xilinx. Mar. 2014. URL: http://www.xilinx.com/support/documentation/data_sheets/ds152.pdf (see p. 203).

[168] **LCD Module S162D Series – Product Specifications**. 2.0. Displaytech Ltd. URL: https://studentspractice.googlecode.com/hg/VHDL/project_00/doc/LCD/S162D-v20.pdf (see p. 204).

[169] JIANMING CHEN, RIHUA MAO, LIYUAN ZHANG, and REN-YUAN ZHU: **Large Size LSO and LYSO Crystals for Future High Energy Physics Experiments**. In: *IEEE Transaction on Nuclear Science*, **54**:3 (June 2007), pp. 718–724. DOI: 10.1109/TNS.2007.897823 (see p. 221).

Glossary

µTCA Micro Telecommunications Computing Architecture

4C four-constraint

8b/10b encoding With this encoding, 8 bit symbols are converted into 10 bit symbols yielding a direct current (DC)-balanced output.

AD Antiproton Decelerator

ADC analog-to-digital converter

APPA Atomic, Plasma Physics and Applications

ARP Address Resolution Protocol

ASIC application-specific integrated circuit

ASIC control link The communication interface for configuring the ASIC.

BaBar The BaBar experiment is a particle detector, built among others to investigate CP violation with e^-e^+ collisions producing B mesons. It is located at the SLAC in Stanford, USA.

Belle The Belle experiment is a particle detector, built among others to investigate CP violation with e^-e^+ collisions producing B mesons. It is located at the KEKB accelerator in Tsukuba, Japan.

BESIII The BESIII experiment, located at IHEP in Beijing, China, measures e^-e^+ collisions with $\sqrt{s} \leq 4.6\,\text{GeV}$.

BIOMAT Biology and Material Research

C++ A widely-used, general-purpose programming language with many possibilities to optimize programs for performance and efficiency, for instance by handling memory blocks manually.

CAD computer-aided design

CAL Chip Access Layer

CBM Compressed Baryonic Matter

CERN European Organization for Nuclear Research

CF CompactFlash

CL confidence level

CLEO CLEO was a general purpose particle detector measuring e^-e^+ annihilations with $\sqrt{s} \approx 10\,\text{GeV}$ at the Cornell Electron Storage Ring in Ithaca, USA.

CM center-of-mass

CMOS complementary metal-oxide-semiconductor

CMS center of mass system

compact event mode Transmit data in a compact event mode without unnecessary information, for instance by subtracting a constant offset in the fine counter.

COSY Cooler Synchrotron

counter wrap-around When a counter reaches its highest value (e.g. 111 for a 3 bit counter), it either remains at this value or wraps around, resulting in the initial state as the next value (`000` in this example).

CPU central processing unit

CR Collector Ring

CRC cyclic redundancy check

CRC-16 A CRC is an error detection code used for stored and transmitted data to detect accidental changes of the raw data. An attached number refers to the length of the polynomial used for the division applied.

CRC-8 As CRC-16 but with 8 bit polynomial.

Crystal-Barrel The Crystal-Barrel experiment was located at the Low Energy Antiproton Ring (LEAR) at CERN and measured $\bar{p}p$ annihilations. Now it has been transferred to the Elektronstretcheranlage (ELSA) in Bonn, Germany.

DAC digital to analog converter

DC direct current

DDR double data rate

DDR3 SDRAM double data rate type 3 synchronous dynamic random-access memory

DESPEC Decay Spectroscopy

DIRC detection of internally reflected Cherenkov light

DPM Dual Parton Model

DUT device under test

ELISe Electron-Ion Scattering in a Storage Ring

EMC Electromagnetic Calorimeter

ENC equivalent noise charge

EvtGen A particle decay simulation package, used for the event generation step in PandaRoot.

EXL Exotic nuclei in light-ion induced reactions at the NESR storage ring

FAIR Facility for Antiproton and Ion Research

FairRoot A software framework based on ROOT, providing basic simulation tasks common for the FAIR experiments.

Fermilab Fermilab, short for Fermi National Accelerator Laboratory, is a research center for particle physics located near Chicago, USA.

FF flip-flop

FIFO first in, first out buffer

finite-state machine A finite-state machine, or simply *state machine*, is a model of describing an operational model. Within this model, the program is always occupying one state alone and switches states based on defined conditions.

first in, first out A method for organizing the sequence of processing data from a buffer. With a first in, first out buffer structure, data that comes in first is queued to be processed first. In other words reading from an FIFO retrieves the oldest data word.

FLAIR Facility for Low-Energy Antiprotons and Heavy Ion Research

flip-flop A flip-flop is an electronic component with two stable output states (high and low) used for sequential logic circuits. The output state changes depending on the input and the flip-flop type. A very common variant is a clocked flip-flop scanning the input on each rising edge of the clock.

FMC FPGA Mezzanine Card

Forschungszentrum Jülich A German research center located in Jülich and part of the Helmholtz association.

Fortran A general-purpose programming language suited for scientific applications and developed since 1957.

Forward Spectrometer The Forward Spectrometer for $\bar{P}$ANDA is oriented downstream of the antiproton beam to measure the forward-boosted particles.

FPGA field programmable gate array

frame ID The frame ID is 32 bit identifier bundling events which fall in a time window of $2^{10} = 1024$ clock cycles. Consequently, the frame ID is a part of the 42-bit-wide global time stamp, namely the 32 bit starting with the MSB.

FSC Forward Spectrometer Calorimeter

FSM finite-state machine

FTOF Forward time of flight

FTS Forward Tracking System

full event mode Transmit the full data stored in the ASIC without suppressing information.

FWHM full width at half maximum

GAL Generic Access Layer

GBT Gigabit Transceiver

GBTX Gigabit Transceiver ASIC

GDSII Graphic Database System II

GEANE A software framework for particle propagation including the errors on track parameters.

GEANT-3 The third version of a framework for simulating the propagation of particles

through matter using MC methods.

Geant4 The fourth version of a framework for simulating the propagation of particles through matter using MC methods.

GEM Gas Electron Multiplier

global controller The digital logic block spanning over all channels and combining the information from all inputs. It also handles the ASIC control link and configuration as well as the formating and transmitting of event data. It is connected to the TDC controller on the left as well as the analog DACs and the in- and output pins.

GPD generalized parton distribution

GSI GSI Helmholtzzentrum für Schwerionenforschung GmbH

GUI graphical user interface

HADES High-Acceptance Dielectron Spectrometer

Hamming encoding A radiation effect measure for a series of registers by introducing parity bits according to the encoding proposed by Hamming. With the added redundancy one SEU can be detected and corrected. A more in-depth explaination is given in Section 5.3.3.3.

HDL hardware description language

HEDgeHOB High Energy Density Matter generated by Heavy Ion Beams

HESR High Energy Storage Ring

HISPEC High-resolution In-flight Spectroscopy

HPC high pin count

HV-MAPS high-voltage monolithic active-pixel sensor

I/O input and output

IC integrated circuit

ILIMA Isometric Beams, Lifetimes and Masses

IP interaction point

IP core IP cores (IP for intellectual property) are modules provided by a vendor like Xilinx to easily implement functions. In case of the ML605 this means first in, first outs, clock generators, access to hardware components (Ethernet chip), and so forth.

IPv4 Version 4 of the Internet Protocol, widely used in network communication and in the JDRS.

ISO International Organization for Standardization

JDRS Jülich Digital Readout System

LAN local area network

LaSpec Laser Spectroscopy

LCD liquid-crystal display

LED light emitting diode

LHC Large Hadron Collider

LMD Luminosity Detector

LOR line of response

LPC low pin count

LSB least significant bit

LVDS low-voltage differential signaling

LYSO Lutetium-yttrium oxyorthosilicate (LYSO) is an inorganic compound used for fast responding scintillating crystals in high energy experiments [169].

MAC address media access control address

MATS Precision Measurement of very short-lived nuclei with Advanced Trapping System

MC Monte Carlo

MC truth MC truth labels the simulated input parameters for the detector response. For instance, a particle's momentum as it is used in the simulation's propagation instead of the reconstructed momentum from the detector.

MCP-PMT micro-channel plate photomultiplier tube

MDC Module Data Concentrator

MDT mini-drift tube

MIP minimum ionizing particle

ML605 The ML605 evaluation board is an electronic development system build around an Virtex-6 FPGA. It features a variety of connections and built-in components enabling different use cases, for instance front-end electronic development.

MMB MVD Multiplexer Board

MMCM Mixed-Mode Clock Manager

MPPC multi-pixel photon counter

MRF MVD Readout Framework

MSB most significant bit

MSV Modularized Start Version
MVD Micro Vertex Detector
Mylar Mylar is the trade name of a thin insulating polyester foil made from polyethylene terephthalate (PET). It may be metallized to make it conductive.
NESR New Experimental Storage Ring
nMOS n-type metal oxide semiconductor
NuSTAR Nuclear Structure, Astrophysics and Reactions
OS operating system
OSI Open Systems Interconnection
$\bar{\text{P}}$ANDA Antiproton Annihilation at Darmstadt
PandaRoot A highly-integrated software framework to simulate the behavior and response of the $\bar{\text{P}}$ANDA detector.
PASTA $\bar{\text{P}}$ANDA Strip ASIC
PC personal computer
PCB printed circuit board
PCI Peripheral Component Interconnect
PDG Particle Data Group
PET positron emission tomography
PID particle identification
p-LINAC Proton Linear Accelerator
PLL phase-locked loop
pMOS p-type metal oxide semiconductor
PMT photomultiplier tube
POCA point of closest approach
pocaQA The POCA is the midpoint of the closest distance of two tracks from a common origin. Ideally, they should meet, so the quality of the approximation is given by their distance, or the *pocaQA*.
QCD quantum chromodynamics
QED quantum electrodynamics
QFT quantum field theory
Qt The Qt framework is an application toolkit, mainly used to generate graphical user interfaces. It is written in and for C++ and can be used on many different plattforms.
R3B Reactions with Relativistic Radioactive Beams
radiation length The radiation length, usually denoted as X_0, is the material-specific mean distance electromagnetic-interacting particles travel before losing a certain fraction of their original energy; for high-energetic electrons until reaching $1/e$.
RAM random-access memory
RD running disparity
refresh A refresh, or TAC refresh, is a reset of the time to analog converter's capacitor after not receiving an event for a set time. This prevents a change in the capacitors baseline which decreases slowly over time due to leakage currents.
RESR Recuperated Experimental Storage Ring
RICH Ring-imaging Cherenkov
RMS root mean square
ROM read-only memory
ROOT Object oriented framework based on C++ to handle and analyze large amounts of data efficiently, especially used for high energy physics.
RTL register-transfer level
SciTil Scintillator Tile Hodoscope
SDR single data rate
SEE single event effect
SEU single event upset
SFP Small Form-factor Pluggable
SiPM silicon photomultiplier
SIS100 Planned synchrotron at the FAIR complex with a rigidity of $100\,\mathrm{T}\cdot\mathrm{m}$.
SIS1100 The original communication interface of the JDRS between ML605 and PC, using an 1 GB/s optical link.
SIS18 A synchrotron ring at GSI that will be also used for the FAIR complex. It has a rigidity of $18\,\mathrm{T}\cdot\mathrm{m}$, hence its name.
SIS300 Planned synchrotron at the FAIR complex with a rigidity of $300\,\mathrm{T}\cdot\mathrm{m}$.
SLAC Stanford Linear Accelerator Center
SM Standard Model
SMC SubMiniature version C
SNR signal to noise ratio
SODA Synchronization of Data Acquisition
SO-DIMM small outline dual in-line memory module
SPARC Stored Particle Atomic Physics Collaboration
standard cell For digital ICs, foundries typically provide a set of predefined cells for

logic operations as basic building blocks. Using such a library immensely speeds up the development process.

state machine See finite-state machine.

stochastic cooling This cooling methods for particle beams measures the particle's transverse momentum and applies a counteracting moment on them later in the beam. Thus, the momentum spread can be reduced and a more unified (cooled) particle beam achieved.

STT Straw Tube Tracker

Super-FRS Super Fragment Separator

SVN Apache Subversion is a software versioning system, enabling revision control for a collaborative development.

TAC time to analog converter

TAC refresh See refresh.

TAL Transport Access Layer

Target Spectrometer The Target Spectrometer of PANDA is centered around the interaction point with a barrel-like structure and a solenoidal magnetic field.

TDC time to digital converter

TDC controller The digital logic controlling the processing of signals coming to a channel. It decides when to take data and charge the necessary capacitors. Each channel has one controller, connected to the analog part on the left and to the global controller on the right.

TDR technical design report

time walk The signal from a charge-collecting sensor builds up over the time of charge collection. Therefore, a threshold above noise level will always determine the rise of the pulse after it started. Depending on the total charge and the threshold level, this offset may vary. This is called *time walk*, because the resulting time stamp will walk depending on these parameters.

TMR triple-mode redundancy – a radiation effect measure, including a redundancy by tripling a register. In case one of these registers gets an upset, the majority of the three registers still holds the correct value.

TOF time of flight

TOFPET Time of Flight for Positron Electron Tomography

ToPix Torino Pixel ASIC

ToPix 4 The fourth prototype of the Torino Pixel ASIC.

TOT time over threshold

TX Transceiver

UCF user constraint file

UDP User Datagram Protocol

Verilog Verilog is a HDL standardized as IEEE 1364 to design ICs on a register-transfer level.

VHDL VHSIC Hardware Description Language – a HDL that is used to design ICs on a register-transfer level. It has been developed in the Very High Speed Integrated Circuit (VHSIC) program by the United States for military purposes.

VHSIC Very High Speed Integrated Circuit

Virtex-6 Virtex® is the flagship FPGA family developed and distributed by Xilinx. Its sixth incarnation is built with a 40 nm process and was released in 2009.

VMC Virtual Monte Carlo

WDM Warm Dense Matter

Acknowledgments

This thesis would not have been possible without the enormous support of many people.

First, I want to thank James Ritman. I am very grateful for the opportunity to write this thesis with your supervision and guidance. Our discussions were always fruitful and constructive. You have my utmost respect for always making up time if needed to, even in the most stressful periods, and never letting my questions feel trivial.

Secondly, I would like to express my deep gratitude to Tobias Stockmanns. Your constantly open door is a token for your helpful character and kind patience. Often, I could stop by to ask for help and was rewarded with practical advice. Throughout the years, you were not only my supervisor but also became a good friend.

Then there are all the other $\bar{\text{P}}$ANDA colleagues at the IKP which made my time worthwhile and enjoyable. Andi, you are the best (man) in many variations, especially when it comes to help others – including me – or just being the colleague and friend that you are. Qiang, Ludovico, Lu, Marius, Huagen, Dariusch, Simone, Jenny, Frank, Michael, Harout, Alexandros, Elisabetta, Peter, and Albrecht: Thank you for this wonderful time in the institute, at conferences, or whenever an occasion for get-togethers emerged. Also thank you to the other IKP members Artur, Daniel, Farha, Florian, Günter, Ilhan, Jette, Maria, and Rene.

During my time in Torino I not only had the pleasure to learn a lot but also to get to know many new friends. Thank you Manuel and Angelo for all your valuable input, your advice and generally the time together. I also want to thank Valentino, Alberto, Paolo, Alessandra, Serena, Sara, Jonathan, Frederico, Markus, Alice, Christina, Hannes, Kris, Osvaldo, Ilaria, Giulio, and Laura for the excellent atmosphere at the INFN and outside of it.

Thanks to all the MVD group members I have not mentioned yet: Hans-Georg, Robert, Tomasso, Gianni, Daniela, Paolo, and Giulio for all your help. Also many thanks to Aaron for your contributions during your stay. And of course to all the other $\bar{\text{P}}$ANDAs!

Vielen Dank an meine Mutter und Schwester, für eure konstante Unterstützung und die Möglichkeiten, die ihr mir geschaffen habt. And finally, my biggest 'thank you' is devoted to you, Saskia, who bore with me and supported me in every way you could.

Thank you!

Lebenslauf *Curriculum Vitae*

Persönliche Daten

Name:	André Zambanini, geb. Goerres
Geburtsdatum:	02.10.1985
Geburtsort:	Aachen

Schulbildung

1992 - 1996	Städt. Kath. Grundschule Auf der Hörn, Aachen
1996 - 2005	Kaiser-Karls-Gymnasium Aachen *Allgemeine Hochschulreife*

Studium

2005 - 2010	Studium der Physik, RWTH Aachen *Diplomarbeit*: »Kalibration und Integration des AMS-02 Anti-Koinzidenz-Detektors«

Promotion

2012 - 2015	Promotion im Fach Physik an der Ruhr-Universität Bochum in Kooperation mit dem Institut für Kernphysik am Forschungszentrum Jülich *Doktorarbeit*: »Development of a Free-Running Readout ASIC for the $\bar{\text{P}}$ANDA Micro Vertex Detector and Investigation of the Performance to Reconstruct $\bar{\text{p}}\text{p} \rightarrow \bar{\Xi}^{+}\Xi^{-}(1690)$«